静平衡柔顺壳体机构的设计与分析

Design and Analysis of Statically Balanced Compliant Shell Mechanisms

一级学科：机械工程

研究方向：柔顺机构

作者姓名：杨晓辰

指导教师：陈 焱

答辩日期	2026 年 1 月 5 日		
答辩委员会	姓名	职称	工作单位
主席	宋轶民	教授	天津大学
委员	周翔	长聘副教授	上海交通大学
	李洋	教授	武汉大学
	李建民	教授	天津大学
	杨绍琼	教授	天津大学

天津大学机械工程学院

二〇二六年一月

独创性声明

本人声明所呈交的学位论文是本人在导师指导下进行的研究工作和取得的研究成果，除了文中特别加以标注和致谢之处外，论文中不包含其他人已经发表或撰写过的研究成果，也不包含为获得 **天津大学** 或其他教育机构的学位或证书而使用过的材料。与我一同工作的同志对本研究所做的任何贡献均已在论文中作了明确的说明并表示了谢意。

学位论文作者签名：　　签字日期：　　年　　月　　日

学位论文版权使用授权书

本学位论文作者完全了解 **天津大学** 有关保留、使用学位论文的规定。特授权 **天津大学** 可以将学位论文的全部或部分内容编入有关数据库进行检索，并采用影印、缩印或扫描等复制手段保存、汇编以供查阅和借阅。同意学校向国家有关部门或机构送交论文的复印件和磁盘。

（保密的学位论文在解密后适用本授权说明）

学位论文作者签名：　　导师签名：

签字日期：　　年　　月　　日　　签字日期：　　年　　月　　日

摘要

静平衡柔顺机构通过组件内部的相互协调，在变形过程中维持机构的总应变能恒定，理论上可实现无需外力及外部供能的自维持运行，在航空航天，医疗辅助，精密仪器等领域应用前景广阔。然而，与传统杆簧式静平衡系统相比，柔顺壳体机构的非线性大变形特性给其结构设计、力学分析与驱动实现等方面均带来诸多挑战。为此，本研究融合结构设计与力学分析，设计了一系列静平衡柔顺壳体机构，并结合刺激响应材料，实现了在恒定刺激下的周期性持续运动。本文的研究重点如下：

首先，设计了由波纹管与壳体平衡器同轴安装构成的多组件静平衡柔顺壳体机构。建立波纹管轴向非线性大变形理论模型，奠定了根据给定应变能曲线进行逆向设计的基础。进而设计了与波纹管应变能相匹配的壳体平衡器，并通过内外层预应力装配，使得整个机构在往复变形过程中的总应变能近似恒定。在最优参数下，该机构的驱动力相比传统波纹管结构降低了 96.38%。

其次，设计了基于多稳态吸管的单组件静平衡柔顺扭矩联轴器。通过解析多稳态吸管的弯曲稳态特性，确定了具有弯曲稳态的几何参数范围。在此基础上建立的简化梁模型，精确预测了联轴器单元处于稳态构型下的弯曲角度。进一步结合数值模拟与扫描实验结果，研究联轴器单元的扭转变形过程，揭示了在扭转过程中的形状保持特性以及应变能重分配机制，实现了该联轴器在大弯曲角度下的高效扭矩传递。

最后，将莫比乌斯带几何与湿度响应材料相结合，提出三重对称莫比乌斯驱动器，在恒定的湿度梯度下实现了自持的周期性运动。结合可展曲面理论与三维扫描提取的关键特征，精确实现了满足对称性边界条件的三重莫比乌斯几何重建，并建立了驱动器自转与公转的理论模型，揭示了其在湿度梯度下的形状保持和持续运动机制，确定了运动速度与几何、环境参数之间的定量关系。参数优化后的驱动器可持续稳定运动超 252 小时，并兼具持续的机械功输出和环境湿度感知功能。

本论文围绕静平衡柔顺壳体机构，系统开展了结构设计、理论建模与驱动策略的研究，为静平衡壳体柔顺机构的创新设计与工程应用奠定理论基础。

关键词：柔顺机构，多稳态，静平衡，吸管结构，莫比乌斯带

ABSTRACT

Statically balanced compliant mechanisms can maintain constant total strain energy through internal coordination during deformation, enabling autonomous operation without external forces or energy input. This gives them great potential for applications in aerospace systems, medical assistive devices and precision instruments. However, unlike conventional beam-based statically balanced compliant mechanisms (SBCMs), nonlinear large deformation of shell-based SBCMs introduces considerable challenges in structural design, mechanical analysis and actuation strategies. This dissertation proposes statically balanced compliant shell mechanisms by combining structural design and mechanical analysis. Moreover, by integrating intelligent materials with SBCMs, autonomous periodic motion can be stably generated under constant stimuli. The highlights of this dissertation are as follows.

First, a multi-component SBCM consisting of a bellow and a coaxially arranged shell balancer is proposed. A theoretical model for the axial nonlinear large deformation of the bellows is established, which enables inverse design according to specified strain energy curves. Then, a shell balancer is inversely designed to match the given strain energy curve. Through prestressed assembly, the bellow-shaped SBCM can remain almost constant strain energy with nearly zero actuation force and input energy. The optimized SBCM could decrease the actuation force by 96.38% of that needed for the stand-alone bellow.

Second, a statically balanced compliant torque coupling comprising only a single component is proposed here. Through investigation of the bending characteristics of multistable straws, numerical simulation is conducted to identify the parameter range for bending stability. Then, a simplified beam model is developed to accurately predict its stable configuration. Moreover, numerical simulation and experimental results demonstrate that the bent coupling unit can maintain unchanged overall geometry through redistribution of strain energy during torsion, thus enabling highly efficient torque transmission at large bending angles.

Third, by integrating the Möbius strip with humidity-responsive materials, a threefold Möbius actuator is proposed to stably generate self-sustainable rotational motion under constant graded humidity. Partially captured morphological surfaces from experimental scanning are utilized to precisely reconstruct this complex surface

on the theory of developable surfaces, which also satisfies symmetric boundary conditions. A theoretical model is built based on moisture diffusion and developable surfaces to reveal the underlying mechanism of curvature-driven rotary motion with shape preservation. The quantitative correlations between the motion speed and the geometric/environmental parameters are established to optimize the design under given constraints. Guided by these correlations, the Möbius actuator can exhibit multifunctional capabilities including long-term motion over 252 hours, continuous mechanical work output, and humidity sensing.

Finally, this dissertation develops systematic investigation on the structural design, mechanical modelling and actuation strategies of statically balanced compliant shell mechanisms. Our research establishes theoretical foundations for innovative SBCM design and practical implementation.

KEY WORDS: compliant mechanism, multi-stability, static balance, straw structure, Möbius strip

Contents

List of Figures

List of Table

Notations

Parameters

$a_0,\ a_1,\ a_2,\ a_3$	Coefficients of the term of degree for the cubic equation
$a_{\mathrm{M}},\ b_{\mathrm{M}}$	Coefficients of the fitted biquadratic curve for the projected curve of the Möbius actuator
$a_{\mathrm{TP}},\ a_{\mathrm{BT}}$	Semi-major axes of the deformed upper and bottom elliptical rims under bending
A_1, A_2	Cross-sectional areas of the bellow unit and balancer unit
$b_{\mathrm{TP}},\ b_{\mathrm{BT}}$	Semi-minor axes of the deformed upper and bottom elliptical rims under bending
d	Width parameter d perpendicular to the line
D_{A}	Distance from the intersection apex point of the neighbouring conical generators to the central axis through any point A
e_{S}	Volumetric strain energy density
$\boldsymbol{e}_r,\ \boldsymbol{e}_\varphi$	Radial and circumferential unit vectors
E	Young's modulus of materials
E_{D}	Kinematic energy of the disk driven by the Möbius actuator
E_{K}	Kinematic energy of the system
E_{mech}	Mechanical energy of the system
f_{C}	Friction force of the contact point C
$f_{\mathrm{C}t_0}, f_{\mathrm{C}n_0}$	Original tangent and normal component of f_{C}
F	Internal force of the system
$F_{(1,i)x},\ F_{(2,i)x}$	Horizontal concentrated forces at the i-th beam segments of the bellow unit and the balancer unit
$F_{(1,i)y},\ F_{(1,i)y}$	Vertical concentrated forces at the i-th beam segments of the bellow unit and the balancer unit
F_{ela}	End force for the generalized elastica-similarity equation

F_{Ax}, F_{Ay}, F_{Az}	Force components at any point A in the x, y, z- direction
F_{At}, F_{An}, F_{Ab}	Force components at any point A in the tangent, normal, and binormal directions of the Frenet-Serret frame
$\boldsymbol{g}(s)$	Generator vector with respect to the length parameter s
h_1, h_2	Heights of the bellow unit and the balancer unit
I_1, I_2	Cross-sectional moments of the bellow and the balancer unit
$I_{1,i}$, $I_{2,i}$	Cross-sectional moments of the i-th segments of the bellow unit and balancer unit
k	Stiffness of the spring
$\boldsymbol{K}$	Stiffness of the system
K_{κ_r}	Fitted constant for generalized radial curvature
K_{ϕ_R}	Fitted constant for stable angle of the right connecting rod with the frame
K_{ξ}	Fitted constant characterizing humidity absorption/desorption capability of the agarose film
K_F	Fitted Constant for the internal force in the Möbius actuator
K_D	Fitted constant for the apex distance
K_Q	Fitted constant for the maximum principal curvature κ_Q of any inflection point Q
l	Length of the Möbius strip
l_0	Lengths of the cross-sectional curved beams of the SBCTC unit
l_1, l_2	Lengths of the cross-sectional curved beams of the bellow and the balancer unit
l_R	Length of the rigid link
l_T	Tape length of the Möbius actuator
L_M	Total length of the visible marker captured by the camera
$\boldsymbol{q} = [q_1, q_2, \ldots, q_n]$	Generalized coordinates for n degrees of freedom (DoFs)
m	The number of discrete line segments of the beam
m_D	Weight of the disk above the Möbius actuator

$\boldsymbol{m}$	Mass matrix of the system
M_1, M_2	Local maximum and minimum moments occurred at the two inflection points of the moment-displacement curve
$M_{1,i}$, $M_{2,i}$	Concentrated moments at the i-th beam segments of the bellow unit and the balancer unit
M_{A}	Concentrated moment at any point A
$M_{\mathrm{A}x}$, $M_{\mathrm{A}y}$, $M_{\mathrm{A}z}$	Moment components at any point A in the x, y, z-direction
$M_{\mathrm{A}t}$, $M_{\mathrm{A}n}$, $M_{\mathrm{A}b}$	Moment components at any point A in the tangent, normal, and binormal directions of the Frenet-Serret frame
M_{ela}	End moment for the generalized elastica-similarity equation
n	The number of discrete elements of the shell structure in the circumferential direction
n_{AX}, n_{AY}, n_{AZ}	Normal vector components of any point A in X, Y, Z directions
n_{D}	Experimental global motion rates of the disk above driven by the Möbius actuator
n_{L}, n_{G}	Experimental local and global motion rates of the Möbius actuator
$n_{\mathrm{L}}^{\mathrm{THE}}$, $n_{\mathrm{G}}^{\mathrm{THE}}$	Theoretical local/global motion rates of the Möbius actuator
n_{IN}, n_{OUT}	Input and output rotational rates of the SBCTC
N	The number of the unit
N_{Tw}	Twisting number of the Möbius strip
$\boldsymbol{p}(s,d)$	Position vector of any arbitrary point on the curved surface parameterized by the length parameter s along the center line and the width parameter d perpendicular to the line
r, R	Inner and outer radii of the SBCTC unit
r_1, r_2	Inner radii of the bellow and the balancer
r_{D}, R_{D}	Inner and outer radii of the disk above the Möbius strip
r_{F1}, r_{F2}	Fillet radii of the bellow unit and the balancer unit
r_{IF}, r_{OF}	Inner and outer fillet radii of the SBCTC unit

r_{TP}, r_{BT}	Radii of the original upper and bottom circular rims
r_{κ}	Radius of curvature of the central axis of the beam
r_{P}	Distance between any inflection point P and the origin O
r_{Q}	Distance between any cylindrical point P and the origin O
$\boldsymbol{r}(s)$	Parametric equation of the curved center line with respect to the arc length parameter s
R_1, R_2	Outer radii of the bellow and the balancer
RH_{am}	Ambient relative humidity at room temperature of 25℃ and 1.0 atmosphere pressure
RH_{up}	Relative humidity on the upper surface of the Möbius actuator at room temperature of 25℃ and 1.0 atmosphere pressure
RH_{sub}	Relative humidity of the substrate at room temperature of 25℃ and 1.0 atmosphere pressure
R_{M}	Global rotational radius of the Möbius actuator
$\boldsymbol{R}_{\boldsymbol{u}}(\varphi_u)$	Rotational matrix for rotating by an angle φ_u about the $\boldsymbol{u}$ vector following the right-hand rule
$\boldsymbol{R}_{\mathrm{X}}$	Rotational matrix for rotating about the X-axis
$\boldsymbol{R}_{\mathrm{Z}}$	Rotational matrix for rotating about the Z-axis
$\boldsymbol{R}_{\mathrm{XZ}}$	Rotational matrix for rotating about the X-axis and Z-axis
s	Arc length coordination of any point A
s_{A}	The arc length coordination of any point A
s_{QM}^{xy}	The projected arc length of the curved center line QM on the xoy plane
t	Thickness of the Möbius strip
t_1, t_2	Thicknesses of the bellow and the balancer
t_{IF}, t_{OF}	Thicknesses of the inner and outer hinge-like filleted regions of the SBCTC unit
t_{TP}, t_{BT}	Thicknesses of the bottom and upper frusta of the SBCTC unit
T_{AG}	Exposure time of the AG film in each test cycle

T_D	Time periods of global motion of the disk above the Möbius actuator
T_{L}, T_{G}	Time periods of local and global motion of the Möbius actuator
$T_{\mathrm{L}j}$	The j-th local motion cycles of one specific Möbius actuator
T_{R}	Time periods of torsion of the SBCTC
$\boldsymbol{T}_{\mathrm{M}}$	Transition matrix of the Möbius actuator
u	Axial displacement along the Euler beam in bending
$U_{\mathrm{S,bd}}$	Bending strain energy
$U_{\mathrm{S,hoop}}$	Hoop strain energy
U_{S}	Strain energy
$U_{\mathrm{S}}^{\mathrm{T}}$, $U_{\mathrm{S}}^{\mathrm{T+\Delta T}}$	Strain energy at the moment T, T+ΔT
v	Transverse deflection of the Euler beam in bending
v_{A}	Resultant velocity of any point A
v_{L}, v_{G}	Velocities of the local and global motion of the Möbius actuator
$v_{1,i}, v_{2,i}$	Transverse deflections of the i-th beam segments of the bellow unit and balancer unit
w	Width of the Möbius strip
$w_{\phi_{\mathrm{R}}}$	General calculation weight applied for the stable angle of the right connecting rod with the frame
$\mathrm{Z_M}$	Height of the motion space above the substrate
Δl	Width of an infinitesimal quadrilateral stripe
Δl_1, Δl_2	Discrete lengths of the cross-sectional curved beams of the bellow and the balancer unit
Δl_{e}	Major-axis absolute elongation of the upper rim during its deformation from a circular to an elliptical shape
ΔRH	Relative humidity difference between the substrate and the top of the Möbius actuator at room temperature of 25℃ and 1.0 atmosphere pressure
∇RH	Gradient of the relative humidity

$\bar{\nabla} RH$	Average gradient of the relative humidity
$\{\boldsymbol{t}_{\mathrm{A}}, \boldsymbol{n}_{\mathrm{A}}, \boldsymbol{b}_{\mathrm{A}}\}$	Basis vector set of the Frenet-Serret frame at any point A, i.e. the tangent, principal normal and binormal vectors
$\{\boldsymbol{t}(s), \boldsymbol{n}(s), \boldsymbol{b}(s)\}$	Basis vector set of the Frenet-Serret frame for the central axis with respect to the length parameter s

Greek Alphabets

α	Slant angles of the bam to the x-axis
α_0	Slant angle of the inflection point P on the projected curve of the central axis of the Möbius actuator on the xoy plane
$\alpha_1,\ \alpha_2$	Slant angles of the bellow and the balancer
$\alpha_{1,i},\ \alpha_{2,i}$	Slant angles of the i-th beam segments of the bellow unit and the balancer unit
α_{A}	Slant angle of any point A on the projected curve of the central axis of the Möbius actuator on the xoy plane
$\alpha_{\mathrm{BF}},\ \alpha_{\mathrm{UF}}$	Slant angles of the bottom and upper frustums
α_{Tw}	Twisting angle of the Möbius strip
β_{A}	Included angle between the binormal vector of the center line and the generator vector through any point A
β_0	Helical angle of the central axis of the Möbius actuator
$\beta(s)$	Included angle between the binormal vector of the center line and the generator vector with respect to the length parameter s
γ_{T}	Torque transition angle of the SBCTC system
$\delta_{\min}$	The minimum distance between the two surfaces
σ_{F}	Fracture stress of materials
σ_{Y}	Yield stress of materials
$\varepsilon_{\mathrm{MAX}}$	The maximum tensile strain of the structure
ε_{F}	Fracture tensile elongation of materials
ε_{Y}	Yield tensile elongation of materials
ε_{ρ}	Circumferential strain induced by radial deformation

ε_{ρ_i}	Circumferential strain induced by radial deformation at the *i*-th segment of the belllow or the balancer
η	Torque transition efficiency of the SBCTC system
θ	Rotation angle of a beam in bending
$\theta_{1,i},\ \theta_{2,i}$	Rotation angles of the *i*-th beam segments of the bellow unit and balancer unit
θ_{AB}	Included angle between line AB and the tangent at point A
θ_{bd}	Bending angle of the SBCTC unit
$\theta_{\mathrm{bd}}^{\mathrm{I}},\ \hat{\theta}_{\mathrm{bd}}^{\mathrm{I}}$	Numerically obtained and theoretically fitted bending angles achieving the maximum strain energy at Stage I
$\theta_{\mathrm{bd}}^{\mathrm{II}},\ \hat{\theta}_{\mathrm{bd}}^{\mathrm{II}}$	Numerically obtained and theoretically fitted bending angles achieving the stable state at Stage II
θ_{ela}	End angle for the generalized elastica-similarity equation
θ_{P}	Included angle between the central axis through any inflection point P and the substrate plane
θ_{Q}	Included angle between the central axis through any cylindrical point Q and the substrate plane
θ^{T}	Included angle between the quadrilateral stripe around point A and the substrate plane
κ_1	Maximum principal curvature on the curved surface
$\kappa_1^{\mathrm{T}},\ \kappa_1^{\mathrm{T+\Delta T}}$	Max principal curvature of any point A at the moment T, T+ΔT
κ_{A}	Maximum principal curvature of any point A on the curved surface
$\overline{\kappa}_{\mathrm{AG}}$	Average curvature of the AG film
$\kappa_r,\ \kappa_\varphi$	Generalized radial and circumferential curvature
κ_r^{MAX}	Maximum radial curvature
$\hat{\kappa}_{\mathrm{Q}}$	Fitted value of the maximum principal curvature κ_{Q} of any inflection point Q
μ_D	Fitted proportional constant for the apex distance
μ_{L}	Parameter for measuring the stability of local motion
ν	Poisson's Ratio of materials

ξ	Humidity absorption/desorption rate per unit area normal to the humid substrate
$\Delta\tau$	Difference of the input and output torque
τ_{IN}, τ_{OUT}	Input and output torque of the SBCTC
φ_{GM}	Included angle between the centripetal direction of global motion trajectory and the direction of $\boldsymbol{v}_{\mathrm{L}}$
φ_{Q}	Included angle between the generator through the cylindrical point Q and the substrate plane
φ_n	Discrete circumferential angle of the beam segments of the bellow unit and balancer unit
φ_{tr}	Torsional angle of the SBCTC unit
$\hat{\varphi}_{\mathrm{Q}}$	Fitted included angle between the generator through the cylindrical point Q and the substrate plane
φ'_{Q}, φ''_{Q}	Measured included angle between the upper/bottom contours and the substrate plane from the side view
φ_{X}, φ_{Y}, φ_{Z}	Rotational angles about the X-, Y-, Z-axis
$\boldsymbol{\phi}$	Modal vector
ϕ_{L}, ϕ_{R}	Angles of the left and right connecting rod with the frame
$\phi_{\mathrm{R}}^{\mathrm{lim}}$, $\phi_{\mathrm{R}}^{\mathrm{sta}}$	Limited angle and stable angle of the right connecting rod with the frame for a SBCTC unit
ω_n	Nature frequency of the system

Abbreviations

3D	Three dimensional
atm	The standard atmosphere
AG	Agarose
DIC	Digital image correlation
DoF	Degree of freedom
FDC	Forward dead centre
FEM	Finite element model
LCE	Liquid crystal elastomers

LC phase	Liquid crystal phase
LE, MAX	The maximum logarithmic strain
LH, RH	Left-handed, right-handed
MOD	Modified model
PET	Polyethylene terephthalate
PMMA	Polymethyl methacrylate
PP	Polypropylene
TPU	Thermoplastic polyurethane
S4R	Four-node shell elements with reduced integration
SBCM	Statically balanced compliant mechanism
SBCTC	Statically balanced compliant torque coupling

Chapter 1 Introduction

1.1 Background and Significance

In common machinery, undesired aspects of system behaviors, including friction, mechanical vibration, material hysteresis and fatigue failure, can not only reduce mechanical efficiency due to excessive energy consumption, but also hinder accurate force transmission and feedback[1]. For instance, non-ideal lever systems consume extra energy to overcome inherent inertia[2], while hydraulic actuators incur additional loads and shortened lifespan under repeated mechanical deformation[3].

Unlike rigid mechanisms, compliant mechanisms transmit force, motion and energy through elastic deformation of the flexible elements[4-8]. Their monolithic manufacturing can effectively avoid assembly-induced errors, which ensures high precision and facilitates micro-electro-mechanical systems (MEMS) applications[9-12]. Among them, compliant shell mechanisms[13-15], with spatially curved thin-walled structures, enable large and predictable deformation, as well as programmable load control[16], excelling in space-constrained applications requiring large motions[17-19] see Fig. 1-1. In common with other machinery, potential energy stored in flexible components as strain energy reduces the energy efficiency of the input and output[20].

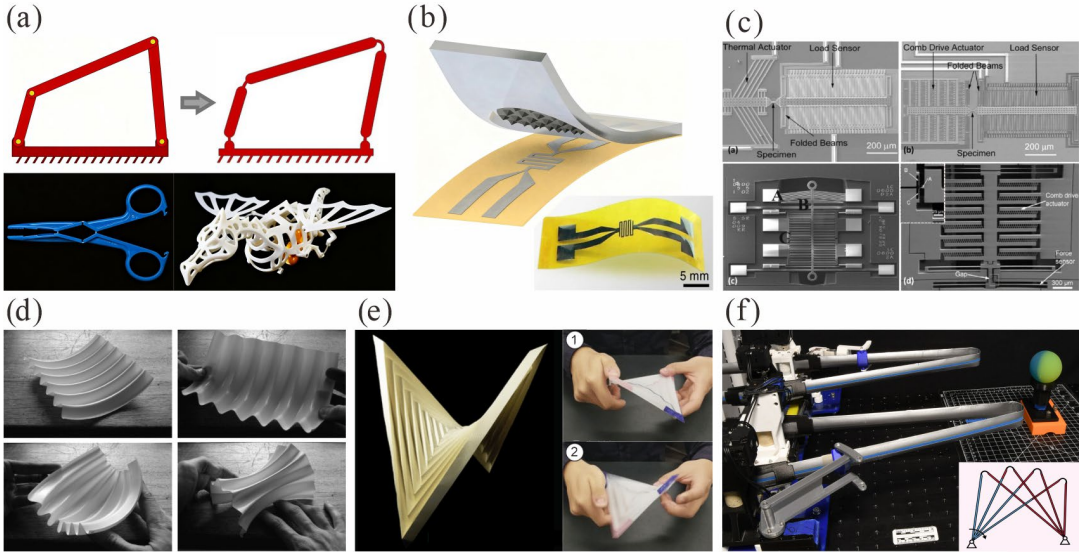

Fig. 1-1 Concept and applications of compliant mechanisms. (a) The rigid and fully compliant four-bar mechanism[4], fully-compliant scissors[5] and bionic dragon skeleton[7]; (b) the compliant m-MEMS platform[9]; (c) the fully compliant cell grasper[11]; (d) a curved corrugated shell[13]; (e) the multi-stable hypar origami structure[16]; (f) the deployable gripper GRIP tape[17].

Statically balanced systems[1], exemplified by ideal fixed pulleys, can maintain continuous equilibrium without additional energy input through coordination and compensation of potential energy, resulting in perfect energy efficiency during motion. In compliant mechanisms, applying this "static balance" principle to compliant mechanisms, statically balanced compliant mechanisms (SBCMs) are designed here by replacing gravitational potential energy in pulleys with strain energy in flexible components[21]. Zero actuation force and ideal efficiency[22] realized in SBCMs have inspired applications from "effortless" surgical forceps for invasive surgery[23], user-friendly exoskeletons including elbow orthosis and hand prosthesis[24,25], to tape springs in deployable space structures[26,27], see Fig. 1-2. With the rapidly growing demands for miniaturization, ultra-high precision, efficiency, cost reduction and environmental sustainability in modern industry[28-32], statically balanced compliant shell mechanisms possess certain potential to fulfill these necessities.

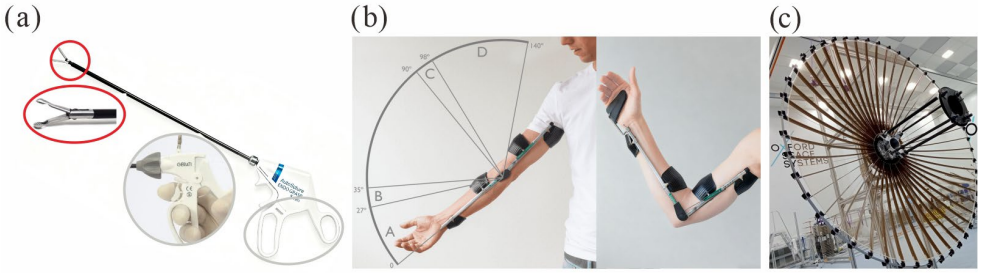

Fig. 1-2 Applications of SBCMs[21,22]. (a) A statically balanced compliant laparoscopic grasper[23]; (b) a Wilmer elbow orthosis[24,25]; (c) space deployable antennas composed of tape springs[26].

Current SBCMs are typically achieved by matching two elastic components that exhibit equal but opposite mechanical behaviors[1,28] under the shared displacement. Summing their opposed load curves of each component yields the resultant force that remains zero throughout motion, with the constant strain energy. In prior studies, such mechanisms are primarily realized in beam elements[10,21-23] with linear deformation. Expanding beam-based SBCMs to shell-based ones holds practical significance[66] due to structural compactness, motion precision and lightweight. The critical issue for shell-based SBCMs still lies in designing precisely matched balancers for shell structures to realize static balance through nonlinear global deformation[13].

In fact, static balance can be achieved either via mutual coordination between components or via self-equilibrated internal stress in single-component mechanisms

with constant strain energy to enhance integration and reliability of the system[66,67]. However, existing self-equilibrated structures remain limited to specific applications, such as prestressed tape springs[87,88] and gearless disk motors[90,91] due to sensitive manufacturing process and restricted workspace. However, such neutral stability can be achieved through structural topology. Closed-loop configurations including Möbius strips and topological knots can intrinsically maintain equilibrium through geometric design. Their intricate geometries lack compatible actuation strategies, severely limiting practical implementation. Although integration with stimuli-responsive materials[116-118] exhibit potentials to overcome this limitation and further unlock fascinating functionalities, developing generalized theoretical models for these coupled systems remains to be accomplished[181,182] for reliable behavior prediction.

Therefore, to advance the application boundaries of SBCMs in shell structures, this dissertation not only focuses on structural design and mechanical analysis, but also explores actuation strategies. These multiple dimensions provide operational guidance and theoretical foundations for enhancing mechanical performance of systems, which not only realizes high-efficiency transmission, but also facilitates the novel contactless driving strategy to unlock potential technological innovation from microscopic biomedical domains to large-scale industrial machinery.

1.2 Literature Review

1.2.1 Compliant Shell Mechanisms

Compliant shell mechanisms, as a distinct category of compliant mechanisms, are defined as spatially curved thin-walled structures that transfer force, motion, or energy through elastic deflection[13,33]. Their ultra-low thickness and diverse geometries enable precise control, large and reversible deformation through inherent structural stability. Notably, multistable compliant shells[34,35] can switch between states through snap-through behavior, which exhibits reconfigurability and negative stiffness that enable designs of mechanical metamaterials[36,37] and adaptive robotics[38,39]. To analyze their complicated behaviors, equivalent compliance methods deliver complete nonlinear characterization, supplemented by numerical analysis of in-plane and out-of-plane deformation[40, 41].

Introducing corrugated patterns on shell surfaces provides an effective strategy for designing compliant structures[46-48]. In planar sheets, corrugations can generate multiple twisted stable states during stretching[42]. By adjusting geometric parameters, multistable sheets with rewritable patterns can provide reliable shape morphing through repeated actuation cycles[43] in Fig. 1-3(a). When applied to open cylindrical surfaces, this method generates diverse configurations with both positive and negative Gaussian curvatures, including doubly-curved geometries and orthogonal saddle shapes[15], see Fig. 1-1(d). For closed tubular structures, uniform corrugations provide reconfigurability and symmetric deformation forming bellows[44] that enable applications including accordion bellows[45], fluid/heat transmission pipelines[46-49] and even oil bladders in buoyancy engines[50-53].

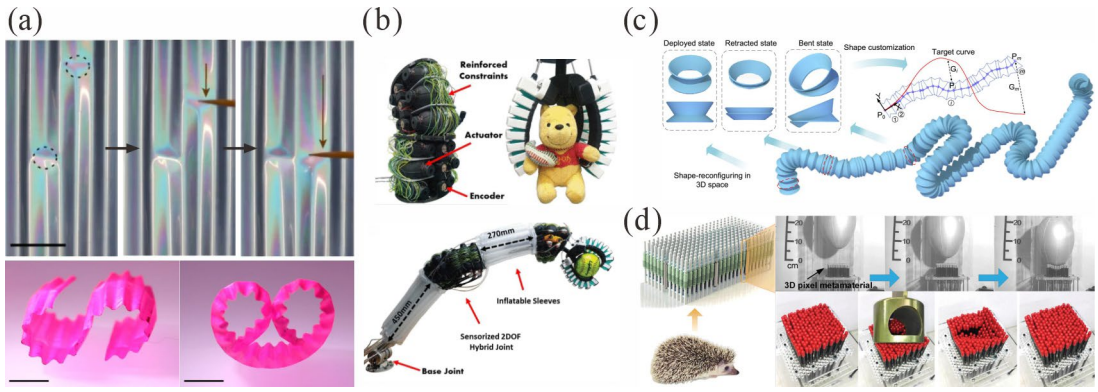

Fig. 1-3 Corrugated compliant shell mechanisms. (a) Multistable sheets with rewritable patterns for switchable shape-morphing[42]; (b) a slime robot gripper using bridle bellows[49]; (c) Multistable shape-reconfigurable metawire in 3D space[57]; (d) 3D pixel mechanical metamaterials for energy absorption[58].

When asymmetric corrugations are introduced, the common drinking straw composed of serially connected cylindrical frustum shells with alternating orientation, exhibits both multistability and neutral stability[54]. Each unit possesses three independent stable states: the original extended state, the retracted state with full inversion of the frustum shell, and the special bent state with partial inversion of the frustum shell[55]. Notably, the bent state can maintain stability at any circumferential position with consistent geometry, demonstrating characteristic neutral stability[58].

Current theoretical research and applications primarily focus on multistability and mutual transitions between stable states. Through numerical simulation based on beam-

hinge and discretized stiffness models[56-58,63], geometric parameters, inherent stress distribution, and cross-sectional profiles on multistable behaviors[56,61] were systematically investigated to design 3D pixel metamaterials for energy absorption and shape reconfiguration[59], metawires for shape transformation[57,58] and soft robots in obstructed environments[60-62]. However, the bent state still lacks detailed analysis of the intrinsic shell morphology. The neutral stability of multi-directional bent states has been primarily limited in static shape morphing, while its dynamic mechanisms and engineering potential remain largely unexplored, and require deep investigations into fundamental principles and expanded practical applications.

1.2.2 Statically Balanced Systems

Static balance occurs when all forces and moments in a mechanical system are mutually counterbalanced, causing zero resultant force and moment. Moreover, if a system that maintains ***continuous equilibrium*** throughout a certain range of motion, rather than merely at discrete positions can be defined as ***a statically balanced system***. This state, characterized by the constant potential energy that exists between stability and instability is also called ***neutral equilibrium*** or ***neutral stability***. Excluding viscosity and friction, such idealized system requires zero energy input during motion, realizing an ***energy-free*** state with theoretically perfect energy efficiency. Here, the meaning conveyed by bold text can be mutually substituted in this dissertation.

The concept of statically balanced systems can be traced back to ancient gravity equilibrators[1,64,65] for efficient cyclic lifting of heavy masses. Exemplified by pulley systems and lever mechanisms, the moments generated by counterweights at both ends exert each other, resulting in zero resultant moment and achieving static equilibrium. In terms of energy, the gravitational potential energy gained at one end is precisely lost by the other end and vice versa, achieving dynamic stabilization of the total potential energy.

Notably, excessive potential energy in compliant mechanism is stored in deformed compliant components as strain energy U_S, which inevitably reduces system efficiency by introducing additional stiffness[21]. This efficiency loss is particularly critical in compliant mechanisms, which transmits motion and force via elastic deformation rather than hinges and joints in traditional rigid mechanisms. To address this, static balance can be combined with compliant mechanisms to maintain constant total strain energy

through internal coordination of components and continuous redistribution of strain energy, enabling perfect energy efficiency during operation.

The flow diagrams of strain energy in Fig. 1-5 clearly illustrate transfer paths in both compliant mechanisms and SBCMs. For common compliant systems, a portion of strain energy has to be stored in deformed compliant components, causing loss in output energy, see Fig. 1-4(a). However, in SBCMs, the stored strain energy can be precisely compensated by strain energy release from other compliant elements, similar to counterweight in a pulley system, see Fig. 1-4(b). In addition, the stored strain energy due to localized deformation can be directly compensated within the single compliant component through internal coordination, ultimately maintaining equal energy input and output, as shown in Fig. 1-4(c).

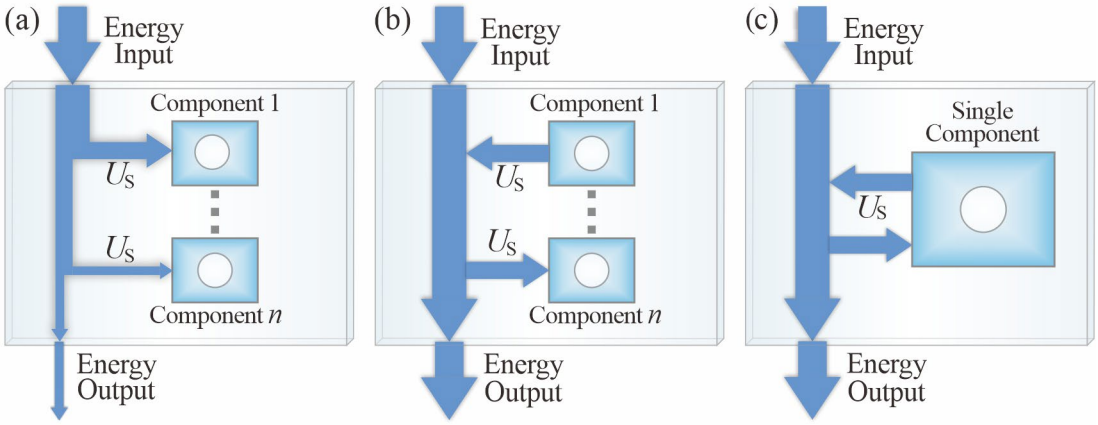

Fig. 1-4 Flow diagram of the energy stream during deformation. (a) Energy flow in common compliant mechanisms; (b) energy flow in SBCMs with multiple compliant components; (c) energy flow in SBCMs with one single compliant components.

1.2.3 Generalized Principle for SBCMs

Based on energy conservation principles, theoretical deduction demonstrates that static balance in isolated SBCMs can maintain constant total mechanical energy E_{mech} composed of kinetic energy E_{K} and the strain potential energy U_{S}. While E_{K} remains conserved in any inertia frame, the strain energy U_{S} must be positive in any deformed structure, implying that prestress is necessarily required in a statically balanced system[21].

In a system with n degrees of freedom (DoFs) described by the generalized coordinates $\boldsymbol{q} = [q_1, q_2, q_3, \ldots q_n]$, the strain energy is a function $U_{\text{S}}(\boldsymbol{q})$. Its derivative

along a path $s(\boldsymbol{q})$ yields the internal force $\boldsymbol{f}$ as $\mathrm{d}U_{\mathrm{S}} = -\boldsymbol{f}\mathrm{d}s = \boldsymbol{0}$. The force components $\boldsymbol{f}_i$ can be obtained by taking the total differential of $U_{\mathrm{S}}(\boldsymbol{q})$.

$$\mathrm{d}U_{\mathrm{S}} = \sum_{i=1}^{n} \frac{\partial U_{\mathrm{S}}}{\partial q_i} \mathrm{d}q_i = -\sum_{i=1}^{n} f_i \mathrm{d}q_i = 0,\ f_i = -\frac{\partial U_{\mathrm{S}}}{\partial q_i} = 0.\ \ i=1, 2, 3,\cdots n. \tag{1-1}$$

From this, the tangential force components f_i to the trajectory should be zero, allowing stable positioning within its range of motion, though the internal force $\boldsymbol{f}$ of the trajectory may not be zero due to normal components.

And the stiffness $\boldsymbol{K}$ of the system can be obtained by the second derivative of U_{S}, which can be expanded as the linearized constitutive equation through a first-order Taylor expansion of Eq. (1-2) as follows.

$$\frac{\partial^2 U_{\mathrm{S}}}{\partial q_j \partial q_i} = -\frac{\partial \boldsymbol{f}}{\partial \boldsymbol{q}} = \boldsymbol{K},\ \Delta \boldsymbol{f} = \boldsymbol{K}\Delta \boldsymbol{q} = \boldsymbol{0}. \tag{1-2}$$

Since $\Delta \boldsymbol{q}$ is not $\boldsymbol{0}$ due to the motion, it follows that the stiffness matrix $\boldsymbol{K}$ must be singular and semi-positive definite for stability, indicating zero stiffness along at least one specific direction.To further explore their dynamic characteristics, the generalized eigenvalue problem can be derived from the basic dynamic formula as follows.

$$(\boldsymbol{K} - \boldsymbol{m}\omega_n^2)\boldsymbol{\phi} = \boldsymbol{0}. \tag{1-3}$$

where ω_n is the nature frequency, $\boldsymbol{m}$ is the positive definite mass matrix and $\boldsymbol{\phi}$ is the modal vector. Substituting Eq. (1-3) into Eq.(1-4), we can obtain

$$(\boldsymbol{K} - \boldsymbol{M}\omega_n^2)\Delta \boldsymbol{q} = \boldsymbol{0},\ \boldsymbol{M}\omega_n^2 \Delta \boldsymbol{q} = \boldsymbol{0}. \tag{1-4}$$

Given that $\Delta \boldsymbol{q} \neq \boldsymbol{0}$ due to the motion and the positive definite matrix $\boldsymbol{M}$, the natural frequency ω_n must be zero. Thus the system can be free from resonance upon perturbation.

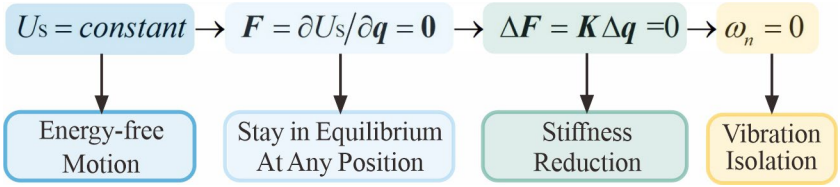

Fig. 1-5 Theoretical deduction of SBCMs and their typical applications

Specially, a 1-DoF system must exhibit zero-stiffness (***K*****=0)** throughout the range of motion. However, this condition alone does not ensure static balance in any SBCMs, as resultant forces must be identically zero. In comparison, conventional constant-force mechanisms only require the resultant forces to remain constant, which is not necessarily zero.

Figure 1-5 graphically concludes the core concept of neutral equilibrium, and the corresponding inherent characteristics of the system. From a fundamental perspective, a system in neutral equilibrium maintains constant positive strain energy within the range of motion. This demonstrates that the prestress is essential for those SBCMs without external energy input, thereby achieving ideal energy efficiency. As indicated in Eq. (1-1), zero tangential forces along the motion trajectory ensure stable positioning across the entire operational range and facilitate applications in flexible spacecraft, rehabilitation, and robotic applications.

The stiffness matrix ***K*** derived from Eq. (1-2) is positive semi-definiteness and singularity, yielding near-zero equivalent stiffness in specific directions. This reduced operational stiffness enhances force feedback transparency between the input and output, thereby greatly improving the precise control of micro-force manipulation and haptic feedback. With the zero natural frequency of the system derived from this stiffness matrix in Eq. (1-4) provides excellent anti-disturbance capability. The system can maintain non-resonant stability under various disturbances, effectively eliminating oscillations upon perturbation and making it an optimal solution for passive isolation systems. The first three properties, i.e. constant strain energy, near-zero resistance motion and stiffness reduction constitute the core focus of our dissertation.

1.2.4 Classification of SBCMs

Statically balanced compliant mechanisms that operate without external forces can be generally classified into two main categories based on the amount of compliant components[66], i.e. “multi-component SBCMs” and “single-component SBCMs”. And each category can be further subdivided according to their distinct underlying energy flows and corresponding applications, which will be analyzed respectively as follows.

1.2.4.1 Multi-component SBCMs

In the multi-component systems, multiple compliant elements are connected in parallel or series, which forms mutually constrained motion with shared DoFs. During assembly, the initial strain energy is introduced and stored within these compliant

elements via ontrolled prestress. Strain energy dynamically flows and compensates between these compliant elements, maintaining constant total strain energy during operation, see Fig. 1-4(b).

Here, for a SBCM containing only two independent compliant elements, their load-displacement curves of these two elements exhibit mirror symmetry relative to the displacement axis, leading to the zero resultant force, and thus static equilibrium without any external forces and energy input.

Taking the double-spring tensegrity mechanism proposed by Herder as a typical example[1], two ideal zero-length springs with identical stiffness k are prestretched and mounted on a rigid link, with one ends aligned collinearly and the opposite ends coincided at point A, see Fig. 1-6(a). When distances l_{OA}, l_{OC} equal to the length of the rigid link l_R, the total strain energy U_S can be derived in Eq. (1-5).

$$U_S=\frac{k}{2}(2l_R\cos\frac{\varphi}{2})^2+\frac{k}{2}(2l_R\sin\frac{\varphi}{2})^2=2kl_R{}^2=constant,\quad \varphi\in[0,\ \pi]. \tag{1-5}$$

At this point, U_S of the system remains constant and unchanged with the rotation angle φ of the rigid link. During clockwise rotation with increasing φ, strain energy transfers from spring OA to spring OC, revealing generalized negative stiffness in OA and positive stiffness in OC.

Moreover, the fundamental design of these 2D tensegrity mechanisms can be extended to 3D structures[67] in Fig. 1-6(b). Then, the practical hybrid pulley-spring mechanisms here are applied to emulate the behavior of ideal zero-length springs, and achieves static equilibrium over a large spatial motion range with the constant strain energy[68]. Beyond this, 2D neutrally stable units are also functioned as fundamental building blocks to create structural metamaterials in Fig. 1-6(c), which can adaptively conform to any arbitrary complex surfaces through morphological deployment driven by heat[69].

Apart from tensegrity structures, the same design principle is also extended to statically balanced compliant joints[70,71]. Two additional pairs of leaf springs are connected in parallel to a central revolute joint on each side to achieve a nearly-zero rotational moment, enabling the joint to stabilize at any position avoiding spring-back behavior, as shown in Fig. 1-6(d).

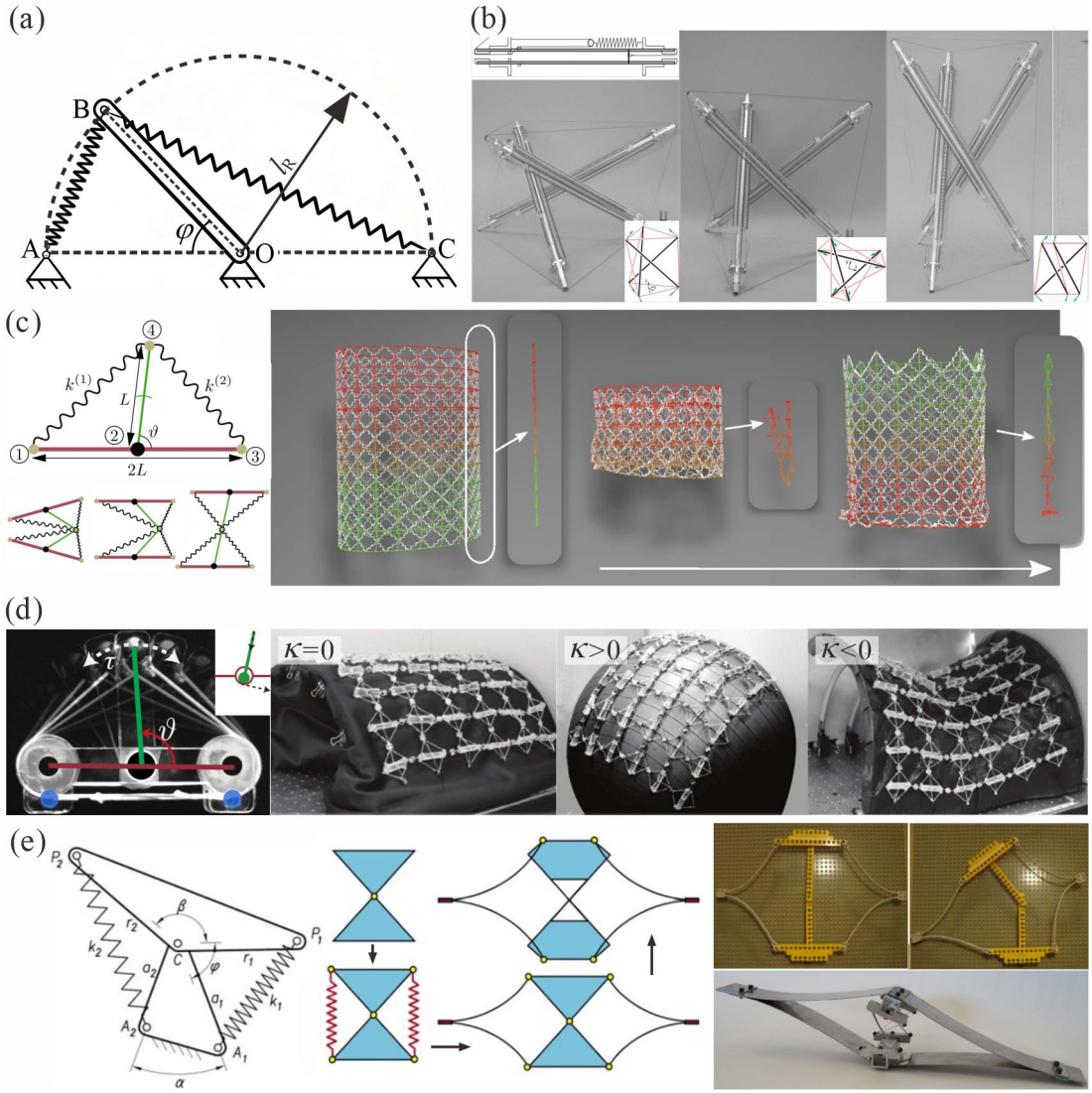

Fig. 1-6 The double-spring tensegrity mechanism. (a) Diagram of spring-to-spring balancer[5,67]; (b) conceptual design of the bars and 3D prototypes of statically balanced tensegrity mechanisms in motion range[68]; (c) programmable Morphologies from totimorphic assemblies of neutrally stable units to heat-driven surfaces with zero, positive, and negative Gaussian curvature[69]; (e) design of a statically compliant pivot, and prototypes of stable balanced compliant joints and cross-axis flexural pivot[71].

For high-precision static balance in MEMS, the fully compliant systems with static balance offer an effective solution by avoiding inherent assembly errors through monolithic fabrication. In such systems, the functional elastic components typically exhibit positive stiffness[72,73] with increasing force (red line in Fig. 1-7(a)), while the opposite negative stiffness is realized through column buckling of a pre-stressed beam

as marked in the blue line. This combination yields zero resultant stiffness and force (black curve) throughout the design domain. Two typical SBCM configurations utilizing beam buckling are presented in Fig. 1-7(a), where external balancing forces are continuously required to maintain the compression of the straight beams. Likewise, Hoetmer and his colleagues also developed a series of negative stiffness balancing blocks for compliant grippers and multipliers[74] based on the second-order buckling of the compressed plate springs, as shown in Fig. 1-7(b), which also requires external loads to induce prestress for bucking, and thus maintain static equilibrium in the system.

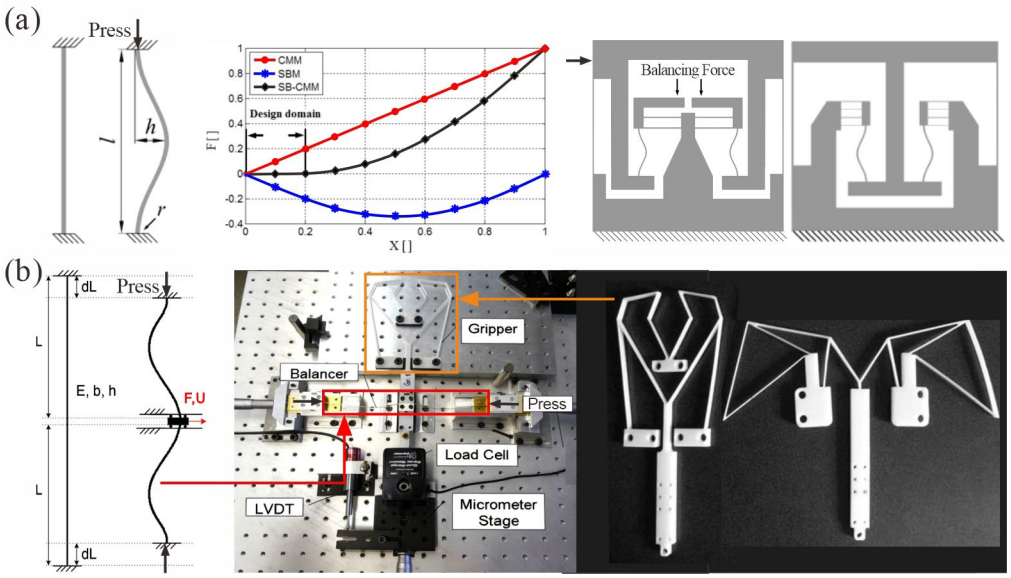

Fig. 1-7 SBCMs based on beam buckling. (a) SBCMs based on buckling of compressed beams[73]; (b) SBCMs based on the second-order buckling of compressed plate springs[74].

Alternatively, negative stiffness can be achieved through geometrically induced bistability without external loads. Figure 1-8 employs a pair of coaxially assembled Von Mises truss structures with varying parameters to achieve neutral stability[75]. After pre-loading along the travel path, beam CMM exhibits positive stiffness with restoring forces after snap-through, while beam SBM generates negative force post its energy peak. This coordinated interaction produced zero resultant force within a limited operational range, thereby forming a collinear SBCM. And, a micron-scale prototype with a maximum dimension of 5000nm was manufactured, as shown in the SEM image of Fig. 1-8.

In addition, bistable units based on a slider-rocker mechanism can be integrated into SBCMs. For instance, in a statically balanced compliant laparoscopic grasper, a pair of symmetrically bistable rocker units is connected in series with a conventional laparoscopic grasper[76], see Fig. 1-9. Numerical analysis also proves that the negative force generated by the bistable unit compensates for the positive force (red curve) required by the conventional grasper, significantly reducing the operational force during grasping[77]. Through further topological optimization, the fully compliant grasper can notably enhance control and precision of force feedback through monolithic manufacture during surgery.

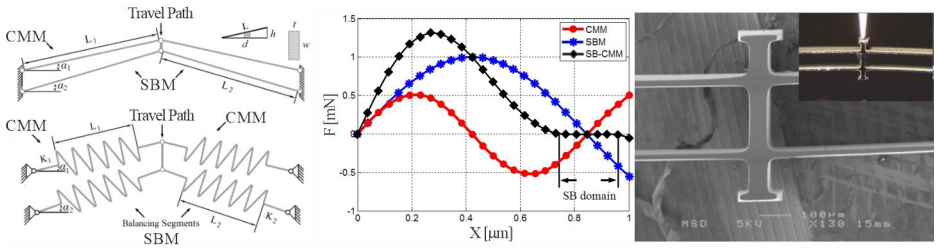

Fig. 1-8 Collinear-type SBCMs based on bistability.

In summary, all the aforementioned multi-component systems primarily leverage counteracting the opposite mechanical behaviors of compliant elements to achieve mutual compensation and coordination during operation, thus realizing static balance in systems. Meanwhile, most existing cases predominantly utilize standard springs or bistable beam models to match the positive linear force-displacement relationship of linkage mechanisms. Therefore, a key research challenge addressed in Chapter 2 is how to expand this design principle from the existing beam models to shell structures, and further counteract the undesired nonlinear force-displacement relationships in actual working conditions.

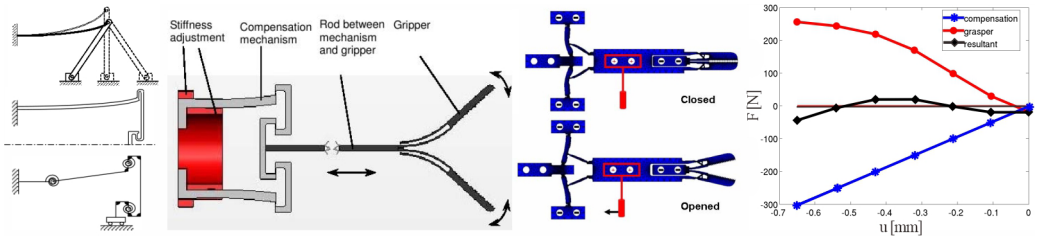

Fig. 1-9 Statically balanced compliant laparoscopic grasper.

1.2.4.2 Single-component SBCMs

In a single-component SBCM, the entire structure contains exclusively one compliant component. At the initial stage, it is essential to introduce the required strain energy to the SBCM through prestress. This is primarily accomplished via the following three methods: (A) utilizing extrinsic boundary conditions to introduce prestress, (B) inducing controllable residual stress through material modification and (C) implementing intrinsic boundary constraints through structural design.

(A) Extrinsic Boundary Conditions

Taking the ideal conveyor belt system as a classic example (Fig. 1-10(a)), its static balance demonstrates a unique mechanism distinct from the aforementioned mechanism containing multiple elastic elements. As the sole compliant component in this SBCM, the tensioned belt stores the total strain energy, while the rigid rollers provide the displacement boundary conditions to generate the internal tension of the conveyor belt. The rigid rollers confine the belt to move along a predetermined path, while the overall geometric configuration remains unchanged during operation. Meanwhile, the strain energy and internal stress within the belt continuously redistribute, propagate and self-compensate, maintaining dynamic equilibrium, which corresponds to the energy flow diagram in Fig. 1-4(c). Nevertheless, this equilibrium mechanism fundamentally depends on external constraints imposed by the rigid boundaries. Once this constraint fails, such as the removal of one roller, the internal equilibrium of the system will collapse, transitioning into an unstable state.

Similar principles are demonstrated in the Rolamite mechanisms[78] proposed in 1967 (Fig. 1-10(b)), where the additional rigid components here confine the compliant thin strips in tension along a fixed trajectory that remains geometrically invariant throughout deformation, resulting in constant strain energy without external forces. Leveraging this design concept, novel devices like rotary bearings[79], rolling hinges for deployable structures[80], can be developed to achieve an infinite range of motion by connecting ends of the strip, see Figs. 1-10(c) and (d).

Figure 1-10(e) exhibits an analogous example, where a leaf spring is compressed between two parallel surfaces, which localizes the specific curved configuration into a specific region and suppresses elastic deformation at both ends[74]. During plate transition, the deformed zone migrates accordingly while the mechanism can maintain

constant elastic strain energy due to preserved curvature distribution, achieving energy-free transitional motion.

Giuseppe Radaelli also utilized this principle to design a neutrally stable compliant revolute joint from several helicoidal shells joined along their shared edges and fixed at both ends[83], see Fig. 1-11. When twisting opposite to the direction of its pitch, the initially stress-free helicoidal shells cause initial buckling, triggering prestress with stored strain energy. With both ends rotationally fixed, the fully reversed region can translate continuously along the axis and stabilize anywhere, resulting in zero-moment rotational joints and neutrally stable bar linkages made of these joints.

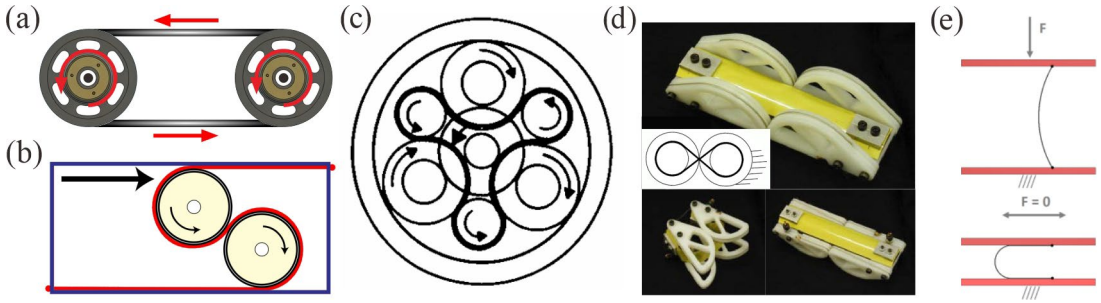

Fig. 1-10 Multiple-element SBCMs with one single compliant mechanism. (a) The ideal conveyor belt system; (b) the classic Rolamite mechanism[78,79]; (c) the rotary bearings; (d) the rolling hinges for deployable structures[80]; (e) an initially straight flexure compressed between surfaces which can shift horizontally[66].

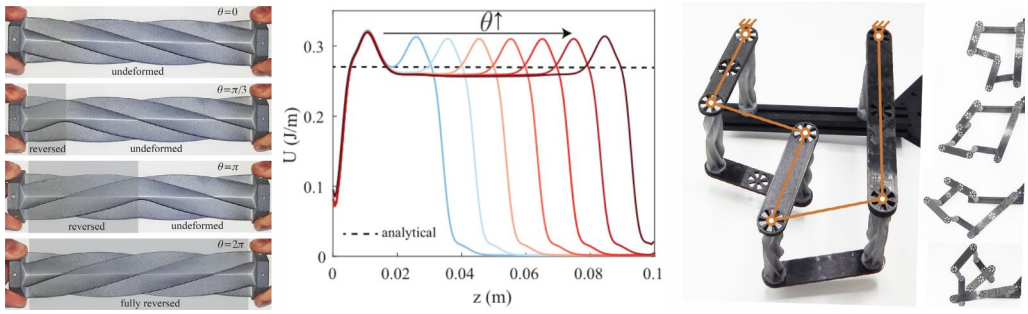

Fig. 1-11 Neutrally-stable linkage mechanism composed of helicoidal shells[83].

Unlike SBCMs with multiple compliant components that achieve neutral stability through systematic optimization, single-component SBCMs can obtain initial strain energy and stress distribution passively introduced by rigid boundaries, and continuously rely on the boundary conditions to maintain internal self-equilibrium

during operation. Although such design strategies have been widely adopted owing to their reduced demands for fabrication precision, inevitable contact between rigid and compliant components and induced material failure severely reduce system efficiency and system lifetime[84], which drive necessities to develop monolithic SBCMs.

(B) Controllable Residual Stress

In addition, the required strain energy can be introduced into the component via generated residual stresses from manufacturing processes. Heated-treated curved steel blades can maintain stability at any extended length, achieving "neutral equilibrium", which is widely applied in steel tape measures[85] and aerospace tape springs (Figs. 1-12(a) and (b)). Neutrally stable blades can be also constructed by bonding two cylindrical shells with opposite curvature directions and mutually orthogonal axes, utilizing anisotropic properties of composite materials, see Fig. 1-12(c).

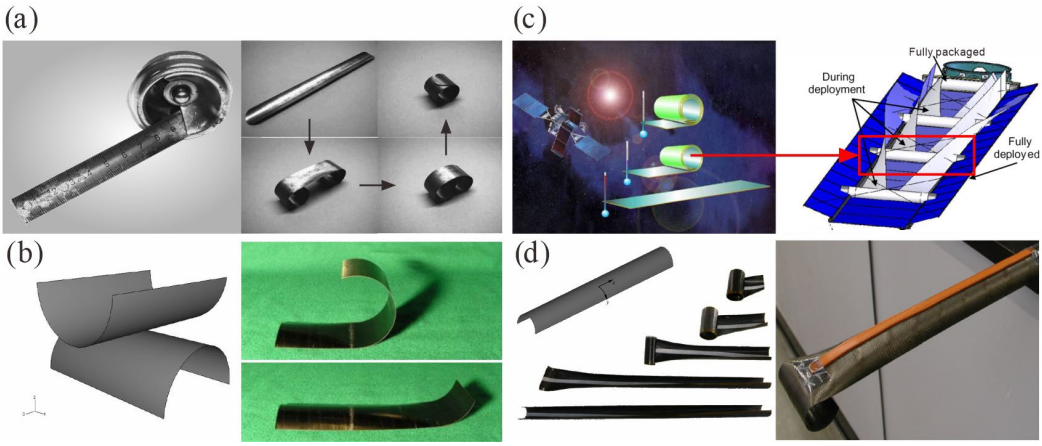

Fig. 1-12 Neutrally stable deployable tape springs. (a) Steel tape measure and transition from extended to rolled-up configurations[85]; (b) a thermally-actuated deployable radiator composed of tape springs in aerospace[86]; (c) a rectangular steel plate composed of two bonded pre-stressed layers[87]; (d) neutrally stable fiber-reinforced composite tape springs[88].

Initial shell elements were fabricated from flat metal sheets and shaped into basic cylindrical surfaces through plastic deformation and heat treatment with residual stress[85]. To meet the lightweight and toughness requirements for aerospace, the composite blades were produced by extending reinforced polymer fibers to induce prestress, followed by moulding them around a cylindrical surface[86]. Regardless of specific material, the stiffness matrix $\boldsymbol{K}$ of these blades must remain positive definite

and singular as deduced from Eq. (1-2) to achieve neutral stability. Therefore, the bending portion of the constitutive equations can be represented as follows[87], where K_{11} equals K_{22}.

$$\boldsymbol{M} = \boldsymbol{K}\Delta\boldsymbol{\kappa} \Rightarrow \begin{Bmatrix} M_x \\ M_y \\ M_{xy} \end{Bmatrix} = \begin{bmatrix} K_{11} & K_{12} & K_{16} \\ K_{12} & K_{11} & K_{26} \\ K_{16} & K_{26} & K_{66} \end{bmatrix} \begin{Bmatrix} \Delta k_x \\ \Delta k_y \\ \Delta k_{xy} \end{Bmatrix}. \tag{1-6}$$

where $\boldsymbol{M}$ is the applied moment, $\boldsymbol{K}$ is the stiffness matrix, and $\Delta\boldsymbol{\kappa}$ is change in curvature matrix. As composite materials are laminates made from unidirectional plies, both K_{16} and K_{26} are simplified to zero to eliminate extension-shear coupling. And the determinant of the singular K should be zero, which means K_{11} equals K_{12}. This stiffness condition can be fulfilled by tailoring the manufacturing process, enabling the composite blade to achieve zero bending stiffness and neutral stability, as applied in aerospace tape springs illustrated in Fig. 1-12(d).

Unlike the aforementioned anisotropic composite shells, Guest proposed a novel homogeneous cylindrical shell that exhibits neutral stability as continuously rotating its generatrix[88,89]. Owing to its constant principal curvature, the total strain energy of the shell remains unchanged throughout its transformation from a cylindrical, to a helical, and finally a cylindrical surface aligned along the perpendicular axis[90], see Fig. 1-13(a). By introducing precise longitudinal bending and residual stress into a flat rectangular strip via heat treatment, the system is transformed from a conventional bistable state into a continuous equilibrium with zero energy barrier, resulting in neutral stability, as evidenced by the concentric contour circles of strain energy[91] in Fig. 1-13(a).

Furthermore, Guest extended this mechanism from the cylindrical strip to a thin circular bimetallic flat disk with superior geometrical symmetry in Fig. 1-13(b)[89]. When the circular disk subjected to heat treatment to form initial cylindrical surfaces with identical residual stress, its overall shape can be maintained during curvature axis rotation[90]. Leveraging this theoretical model, piezoelectric composite actuators are evenly distributed on the shell surface at equal angular intervals[91]. Each actuator is triggered sequentially in cycles with a fixed phase delay, inducing rotation of the generatrix axis along a neutrally stable precessional trajectory. This process generates an infinite cyclic motion of the propagating wave on the deformed shell surface, forming a flexible gearless motor.

However, in practice, current manufacturing processes to introduce controllable prestress or adjust stiffness in materials is not only complex and sensitive, but also hard to strictly meet the theoretical requirements. Consequently, actuation force of the system can be significantly reduced instead of entirely eliminating, which imposes considerable limitations in widespread practical applications[66].

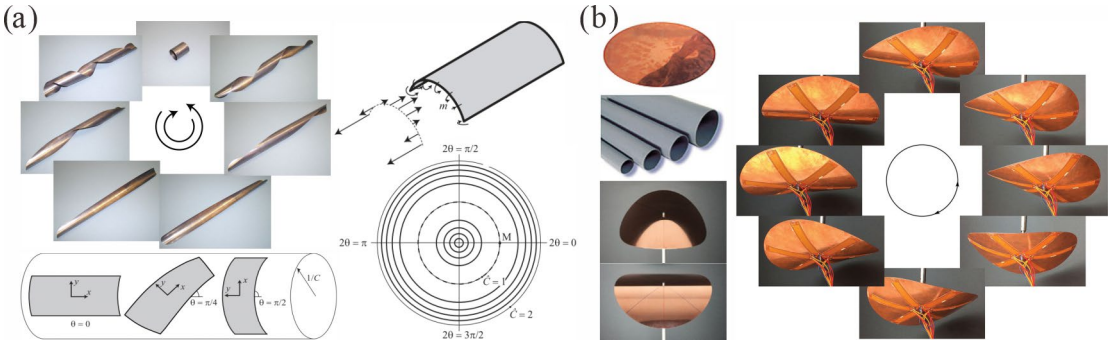

Fig. 1-13 Neutrally stable shell structures. (a) The zero-stiffness shell structures transformed from extended to rolled-up configurations[89] and contour plots of strain energy[90]; (b) a neutrally stable circular disc and a flexible gear-less motor driven by evenly distributed actuators[91].

(C) Intrinsic Boundary Conditions

As previously demonstrated, multi-component SBCMs inevitably face challenges of assembly error and interfacial contact, while introducing modified prestress into the individual compliant element through material processing also encounters practical limitations. Instead, it is more feasible to establish intrinsic boundary conditions via elaborate structural design, which in turn induces appropriate self-equilibrium stress and store initial strain energy in the only compliant component.

Through sophisticated geometrical design, Kok et al. fabricated a shell-based SBCM by bonding two flat arch-shaped compliant sheets along the short curved edges, and then partially inverted one end into a stable state with self-equilibrated stress field, see Fig. 1-14(a). When flipping both ends, the flat transition region can propagate continuously along the arched hinges. Within a predefined structural domain, it can maintain stable at any position between both ends with constant strain energy[93]. Here, the initial flip-over process, combined with well-designed geometry provides intrinsic boundary conditions in this mechanism. Figure 1-14(b) depicts 3D-printed prototypes placed in a pinching-constrained experimental setup, which exhibits continuous equilibrium during transition, thereby verifying the design[92,94] .

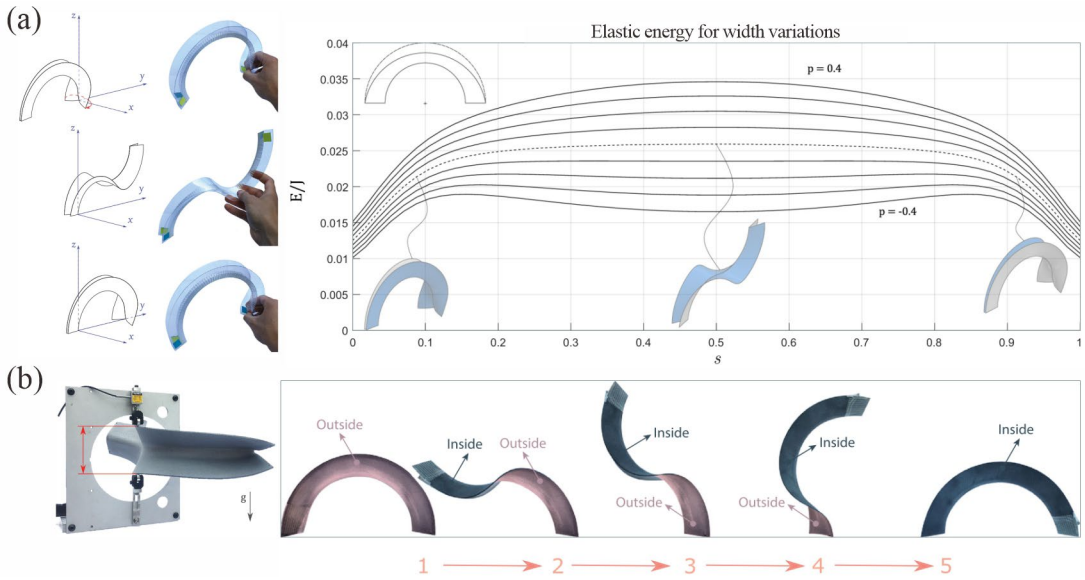

Fig. 1-14 Neutrally stable curved-crease shell structures. (a) Transitions between two stable zero-energy states, and the energetic paths during transition[93]; (c) experimental setup of the 3D prototype, and physical model in several stable configurations during transition[92,94].

In fact, a common design approach is to utilize closed-loop structures. As early as 1867, the concept of neutral stability was first proposed, based on the observation that when an initially straight rod is bent into a circular loop, the formed ring can continuously and infinitely rotate around its centroidal axis, with its shape and total strain energy remaining unchanged[95], which aligns with the DNA molecular motor designed by Kulić[96,97], see Figs. 1-15(a) and (b). Another example is closed-loop tape springs, in which the localised folds served as rotational joints, while straight sections acted as variable-length links, together forming a series of *N*-fold mechanisms[98,99]. In this closed-loop structure, the straight sections are almost undeformed, while the localized folds form circular cylindrical surfaces of identical curvature $1/R$ and store majority of the strain energy[100,101] (Fig. 1-15(c)). Regardless of fold number, the total fold angle always sum to 360°, resulting in consistent strain energy of the system, which allows folds propagate freely along the central axis of the tape (Fig. 1-15(d)).

Likewise, in curved-crease origami, concentric alternating mountain-valley folds were introduced into a circular annulus of flat sheet to form saddle surfaces with equilibrium internal stress, also known as origami circular hypar[16,102], as shown in Fig. 1-15(e). Owing to the highly rotational symmetry of the ring, the concave or convex

regions can occur arbitrarily along the circumference, allowing the system to maintain neutral equilibrium during torsion. Actually, for closed structures made of homogeneous materials, deformation can localize at any position and migrate along the loop with unchanged overall geometry, infinitely maintaining constant strain energy. Therefore, such design strategy can also extend to other smooth closed geometries with inherent prestress including topological knots[103-107], Möbius strips [108-112], also known as Seifert ribbons[113-115], see Figs. 1-15(f) and (g).

Although such neutrally stable closed-loop structures are easy to fabricate, the inherent geometric complexity poses challenges in actuation, which fundamentally restricts their practical applications. Currently, identifying suitable actuation strategies to expand application scenarios have yet to be adequately addressed. Besides these close-loop structures, these SBCMs with unchanged overall shape during motion including the ideal convey belt, the neutrally stable circular disk[91] demands further exploration to their underlying mechanism.

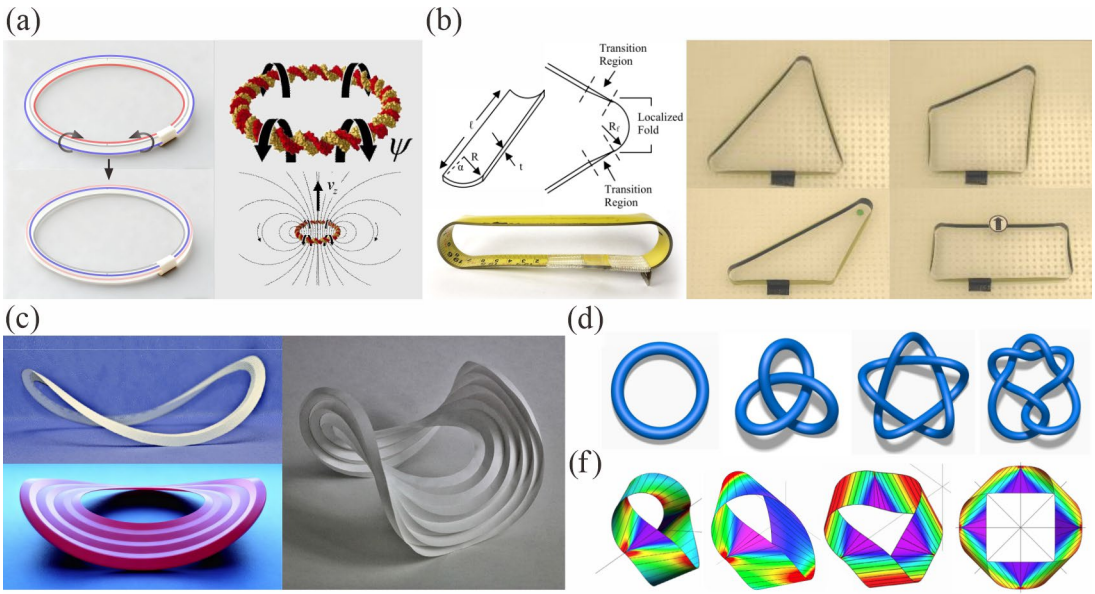

Fig. 1-15 Neutrally stable closed-loop structures. (a) Rotation around the centroidal axis of the circular ring[95], and the similar rotation in DNA-minicircle propeller[96,97]; (b) segment of the tape spring and the basic tape loop[98]; and the three-/four-fold mechanism at different positions[99]; (c) circular origami hypars[16,102]; (d) torus knots[103,104]; (e) the generalized Möbius strips[111,112].

1.2.5 Actuation Strategies for SBCMs

As discussed in Section 1.2.4.2, traditional actuation methods are adequate for driving the majority of statically balanced systems with predictable motion patterns.

However, for SBCMs with complex geometry, the strong non-linearity in their deformation and motion patterns pose great barriers for automatic actuation, other than manual manipulation.

1.2.5.1 Stimuli-responsive Materials

With advances in combination of intelligent materials and complex systems, autonomous locomotion and programmable shape morphing can be simply driven under controllable external stimuli without contact, which unlocks a wide range of functionalities. Unlike conventional rigid actuators, soft actuators inherently rely on soft materials with superior flexibility, adaptability, and reconfigurability[116,117] to fulfill tasks including biomimetic motion[118,119], adaptive grasping[120,121], non-contact sensing[122-124] and human-machine interactions[125-127] in unstructured environments, as concluded in Fig. 1-16(a). When exposed to one or multiple external stimuli such as heat[128,129], light[130-132], electricity[133,134], magnet[135-137], chemical substances[138,139] like humidity[140,141], intelligent stimuli-responsive materials[142-144] utilized in these actuators usually experience internal reorganization including volume change due to molecule absorption and change in molecular order due to phase transition[145,146]. This triggers corresponding local isotropic or anisotropic swelling, and ultimately causes material bending and unbending under localized stimuli.

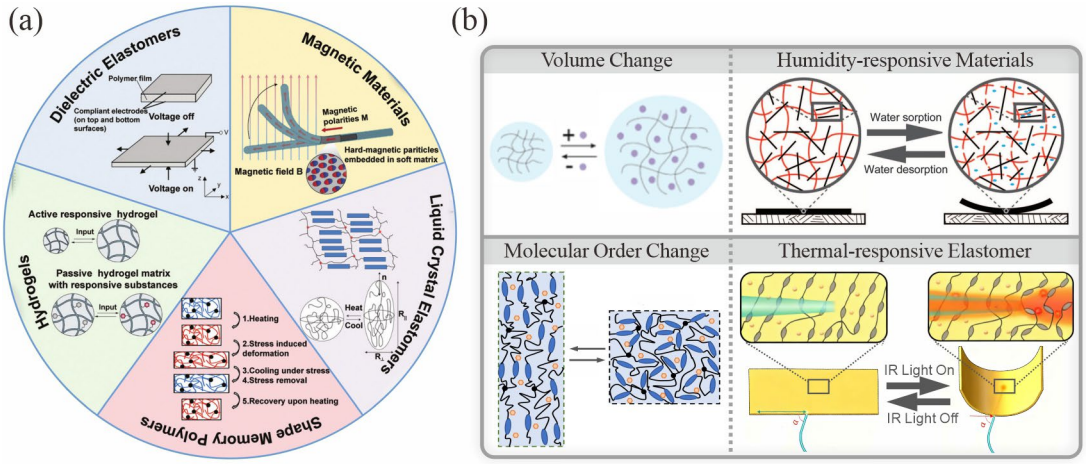

Fig. 1-16 Stimuli-responsive materials. (a) Overview of typical stimuli-responsive materials and their applications[116]; (b) classification of materials according to actuation mechanisms[146], and corresponding typical materials[147].

For example, humidity-responsive materials undergo hygroscopic expansion due to interaction between water molecules and hydrophilic groups. Such materials exhibit

great potential for compliant systems due to their relatively speedy responses, low energy consumption, and the ubiquitous and abundant humidity resource at the Earth's surface[141,147], but have yet been extensively explored.

In addition, as the most commonly applied responsive materials in soft actuators, thermal-responsive elastomers experience isotropic phase transitions from anisotropy to isotropy resulting in simultaneous contraction and elongation in perpendicular directions when actuated by heat, or infrared light[148,149].

Soft actuators fabricated from stimuli-responsive materials often require manual manipulation of external stimuli, such as altering the orientation of electric or magnetic fields, modulating light intensity or position of light sources, and adjusting temperature to trigger predictable deformation in smart materials, to realize real-time environmental response, exceptional mobility and diverse motion patterns[116-119] of actuators.

For example, for soft grippers, adjustable grasping operations are achieved by modulating electrical voltages[150] (Fig. 1-17(a)) or switching infrared light on and off to control material temperature[151] (Fig. 1-17(b)). Similarly, controlled magnetic fields enable real-time regulation of posture and orientation to achieve directional jumping in a millimeter magnetic robot[152] (Fig. 1-17(c)) and forward swimming of the flagellated micromachine[153] (Fig. 1-17(d)). Furthermore, even basic rectangular sheets of stimuli-responsive materials, can crawl forward like an inchworm driven by asymmetric friction at both ends during cyclic bending and unbending under periodic stimuli including altering electricity[154] or humidity resources[155] and infrared radiation[156,157], see Figs. 1-17(e-g).

Notably, certain soft actuators of uniquely designed geometries can also stably generate self-sustaining motions for long duration, even under constant stimuli without any manual control[157-159]. As shown in Figs. 1-18(a-d), wheel-like soft actuators including circular rolls[160], straight rods[131], helical strips[153,160], and twisted strips[161,162] can achieve rapid directional self-rolling through cyclic shape transformations induced by periodic shifts of the gravitational center. Geometric optimization and material orientation control of actuators (Figs. 1-18(e-f)) can further enhance locomotion capabilities, which enables well-defined motion trajectories and self-regulated rolling for autonomous terrain exploration[153,163].

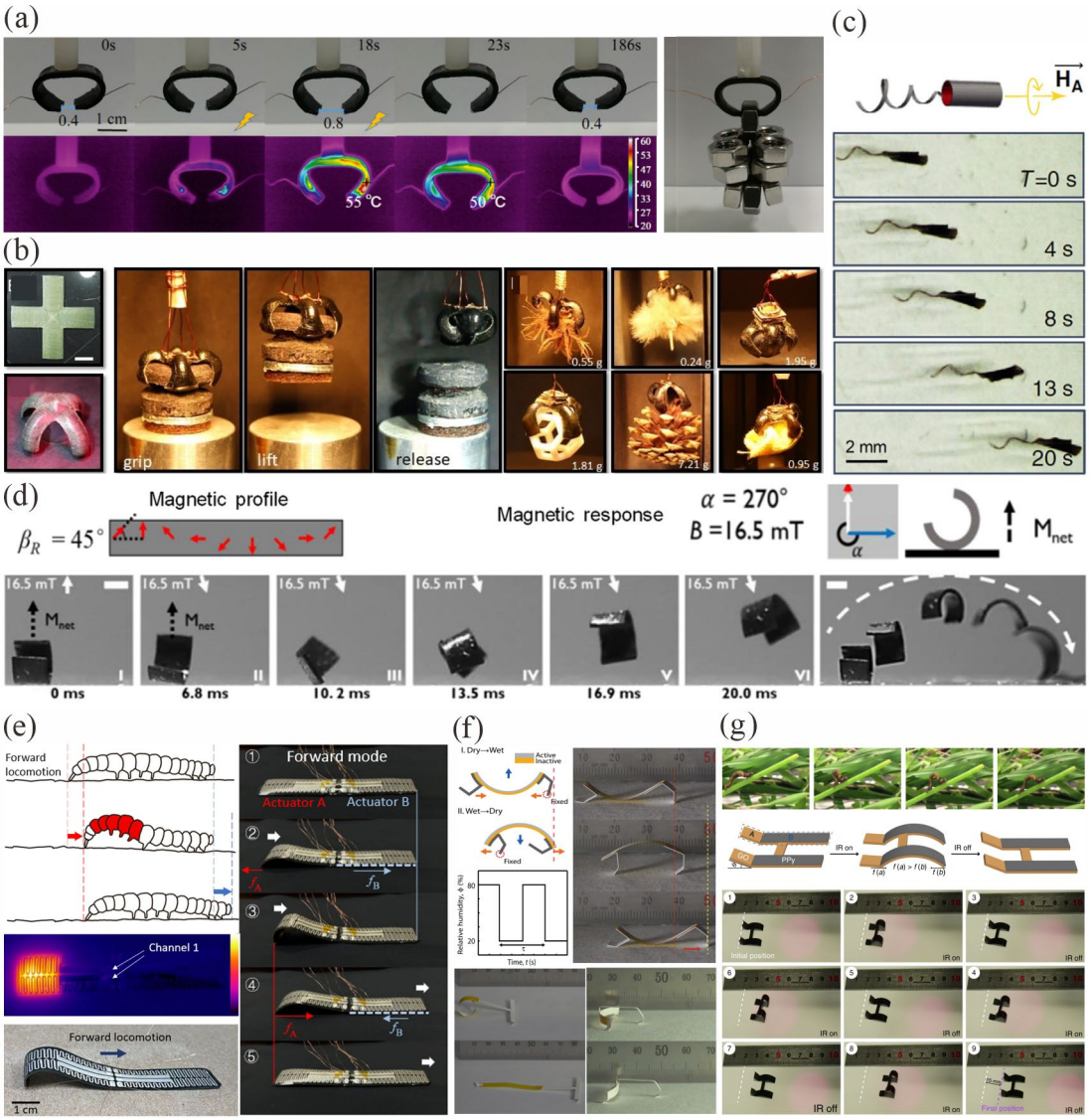

Fig. 1-17 Soft actuators driven by real-time manipulation of external stimuli. (a) the mechanical gripper made from POE/CNT composites[150]; (b) an LCE Gaussian gripper driven by altering IR light[151]; (c) the forward swimming flagellated soft micromachines under rotating magnetic fields[152]; (d)directional jumping in a millimeter magnetic robot[153]; (e)forward crawling of soft robot with distributed programmable thermal actuation[154]; (f) the hygrobot powered by environmental humidity[155] and (g) biomimetic soft walking robot[156].

Given the inherent limitations of manual control including high control demands, and operational inconvenience, the strategy of constant stimuli highly aligns with our requirement for actuation simplification. Thus the major challenge lies in effectively integrating constant stimuli with SBCMs through geometric optimization, material

selection and actuation modification for self-regulated locomotion, thereby enabling autonomous execution of multiple tasks.

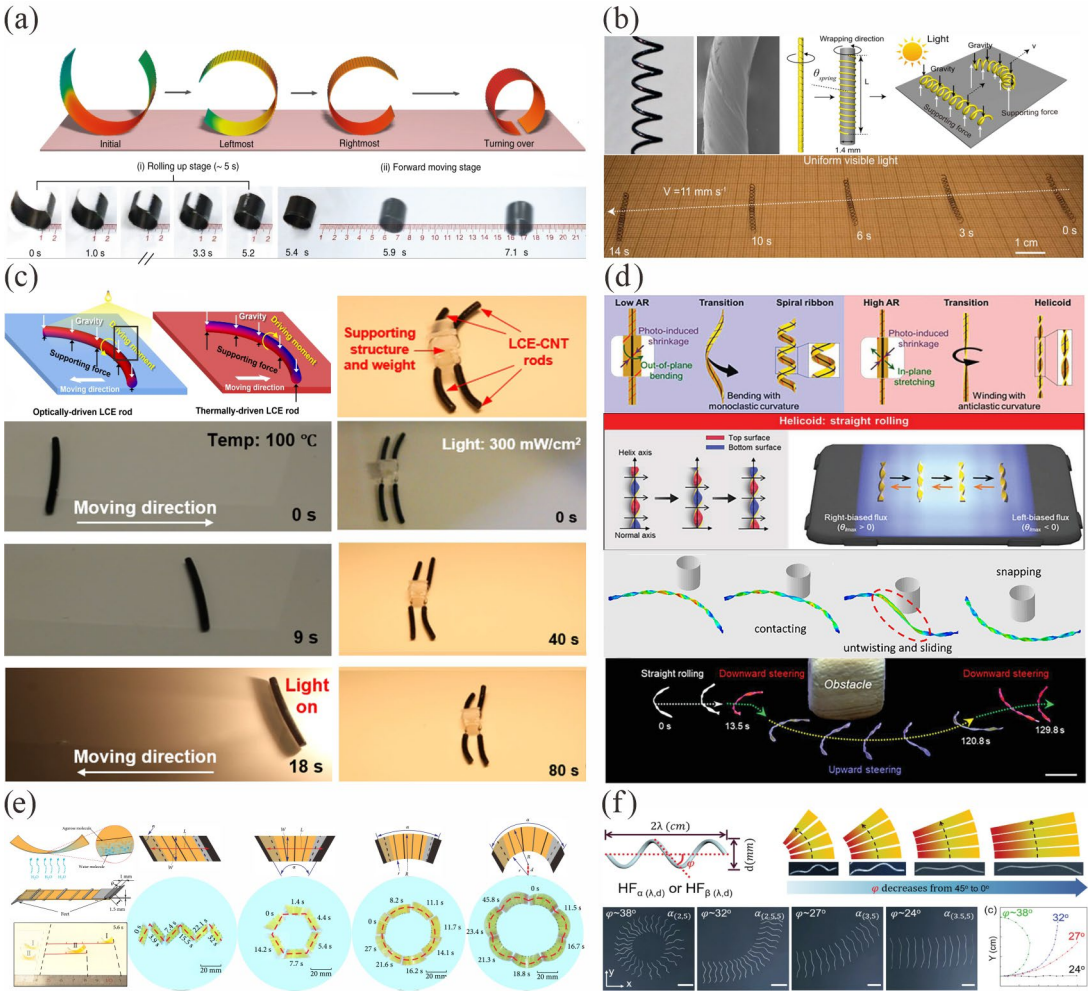

Fig. 1-18 Soft actuators driven by constant stimuli. (a) Self-shaping and rolling motion of a PDG-CNT/PVDF bimorph on a hot surface[153]; (b) self-rolling motion of the twisted helical LCE spring actuators[131]; (c) autonomous rolling of an LCE rod on a hot surface and corresponding vehicles[157]; (d) autonomous self-rolling of the twisted LCE ribbons with environmental obstacles via snapping[162]; (e) programmable trajectories of the humidity-driven Hydrollbots[163]; (f) Rattlesnake-inspired lateral rolling of the helical LCE robot with different paths[164].

1.2.5.2 Zero Elastic Energy Modes

The combination of neutrally stable structures with stimuli-responsive materials was first proposed and analyzed by physicists Ziebert, Kulić and co-workers in 2018[165]. Taking the neutrally stable circular ring[166] by closing a thermal-responsive polymer fiber as a classical example, the prestressed ring can autonomously rotate around its

centroidal axis when placed on a heat plate, as shown in Fig. 1-19(a). The topological stress field generated from the temperature gradient breaks continuous symmetry and initial prestress distribution in the polymer ring (Fig. 1-19(b)), which can be explained by the "hydrodynamic" mode in condensed matter physics [166,173]. In ideal elastic materials without defects and viscous loss, the actuator always maintains its global configuration and total strain energy without additional energy during rotation, which leads to "zero-elastic-energy modes" (ZEEMs) for stimuli-responsive actuators. Essentially, this mode is a state of neutral stability characterized by the unchanged global shape with constant strain energy during continuous deformation. Ziebert et al. also predicted that global ZEEMs can occur in other pre-strained elastic structures like Möbius strips, edge-crumpled disks with continuous symmetry (Fig. 1-19(a))[165]. In particular, closed-loop structures impart intrinsic boundary conditions through end closure, resulting in inherent self-equilibrium prestress, which is highly consistent with the design principle of method (C) in Section 1.2.4.2.

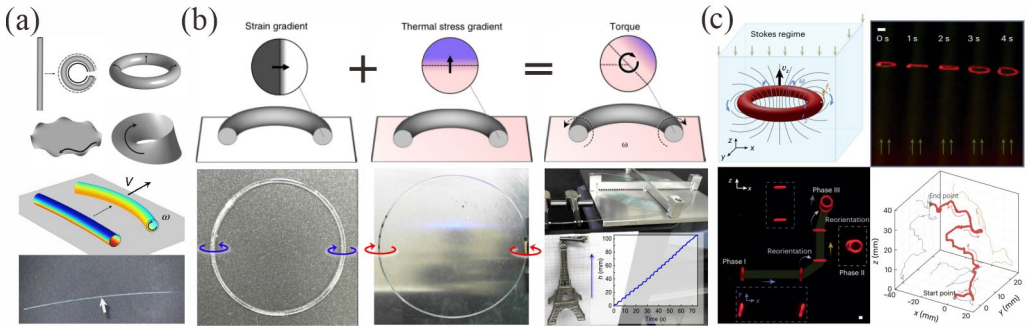

Fig. 1-19 Typical ZEEM-based actuating mechanisms. (a) Various geometries exhibiting ZEEMs and rolling of polymer fibers on the heat plate[164]; (b) in-place rotation driven by thermal prestrain induced by temperature gradient and corresponding motion of ring actuators fabricated from other polymers[165]; (c) multirealm swimming of the light-steerable torus in the Stokes regime[167,168].

In fact, by twisting photo/thermal-responsive anisotropic elastomer rods or strips into closed-loop geometries with developable surfaces and continuous symmetry, a series of ZEEM actuators have been developed. Propelled by topological prestrain and symmetry breaking, materials in rod-based geometries like the basic circular rings, topological knots[169] (Fig. 1-20(a)) exhibit local rotation around the centroidal axes, while materials in strip-based structures like Möbius strips[171], and Seifert ribbons[170,172] (Fig. 1-20(b)), undergo transitional motion along their center line. When placed on the

plate surface, symmetric frictions between actuators and substrates can trigger the basic global motion, autonomous in-place rotation under constant stimuli.

To achieve more advanced locomotion, the introduction of unidirectional motion is essential, as exemplified by vertical climbing, horizontal crawling with loads[170]. Furthermore, asymmetric Möbius actuators with engineered defects enable the complex flip-spin-orbit motion enabling autonomous mapping of unstructured environments[173] in Fig. 1-20(c). Specially, the distinct friction drags generated on the inner and outer side of the active ring in the Stokes regime enable directional swimming at low Reynolds numbers[167,174] (Fig. 1-19(c)).

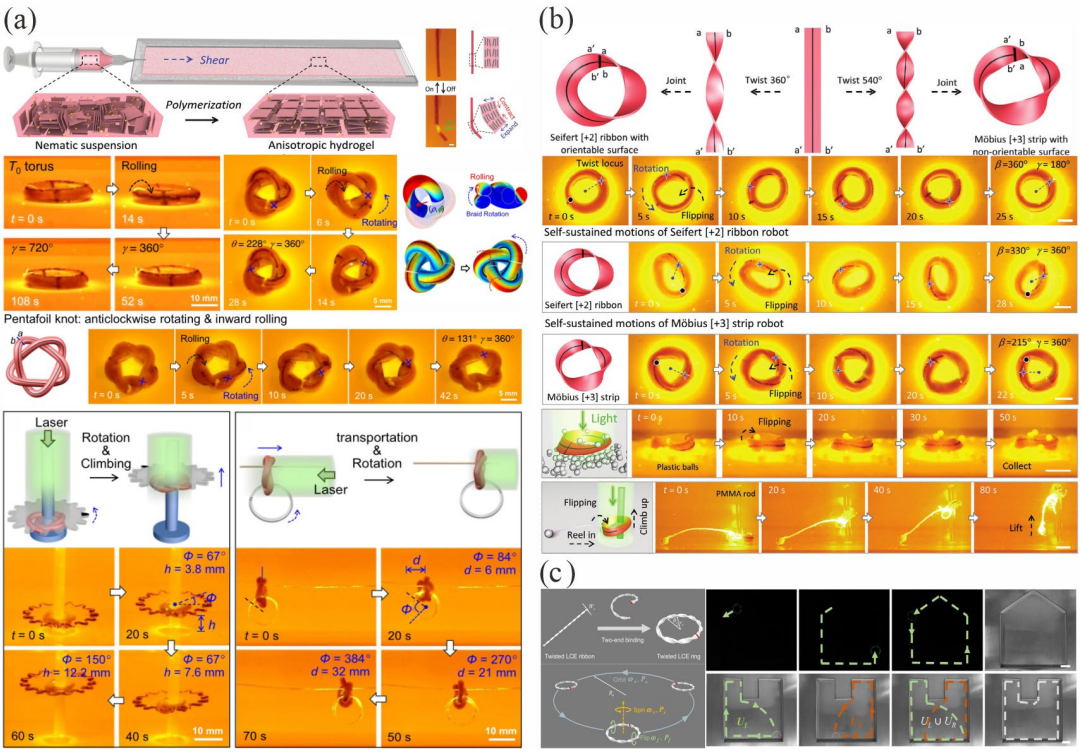

Fig. 1-20 Typical ZEEM-based actuators. (a) In-place rotation of twisted rob-based knot actuators driven by constant light irritation, and vertical climbing, horizontal transportation of twisted knot actuators with loads[169]; (b) in-place rotation of Seifert ribbon and Mobius strip actuators driven by constant light irritation, and collection of plastic beads by a Möbius strip actuator with continuous flipping and climbing on a vertically placed rod to lift a plastic ball[172]; (c) periodic flip-spin-orbit motions and autonomous mapping of another twisted Möbius actuator on a heat plate[173].

However, the mathematical modeling of actuators with continuous neutral stability remains challenging due to topological complexity and material non-linearity, which hinders understanding of their intrinsic motion mechanism. Existing theoretical models

are currently limited to the self-propelling mechanism of the basic polymer ring on a hot plate by coupling hyper-elasticity and thermal radiation [131]. For other topologically complex actuators, experimental and numerical methods were utilized to roughly explain dynamic behavior and generally analyze key design parameters[131,165]. Establishing generalized theoretical models remains essential to uncover underlying mechanisms of ZEEMs, and provides effective guidance for matching complex SBCMs with suitable stimuli, which remains to be accomplished. Furthermore, with the support of quantitative predictions of motion behaviors, the exploration of novel, advanced functions for SBCMs can be significantly accelerated, paving the way for next-generation autonomous soft robots and smart actuators.

1.3 Aim and Scope

The primary objective of this dissertation is to establish a design methodology for shell-based SBCMs through structural design and mechanical characterization. Leveraging continuous deformation without external energy or loads, this design can further integrate with advanced materials, which lays a robust theoretical foundation to engineering applications in emerging domains.

This research begins with geometrical design of a mechanically coupled balancer for a predefined mechanical component for static balance in multi-component systems through coordinated global deformation. Based on systematic analysis of internal energy flow and stress redistribution, a single-component system is then proposed to achieve high-efficiency torque transmission via unique shape preservation mechanism, which provides guidance to develop SBCM actuators. However, the inherent driving complexity demands the effective actuation strategy.

To address this, intelligent materials are introduced with specifically tailored geometries to enable autonomous untethered locomotion for diverse applications under constant stimulation alone. Furthermore, a comprehensive physical model is built to unveil the correlations between topology, mechanics and actuation, thereby offering fundamental guidance for the extension of intelligent statically balanced systems.

1.4 Outlines of Dissertation

This dissertation consists of five chapters, which are described as follows, while a diagram of the main contents is shown in Fig. 1-21.

Chapter 1 introduces the mechanical theory and current design methodologies in the analysis and design of various SBCMs as well as the development status of research. Besides, actuation strategies based on stimuli-responsive materials and their corresponding cases are also reviewed here.

Chapter 2 proposes a novel shell-based SBCM comprising a predefined bellow coaxially aligned with a matching straw-inspired balancer with mirrored mechanical behaviors to achieves precise control with the near-zero driving force during operation. Moreover, a theoretical model is developed to predict global deformation and strain energy evolution, which guides design optimization through parametric study. Both numerical simulation and experiments demonstrate a significant reduction in the operational force required for the SBCM in comparison to the stand-alone bellow.

Chapter 3 introduces a single-component SBCM that maintains neutral stability through structural self-coordination instead of interactions and compensation between multi components. Here, inspired by the circumferential stability of the bent drinking straw, a statically balanced compliant torque coupling (SBCTC) for high-efficiency torque and rotation transmission is proposed. According to numerical analysis of the bending behaviors to identify the bistable range, a simplified beam model is developed to facilitate programmable geometric design. Combined experimental and numerical studies demonstrate that the underlying mechanisms of shape preservation and internal energy evolution during torsion are elucidated. Moreover, precision prototype experiments confirm its outstanding torque transmission performance, compared to traditional flexible couplings.

In Chapter 4, leveraging aforementioned shape preservation in SBCM structures, the generalized threefold Möbius strips are implemented as the conceptual design for a shell-based actuator. Prior to physical prototyping, the selected core geometry is reconstructed according to the theory of inextensible and developable surfaces while satisfying symmetric boundary conditions. Meanwhile, parametric geometric models and stress distribution analysis are investigated to provide geometrical foundations for subsequent material selection, actuation matching and the physical modelling.

Chapter 5 presents a Möbius actuator through integration of the threefold Möbius strip in Chapter 4 with humidity-responsive agarose films to achieves self-sustainable periodic motion under constant stimulation. A physical model was subsequently built based on humidity diffusion and geometric characteristics to unveil the underlying

mechanisms of curvature-driven rotary motion with shape preservation, and establish quantitative correlations between the motion speed, and geometric and environmental parameters. The Möbius actuator demonstrates multifunctional capabilities, including long-term motion, mechanical work output, and ambient humidity sensing, enabling a versatile design framework for diverse applications in advanced fields. Furthermore, our proposed threefold Möbius structure has been also extended to other intelligent materials, such liquid crystal elastomers, validating the universal applicability of the structure.

As the conclusion of this dissertation, Chapter 6 summarizes main achievements and future works. This dissertation develops a theoretical framework and design principles for statically balanced compliant shell mechanisms through geometric optimization and mechanical analysis, ultimately paving the way for expanded applications in engineering practice.

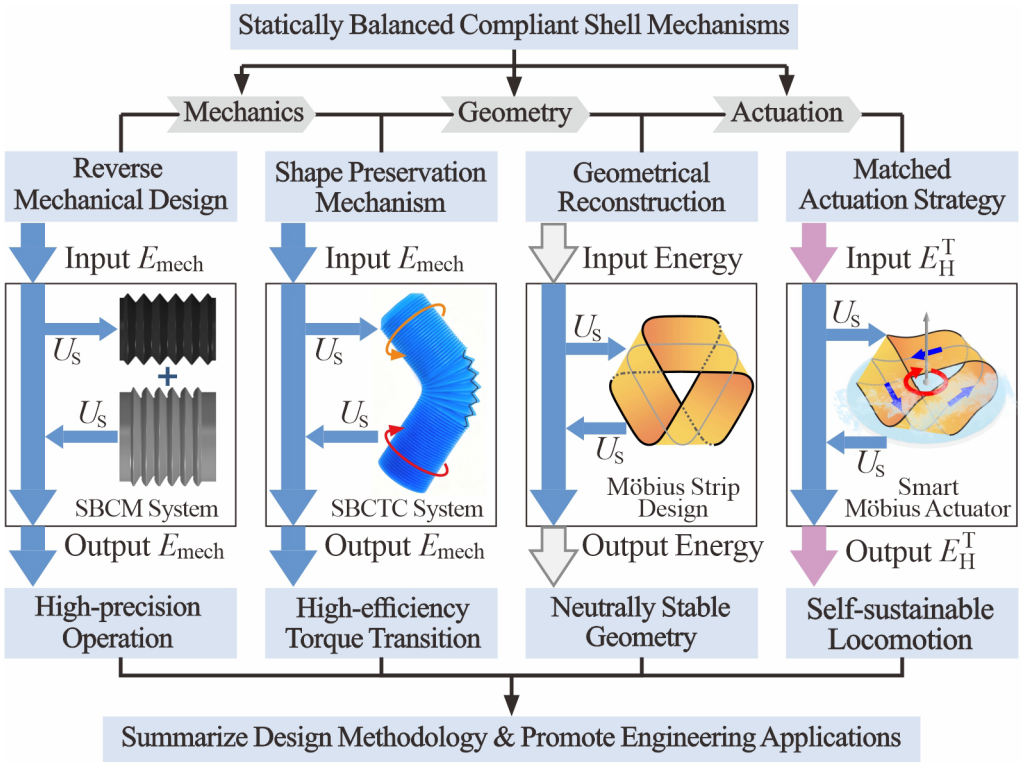

Fig. 1-21 Main contents of this dissertation

Chapter 2 Theoretical Design of the Bellow-shaped SBCM

2.1 Introduction

SBCMs have been widely applied in diverse engineering fields, owing to their monolithic design of compliant mechanism and zero actuation force of static balance. With marked advantages of shell structures in design freedom, load-bearing efficiency and functional integration, the focus of the recent research has shifted from existing beam-based SBCMs to statically balanced compliant shell mechanisms with nonlinear global deformation to tackle practical challenges.

Here, the bellow-shaped oil bladders have been widely adopted in the buoyancy engines of underwater gliders. Functioning as a hydraulic system, the engine modulates the buoyancy of the glider through precise control of the liquid volume within the oil bladder for real-time position adjustment[51,52]. During operation, the buoyancy engine needs to overcome the increasing loads of the bellow-shaped oil bladder under axial compression, which results in increased energy consumption and degraded operating precision. This issue can be potentially addressed by introducing the concept of multi-component SBCMs, i.e., designing a compliant shell balancer with mirrored mechanical behavior of the bellow to form an SBCM so as to achieve zero actuation force during operation.

In this chapter, we innovatively designed and studied a novel shell-based SBCM, which is composed of a bellow and a straw-inspired balancer positioned coaxially to achieve static balance, thus significantly reducing driving force, see Fig. 2-1. To overcome the challenges of undetermined balancer geometry and globally nonlinear deformation of the system, theoretical models based on structural mechanics were developed for both components, which enables us to predict the evolution of deformation and strain energy. These models were further verified through numerical simulation and prototype experiments. Furthermore, the effect of geometric parameters on the behavior of the balancer was investigated, thereby identifying the key parameters that govern the shape and magnitude of the strain energy curve respectively.

The layout of the chapter is listed as follows. Section 2.2 presents the geometry of the bellow and the theoretical analysis of its deformation and strain energy during compression. In Section 2.3, a straw-inspired balancer is designed to satisfy the criteria of static balance. Theoretical derivation of the strain energy during tension and a

parametric study is also conducted in this section, offering guidance on how to select design parameters for the balancer. Subsequently, the theoretical models and the novel SBCM design are verified through finite element modelling and experiments in Section 2.4. Finally, discussion and conclusions are included in Sections 2.5 and 2.6, which summarize this chapter.

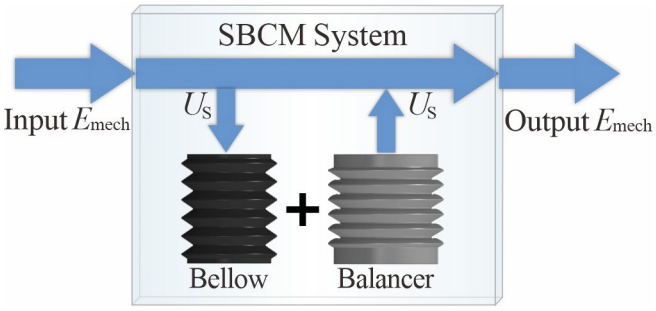

Fig. 2-1 Energy flow of the bellow-shaped SBCM.

2.2 Geometry and Strain Energy of the Bellow

The bellow, see Fig. 2-2(a), is composed of a series of interconnected conical frustums with identical geometry. A unit of the bellow as shown in Fig. 2-2(b) can be described by its outer radius R_1, slant angle α_1, height h_1, and shell thickness t_1. In addition, the regions, where two frustums are connected are filleted by a chamfer circle of radius r_{F1}. Those parameters, together with the number of units in the axial direction N completely define the geometry of the bellow. Then its inner radius r_1 can be obtained as follows.

$$r_1 = R_1 + 2r_{F1}(1-\cos\alpha_1) + (0.5h_1 - 2r_{F1}\cos\alpha_1)\cos\alpha_1. \tag{2-1}$$

When a bellow is axially compressed, global deformation occurs not only around the hinge-like areas where neighboring frustums are connected but also in the straight shells. The strain energy of the bellow consists of two parts: bending strain energy $U_{S,bd}$ and hoop strain energy $U_{S,hoop}$. To calculate the strain energy of the bellow, three basic assumptions are made. First, the deformations of all the units are identical. Therefore, the total energy of the bellow is the summation of that of each unit. Second, the deformation of one unit is symmetric about its axis.

Consequently, the unit can be evenly discretized into a series of slender curved beams along its circumferential direction, as shown in Fig. 2-3(a), and the total energy

of the unit can be obtained as that of one beam multiplied by the number of beams n. Finally, the material for the bellow is assumed to be linear elastic.

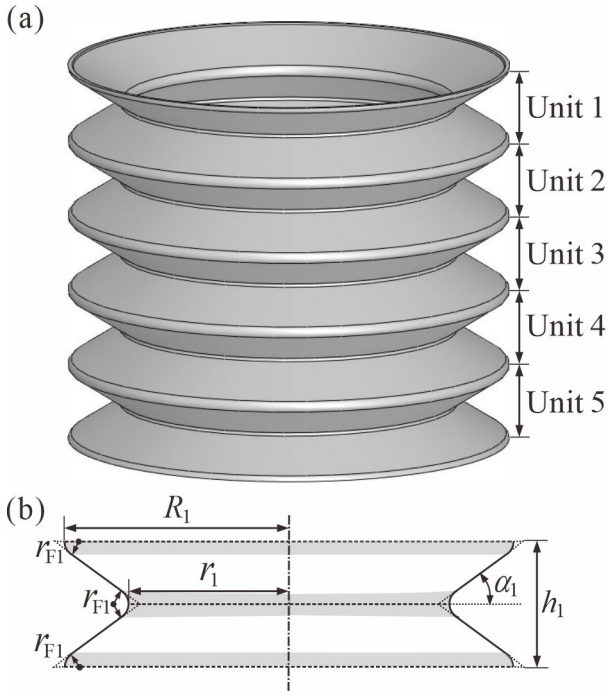

Fig. 2-2 Geometry of the bellow. (a) A bellow composed of five units in the perspective view, (b) geometry of a unit of the bellow in the sectional view.

First, consider a single beam AE in Fig. 2-3(b) with the central angle φ_n equal to $2\pi/n$. Points B and D are respectively the middle point of AC and CE. For the convenience of subsequent calculation, a Cartesian coordinate system *oxy* is created, in which *o* is the midpoint between points B, D, and the *x*-axis passes through point C.

Although the overall displacement of beam AE is significant upon compression of the bellow, the material remains linearly elastic with limited strain. The deflection differential equation based on the Euler-Bernoulli beam model can be obtained[39,40].

$$EI_1\left(\frac{\mathrm{d}\theta}{\mathrm{d}s}+\frac{v}{r_\kappa{}^2}\right)=EI\left(\frac{\mathrm{d}^2u}{\mathrm{d}s^2}+\frac{v}{r_\kappa{}^2}\right)=M_\mathrm{A}+F_{\mathrm{A}x}(y_\mathrm{A}-y)+F_{\mathrm{A}y}(x_\mathrm{A}-x), \tag{2-2}$$

$$\frac{\mathrm{d}u}{\mathrm{d}s}-\frac{v}{r_\kappa}=\frac{F_{\mathrm{A}y}\cos\alpha+F_{\mathrm{A}x}\sin\alpha}{EA_1}+\frac{M_\mathrm{A}+F_{\mathrm{A}x}(x_\mathrm{A}-x)+F_{\mathrm{A}y}(y_\mathrm{A}-y)}{EA_1r_\kappa}. \tag{2-3}$$

Here, E is the Young's modulus of the material, I_1 is the moment of inertia, and A_1 is the cross-sectional area of the bellow. x_A and y_A are the Cartesian coordinates of the

starting point A. At an arbitrary point on the beam with coordinates x and y, r_κ is the radius of curvature of the central axis, θ is the rotational angle at the specific point. u and v are the displacements along and perpendicular to the central axis of the beam, respectively. F_{Ax}, F_{Ay} and M_A are respectively the horizontal force, vertical force, and moment at point A, also see Fig. 2-3(b).

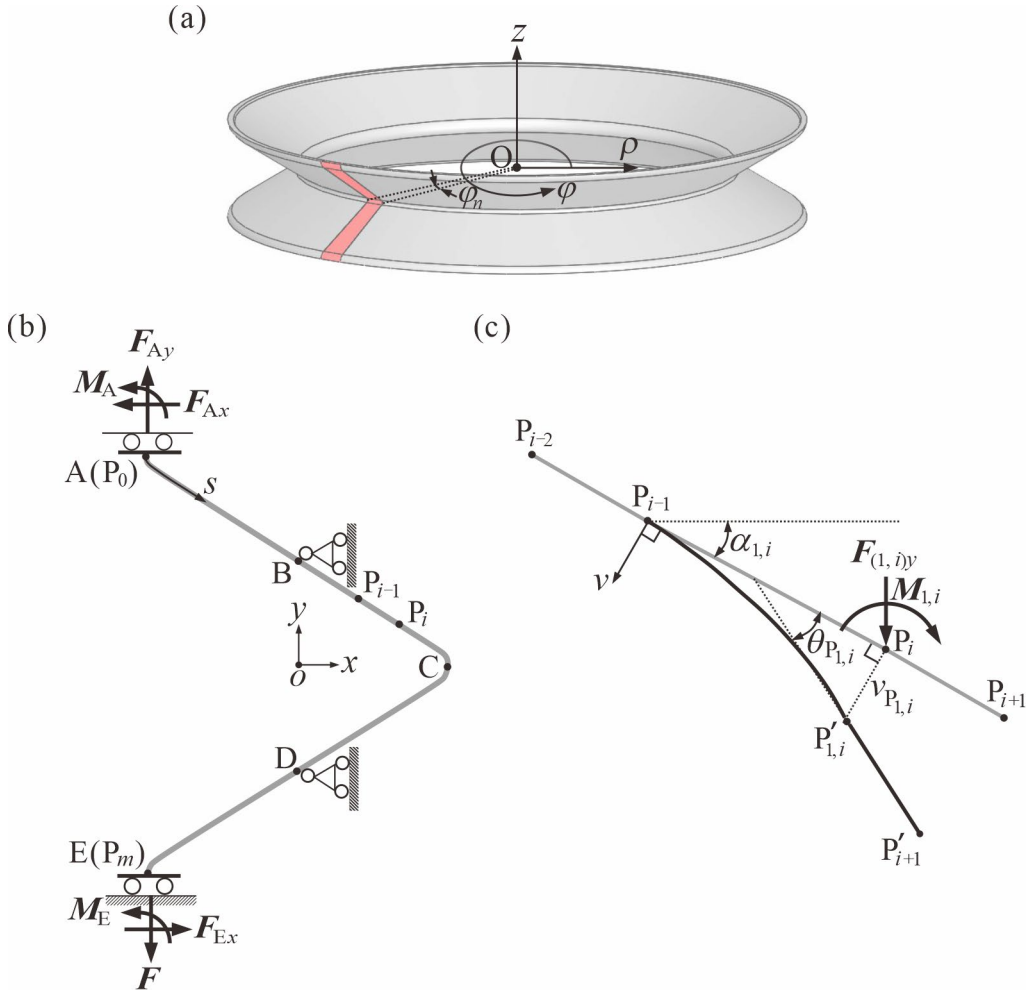

Fig. 2-3 Theoretical analysis of the bellow. (a) Cutting of a slender beam from a unit of the bellow, (b) boundary condition and force analysis of the beam, and (c) force analysis of a beam segment.

And the arc length s from the arbitrary point to the starting point A can be derived as follows. The original length of the beam l_1 is

$$s=\int_{y}^{h_1/2}\sqrt{1+\left(\frac{\mathrm{d}x}{\mathrm{d}y}\right)^2}\,\mathrm{d}y,\ l_1=\int_{-h_1/2}^{h_1/2}\sqrt{1+\left(\frac{\mathrm{d}x}{\mathrm{d}y}\right)^2}\,\mathrm{d}y. \tag{2-4}$$

Theoretically, the cross section of the beam has a sector profile. However, when n is sufficiently large, it can be approximated to a rectangular profile with side lengths $\rho\varphi_n$ and t_1. Therefore, the cross-sectional area A_1 and the cross-sectional moment I_1 of any point on the beam can be calculated as follows.

$$A_1 = \rho\varphi_n t_1,\ I_1 = \rho\varphi_n t_1^3/12, \tag{2-5}$$

in which $\rho = -x + 0.5(R_1 + r_1)$.

Having obtained the equilibrium equation, we then consider the boundary conditions. Since all the units deform identically, points A and E which are located on the plane of symmetry between neighboring units should have zero change in rotation angle, and the horizontal force F_{Ax} should also be zero, i.e.,

$$\text{A: } s = 0,\ \mathrm{d}\theta = 0;\ \text{E: } s = l_1,\ \mathrm{d}\theta = 0,\ G_A = 0. \tag{2-6}$$

Moreover, due to the symmetry of the geometry and loading condition, point C should have zero change in rotation angle, i.e.,

$$\text{C}: s = l_1/2,\ \mathrm{d}\theta = 0. \tag{2-7}$$

A further investigation reveals that the boundary conditions above are not sufficient to obtain one unique solution of Eqs. (2-2) and (2-3). We then assume that points B and D have zero displacement along the x-axis. We shall prove the validity of this assumption later in the paper. Thus, the following boundary conditions are added.

$$\text{B: } s = l_1/4,\ \mathrm{d}x = 0;\ \text{D: } s = 3l_1/4,\ \mathrm{d}x = 0. \tag{2-8}$$

Substituting Eqs. (2-4)-(2-8) into the deflection differential equations (2-2) and (2-3), the beam is found to be statically indeterminate with one unknown moment M_A. For a given F_A, M_A can be solved by applying the boundary conditions on the beam, and then the deformation of the beam can be achieved. However, it is rather difficult to solve the differential equations explicitly due to two reasons. First, the beam is geometrically complicated with both curves and straight segments. Second, A_1 and I_1 varies along the beam. Therefore, we adopted a numerical approach to solve the theoretical governing equation.

We first further discretize the beam into m rigidly connected piecewise segments of equal length l_1.

$$\Delta l_1 = l_1/m. \tag{2-9}$$

Here, we define the segment i as bounded by points P_{i-1} and P_i, see Fig. 2-3(b). Since each segment is short, it can be approximated as a straight beam with the radius of curvature $r_\kappa \to +\infty$. Then the deflection differential equations (2-2) and (2-3) can be both simplified.

$$EI_1 \frac{\mathrm{d}\theta}{\mathrm{d}s} = EI_1 \frac{\mathrm{d}^2 w}{\mathrm{d}s^2} = M_\mathrm{A} + F_{\mathrm{A}y}(x_\mathrm{A} - x), \tag{2-10}$$

$$\frac{\mathrm{d}u}{\mathrm{d}s} = \frac{F_{\mathrm{A}y}\cos\alpha}{EA_1}. \tag{2-11}$$

Under exterior loads F_A and M_A acted on the end of the beam, segment i as shown in Fig. 2-2(c) can be considered as a cantilever beam with point P_{i-1} being fixed and point P_i being loaded by vertical force $F_{(1,i)y}$ and moment $M_{1,i}$, which are calculated by Eq. (2-12).

$$F_{(1,i)x} = F_{\mathrm{A}x} = 0,\ F_{(1,i)y} = F_{\mathrm{A}y},\ M_{1,i} = M_\mathrm{A} + F_\mathrm{A}(x_\mathrm{A} - x_{1,i}). \tag{2-12}$$

Then, the deflection $v_{1,i}$ and the rotation angle $\theta_{1,i}$ at point P_i can be obtained from Eq. (2-13) as

$$v_{1,i} = \frac{F_{(1,i)y}\sin\alpha_{1,i}\Delta l_1^3}{3EI_{1,i}} + \frac{M_{1,i}\Delta l_1^2}{2EI_{1,i}},\ \theta_{1,i} = \frac{F_{(1,i)y}\sin\alpha_{1,i}\Delta l_1^2}{2EI_{1,i}} + \frac{M_{1,i}\Delta l_1}{EI_{1,i}}. \tag{2-13}$$

Here, $I_{1,i}$ is the average cross-sectional moment for the i-th segment of the beam. To obtain the deformation of the entire beam, we start from segment 1 bounded by points P_0(A) and P_1. Using the boundary condition at point A, the deflection $v_{1,i}$ and rotation angle $\theta_{1,i}$ of point P_i can be deduced from Eq. (2-13). Following the same procedure, the deformation of all the other segments can be successively obtained. Again, since the beam is statically indeterminate, M_A should be determined based on F_A and boundary conditions. Finally, given that Eq. (2-13) is only valid for small deflection, when a large deformation is required from the bellow, the exterior load F_A should be gradually increased to make sure the deflection at each load increment is small.

When the deformed configuration of the beam is obtained, the bending strain energy of a unit of the bellow can also be calculated as

$$U_{\mathrm{S,bd}} = Nn\int_0^{l_0} \frac{[M_\mathrm{A} + F_{(1,i)y}(x_\mathrm{A} - x)]^2}{2EI_1}\mathrm{d}s = n\sum_{i=1}^{m}\left(\frac{{M_{1,i}}^2}{2EI_{1,i}}\Delta l_1\right). \tag{2-14}$$

Besides bending deformation, radial displacement of the bellow walls along the ρ axis also occurs accompanied by bending, thereby causing hoop strain in the circumferential direction. To account for the hoop strain energy, ρ_0 is defined as the initial distance between an arbitrary point on the wall of the bellow and ρ' as the distance after deformation. For the very short segment i, the distance ρ_{0i} and ρ_i' can be considered as uniform along the segment and determined based on the middle point of the segment. Thus the hoop strain and corresponding strain energy of a unit of the bellow can be calculated as

$$\varepsilon_{\rho_i} = \left|\rho_i' - \rho_{0i}\right| / \rho_{0i}, \tag{2-15a}$$

$$U_{\mathrm{S,hoop}} = N\left[nE\int_0^{l_1}(\varepsilon_\rho)^2\pi\rho_0 t_1 \mathrm{d}s\right] = N\left[nE\sum_{i=1}^{m}(\varepsilon_{\rho_i})^2\pi\rho_{0i}t_1\Delta l_1\right]. \tag{2-15b}$$

Therefore, the total strain energy of the bellow U_S can be obtained as

$$U_\mathrm{S} = U_{\mathrm{S,hoop}} + U_{\mathrm{S,bd}}. \tag{2-16}$$

Consider a typical bellow-shaped oil bladder with the following geometric parameters $N = 5$, R_1=74.46 mm, r_1=52.86 mm, α_1=32°, h_1=25 mm, r_{F1}=1.20 mm and t_1=1.20 mm. The material adopted here is thermal plastic polyurethane (TPU) with density of 1820kg/m^3, Young's modulus of $E = 39.82$ MPa and Poisson's Ratio of $\nu = 0.45$.

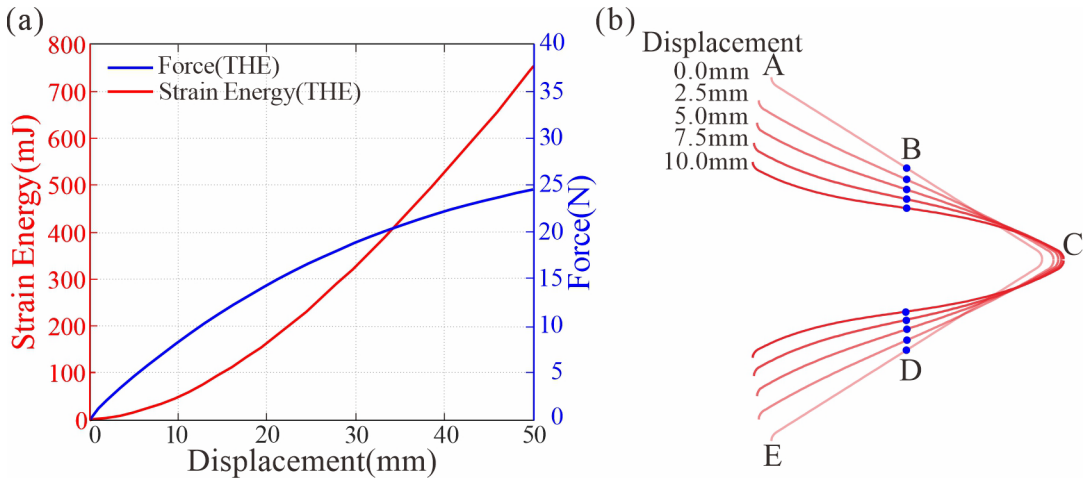

Fig. 2-4 Theoretical mechanical performance of the bellow. (a) The theoretical strain energy and force vs. compression displacement curves of the bellow; (b) sectional profiles of a single unit under compression.

Applying an axial displacement of 50 mm to the bellow-shaped bladder, the theoretical (THE) strain energy and compression force vs. compression displacement curves are calculated and drawn in Fig. 2-4(a). Here, *n* and *m* are respectively selected to be 500 and 120. Moreover, the sectional profiles of a single unit compressed by 0 mm, 2.5 mm, 5.0 mm, 7.5 mm and 10.0 mm can be also derived and represented in Fig. 2-4(b).

2.3 Design and Strain Energy of the Balancer

2.3.1 Geometrical Design of the Balancer

To achieve zero actuation force during compression of the bellow, we introduce a tubular shell balancer assembled coaxially and outside of the bellow, thereby forming a statically balanced compliant shell mechanism.

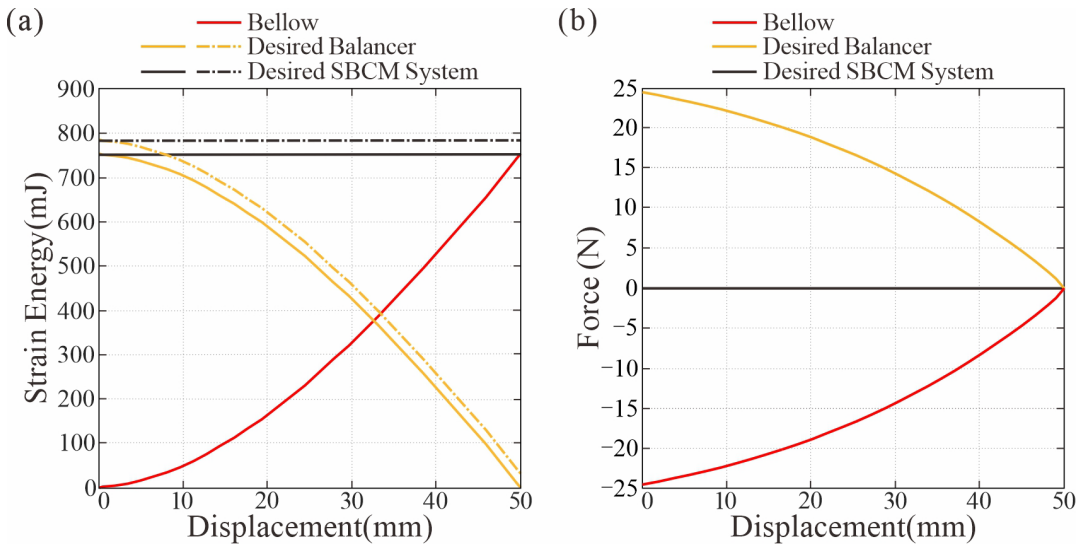

Fig. 2-5 Mechanical behavior of the desired SBCM. (a) Strain energy vs. compression displacement curves and (b) force vs. tensile displacement curves for the bellow, the desired SBCM, and the balancer, respectively.

For the bellow considered in Section 2.2, the desired SBCM should exhibit constant strain energy in Fig. 2-5(a). From this, the strain energy vs. displacement curve of the balancer can be deduced. Note that the magnitude of the strain energy of the SBCM is variable, resulting in a family of parallel strain energy curves for the desired

balancer. Here, the minimum strain energy of the SBCM is equal to the maximum strain energy of the bellow, marked in the solid black line in Fig. 2-5(a). Figure 2-5(b) presents the descending force-displacement relationship of the balancer under tension.

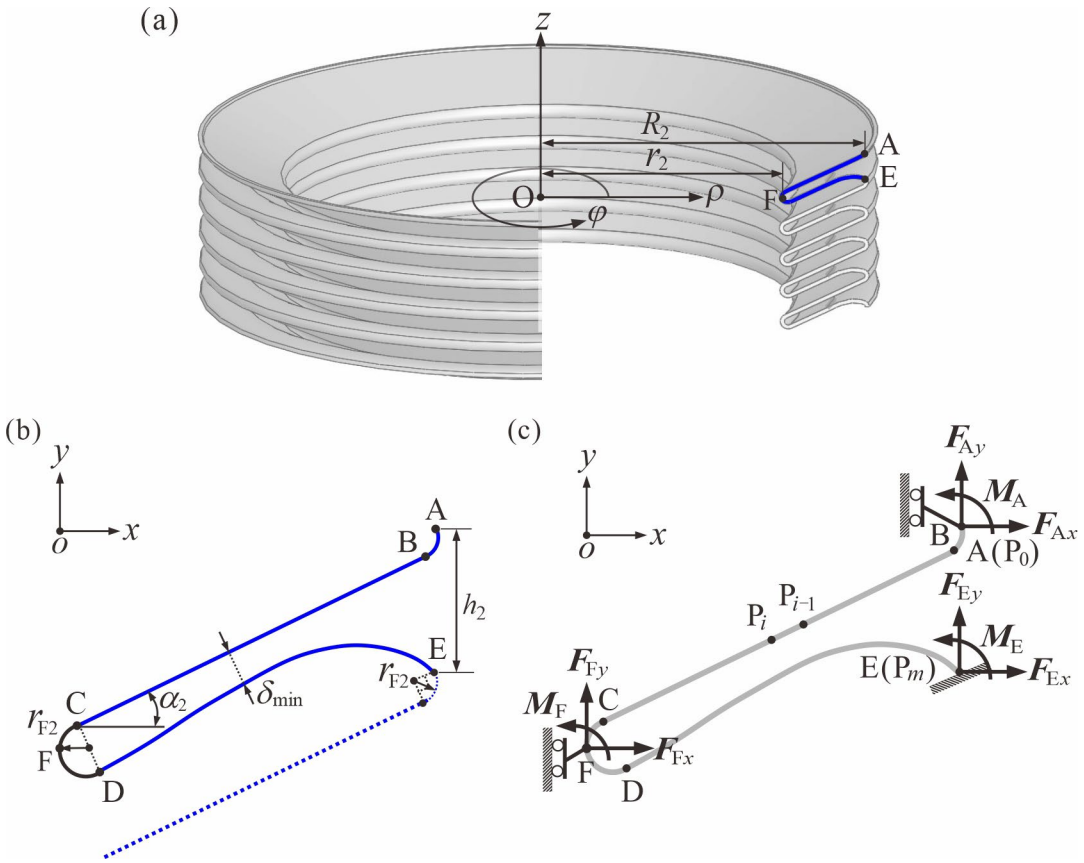

Fig. 2-6 Geometric and theoretical model of the designed balancer. (a) A balancer composed of 5 units in the perspective view; (b) geometry of a balancer unit in the sectional view; (c) boundary condition and force analysis of a slender curved beam cut from a balancer unit.

Inspired by the stretching process of the multistable straw[54,63], a balancer generally in the form of a compressed straw as shown in Fig. 2-6(a) is designed. The outer balancer is also composed of a series of conical frustums, but more complicated compared with those of the bellow. The sectional profile of a unit of the balancer, see Fig. 2-6(b), comprises of a quarter-circle AB, a straight line BC, a semi-circle CD, and a cubic polynomial curve DE. The continuity condition is enforced at all the joining points. Moreover, geometric incompatibility is introduced into the balancer by fixing its inner and outer radii, thus matching the desired decreasing force and displacement

relationship. Rigid rings are introduced at the exterior (points A, E) and interior (point F) cross sections of the balancer to keep its maximum and minimum radii unchanged.

The geometry of a unit of the balancer can be completely defined by six parameters, i.e. the outer and inner radii R_2 and r_2 respectively, slant angle α_2, radius of curvature r_{F2} of the quarter-circle AB and the semi-circle CD, unit height h_2 and shell thickness t_2.

Defining a local Cartesian coordinate system *oxy*, in which *x* axis passes through point A and *y*-axis passes through point F, the cubic polynomial DE is expressed as

$$y = a_3x^3 + a_2x^2 + a_1x + a_0. \tag{2-17}$$

in which a_0, a_1, a_2 and a_3 are polynomial coefficients determined by satisfying from the continuity condition at the end point D.

$$\text{D: } \begin{cases} x_D = r_{F2}\sin\alpha_2 + r_{F2} \\ y_D = -(R_2 - r_2 + 2r_{F2}\sin\alpha_2 - r_{F2})\tan\alpha_2 - 3r_{F2}\cos\alpha_2, \\ (\mathrm{d}y/\mathrm{d}x)_D = -\cot\alpha_2 \end{cases} \tag{2-18}$$

and the condition at the end point E can be

$$\text{E: } \begin{cases} x_E = R_2 - r_2 \\ y_E = -h_2 \\ (\mathrm{d}y/\mathrm{d}x)_E = \tan\alpha_2 \end{cases}. \tag{2-19}$$

Then the coefficients can be derived by solving the following equation set.

$$\begin{bmatrix} x_D^3 & x_D^2 & x_D & 1 \\ 3x_D^2 & 2x_D & 1 & 0 \\ x_E^3 & x_E^2 & x_E & 1 \\ 3x_E^2 & 2x_E & 1 & 0 \end{bmatrix} \begin{bmatrix} a_3 \\ a_2 \\ a_1 \\ a_0 \end{bmatrix} = \begin{bmatrix} y_D \\ (\mathrm{d}y/\mathrm{d}x)_D \\ y_E \\ (\mathrm{d}y/\mathrm{d}x)_E \end{bmatrix}. \tag{2-20}$$

Considering the wall thickness of the balancer, interference of the curved surface should be avoided by checking the shortest distance δ_{min} between the straight line BC and the polynomial curve DE larger than t_2, as shown in Fig. 2-6(b).

2.3.2 Strain Energy of the Balancer

Similar to the bellow, strain energy of the balancer is the summation of bending strain energy $U_{S,bd}$ and hoop strain energy $U_{S,hoop}$. Adopting the same three basic assumptions and discretization method as in the case of the bellow, the strain energy

under tension for the balancer can also be derived by analyzing one slender curved beam as shown in Fig. 2-6(c). The boundary conditions of the beam are set as: points A, F, and E have zero displacement along the *x* axis and zero rotation, and point E has zero displacement along the *y* axis, thus

$$\mathrm{A}:\ \mathrm{d}x=0,\ \mathrm{d}\theta=0; \tag{2-21a}$$

$$\mathrm{F}:\ \mathrm{d}x=0,\ \mathrm{d}\theta=0; \tag{2-21b}$$

$$\mathrm{E}:\ \mathrm{d}x=0,\ \mathrm{d}y=0,\ \mathrm{d}\theta=0. \tag{2-21c}$$

In addition, the moment of inertial I_2 of any point on the balancer can be expressed as

$$I_2=\frac{\rho\varphi_n t_2^{\,3}}{12}=\frac{(x+r_2)\varphi_n t_2^{\,3}}{12}. \tag{2-22}$$

Starting from point A, the governing equation for segment *i* of the beam bounded by $\mathrm{P}_{i\text{-}1}$ and P_i can be expressed as

$$F_{(2,i)x}=F_{\mathrm{A}x},\ F_{(2,i)y}=F_{\mathrm{A}y},M_{2,i}=M_{\mathrm{A}}+F_{\mathrm{A}}\left(x_{\mathrm{A}}-x_{2,i}\right)+G_{\mathrm{A}}\left(y_{\mathrm{A}}-y_{2,i}\right). \tag{2-23}$$

Then, the deflection $v_{2,i}$ and the rotation angle $\theta_{2,i}$ at point P_i on the balancer beam can be derived as follows.

$$v_{2,i}=\frac{(F_{(2,i)x}\cos\alpha_{2,i}+F_{(2,i)y}\sin\alpha_{2,i})\Delta l_2^{\,3}}{3EI_{2,i}}+\frac{M_{2,i}\Delta l_2^{\,2}}{2EI_{2,i}}, \tag{2-24}$$

$$\theta_{2,i}=\frac{(F_{(2,i)x}\cos\alpha_{2,i}+F_{(2,i)y}\sin\alpha_{2,i})\Delta l_2^{\,2}}{2EI_{2,i}}+\frac{M_{2,i}\Delta l_2}{EI_{2,i}}. \tag{2-25}$$

After solving Eqs. (2-24) and (2-25), the total strain energy of the balancer, also composed of bending strain energy and hoop strain energy, can be calculated from Eqs. (2-15) and (2-16).

Using the theoretical model, we can design the balancer to match the desired strain energy and force curve in Fig. 2-6. It has been mentioned in Section 2.3.1 that six parameters R_2, r_2, α_2, h_2, $r_{\mathrm{F}2}$ and t_2 completely define the geometry of a unit of the balancer. In the design, r_2 can be practically selected as the minimum value that guarantees no interference between bellow and balancer. Moreover, $r_{\mathrm{F}2}$ has little effect on the performance of the balancer, and thus can be chosen to be identical to $r_{\mathrm{F}1}$ for convenience. To simplify the design process, we specify that: the inner radius of the

balancer $r_2 = R_1 + 2 = 76.46$ mm; the radius of curve $r_{F1} = r_{F2} = 1.20$ mm the width of the corrugated wall of the balancer $R_2 - r_2$, is equal to that of the bellow $R_1 - r_1$ and therefore $R_2 = 96.06$ mm; the balancer and the bellow have the same number of units and use the same material. Therefore, the behavior of the balancer upon tension are determined by α_2, h_2 and t_2. By varying those parameters, it is found that a balancer with $\alpha_2 = 26^\circ, h_2 = 7.98$ mm and $t_2 = 0.95$ mm generates strain energy and force curves that match well the desired ones as shown in Fig. 2-7(a).

It can be observed that to match the objective curve shape, the balancer needs to be prestressed, by 11.5 mm in this case. The reason is that the desired tensile force curve, corresponding to the desired strain energy of the SBCM with any magnitude, starts from a non-zero force and gradually deceases throughout the tensile process. This cannot be achieved by a balancer that is stable initially with zero force and energy. Therefore, when assembled with the bellow to form a SBCM, the outer balancer is first stretched by 11.5 mm with prestress and then connected to the inner bellow. The work range of the balancer is between 11.5 mm and 61.5 mm, providing an effective working range of 50.0 mm, which aligns with that of the bellow. The corresponding deformation process of a single balancer unit under tension is illustrated in Fig. 2-7(b), demonstrating its geometric evolution.

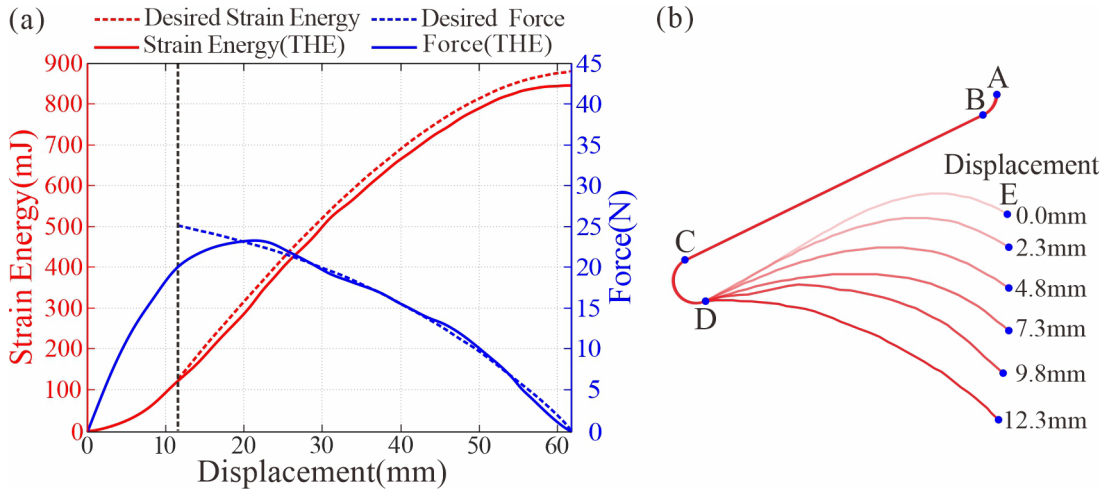

Fig. 2-7 Theoretical mechanical performance of the outer balancer. (a) Desired and theoretical strain energy and tensile force vs. tension displacement curves of the balancer; (b) sectional profiles of a single unit under tension.

2.3.3 Effects of Geometrical Parameters

It has been shown in Section 2.3.2 that α_2, h_2 and t_2 mainly determine the strain energy of the balancer. To investigate the effect of those parameters, 55 models, with varying α_2 from 16° to 36° at an interval of 5°, h_2 from 8 mm to 12 mm at an interval of 1 mm, and t_2 from 0.80 mm to 1.20 mm at an interval of 0.2 mm, are analyzed theoretically. All the models have identical $r_2 = 76.46$ mm , $r_{F2} = 1.20$ mm. The geometric parameters of the models are listed in Tab. 2-1, in which the notation h_2-α_2-t_2 is adopted.

While all the models deform in a similar manner, the strain energy vs. tension displacement curves are found to fall into three different shapes, i.e., the degressive shape in which the tangent of the curve reduces with displacement, the quasi-linear shape in which the strain energy increases nearly linearly against displacement with the R-square in Curve Fitting Tools of MATLAB 2023a smaller than 0.45, and the progressive shape in which the tangent of the curve increases with displacement. The curve shapes of all the models are also compiled in Tab. 2-1, and representative curves in each shape are drawn in Fig. 2-8(a).

A careful examination of the results reveals that models with identical α_2 and h_2 have the same curve shape irrespective of t_2, indicating that the curve shape is decided only by the slant angle and unit height. To further clarify the effects of those two parameters, the curve shapes of all the models with $t_2 = 1.0$ mm are compiled, as shown in Fig. 2-2. Two trends can be observed from the phase map in Fig. 2-9. First, α_2 is the main factor in forming the degressive curve shape. Within the range of study, an α_2 of 16° leads to progressive curves only, while that of 36° results in degressive ones only. Second, when α_2 is fixed, an increase in h_2 causes the transition from degressive to progressive, see the models with $\alpha_2 = 26^\circ$ Therefore, a relatively large slant angle combined with a relatively small unit height help to create a degressive curve so as to balance the bellow.

Furthermore, when a degressive curve is obtained, the maximum strain energy is found to increase roughly linearly with the cubic power of shell thickness t_2, which is clearly shown in Fig. 2-8(b). The reason is that during deformation of the balancer, shear energy is neglected due to the adoption of Euler beam model, and bending energy is much larger than hoop strain energy. As a result, the total strain energy has an

approximately cubic relationship with t_2. This also explains why the curve shape is independent of wall thickness.

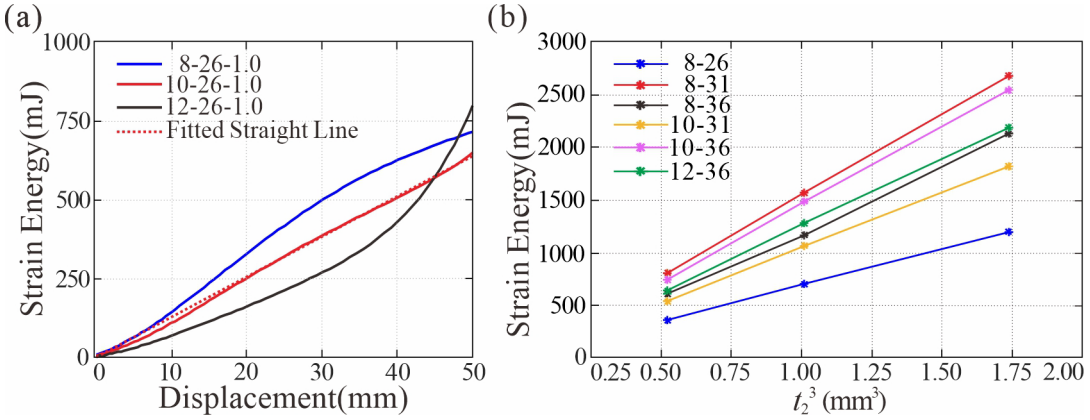

Fig. 2-8 Parametric analysis of the outer balancer. (a) Strain energy vs. tensile displacement curves of models 8-26-1.0, 10-26-1.0, and 12-26-1.0 with degressive, quasi-linear, and progressive curves, and fitted straight line for 10-26-1.0; (b) relationship between maximum strain energy and the cubic power of shell thickness for models 8-26-0.8/1.0/1.2, 8-31-0.8/1.0/1.2, 8-36-0.8/1.0/1.2, 10-31-0.8/1.0/1.2, 10-36-0.8/1.0/1.2 and 12-36-0.8/1.0/1.2.

According to the aforementioned parametric analysis, the desired balancer for a prerequisite bellow can be designed by the following three steps: (1) calculate the strain energy curve of the bellow, from which that of the balancer can be obtained; (2) determine the slant angle and unit height to get the desired degressive energy curve shape; and (3) adjust the wall thickness to fit the magnitude of the desired strain energy.

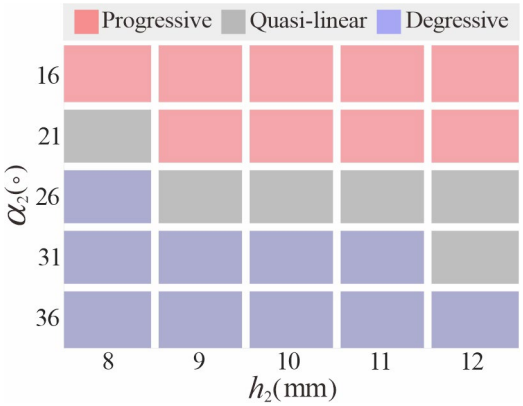

Fig. 2-9 Relationship between slant angle α_2, unit height h_2 and energy curve shape.

Tab.2-1 Geometries of the balancer and strain energy curve shape.

Model	h_2 (mm)	α_2 (°)	t_2 (mm)	Shape
8-16-0.8	8	16	0.8	Degressive
8-16-1.0	8	16	1.0	Progressive
8-16-1.2	8	16	1.2	Progressive
8-21-0.8	8	21	0.8	Quasi-linear
8-21-1.0	8	21	1.0	Quasi-linear
8-21-1.2	8	21	1.2	Quasi-linear
8-26-0.8	8	26	0.8	Degressive
8-26-1.0	8	26	1.0	Degressive
8-26-1.2	8	26	1.2	Degressive
8-31-0.8	8	31	0.8	Degressive
8-31-1.0	8	31	1.0	Degressive
8-31-1.2	8	31	1.2	Degressive
8-36-0.8	8	36	0.8	Degressive
8-36-1.0	8	36	1.0	Degressive
8-36-1.2	8	36	1.2	Degressive
9-16-1.0	9	16	1.0	Progressive
9-21-1.0	9	21	1.0	Progressive
9-26-1.0	9	26	1.0	Quasi-linear
9-31-1.0	9	31	1.0	Degressive
9-36-1.0	9	36	1.0	Degressive
10-16-0.8	10	16	0.8	Progressive
10-16-1.0	10	16	1.0	Progressive
10-16-1.2	10	16	1.2	Progressive
10-21-0.8	10	21	0.8	Progressive
10-21-1.0	10	21	1.0	Progressive
10-21-1.2	10	21	1.2	Progressive
10-26-0.8	10	26	0.8	Quasi-linear
10-26-1.0	10	26	1.0	Quasi-linear
10-26-1.2	10	26	1.2	Quasi-linear
10-31-0.8	10	31	0.8	Degressive
10-31-1.0	10	31	1.0	Degressive
10-31-1.2	10	31	1.2	Degressive
10-36-0.8	10	36	0.8	Degressive
10-36-1.0	10	36	1.0	Degressive
10-36-1.2	10	36	1.2	Degressive
11-16-1.0	11	16	1.0	Progressive
11-21-1.0	11	21	1.0	Progressive
11-26-1.0	11	26	1.0	Quasi-linear
11-31-1.0	11	31	1.0	Degressive
11-36-1.0	11	36	1.0	Degressive
12-16-0.8	12	16	0.8	Progressive
12-16-1.0	12	16	1.0	Progressive
12-16-1.2	12	16	1.2	Progressive
12-21-0.8	12	21	0.8	Progressive
12-21-1.0	12	21	1.0	Progressive
12-21-1.2	12	21	1.2	Progressive
12-26-0.8	12	26	0.8	Progressive
12-26-1.0	12	26	1.0	Progressive
12-26-1.2	12	26	1.2	Progressive
12-31-0.8	12	31	0.8	Quasi-linear
12-31-1.0	12	31	1.0	Quasi-linear
12-31-1.2	12	31	1.2	Quasi-linear
12-36-0.8	12	36	0.8	Degressive
12-36-1.0	12	36	1.0	Degressive
12-36-1.2	12	36	1.2	Degressive

2.4 Verification of the bellow-shaped SBCM

To verify the theoretical design approach of the SBCMs, numerical models of the bellow, the balancer, and the SBCM were built and analyzed with commercial software package ABAQUS/Explicit.

The bellow adopted the same geometric and material parameters as listed in Section 2.2, and each end was extended by a short cylinder of 12.5 mm in height, as shown in Fig. 2-10(a). The axial compression process was modeled as the structure standing on a stationary rigid panel and a mobile rigid panel moving downward to press it. The upper and lower ends of the bellow were respectively tied to the mobile and stationary panels. All the degrees of freedom of the stationary panel were fixed, whereas only the translational DoF of the mobile one in the axial direction was free of constraint. A prescribed displacement of 50.0 mm was assigned to the free translational DoF of the mobile panel to control the compression distance. The bellow was meshed with S4R, a four-node shell element with reduced integration. Self-contact was employed to model the contact among different parts of the bellow. Friction was taken into consideration by assigning the friction coefficient of 0.30[180].

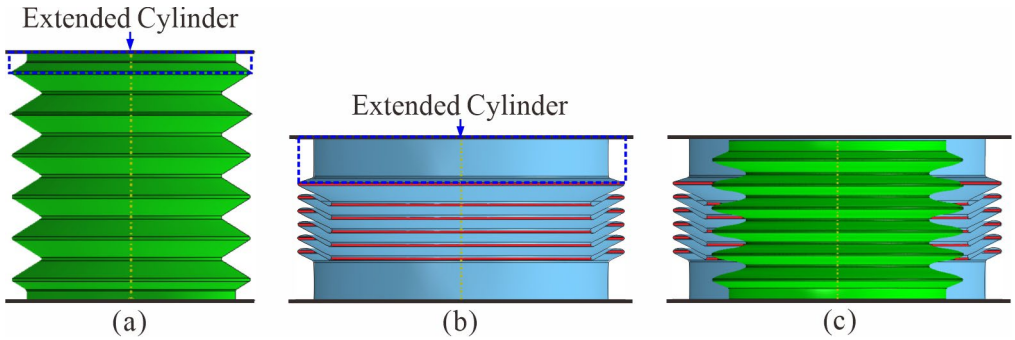

Fig. 2-10 Numerical models of (a) the bellow, (b) the balancer in sectional view, and (c) the SBCM in sectional view.

The balancer also had the same design parameters with the one theoretically studied in Section 2.3.2, and extended cylinders of 24.25 mm were also added at both ends as shown in Fig. 2-10(b). In addition, a series of rigid rings highlighted in red were tied at the exterior and interior cross sections of the balancer to keep its maximum and minimum radii unchanged, thereby satisfying the boundary conditions Eq. (2-21) in the theoretical analysis. The axial tension process was simulated using the same setup as that for the bellow, with the exception that the mobile panel moved away from the fixed

one instead of toward it. Moreover, the same S4R mesh, self-contact, and friction as in the case of the bellow were also adopted.

To assemble the SBCM, the bellow was compressed by 50.0 mm and the balancer was tensioned by 11.5 mm to reach the same height. Subsequently, the two components were placed coaxially as shown in Fig. 2-10(c), and the two ends of the components were respectively tied to two rigid panels. Then the SBCM was axially stretched as a whole by 50.0 mm, and the strain energy and force were extracted and recorded.

Finally, convergence tests in terms of mesh density and analysis time were also conducted, from which an element size of 1.0 mm and an analysis time of 0.5 s were determined suitable and adopted in the analysis.

2.4.1 Numerical Simulation of the Bellow

The deformation process of the bellow with corresponding logarithmic strain (LE) contour maps is presented in Fig. 2-11(a). During compression, all the units of the bellow are deformed simultaneously. At the beginning, the convex hinge-like regions are gradually pushed outwards radially while the concave ones move inwards, keeping the shells in between straight up to a displacement of 24.85 mm. Under further compression, the inward and outward motion of the hinge-like regions are decreased, accompanied by a slight bending of the initially straight shells, which is more clearly seen in the sectional profile of the middle unit represented by blue lines in Fig. 2-11(b). Moreover, the midpoint B of line AC and the midpoint D of line CE in Fig. 2-4(b) are found to move mainly vertically with negligible horizontal movement, indicating that the boundary conditions Eqs. (2-6)-(2-8) in the theoretical analysis are validated.

The theoretical deformed profiles of the middle unit of the bellow represented by the red dotted lines are calculated and compared with the corresponding numerical ones at the displacements of 12.13 mm, 24.85 mm, 38.25 mm and 50 mm in Fig. 2-10(b), from which a good match can be observed. Furthermore, the strain energy and compression force vs. compression displacement curves in Fig. 2-11(c) indicate that a good agreement between the theoretical and numerical results is obtained with the largest difference below 2.67%. Therefore, the derived theoretical model for the bellow can accurately describe its deformation process.

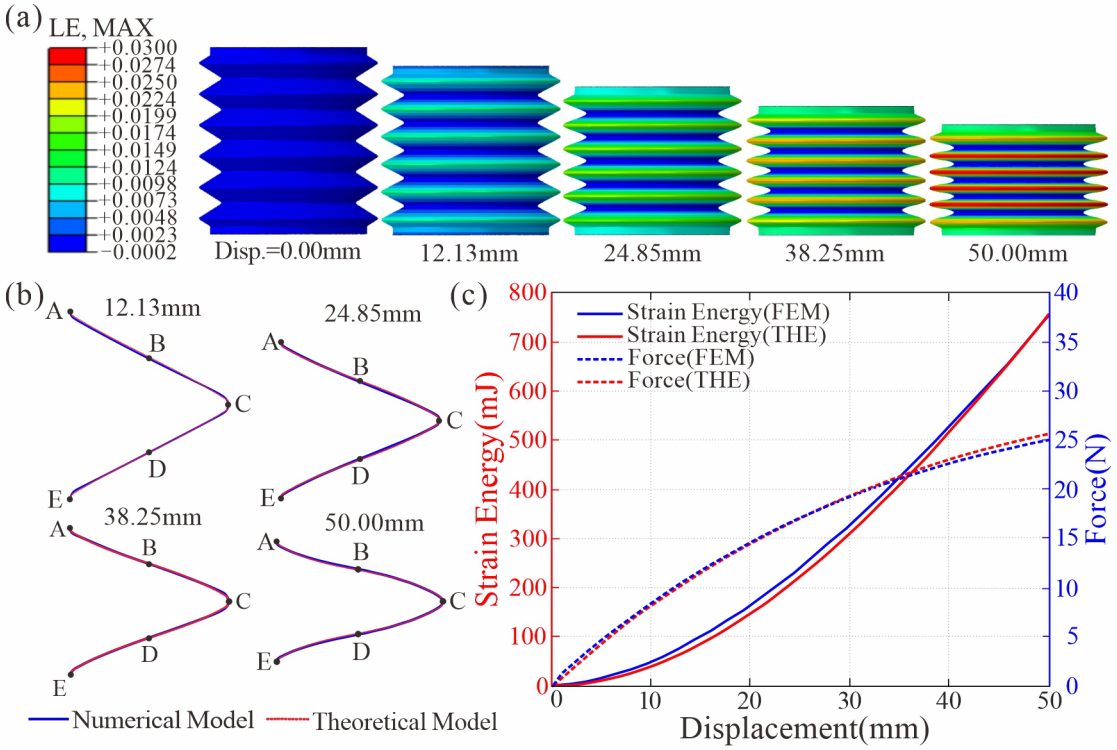

Fig. 2-11 Numerical validation of the bellow under compression. (a) Numerical deformation process of the bellow; (b) numerical and theoretical deformed sectional profiles of the below; and (c) numerical and theoretical strain energy and compression force vs. compression displacement curves of the bellow.

2.4.2 Numerical Simulation of the Balancer

The deformed configurations of the balancer at various stages of tension together with the logarithmic strain contour maps are shown in Fig. 2-12(a). Similar to the bellow, the deformation of all the five units of the balancer is synchronized. Figure 2-12(b) compares the theoretically derived deformed sectional profiles of the middle unit with the corresponding numerical ones. Again, a good match between theoretical and numerical results is obtained. Moreover, it can be observed that the straight shell is almost undeformed due to the rigid rings at the convex and concave hinge-like regions, whereas the shell with polynomial profile is bent to accumulate strain energy.

The theoretical strain energy and tensile force for the balancer are also calculated and compared with those of the numerical model in Fig. 2-12(c). It is found that the theoretical strain energy is in good agreement with the numerical one, with the largest deviation being 4.57%. The slightly lower theoretical value is probably due to the fact that only axial bending and circumferential tension/compression are accounted for in

the theoretical analysis, while circumferential bending is ignored. With respect to force, the discrepancy is relatively large at the beginning, indicating that ignoring the circumferential bending has a larger effect on the force. However, the two force curves converge quickly with displacement and achieve a reasonably good overall agreement. Therefore, the theoretical model for the balancer can also predict its tensile behavior.

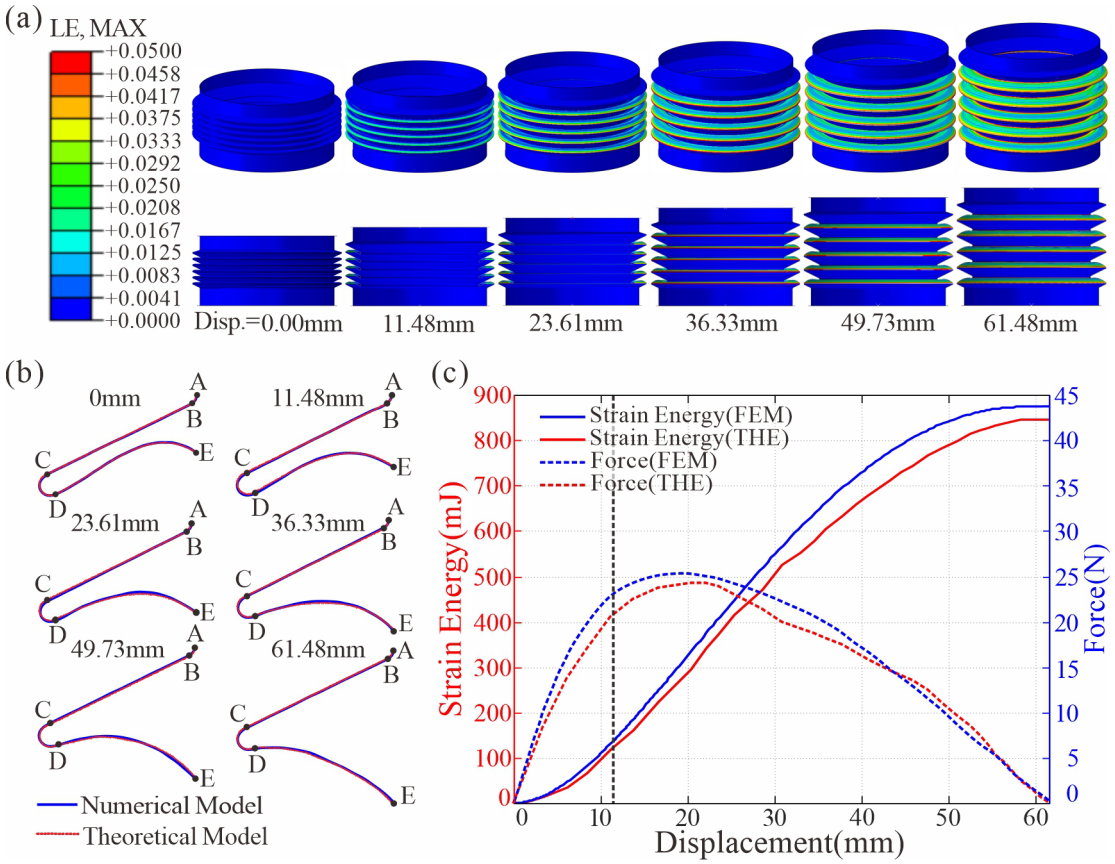

Fig. 2-12 Numerical validation of the balancer under tension. (a) Numerical deformation process of the balancer; (b) numerical and theoretical deformed sectional profiles of the balancer; (c) numerical and theoretical strain energy and tensile force vs. tensile displacement curves of the balancer.

2.4.3 Numerical Simulation of the SBCM

Finally, the assembled bellow-shaped SBCM is analyzed through numerical simulation. The deformation process under tension is shown in Fig. 2-13(a) and the associated strain energy and force vs. displacement curve are presented in Figs. 2-13(b) and (c). Despite the small discrepancy between the theoretical and numerical results for the two components, a tiny reaction force with the largest value of 0.97N, or only 3.62% of the maximum reaction force of the bellow, is achieved for the SBCM. To this point,

we can safely draw the conclusion that the proposed design approach and associated theoretical framework can effectively generate an SBCM with nearly zero reaction force.

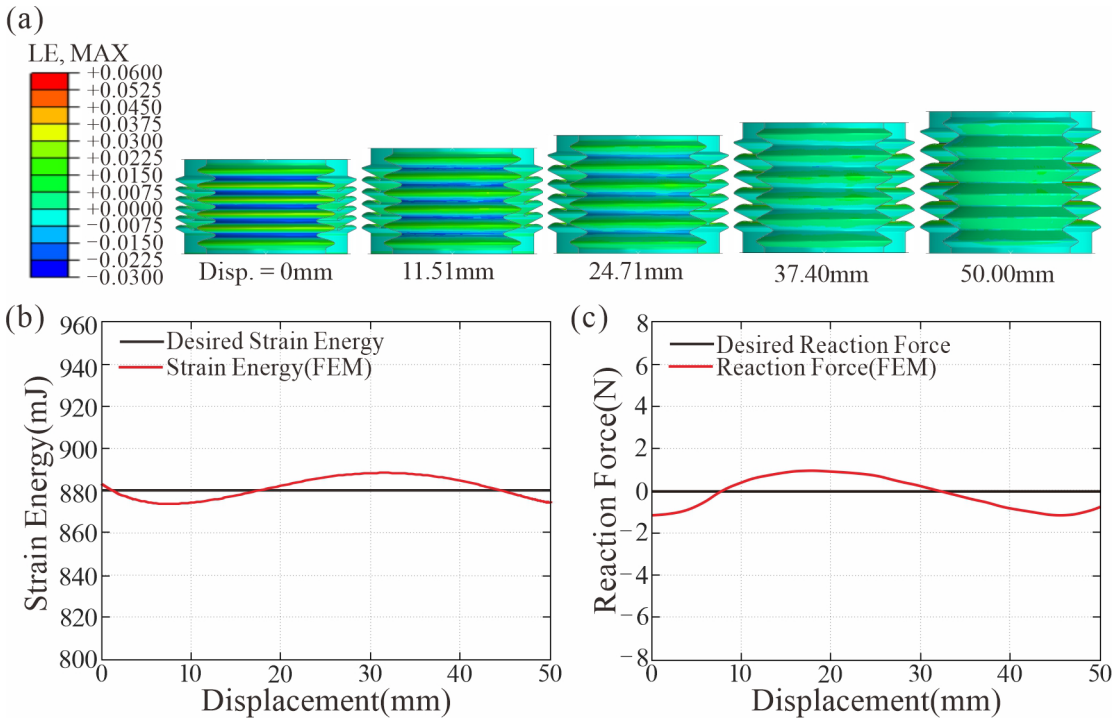

Fig. 2-13 Numerical validation of the SBCM under tension. (a) Deformation process of the SBCM; (b) desired and numerical strain energy vs. tensile displacement of the system, and (c) desired and numerical reaction force vs. tensile displacement of the system.

2.4.4 Fabrication and Experiments

A prototype of the SBCM was fabricated out of TPU using 3D printing technology and tested as shown in Fig. 2-14(a). The predetermined geometry of the bellow was: $N = 5$, $R_1 = 74.46$ mm, $r_1 = 52.86$ mm, $\alpha_1 = 32^\circ$, h_1=25 mm, t_1=1.70 mm and $r_{F1} = 1.40$mm. The geometry of the balancer was: $R_2 = 96$ mm, $r_2 = 76.46$ mm, α_2=34°, $h_2 = 9$ mm, $r_{F2} = 1.40$ mm and $t_2 = 1.20$ mm.

Moreover, steel rings were placed at the exterior and interior edges of the balancer to keep its maximum and minimum radii unchanged. To form the SBCM, the bellow was compressed by 50 mm and the balancer was stretched by 30 mm, and then the two were joined by plastic caps with circular grooves of 20 mm in depth.

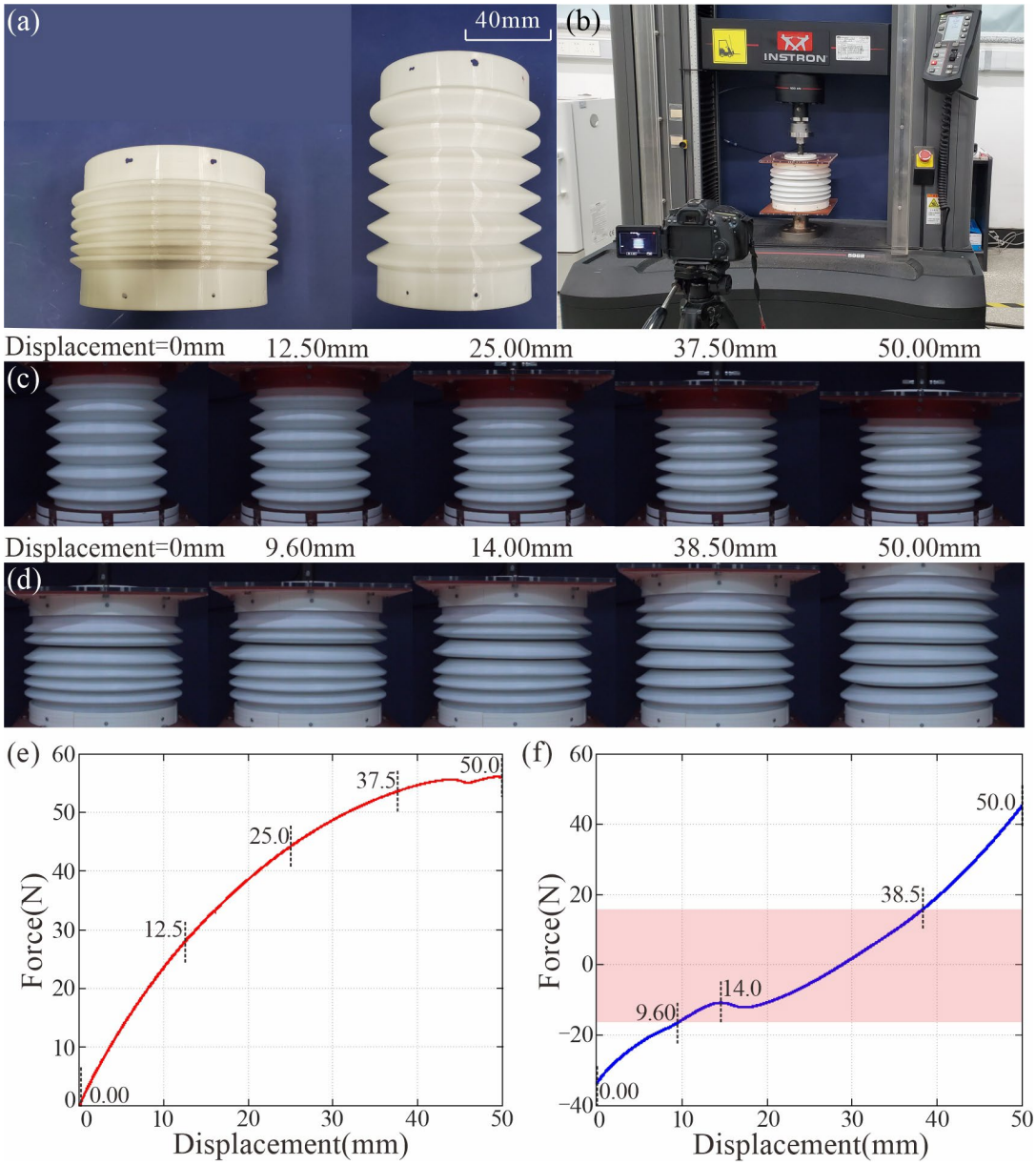

Fig. 2-14 Experimental validation of the SBCM. (a) The 3D-printed SBCM components; (b) experimental setup; (c) compression process of the bellow; (d) tension process of the SBCM; (e) force vs. compression displacement curve of the bellow; (f) force vs. tensile displacement curve of the bellow-shaped SBCM.

Quasi-static compression of the stand-alone bellow and tension of the SBCM were conducted on an INSTRON Universal Testing Machine (type 5982) at a loading speed of 2.0 mm/min, see Fig. 2-14(b). In the tests, the ends of the specimen were respectively connected to two acrylic plates. The tests were recorded by a standard digital camera (Canon 70D).

The deformation processes of the bellow and the SBCM are respectively shown in Figs. 2-14(c-d), and the corresponding force vs. displacement curves are drawn in Figs. 2-14(e-f). It can be seen that the bellow deforms in a reasonably synchronized manner except for the small range near the end of the loading process. As a result, the force curve shape matches the theoretically derived one quite well, suggesting the accuracy of the theoretical model for bellow.

Regarding the bellow-shaped SBCM, the deformation of the units of the balancer is less simultaneous. A careful examination of the specimen reveals that the balancer has inaccurate geometry especially near the curved interior and exterior edges, mainly owing to its initial folded configuration. The wall thickness of those edges is found to show noticeable divergence between 1.54 mm and 1.96 mm. Non-identical wall thickness leads to unsynchronized deformation of the units, which in turn causes deviation from the theoretical force. Despite that, the reaction force of the SBCM is reduced to ± 30% of that of the bellow between the displacement of 9.6 mm and 38.5 mm, or 72.3% of the designed statically balanced deformation range. Therefore, it is reckoned that the proposed design approach is reasonably effective to create SBCMs. However, developing a more accurate fabrication approach, or a way to print the balancer from a extended state, is essential for this SBCM to achieve the expected performance.

2.5 Discussion

It has been demonstrated in Section 2.4 that the proposed design performs quite well as a statically balanced compliant mechanism with nearly constant strain energy and zero force. Here in this section several key points are further elaborated.

First, two main assumptions were made in the derivation of the theoretical model. One is that all the units deform simultaneously. The other is that only the longitudinal bending strain energy and circumferential hoop strain energy are considered, while shear strain energy and circumferential bending energy are ignored. Numerical analysis demonstrates that the maximum in-plane shear strain is less than 4.2 % of the maximum principal strain $\varepsilon_{\mathrm{MAX}}$ of the shell, and thus its influence on the overall mechanical behavior is limited. Numerical models of both the bellow and balancer in Fig. 2-13(a) show that during deformation all of the units are well synchronized.

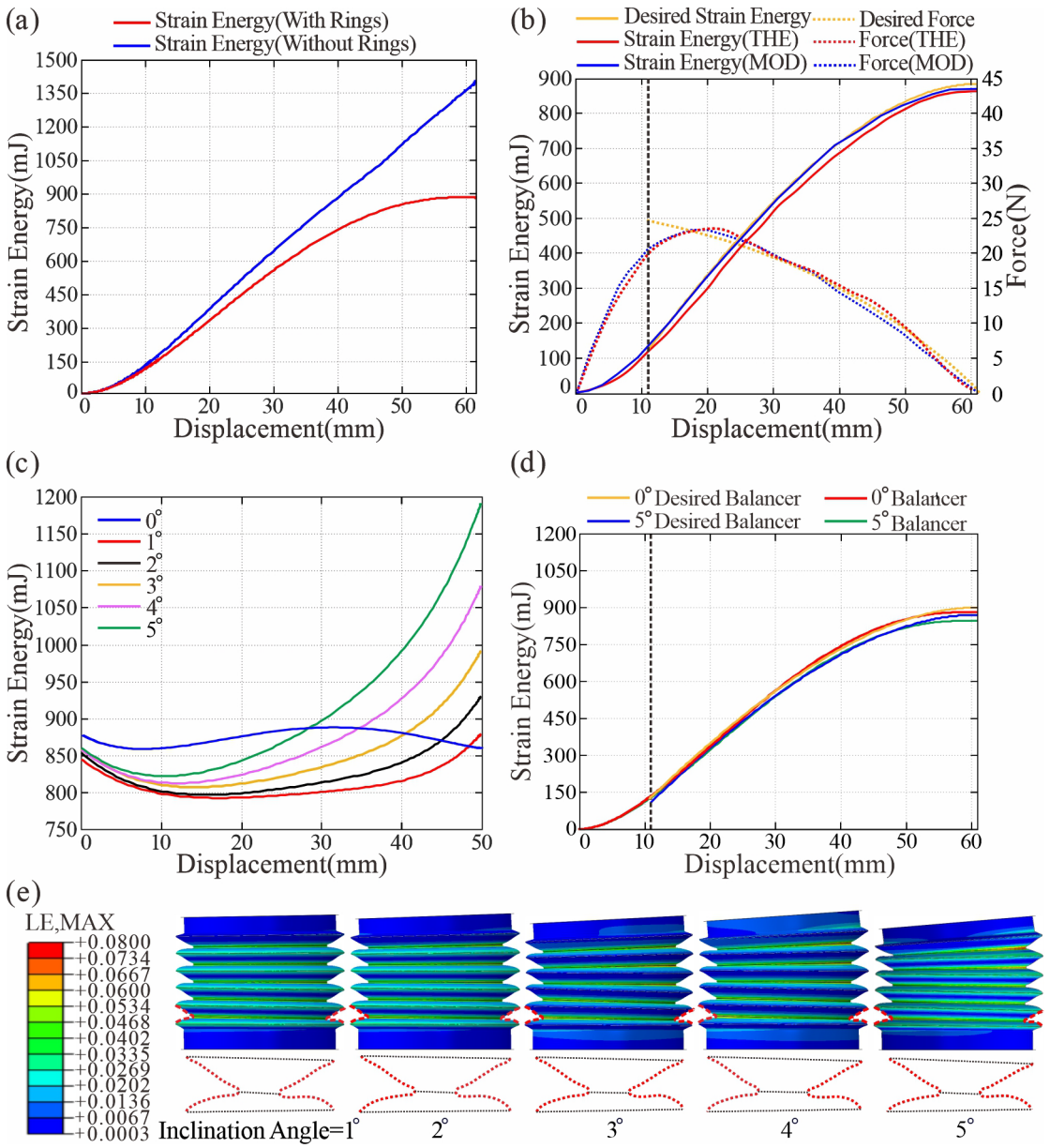

Fig. 2-15 Comparative study on the mechanical behaviors of the SBCMs. (a) Strain energy of the balancers with and without rings; (b) theoretical strain energy vs. tensile displacement of the system; (c) numerical strain energy vs. tensile displacement of the system compressed by plates with inclination angle of 0°-5°; (d) numerical strain energy and tensile force vs. tension displacement curves of the balancer compressed by horizontal plates and plates with inclination angle of 5°; and (e) deformed configurations of the balancers and sectional profile compressed by plates with inclination angle of 1°-5°.

In the experiment, the synchronization is less satisfactory, see Figs. 2-14(c) and (d), mainly due to geometric imperfection. However, the resultant force is still

significantly reduced in comparison with a stand-alone bellow, indicating the validity of the deformation assumption. With more refined fabrication approach such as moulding, the geometric accuracy and therefore the deformation synchronization will be further improved, leading to better performance of the SBCM. Regarding energy assumption, it is found from the numerical results that the summation of shear strain energy and circumferential bending energy accounts for 2.87% of the total energy of the bellow and 2.01% of that of the balancer. Therefore, the energy assumption is also valid.

Second, rigid rings were applied on the balancer to keep the maximum and minimum radii unchanged. The reason is that we learned from preliminary design and analysis of the balancer that without the rings, it was difficult to obtain the requested energy curve shape. Figure 2-15(a) shows comparison of two balancers with and without rigid rings, which had identical geometry and materials with that in Section 2.3.2. It can be seen that those without rigid rings is unable to generate a degressive curve shape.

Third, when searching for the balancer to pair with the below in Section 2.3.2, we put some restraints on the geometric parameters of the balancer to reduce the design variables from six to three, for the sake of simplifying the design process. In fact, those restraints are not compulsory. We also tried varying all the six parameters in the hope of finding a better fitted solution. The results, noted as strain energy (MOD) and force (MOD), are plotted in Fig. 2-15(b) together with the results in Section 2.3.2. The geometric parameters of the modified balancer are: outer radius $R_2 = 100.66$ mm, inner radius $r_2 = 76.46$ mm, radius of curve $r_{F2} = 1.60$ mm, height $h_2 = 9.00$ mm, slant angle $\alpha_2 = 26^\circ$, and thickness $t_2 = 0.93$ mm. Despite the significantly increased complexity, the improvement seems quite marginal. Certainly, finding the optimum balancer design is an open question. From the engineering point of view, nevertheless, the proposed approach in Section 2.3.2 can conveniently generate designs that are practically usable.

Fourth, we considered the proposed theoretical models in Sections 2.2 and 2.3.2 when they are analyzed based on the deformation feature of the structure, made corresponding assumptions, and obtained governing equations and boundary conditions. To solve the equations, nevertheless, numerical approaches including discretization and iteration are required due to the complicated geometry. Compared with a purely

numerical method such as FEA, the theoretical model can quickly generate a large number of strain energy curves by inputting a small number of geometric and material parameters, thereby avoiding the relatively tedious numerical model building process. This would greatly facilitate the search for the optimum geometry of the balancer. In addition, it can also give a deeper insight into the deformation mechanism of the structure and the key design parameters. For instance, we have found from the theoretical model that the curve shape of the balancer is independent of wall thickness, while the total strain energy has a cubic relationship with it.

Fifth, straight loading in the longitudinal direction of the SBCM is also considered in the study. In practical application, however, the loading may be less ideal, e.g., the loading plate could be inclined instead of perfectly horizontal. To investigate the effects of oblique loading, the SBCM was tensioned by plates with inclination angle of 1°-5°, and the corresponding strain energy curves are drawn in Figs. 2-15(c-e). It can be seen that as the inclination angle increases, the strain energy deviates quickly from constant energy. A further analysis of the result indicates that the deviation is mainly caused by the balancer. As can be seen in Fig. 2-15(d), when the inclination angle reaches 5°, the curve shape of the balancer is no longer degressive. Therefore, for the SBCM to achieve optimal performance, the load should be as straight in the longitudinal direction as possible.

Finally, while being able to significantly reduce the driving force, the current SBCM design is formed by two components, the bellow and the balancer, thereby raising the question whether both can be integrated into a single part. In fact, a single-component SBCM with zero force is an ideal mechanism. Under the current design framework, it is not likely to achieve this in a single structure by redesigning the geometry of the bellow or the balancer.

2.6 Conclusions

In this chapter, we have designed a SBCM composed of an inner bellow and an outer balancer, which are arranged coaxially to achieve nearly zero actuation force during axial deformation. A theoretical model has been established to calculate the strain energy of the bellow when axially compressed. Based on the determined bellow, a straw-inspired balancer composed of straight, circular, and cubic polynomial segments has been proposed, and the associated strain energy during tension has been

derived theoretically. A parametric analysis has also been carried out for the balancer, which reveals that the slant angle and unit height mainly affect the shape of the strain energy curve while shell thickness determines the magnitude of the energy. Finally, numerical model and physical prototype of a statically balanced compliant mechanism have both been built and analyzed to demonstrate the effectiveness of the proposed design approach, from which a nearly zero reaction force accounting for only 3.62% of that of the bellow has been achieved. In the future, specimens made with more accurate fabrication approaches such as moulding will be constructed and tested. Moreover, the SBCM will be further modified to achieve robust performance when subjected to non-ideal loading.

Chapter 3 A Straw-inspired Statically Balanced Compliant Torque Coupling

3.1 Introduction

Although SBCMs enable precise force and displacement transmission without external energy input, structural designs to achieve high-efficiency torque and rotation transmission through neutral stability remain underdeveloped. Different from the bellow-shaped SBCM mentioned in Chapter 2, static balance can also be realized in a single-component SBCM through internal coordination of the component, instead of the mutual compensation between the components.

Inspired by the circumferential stability of the bendy straw in its bent state, a statically balanced compliant torque coupling (SBCTC) composed of series-connected frustum shells is presented, whose energy flow is shown in Fig. 3-1. Guided by numerical simulation, parameter analysis was conducted to identify the key geometric parameters governing the bistable behaviors between the extended and bent states. A simplified beam model was developed to accurately predict the bent configuration, thereby facilitating the programmable SBCTC design. Meanwhile, the bent SBCTC under torsion was also analyzed through numerical simulation, which unveils that all material elements experience periodic deformation along the closed circumferential path of the frustum shell. Meanwhile, strain energy within the component compensates and coordinates each other, thereby maintaining the constant total strain energy with the unchanged overall geometry during torsion. High-precision CT scanning was utilized on the physical prototype to quantitatively validate our numerical results and shape preservation. To evaluate torque transmission under load, a specialized test platform was built here. Experimental tests confirmed that the SBCTC can bend over 90° while maintaining the transmission efficiency of over 75%, significantly surpassing existing industrial flexible couplings.

This chapter is structured as follows. In Section 3.2, we present the geometry of the SBCTC unit and the fundamental setup for numerical simulation of the SBCTC unit. In Section 3.3, by abstracting the geometric characteristics from the numerical model, a simplified beam model is established to elucidate the geometric features and predict the bent state for the optimal parameter selection of the SBCTC. Section 3.4 provides numerical methods to unveil the constant strain energy of the SBCTCs with unchanged

shape during torsion, further verified by geometrical construction of 3D scanning results. Subsequently, precise experiments were conducted to validate the stable and efficient torque transmission performance of the SBCTCs in different working scenarios in Section 3.5. Finally, conclusions are included in Section 3.6, which ends this chapter.

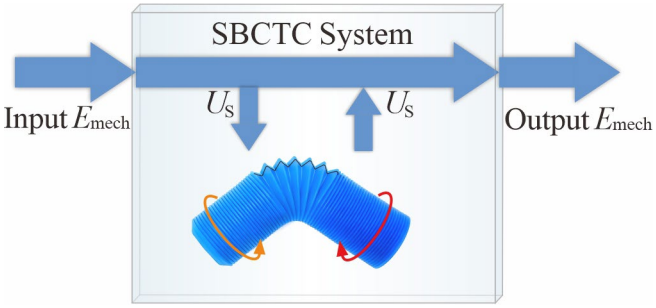

Fig. 3-1 Energy flow of the straw-inspired SBCTC.

3.2 Geometric Design and Numerical Modelling

To design a compliant coupling capable of transmitting torques stably at variable angles, the core is to develop a closed curved surface. The surface must maintain static balance during torsion and possess bistability in its bent state to ensure stable torque transmission at variable angles. Inspired by a bendy straw, the basic unit of the SBCTC is a tandem pair of different conical frustum shells connected at a special "crease"-like region. Similar large-sized structures are also applied in drain hoses and toy Pop Glow Tubes (Ningbo Mideer Creative Technology Co. Ltd.), typically fabricated from polypropylene (PP) via a blow-moulding process, as detailed in Fig. 3-2(a).

This manufacturing process leads to the thinnest convex hinge-like regions with wrinkles, followed by the bottom conical frustum shell with medium thickness, while the upper frustum shell is the thickest. Therefore, the simplified SBCTC unit as shown in Figs. 3-2(b) and (c) can be described by the identical outer radius R, inner radius r, slant angle α_{BF} and shell thickness t_{BF} for the bottom frustum shell, and slant angle α_{UF} and shell thickness t_{UF} for the upper frustum shell. In addition, the convex hinge-like region where two frustum shells are connected is filleted by the smaller and inner chamfer circles of radius r_{IC} with shell thickness t_{IC}, and the concave hinge-like region is filleted by the larger and outer chamfer circles of radius r_{OC} in shell thickness of t_{OC}. All the parameters R, r, r_{IC}, r_{OC}, t_{IC}, t_{OC}, α_{UF}, α_{BF}, t_{UF} and t_{BF} above define the geometry of the SBCTC unit completely.

Its unit height h can then be obtained as

$$h=(R-r)(\tan\alpha_{UF}+\tan\alpha_{BF})+(r_{IC}+r_{OC})(\frac{1-\sin\alpha_{UF}}{\cos\alpha_{UF}}+\frac{1-\sin\alpha_{BF}}{\cos\alpha_{BF}}). \quad (3\text{-}1)$$

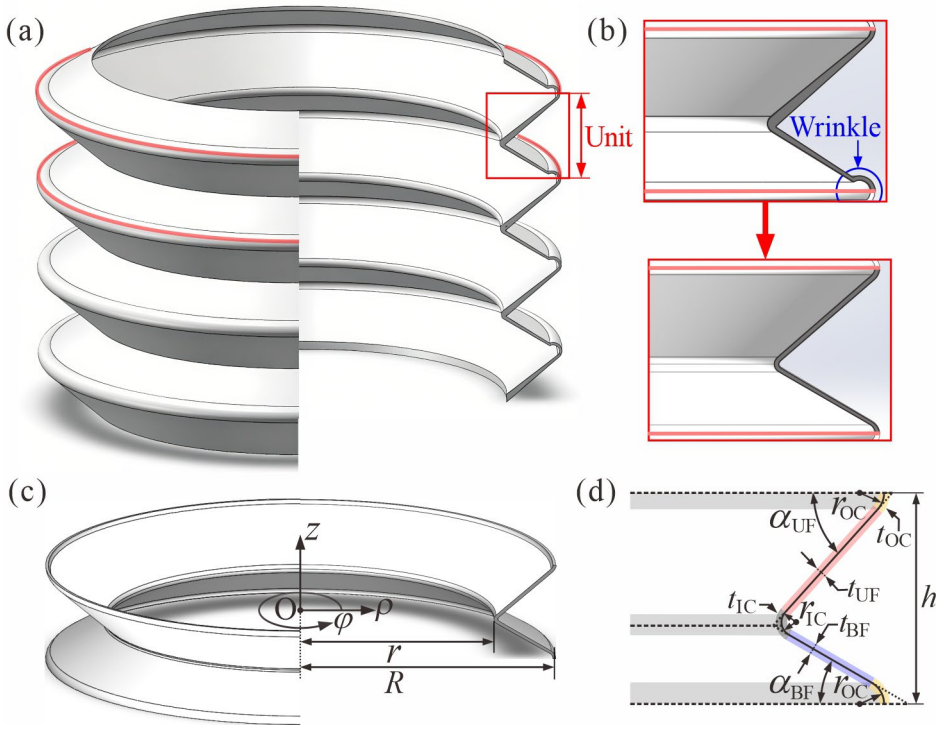

Fig. 3-2 Geometric characterization of the proposed SBCTC unit. (a) Pop glow tube composed of five units from a perspective view; (b) detailed geometry of one unit of the Pop tube and optimized geometry from a sectional view; (c) SBCTC unit from a perspective view; (d) geometry of a SBCTC unit from a sectional view.

To investigate the influence of design parameters on stability during the bending and torsion process, three independent parameters r, α_{BF} and t_{BF} are systematically varied on the premise that $\alpha_{BF}+\alpha_{UF}=78^{\circ}$ and $t_{BF}:t_{UF}:t_{IC}:t_{OC}=3:4:3:2$ remain unchanged according to the actual conditions of blow-moulded formation. The outer radius R of the circular tube is maintained at 14.50 mm to ensure broad applicability of the coupling. Numerical models of the SBCTC units were built and analyzed using the static/implicit commercial software package ABAQUS/Standard. PP is adopted as the material for the SBCTC unit, with the material properties: density of 897 kg/m^3, Young's modulus $E=1.32$ GPa, Poisson's ratio $v=0.42$, yield stress $\sigma_Y=33$ MPa and yield tensile elongation $\varepsilon_Y=0.23$. The material was modeled as a hyperelastic material using the Marlow strain energy function, calibrated against our experimental stress-strain data. The SBCTC unit was meshed using S4R elements with an average mesh

size of 0.25 mm, while additional refinement was applied to the hinge-like regions, as shown in Fig. 3-3(a). Convergence tests in terms of mesh density and analysis time were also conducted, from which an analysis time of 1.0 s was determined to be suitable and adopted in the analysis.

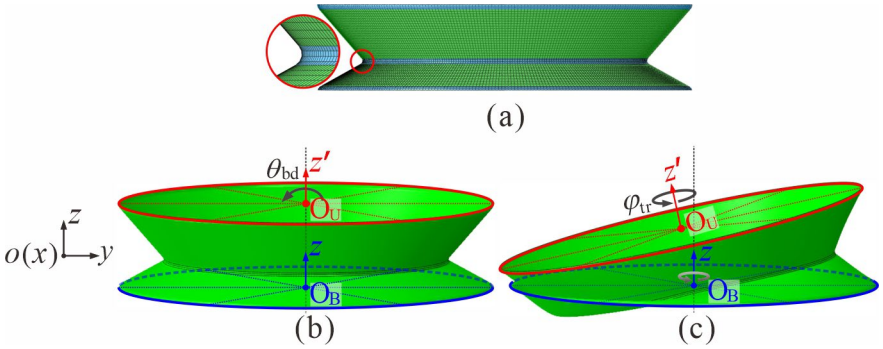

Fig. 3-3 Numerical models of (a) the meshed SBCTC unit with refined mesh at a hinge-like region marked in blue; (b) the SBCTC unit for bending, and (c) the SBCTC unit for torsion.

Then, kinematic coupling constraints rigidly link all 6 degrees of freedom (DoFs) of the bottom-rim node set (marked in blue) to the circle centre OB, which was fully fixed in space, while the top-rim node set marked in red was also rigidly coupled to the circle centre O_U, enabling a θ_{bd} unidirectional rotation about the x-axis by constraining rotation about the y-axis, z-axis, which allowed the straw to bend into its stable state, as shown in Fig. 3-3(b). During the torsion process, the constraint of the bottom coupling point O_B was released, which allowed the free in-plane rotation of the bottom rim about the z-axis. Meanwhile, the upper coupling point O_U was configured for a φ_{tr} unidirectional rotation about the z'-axis, see Fig. 3-3(c). Self-contact was employed to model the contact among different parts of the SBCTC unit. Friction was taken into consideration with the friction coefficient was taken as 0.44[180]. The strain energy and responsive moment during deformation were both extracted and recorded.

3.3 Bending Behavior Analysis

3.3.1 Numerical Simulation of Bending Process

The deformation process of the SBCTC unit with corresponding logarithmic strain (LE) contour maps is presented in Fig. 3-4(a). During bending, the overall deformation of the unit predominantly occurs in the inverted region of the bottom frustum, while the upper frustum exhibits relatively minor deformation $\varepsilon_{MAX} < 0.024$. Although noticeable

local deformation also occurs at the hinge-like regions connecting adjacent frustums, its contribution to the total strain energy remains below 3.64%. Therefore, we focus solely on the behavior of the bottom frustum in the following analysis, neglecting the influence of the hinge-like region and the upper frustum.

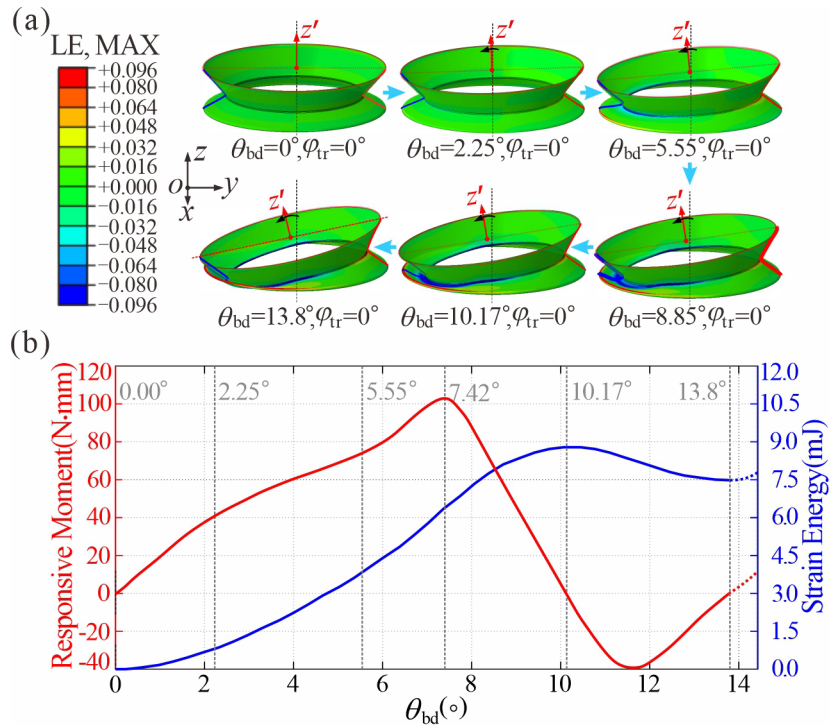

Fig. 3-4 Numerical simulation of the SBCTC unit during bending. (a) Numerical deformation process of the SBCTC unit; (b) numerical strain energy and responsive moment vs. bending angle θ_{bd}.

Furthermore, the responsive moment and strain energy vs. bending angle θ_{bd} in Fig. 3-4(b) both exhibit typical "*N*"-shaped curves, indicating the bistability of the structure. The points where the moment is zero and the strain energy reaches its extreme correspond to the stable extended state and bent state with θ_{bd} reaching 13.80° for an SBCTC unit with parameters $r = 11.0\,\text{mm}$, $\alpha_{BF} = 30^{\circ}$ and $t_{BF} = 0.40\,\text{mm}$ consistent with the measured geometry of the toy Pop Glow Tube. The distinct plateau values observed at the peak and trough points in the torque vs. angle curve are primarily attributed to the asymmetric deformation of the bistable structure. Meanwhile, the SBCTC unit maintains purely elastic deformation during bending, with peak strain ($\varepsilon_{MAX} = 0.176$) lower than the yield threshold $\varepsilon_{Y} = 0.23$.

To further conduct morphological characterization of the partially-inverted bottom frustum, a cylindrical coordinate system is set here with its original point O_B, where the global x- and z-axes correspond to the radial ρ and z directions of the cylindrical system, respectively, and the circumferential φ direction is determined by the right-hand rule. The cross-sectional contour is marked with compressed blue generator AB (φ = 180°) and stretched red generator CD (φ = 0°). Here, the geometric configuration can be characterized by the generalized radial and circumferential curvatures κ_r, κ_φ of any point K on the deformed bottom frustum, as shown in Fig. 3-5.

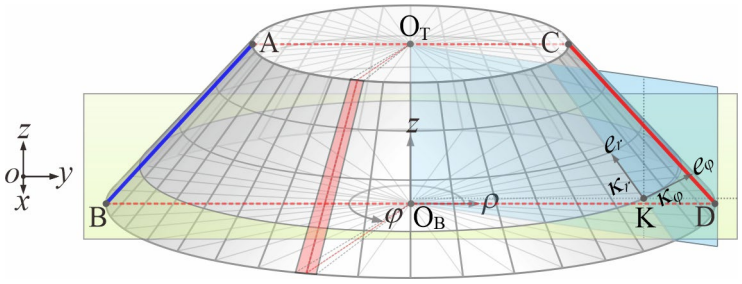

Fig. 3-5 Geometric definition of the bottom frustum.

Following this, the spatial coordinates of the partially-inverted bottom frustum during bending are extracted along both the radial and circumferential directions $\boldsymbol{e}_r$, $\boldsymbol{e}_\varphi$. Polynomial curve fitting was performed using the MATLAB Curve Fitting Toolbox ($R^2 > 0.98$) to calculate the corresponding curvatures κ_r (Fig. 3-6(b)) and κ_φ (Fig. 3-6(c)), in comparison with LE contour maps, as illustrated in Fig. 3-6(a). To further elucidate its mechanism, the circumferential distribution of radial strain energy is analyzed by integrating the strain energy of a random set of elements distributed along generators (marked in pale red in Fig. 3-5) and plotting the corresponding angular energy density e_S distribution along the circumferential angle φ during bending in Fig. 3-7. Additionally, the deformation process of the blue generator AB and the red generator CD in the cross-section is illustrated in Fig. 3-8.

The contour maps in Figs. 3-6(a) and (b) reveal highly consistent colour distributions with a ratio of about half the thickness $t_{BF}/2$, which indicates that surface deformation is primarily induced by changes in radial curvature κ_r. Initially, the inner zone of the blue generator AB, starting from point A, develops negative curvature κ_r with reverse material bending, while κ_r remains positive in other regions. At this stage,

the energy density e_S of generator AB (φ = 180°) surpasses all other regions, as illustrated in Fig. 3-6. Meanwhile, the circumferential flow of the material causes the stretching angle ϕ_R between BD and CD to rapidly increase in this stage and quickly reach its stable position, after which the angle remains constant during bending as shown in Fig. 3-7.

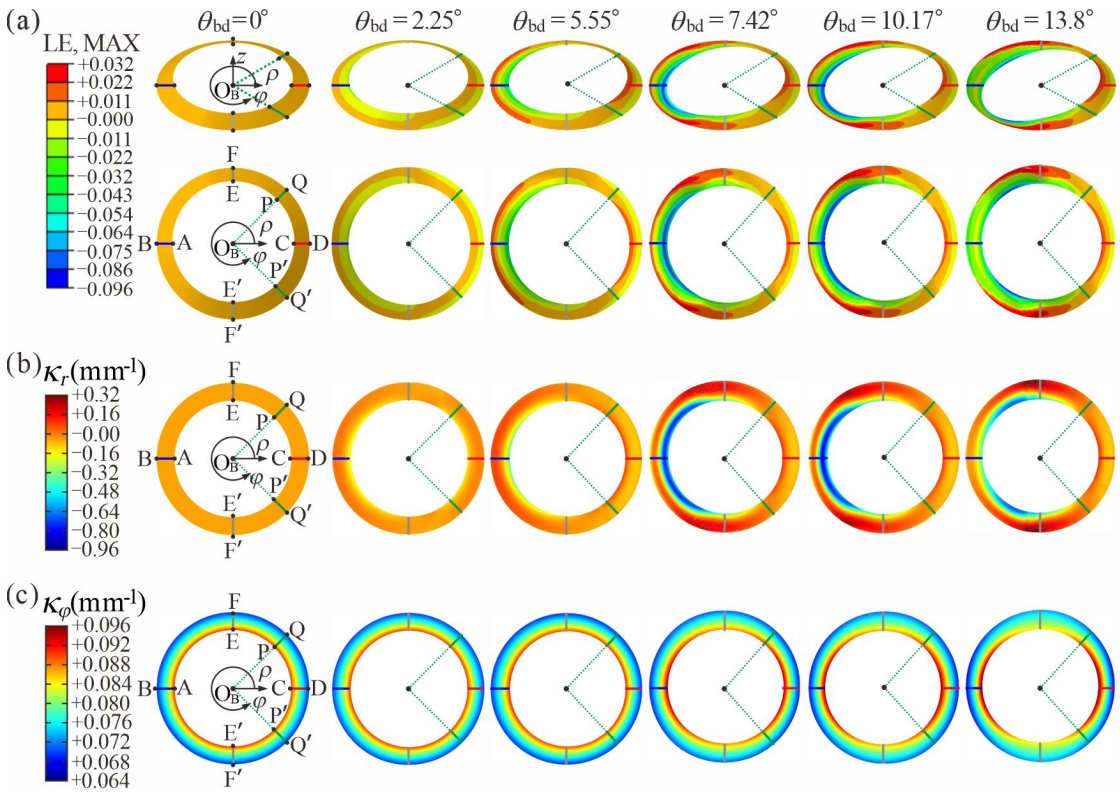

Fig. 3-6 Deformation and curvature distribution of the bottom frustum during bending. (a) Numerical deformation process of the bottom frustum during bending; (b-c) the contour map of (b) the radial curvature κ_r, and (c) the circumferential curvature κ_φ calculated from the numerical results.

Then, the negative curvature zone expands radially and circumstantially from point A with intensified reverse bending. Meanwhile, material adjacent to the reverse bending region is compressed and flows in circumferential and radial directions, causing a remarkable increase on positive κ_r of the compressive side, while positive κ_r on the tensile side around generator CD remains unchanged. Once the bending angle θ_{bd} reaches 8.85°, the circumferential energy density e_S attains its peak value of 3.52 mJ at generator AB (φ=180°) during the entire bending process, corresponding to the

curvature trough $\kappa_r = -0.7655\ \mathrm{mm}^{-1}$ in Fig. 3-7, which can be referred to as "the local maximum energy state".

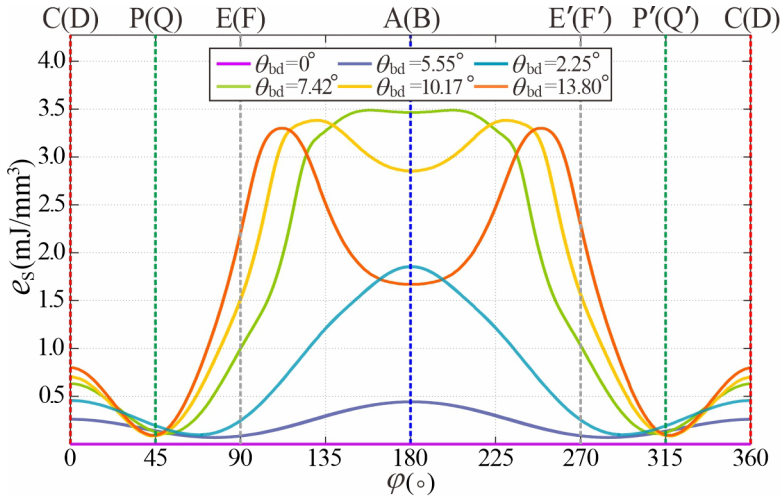

Fig. 3-7 Angular energy density distribution e_S vs. circumferential angle φ during bending.

During advanced bending stages, the region of negative κ_r exhibits simultaneous radial contraction and circumferential expansion, accompanied by the decreasing absolute κ_r. At this stage, the continuous circumferential flow of the nearby material causes further bending deformation in the region of positive κ_r. The phenomenon is echoed by the energy distribution in Fig. 3-7, which demonstrates that while e_S at generator AB ($\varphi = 180°$) declines, the spatial extent of the high-energy zone widens, resulting in an overall energy peak for the entire bottom frustum at θ_{bd} of 10.17°. It should be particularly noted that the tangent line at point B of generator AB in Fig. 3-8 completely coincides with line AC.

As the subsequent bending process towards a stable state at θ_{bd} of 13.80°, the majority of the compressive region becomes flat, in which negative κ_r only exists in a narrow region near the inner diameter. Meanwhile, the region of high positive κ_r continuously migrates towards the mid-circumferential position. It can also be inferred that at the transitional junction between the compressive and tensile radiation zones, there will be a transition region where the curvature approaches zero. In Fig. 3-7, the energy density e_S around $\varphi = 45°$ and 315° remains the lowest throughout the entire bending process, which exactly corresponds to this transition region. Moreover, the generators PQ ($\varphi = 45°$) and P′Q′ ($\varphi = 315°$) marked in green in Fig. 3-6(b) also maintain

the near-zero curvature during the whole bending process, further validating this conclusion.

Figure 3-6(c) shows that the circumferential curvature κ_φ is distributed symmetrically in both the left-right and top-bottom directions during bending. Thus, we only need to focus on one-quarter of the bottom frustum (section ABEF). Throughout the initial bending process with θ_{bd} from 0° to 5.55°, the curvature κ_φ of both top and bottom rims remains constant, consistently maintaining their initial circular geometry. In the subsequent deformation process, the curvature κ_φ decreases gradually from point A to point E at the top rim, whereas κ_φ increases progressively from point B to point F at the bottom rim. This is because material flows circumstantially from region AB towards the mid-circumferential position on both sides, resulting in compression along the EE′ direction at the top rim and simultaneous tension along the FF′ direction at the bottom rim. Conversely, in the perpendicular direction, the top rim is stretched in the AC direction, while the bottom rim is compressed in the BD direction. As shown in the enlarged figure in Fig. 3-8, the distance between points B and D becomes shorter.

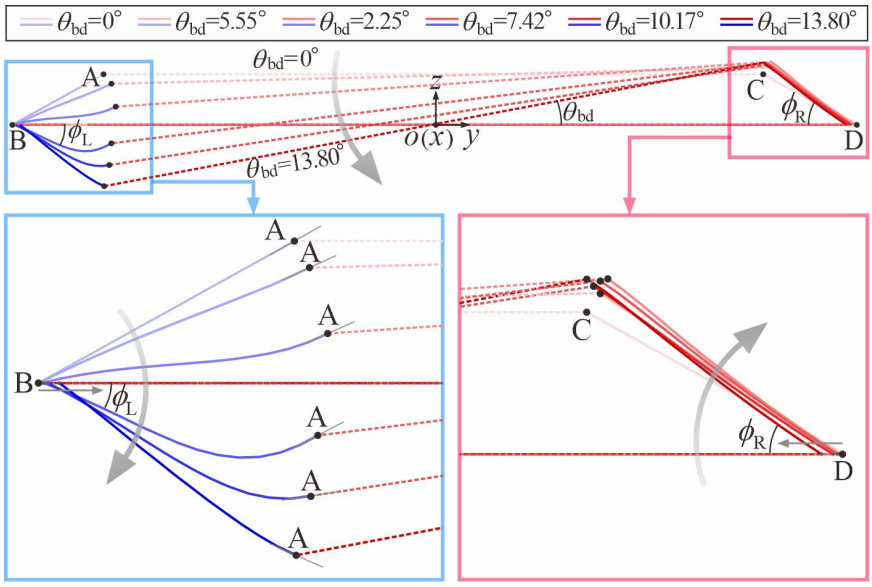

Fig. 3-8 Deformation process of the blue generator AB and the red generator CD during bending.

3.3.2 Simplified Beam Model for the Bent Stable State

Based on the aforementioned underlying mechanism of the bending process, a simplified beam model is established from the geometric perspective, as shown in Fig. 3-9(a). During the entire deformation process, the lengths of all generators remain

unchanged, as bending dominates the mechanical response. Their original length l_0 can be derived as follows.

$$l_0 = \frac{(R-r)}{\cos\alpha_{BF}} + (r_{IF} + r_{OF})\left(\frac{1-\sin\alpha_{BF}}{\cos^2\alpha_{BF}}\right). \tag{3-2}$$

Specifically, it can be assumed that the beams CD ($\varphi = 0°$), PQ($\varphi = 45°$) and P′Q′($\varphi = 315°$) consistently maintain a nearly zero curvature while remaining perfectly straight.

$$l_{CD} = l_{PQ} = l_{P'Q'} \equiv l_0. \tag{3-3}$$

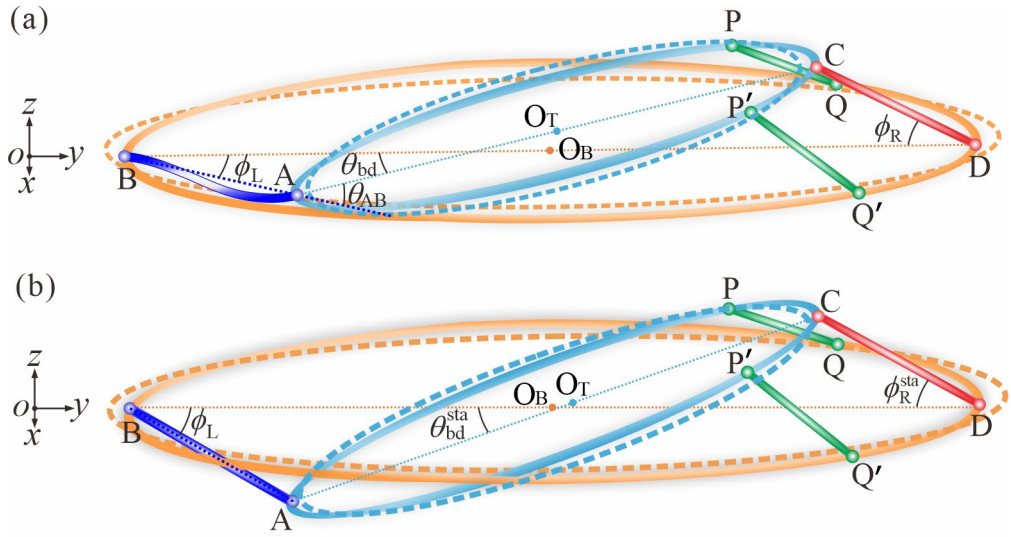

Fig 3-9 A simplified beam model for the bottom frustum. (a) containing maximum strain energy during bending and (b) at the stable bent state.

Meanwhile, beam AB exhibits a typical bistable response. Starting from its initial straight state, it bends under compressive buckling, with curvature κ_r reaching a peak at “the local maximum energy state”. It then returns to a near-zero curvature state in the steady-state phase, returning to a straight line. According to Fig. 3-6(c), elliptical equations are employed to fit the top and bottom rims, whose forci are located on segments AC and FF′. And the major axis of the top elliptical edge is AC, while the minor axis of the bottom elliptical edge is BD. The original semi-axes of the circular top and bottom rims are

$$r_{TP} = a_{TP} = b_{TP} = r + r_{IF}(1-\cos\alpha_{BF}), \tag{3-4a}$$

$$r_{BT} = a_{BT} = b_{BT} = R + r_{OF}(1-\cos\alpha_{BF}). \tag{3-4b}$$

Based on numerical results, we assume that the elongation Δl_e of beam AC on the top rim roughly matches the contraction Δl_e of beam BD on the bottom rim during bending, corresponding to the changed $a_{TP} = r_{TP} + \Delta l_e / 2$ and $b_{BT} = r_{BT} - \Delta l_e / 2$. Due to energy minimization, the rims are more likely to bend rather than to stretch, which keeps the lengths of the top and bottom rims nearly constant. Thus, b_{TP} and a_{BT} can be derived according to Ramanujan's approximation formula:

$$a_{BT} = \frac{-B_{BT} + \sqrt{B_{BT}^2 - 4A_{BT}C_{BT}}}{2A_{BT}}, \tag{3-5a}$$

$$b_{TP} = \frac{-B_{TP} + \sqrt{B_{TP}^2 - 4A_{TP}C_{TP}}}{2A_{TP}}; \tag{3-5b}$$

where

$$A_{TP} = 2.25,\ B_{TP} = 3.5a_{TP} - 6r_{TP},\ C_{TP} = (2r_{TP} - 1.50a_{TP})^2; \tag{3-5c}$$

$$A_{BT} = 2.25,\ B_{BT} = 3.5b_{BT} - 6r_{BT},\ C_{BT} = (2r_{BT} - 1.50b_{BT})^2. \tag{3-5d}$$

Then the top and bottom elliptical rims are both expressed respectively in cylindrical coordinates $O_T(\rho', \varphi', z')$ and $O_B(\rho, \varphi, z)$, where $z = z' = 0$.

$$\frac{\rho'^2 \sin^2\varphi'}{a_{TP}^2} + \frac{\rho'^2 \cos^2\varphi'}{b_{TP}^2} = 1,\ \frac{\rho^2 \cos^2\varphi}{a_{BT}^2} + \frac{\rho^2 \sin^2\varphi}{b_{BT}^2} = 1. \tag{3-6}$$

Substituting PQ($\varphi = 45°$) and P′Q′($\varphi = 315°$) into Eq. (3-5), the radial coordinates of points P, P′, Q and Q′ can, respectively, be derived as

$$\rho'_P = \rho'_{P'} = \frac{a_{TP} b_{TP} \sqrt{2a_{TP}^2 + 2b_{TP}^2}}{a_{TP}^2 + b_{TP}^2}, \tag{3-7a}$$

$$\rho_Q = \rho_{Q'} = \frac{a_{BT} b_{BT} \sqrt{2a_{BT}^2 + 2b_{BT}^2}}{a_{BT}^2 + b_{BT}^2}. \tag{3-7b}$$

We obtained points $P(\rho'_P, 45°, 0)$, $P'(\rho'_P, 315°, 0)$, $Q(\rho_Q, 45°, 0)$, $Q'(\rho_{Q'}, 315°, 0)$ in cylindrical coordinates O_T and O_B respectively. Then geometric constraints of the four-bar linkage are applied here to transform them into the global Cartesian coordinate system *oxyz*, whose origin *o* coincides with point O_B.

First, ϕ_R is defined as the included angle between beams AB and BD. It should be noticed that angle ϕ_R nearly reaches its stable position during the initial bending stage in Fig. 3-7. The system is simplified to a planar four-bar linkage mechanism for analysis. The limited angle ϕ_R^{lim} is calculated in Eq. (3-8), when beam CD reaches the forward

dead centre (FDC) with collinear beam AC and beam AB.

$$\phi_{\mathrm{R}}^{\lim}=\operatorname{acos}[\frac{4r_{\mathrm{BT}}^2+l_0^2-(2r_{\mathrm{TP}}+l_0)^2}{4l_0r_{\mathrm{BT}}}]. \tag{3-8}$$

Through massive numerical analysis, the fitted relationship between the initial angle α_{BF}, the limit angle $\phi_{\mathrm{R}}^{\lim}$ and the inner/outer radii r, R can be mathematically derived as follows.

$$\omega_{\phi_{\mathrm{R}}}=K_{\phi_{\mathrm{R}}}(R-r)^2,\ \phi_{\mathrm{R}}^{\mathrm{sta}}=\omega_{\phi_{\mathrm{R}}}\alpha_{\mathrm{BF}}+(1-\omega_{\phi_{\mathrm{R}}})\phi_{\mathrm{R}}^{\lim}. \tag{3-9}$$

where the constant $K_{\phi_{\mathrm{R}}}$ equals 0.01306. At this point, the included angle ϕ_{L} between beams AB, BD and the theoretical bending angle θ_{bd} can also be obtained with the undetermined length l_{AB}.

$$l_{\mathrm{BC}}^2=l_{\mathrm{BD}}^2+l_{\mathrm{CD}}^2-2l_{\mathrm{BD}}l_{\mathrm{CD}}\cos\phi_{\mathrm{R}}=4(b_{\mathrm{BT}})^2+l_0^2-4b_{\mathrm{BT}}l_0\cos\phi_{\mathrm{R}}, \tag{3-10a}$$

$$\phi_{\mathrm{L}}=\operatorname{acos}(\frac{l_{\mathrm{AB}}^2+l_{\mathrm{BC}}^2-l_{\mathrm{AC}}^2}{2l_{\mathrm{AB}}l_{\mathrm{BC}}})-\operatorname{asin}(\frac{l_0\sin\phi_{\mathrm{R}}}{l_{\mathrm{BC}}})=\operatorname{acos}[\frac{l_{\mathrm{AB}}^2+l_{\mathrm{BC}}^2-4(a_{\mathrm{TP}})^2}{2l_{\mathrm{AB}}l_{\mathrm{BC}}}]-\operatorname{asin}(\frac{l_0\sin\phi_{\mathrm{R}}}{l_{\mathrm{BC}}}), \tag{3-10b}$$

$$\theta_{\mathrm{bd}}=\operatorname{acos}(\frac{l_{\mathrm{AC}}^2+l_{\mathrm{BC}}^2-l_{\mathrm{AB}}^2}{2l_{\mathrm{AC}}l_{\mathrm{BC}}})+\operatorname{asin}(\frac{l_0\cdot\sin\phi_{\mathrm{R}}}{l_{\mathrm{BC}}})=\operatorname{acos}[\frac{4(a_{\mathrm{TP}})^2+l_{\mathrm{BC}}^2-l_{\mathrm{AB}}^2}{4a_{\mathrm{T}}l_{\mathrm{BC}}}]+\operatorname{asin}(\frac{l_0\cdot\sin\phi_{\mathrm{R}}}{l_{\mathrm{BC}}}). \tag{3-10c}$$

Now, the transformation relationships between the cylindrical coordinate system $O_B(\rho, \varphi, z)$ and the global Cartesian coordinate system $oxyz$ can be expressed as

$$\mathbf{O_B}=\begin{bmatrix}x_{\mathrm{B}}\\y_{\mathrm{B}}\\z_{\mathrm{B}}\end{bmatrix}=\begin{bmatrix}0\\0\\0\end{bmatrix}\Rightarrow\begin{cases}x=\rho\cos(\varphi+\pi/2)\\y=\rho\sin(\varphi+\pi/2)\\z=z'=0\end{cases}, \tag{3-11}$$

and the transformation of the cylindrical coordinate system $O_T(\rho', \varphi', z')$ is

$$\mathbf{O_T}=\begin{bmatrix}x_{\mathrm{T}}\\y_{\mathrm{T}}\\z_{\mathrm{T}}\end{bmatrix}=\begin{bmatrix}0\\b_{\mathrm{BT}}-l_0\cos\phi_{\mathrm{R}}-a_{\mathrm{TP}}\cos\theta_{\mathrm{bd}}\\l_0\sin\phi_{\mathrm{R}}-a_{\mathrm{TP}}\sin\theta_{\mathrm{bd}}\end{bmatrix}\Rightarrow\begin{cases}x=\rho'\cos(\varphi'+\pi/2)\\y=\rho'\sin(\varphi'+\pi/2)\cos\theta_{\mathrm{bd}}+y_{\mathrm{T}}\\z=\rho'\sin(\varphi'+\pi/2)\sin\theta_{\mathrm{bd}}+z_{\mathrm{T}}\end{cases}. \tag{3-12}$$

Substituting coordination of P, P′, Q and Q′ into Eq. (3-10), l_{PQ} and $l_{\mathrm{P'Q'}}$ can be obtained and satisfy the boundary condition in Eq. (3-3).

$$\overrightarrow{\mathrm{PQ}}=\overrightarrow{\mathrm{P'Q'}}=\begin{bmatrix}0.5\sqrt{2}\rho_{\mathrm{Q}}\\0.5\sqrt{2}\rho_{\mathrm{Q}}\\0\end{bmatrix}-\begin{bmatrix}0.5\sqrt{2}\rho'_{\mathrm{P}}\\0.5\sqrt{2}\rho'_{\mathrm{P}}\cos\theta_{\mathrm{bd}}+y_{\mathrm{T}}\\0.5\sqrt{2}\rho'_{\mathrm{P}}\sin\theta_{\mathrm{bd}}+z_{\mathrm{T}}\end{bmatrix}. \tag{3-13}$$

Here, we observe that in Eq. (3-13), parameters ρ_{Q} and ρ'_{P} depend solely on the

unknown parameter Δl_C. The other parameters θ_{bd}, y_T and z_T are related to unknown parameters Δl_C and l_{AB} according to Eqs. (3-10) to (3-12). Our analysis in Section 3.3.2 has illustrated that beam AB experiences compression during bending. While its beam length s_{AB} remains constant at original l_0, the distance l_{AB} shortens significantly. This small-strain, large-deformation characteristic of these models can be expressed by the following generalized elastica-similarity equation in Eq. (3-14) to fit the curved beam AB.

$$\frac{\mathrm{d}^2\theta}{\mathrm{d}s^2} = F_{ela}\sin\theta,\ \frac{1}{2}\left(\frac{\mathrm{d}\theta}{\mathrm{d}s}\right)^2 = F_{ela}\sin\theta + M_{ela}; \tag{3-14a}$$

$$\kappa_r = \frac{\mathrm{d}\theta}{\mathrm{d}s} = \sqrt{2(F_{ela}\sin\theta + M_{ela})}, \tag{3-14b}$$

$$\int \mathrm{d}s = \int \frac{\mathrm{d}\theta}{\sqrt{2(F_{ela}\sin\theta + M_{ela})}}. \tag{3-14c}$$

In the original formulation, F_{ela}, M_{ela} characterize the end force and moment, whereas they are treated as undetermined coefficients during parameter optimization. The boundary conditions of the endpoints A, B here also need to be satisfied.

$$\mathrm{A}: s = 0,\ \theta = \theta_{ela};\ \mathrm{B}: s_{AB} = l_0,\ l_{AB} = \left\|\overrightarrow{AB}\right\|. \tag{3-15}$$

For beam AB, three parameters F_{ela}, M_{ela} and θ_0 in Eqs. (3-14) and (3-15) need to be determined requiring three extra conditions. First, the maximum radial curvature $\kappa_r^{MAX} = \sqrt{2(F_{ela} + M_{ela})}$ at $\theta_{ela} = 90^\circ$ can also be fitted here with the inner/outer radii *r, R* and slant angle α_{BF}, where K_{κ_r} equals 0.7483.

$$\kappa_r^{MAX} = \sqrt{2(F_{ela} + M_{ela})} = \frac{K_{\kappa_r}\alpha_{BF}}{\sqrt{R-r}}. \tag{3-16}$$

When the bottom frustum reaches the peak of its overall strain energy, the maximum curvature κ_r^{MAX} of beam AB occurs close to point A, hence θ_0 equals 90°. Additionally, the line segment AC is tangent to the curved beam AB at point B, as shown in Fig. 3-9(a). We define the angle θ_{AB} between line AB and the tangent line at point A. The boundary condition can be derived as

$$\mathrm{A}:\ s = 0,\ \theta_0 = 90°;\ \mathrm{B}:\ s_{AB} = l_0,\ \theta_{AB} = \operatorname{acot}\frac{\int_0^{l_0}\sin\theta\cdot\mathrm{d}s}{\int_0^{l_0}\cos\theta\cdot\mathrm{d}s} = \theta_{bd} + \phi_L. \tag{3-17}$$

Now, the three independent conditions in Eqs. (3-16) and (3-17) are sufficient to

uniquely define the geometry of beam AB. By substituting the derived distance l_{AB} into Eqs. (3-10) to (3-12), we can completely reconstruct the beam model and calculate the bending angle θ_{bd}^{I} when the bottom frustum reaches its maximum strain energy. Considering a typical SBCTC unit with the geometric parameters: r = 11 mm, $\alpha_{BF} = 30^{\circ}$ and $t_{BF} = 0.40$ mm. Figure 3-10 illustrates good agreement between our beam model in blue solid lines with the corresponding numerical cross-sectional profiles in blue dotted lines. The fitted result $\hat{\theta}_{bd}^{I}$ here is 9.87° in comparison to numerical θ_{bd}^{I} of 10.17°, thereby validating the accuracy of our beam model.

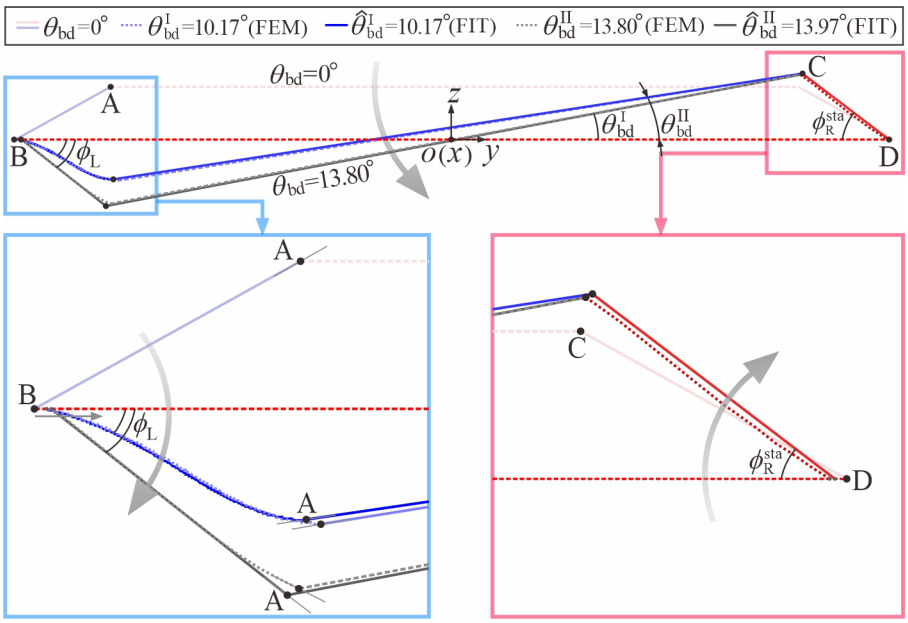

Fig. 3-10 Cross-sectional comparison of the numerical results in dotted lines and the beam model result in solid lines. The blue line represents the maximum strain energy state, while the black line represents the stable bent state.

Furthermore, when the bottom frustum achieves its stable bent state, beam AB straightens, and the distance l_{AB} return to its original length l_0, as shown in Fig. 3-9(b). Thus we can derive Δl_e by solving Eq. (3-11), and the fitted bending angle $\hat{\theta}_{bd}^{II}$ at in the stable state can be obtained through Eq. (3-10). Considering a typical SBCTC unit with the same geometric parameters as above, the calculations yield an elongation Δl_e of 0.394 mm and $\hat{\theta}_{bd}^{II}$ of 13.97°, showing minimal deviation from the finite element anal results($\Delta l_e = 0.401$ mm , $\theta_{bd}^{II} = 13.80^{\circ}$).This agreement is further validated by the

almost-identical numerical and fitted profiles (black dotted vs. solid lines) in Fig. 3-10,confirming the reliability and precision of our simplified beam model.

3.3.3 Effects of Geometric Parameters on Bending Stability

Having investigated the underlying mechanism of the SBCTC unit during the bistable behavior, the effects of three design parameters (r, α_{BF} and t_{BF}) are further studied in this section to fulfil the task of programmability. A total of 60 models, with inner radius r from 6.625 mm to 12.75 mm at an interval of 0.875 mm, slant angle α_{BF} varying from 12° to 30° at an interval of 3° and fixed thickness t_{BF} from 0.24 to 0.36 mm at an interval of 0.03 mm are analyzed numerically, whose ranges align with the actual conditions of blow-moulding production for plastic tubular structures. The geometric parameters of the models are listed in Tab. 3-1, in which the notation r-α_{BF}-t_{BF} is adopted.

First, consider the effect of inner diameter r and slant angle α_{BF}, while fixing the thickness t_{BF} of 0.40 mm. The phase map in Fig. 3-11(a) outlines the bistability conditions of an SBCTC unit derived from numerical analysis, which identifies two distinct regions: bistable and monostable. Local maximum (M_1) and minimum (M_2) moments occur at two inflection points, as shown in Fig. 3-11(c). The ratio M_2/M_1 is used to evaluate their bending stability and classify the parameter ranges into bistable ($M_2/M_1 < 0$) and monostable ($M_2/M_1 > 0$) categories, with boundary lines at $M_2/M_1 = 0$. Generally, higher α_{BF} and smaller r values both increase the likelihood of bistability in the SBCTC unit. However, when r is too small, the significant increase in the bending angle θ_{bd}^{II} leads to a slower bistable transition rate, reducing the absolute values of both M_1 and M_2. As a result, the ratio M_2/M_1 decreases slightly, as seen in the upper-left region, but the unit still maintains its bistable state.

The contour map in Fig. 3-11(b) demonstrates that increasing the slant angle α or decreasing the inner radius r significantly enhances the bending angle θ_{bd}^{II} of the stable state, with excellent agreement (error < 2.35%, Tab. 3-1) with predicted $\hat{\theta}_{bd}^{II}$ from the beam model. A set of typical parameters was selected based on the slant angle α_{BF} and the inner radius r respectively, with the corresponding points of these parameters marked in blue and red in Figs. 3-11(a) and (b). The moment vs. bending angle corresponding to models with the same slant angle α_{BF} are marked in red, while those corresponding to models with the same inner radius r are marked in blue (Figs. 3-11(c) and (d)). Regardless of specific values, all curves exhibit a typical "*N*"-shaped profile.

Specifically, with constant angle α_{BF}, reducing the inner diameter r simultaneously increases both the magnitude of M_2 and the stable angle θ_{bd}^{II}.

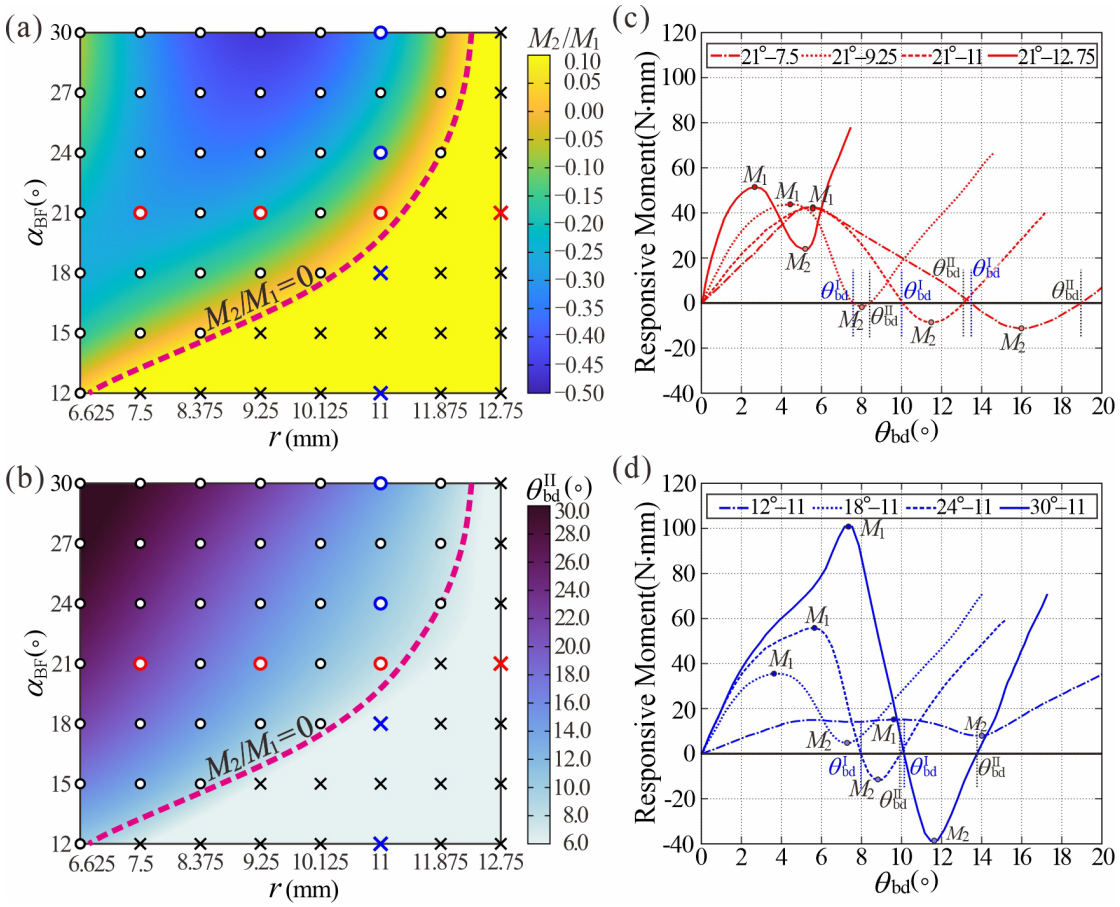

Fig. 3-11 The bistability of the SBCTC unit with fixed thickness $t_{BF} = 0.40$ mm. (a) Phase maps showing the outcomes of bistability from numerical analysis across various α_{BF} and r values, and (b) showing the stable angle θ_{bd}^{II} from numerical analysis across various α_{BF} and r values; (c) characteristic moment–angle curves for SBCTC units with identical α_{BF} that distinguish between bistable and monostable. (d) Characteristic moment–angle curves for SBCTC units with identical r that distinguish between bistable and monostable.

While at fixed inner diameters r, increasing the slant angle α_{BF} increases the stable angle θ_{bd}^{II} with the lower M_2 value. In contrast, the angle θ_{bd}^{I} at which the maximum strain energy occurs follows the same trend as θ_{bd}^{II}, with $\hat{\theta}_{bd}^{I}$ obtained from the beam model, exhibiting a deviation of 3.29% from the numerical results, further validating the accuracy of the simplified beam model. These systematic variations further confirm that enhanced geometric incompatibility is the key factor governing the bistable behavior of SBCTC units.

First, consider the effect of inner diameter r and slant angle α_{BF}, while fixing the thickness t_{BF} of 0.40 mm. The phase map in Fig. 3-11(a) outlines the bistability conditions of a SBCTC unit derived from numerical analysis, which identifies two distinct regions: bistable and monostable. Local maximum (M_1) and minimum (M_2) moments occur at two inflection points, as shown in Fig. 3-9(c). The ratio M_2/M_1 is used to evaluate their bending stability and classify the parameter ranges into bistable ($M_2/M_1 < 0$), monostable ($M_2/M_1 > 0$) categories, with boundary lines at $M_2/M_1 = 0$. Generally, higher α_{BF} values and smaller r values both increase the likelihood of bistability in the SBCTC unit. However, when r is too small, the significant increase of the bending angle θ_{bd}^{II} leads to a slower bistable transition rate, reducing the absolute values of both M_1 and M_2. As a result, the ratio M_2/M_1 decreases slightly, as seen in the upper-left region, but the unit still maintains its bistable state.

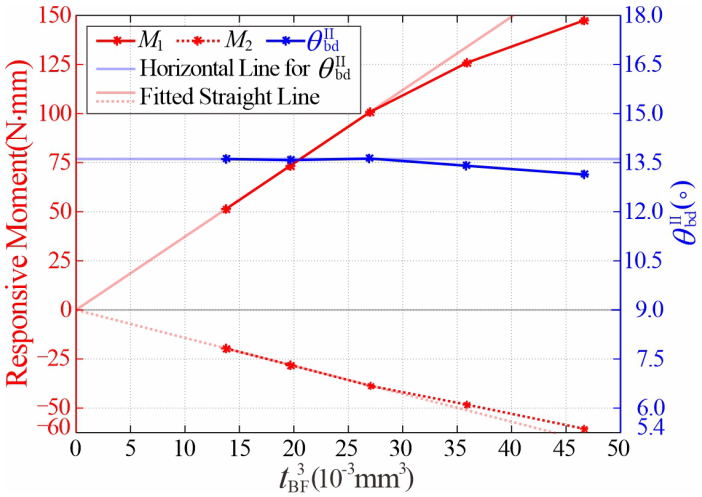

Fig. 3-12 Relationship between maximum moment, minimum moment and stable angle θ_{bd}^{II} vs. the cubic power of shell thickness t_{BF} for models with $\alpha_{BF} = 30^\circ$, r = 11 mm and t_{BF} = 0.24, 0.27, 0.30 , 0.33, 0.36 mm.

Furthermore, when α_{BF} and r have been obtained to achieve a bistable SBCTC unit, the maximum and minimum moments M_1 and M_2 are found to increase approximately linearly with the cubic power of shell thickness t_{BF} lower than 0.33mm, which is clearly shown in Fig. 3-12. Moreover, θ_{bd}^{II} also remains consistent. The reason for this is that bending strain energy dominates during the deformation of the SBCTC unit, which causes the total strain energy to exhibit an approximately cubic relationship with t_{BF}. When the thickness t_{BF} increases to 0.33 mm, the bottom and top frustums

touch prematurely before the unit reaches the bending angle θ_{bd}^{II}, causing both the maximum moment M_1 and the minimum moment M_2 to decrease in magnitude, which is lower than the predicted cubic relationship.

Tab. 3-1 Bending Stability for the SBCTCs with different geometric parameters.

Model (r-α_{BF}-t_{BF})	Stability	θ_{bd}^{I} (°)	$\hat{\theta}_{bd}^{I}$ (°)	θ_{bd}^{II} (°)	$\hat{\theta}_{bd}^{II}$ (°)
6.625-12-0.30	bistable	8.64	8.32	10.24	10.48
6.625-15-0.30	bistable	11.04	11.26	14.01	13.97
6.625-18-0.30	bistable	12.62	11.98	17.49	16.99
6.625-21-0.30	bistable	14.42	14.05	19.88	19.44
6.625-24-0.30	bistable	15.98	15.63	21.97	21.78
6.625-27-0.30	bistable	18.00	17.68	23.90	23.85
6.625-30-0.30	bistable	19.22	18.76	24.39	24.69
7.50-12-0.30	monostable	—	—	—	—
7.50-15-0.30	bistable	10.17	9.67	11.61	11.68
7.50-18-0.30	bistable	11.32	11.85	14.85	14.64
7.50-21-0.30	bistable	12.74	12.62	17.41	17.52
7.50-24-0.30	bistable	14.63	14.27	19.42	18.97
7.50-27-0.30	bistable	16.06	16.52	21.10	21.38
7.50-30-0.30	bistable	17.73	17.36	23.23	22.70
8.375-12-0.30	monostable	—	—	—	—
8.375-15-0.30	bistable	8.65	8.43	10.68	10.47
8.375-18-0.30	bistable	9.83	10.02	12.20	12.35
8.375-21-0.30	bistable	10.98	10.78	14.46	14.39
8.375-24-0.30	bistable	12.65	13.02	16.35	16.76
8.375-27-0.30	bistable	14.22	13.96	18.67	18.52
8.375-30-0.30	bistable	17.00	17.28	21.25	20.97
9.25-12-0.30	monostable	—	—	—	—
9.25-15-0.30	monostable	—	—	—	—
9.25-18-0.30	bistable	9.46	9.35	9.97	9.67
9.25-21-0.30	bistable	9.81	10.25	11.78	12.06
9.25-24-0.30	bistable	10.64	11.24	14.14	13.85
9.25-27-0.30	bistable	12.29	12.05	15.23	14.82
9.25-30-0.30	bistable	13.66	14.21	17.98	18.15
10.125-12-0.30	monostable	—	—	—	—
10.125-15-0.30	monostable	—	—	—	—
10.125-18-0.30	bistable	7.68	7.52	8.67	8.42
10.125-21-0.30	bistable	8.32	8.09	9.47	9.89
10.125-24-0.30	bistable	9.16	9.43	11.48	11.25

Model (^{r}-α_{BF}-t_{BF})	Stability	θ_{bd}^{I} (°)	$\hat{\theta}_{bd}^{I}$ (°)	θ_{bd}^{II} (°)	$\hat{\theta}_{bd}^{II}$ (°)
10.125-27-0.30	bistable	9.99	10.25	13.23	13.38
0.125-30-10.30	bistable	11.45	11.65	14.89	14.53
11.0-12-0.30	monostable	—	—	—	—
11.0-15-0.30	monostable	—	—	—	—
11.0-18-0.30	monostable	—	—	—	—
11.0-21-0.30	bistable	7.14	7.45	7.95	7.87
11.0-24-0.30	bistable	7.40	7.55	9.29	9.67
11.0-27-0.30	bistable	7.92	7.79	10.59	10.38
11.0-30-0.30	bistable	10.17	9.87	13.80	13.97
11.875-12-0.30	monostable	—	—	—	—
11.875-15-0.30	monostable	—	—	—	—
11.875-18-0.30	monostable	—	—	—	—
11.875-21-0.30	monostable	—	—	—	—
11.875-24-0.30	bistable	6.39	5.96	7.37	7.53
11.875-27-0.30	bistable	6.52	6.35	8.08	7.86
11.875-30-0.30	bistable	6.93	7.08	8.92	8.73
12.75-12-0.30	monostable	—	—	—	—
12.75-15-0.30	monostable	—	—	—	—
12.75-18-0.30	monostable	—	—	—	—
12.75-21-0.30	monostable	—	—	—	—
12.75-24-0.30	monostable	—	—	—	—
12.75-27-0.30	monostable	—	—	—	—
12.75-30-0.30	monostable	—	—	—	—
11.0-30-0.24	bistable	10.17	9.87	13.80	13.97
11.0-30-0.27	bistable	10.17	9.87	13.80	13.97
11.0-30-0.33	bistable	10.17	9.87	13.80	13.97
11.0-30-0.36	bistable	10.17	9.87	12.	13.97

According to the parametric analysis, designing a desired torque coupling with a fixed outer radius R can be carried out in the following three steps: (1) divide the required transmission angle to determine a suitable stable angle θ_{bd}^{II} between 10° and 30° for a single SBCTC unit; (2) derive feasible pairs of the slant angle α_{BF}, inner radius r that satisfy the bent angle θ_{bd}^{II} and the bistable conditions in reverse, with preference for larger α_{BF} and smaller r; and (3) increase thickness t_{BF} appropriately while keeping θ_{bd}^{II} constant, ultimately enhancing bistable behavior by minimizing the M_2/M_1 ratio and M_2. Our theoretical model is subject to specific boundaries and

limitations, and only applies to bistable models within our defined geometric parameter range. In particular, the frustum thickness must not exceed a critical value to ensure the structure reaches its bistable position. Moreover, the PP material should always remain within its elastic range during motion.

3.4 Torsion Behavior Analysis

3.4.1 Numerical Simulation of Torsion Process

In the previous sections, we have systematically investigated the bending stability of the SBCTC unit. Numerical analysis of the torsion process is conducted following the numerical setup in Section 3.2, and the corresponding LE contour maps, stain energy and responsive moment vs. twisting angle φ_{tr} during torsion are presented in Fig. 3-13(b). It can be observed that during a complete 360° anticlockwise torsion cycle (T_R), the SBCTC unit maintains constant strain energy and zero responsive moment, thereby achieving the typical neutral stability.

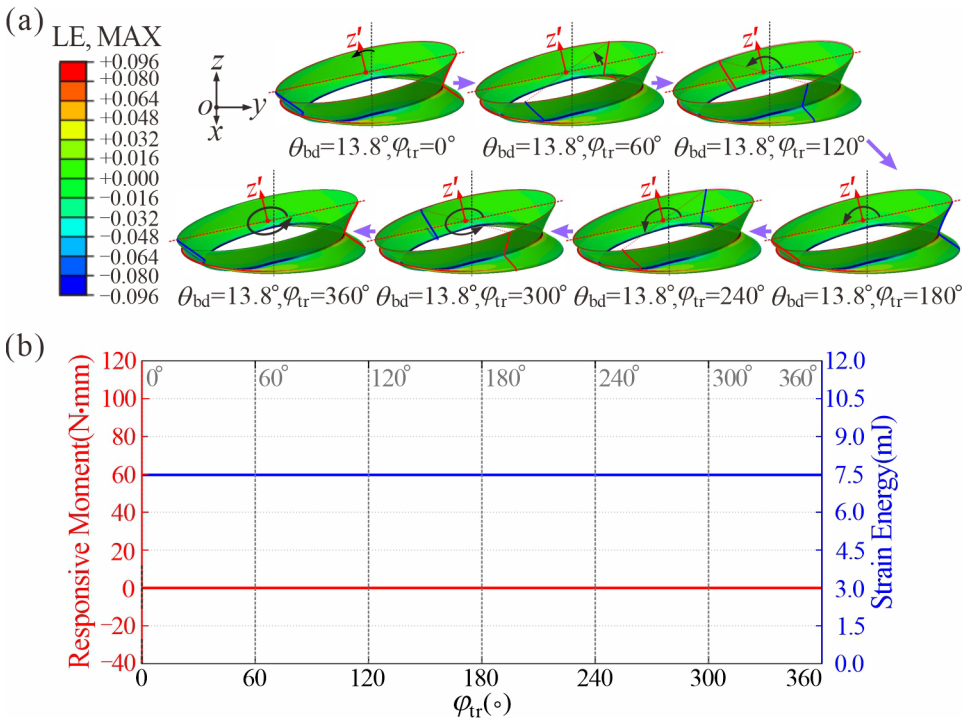

Fig. 3-13 Numerical simulation of the SBCTC unit during torsion. (a) Numerical deformation process of the SBCTC unit; (b) numerical strain energy and responsive moment vs. twisting angle φ_{tr} of the bellow.

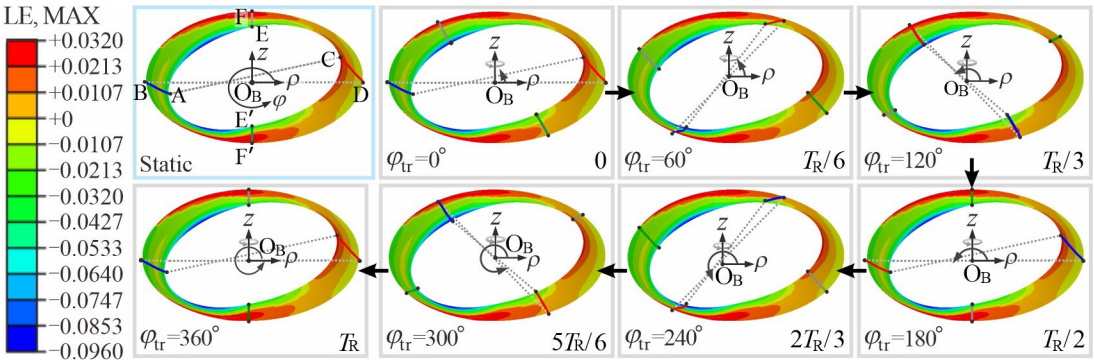

Fig. 3-14 Numerical deformation process of the bottom frustum during torsion.

Consistent with the bending process, we also focus on the deformation of the bottom frustum during torsion. Figure 3-14 illustrates LE contour maps during torsion, where the strain distribution remains nearly constant throughout the torsion process and aligns with the distribution of the bent bottom frustum.

To elucidate the underlying neutral stability mechanism during torsion, the evolution of strain energy density e_S along generators CD, AB, EF, E′F′ at $\varphi = 0°$, 90°, 180° and 270° are tracked over a complete torsional cycle. Tracking the blue generator ($\varphi = 0°$) along the circumferential direction as shown in Fig. 3-15, the deformation proceeds as follows. Starting at $\varphi_{tr} = 0°$ in the tensile zone, the generator first encountered the compressive-tensile transition interface near $\varphi_{tr} = 45°$, where curvature κ_r flattened to near-zero while strain energy density e_S drops to its global minimum.

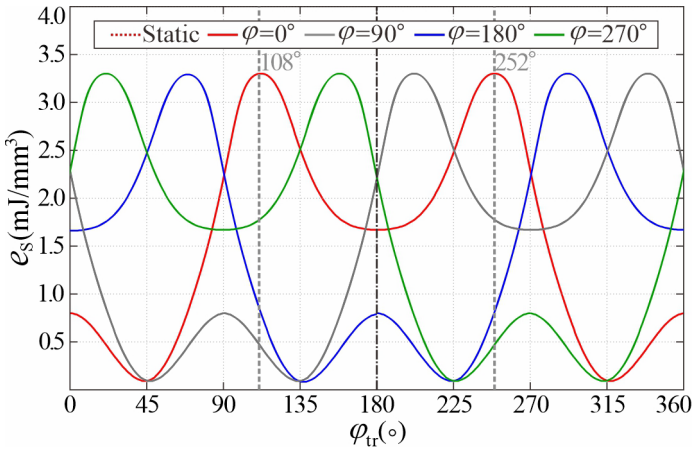

Fig. 3-15 Angular energy density distribution e_S vs. generators at φ in one complete torsion cycle.

As the generator rotates into the compressive region, e_S increases continuously with the radial curvature κ_r until achieving its peaks at $\varphi_{tr} = 108°$ due to the maximum

κ_r induced by material accumulation. Thereafter, it arrives at the mirror-symmetric compressive position at $\varphi_{tr} = 180°$ with e_S dropping back down, completing the first half-cycle. From $\varphi_{tr} = 180°$ to 360°, the path is retraced in reverse through compression, transition, and the tension zone, while the e_S profile remains a perfect mirror of the 0°-180° segment, yielding a closed and symmetric loop.

And, its periodicity can be expressed by the typical 2π periodic function as $e_S(\varphi_{tr}) = e_S(\varphi_{tr} + 2\pi)$. Here, the φ_{tr}-e_S curve of $\varphi = 0°$ is observed to coincide exactly with the angular energy distribution of the static bent bottom frustum in Fig. 3-6. From the energy perspective, the generator under torsion "traversed" the known steady-state distribution around the circumference. Likewise, the φ_{tr}-e_S curves for the generators at $\varphi = 90°$, 180°, and 270° retain the same shape as the $\varphi = 0°$ curve and are simply shifted along the φ_{tr} axis by their respective phase angles φ, each differing by a quarter of the period. The strain energy density e_S of the generator at φ after twisting φ can be described as $e_S(\varphi,\ \varphi_{tr}) = e_S(\varphi + \varphi_{tr})$. Now, the strain energy of the bottom frustum can be integrated as

$$U_S = \int_0^{2\pi} e_S(\varphi, \varphi_R)\mathrm{d}\varphi = \int_0^{2\pi} e_S(\varphi + \varphi_R)\mathrm{d}\varphi = \int_0^{2\pi} e_S(\varphi)\mathrm{d}\varphi = const. \tag{3-18}$$

3.4.2 Shape Verification via CT Scanning

To verify their twisted geometric configuration, the industrial computed tomography (CT) technology (GE Phoenix v tome x s240) was applied here to capture the 3D profile of the bent prototype, the Pop Glow Tube with speckles in density of 31.52 mm^{-2}.

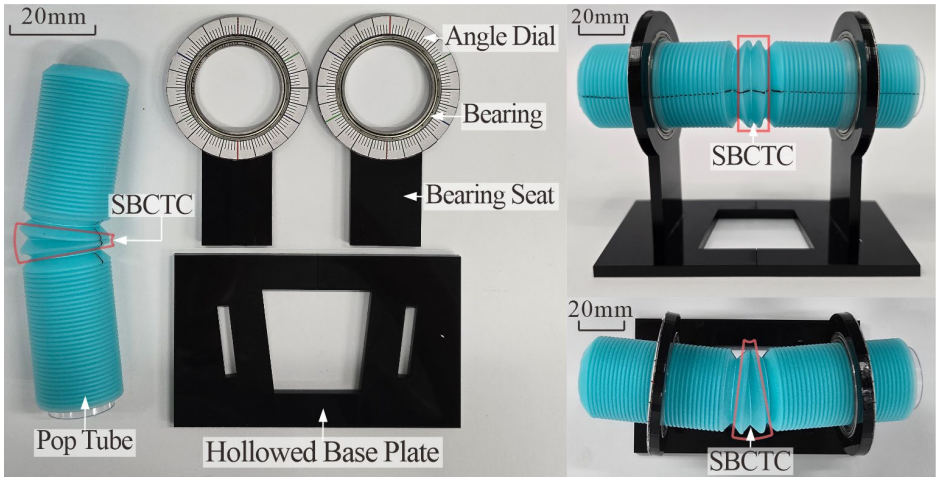

Fig. 3-16 Assembled torsion equipment for scanning

One unit of the pop tube was bent as a specific SBCTC unit and its adjacent units were stretched to prevent scanning interference from corrugated wrinkles. The bent specimen was secured on a hollow-bottomed fixed bearing bracket, with angle dials marked on the bearing seats to read the rotation angle φ_{tr}, see Fig. 3-16.

Subsequently, the bracket and specimen were placed into the CT machine for scanning, and the sample was twisted from φ_{tr} = 0° to 360° at an interval of 60° for a scan until completing a full torsion T_R. Fig. 3-17(a) presents the surface profiles of the bent bottom frustum unit extracted and reconstructed from each scanning result.

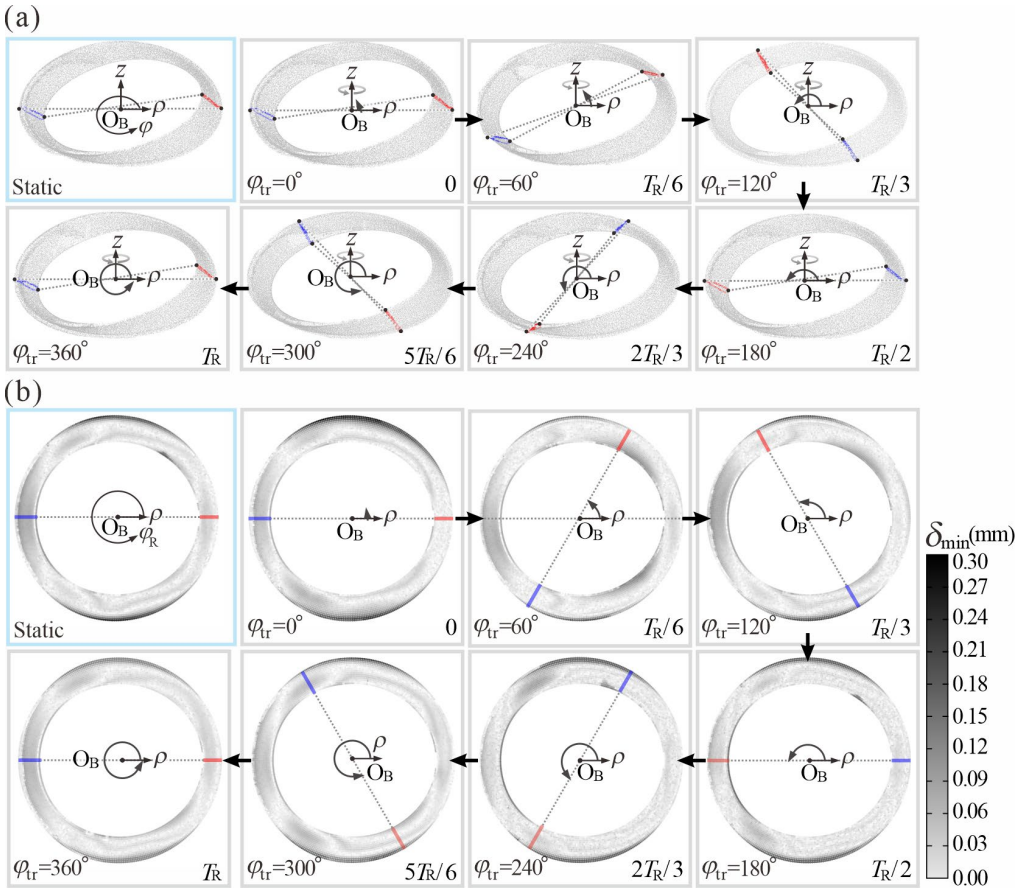

Fig. 3-17 3D-scanned result of the SBCTC under torsion. (a) Experimentally reconstructed geometric bottom frustum during one complete torsion cycle T_R; (b) comparison of the numerical model and the experimentally reconstructed bottom frustum based on CT scanning.

Here, we quantitatively assessed the geometrical similarity of numerical and experimental models by measuring the shortest distance between corresponding points on the numerical simulation surface and the scanned surface. For the specimen in both

the initial bent state and various twisting angles φ_{tr}, the 3D scanning results of the bottom frustum (Fig. 3-17(a)) are compared with the simulated geometric profiles in Fig. 3-14 under corresponding φ_{tr}. As shown in Fig. 3-16(b), the deviation δ_{min} is found to be within 0.30 mm in 98.4% of the areas and with a mean deviation of 0.087 mm, indicating the accuracy of the numerical model. It can also be noted that the derivation primarily focuses on the outer rims of the bottom frustum, which echoes the geometric optimization presented in Fig. 3-2. According to geometric preservation observed in the numerical results in Fig. 3-14, the small derivation δ_{min} also further demonstrates that the entire geometry of the bottom frustum remains almost unchanged during torsion, thus its strain energy remains almost constant, indicating its neutral equilibrium for energy-free motion with perfect torque transmission.

3.5 Torque Transmission Experiments

3.5.1 Experimental Setup

The numerical simulations and CT-scanned results in Section 3.4 indicated that the SBCTC unit can maintain static balance with shape preservation and negligible energy dissipation, thus theoretically reaching 100% torque transmission efficiency during torsion. This can be validated through the following experiments. For the experimental setup, *N* units of the Pop Glow Tube were bent and selected for the soft coupling test, while the non-test units were kept in a contracted state to serve as fixed ends (Fig. 3-18(a)). Despite the independent mechanical behavior between units, 502 adhesive glue was also utilized to lock the non-test units and inserted a PVC pipe with an outer radius of *R* to enhance their radial stiffness and prevent deformation in the non-test area. Before experiments, radial reference lines marked in blue and red were used as deformation calibration, see Fig. 3-18(b). Then, the specimen was horizontally assembled between two fixed bearing seats (YLV Explorer UCP206 D1) with perpendicular alignment, with their included angle as torque transmission angle γ_T.

The testing system was composed of three parts connected in series: the input end, the transmission coupling, and the output end. The input end was driven by a stepper motor connected to a dynamic torque tester for real-time input torque τ_{IN} monitoring, while the output end was equipped with an adjustable torque damper as the load τ_{OUT}. The input end was driven by a geared speed-adjustable stepper motor (Shinano Kenshi, S43D114-MC020) and connected to a dynamic torque sensor (STBD, S2000A-2NM,

error < 0.20%) to monitor the input torque τ_{IN} at a 20 Hz sampling rate for real-time monitoring. The output end was equipped with an adjustable torque damper (Hongli MTB-06, range 100-500 N·mm) as the output torque τ_{OUT}, as shown in Fig. 3-18(c).

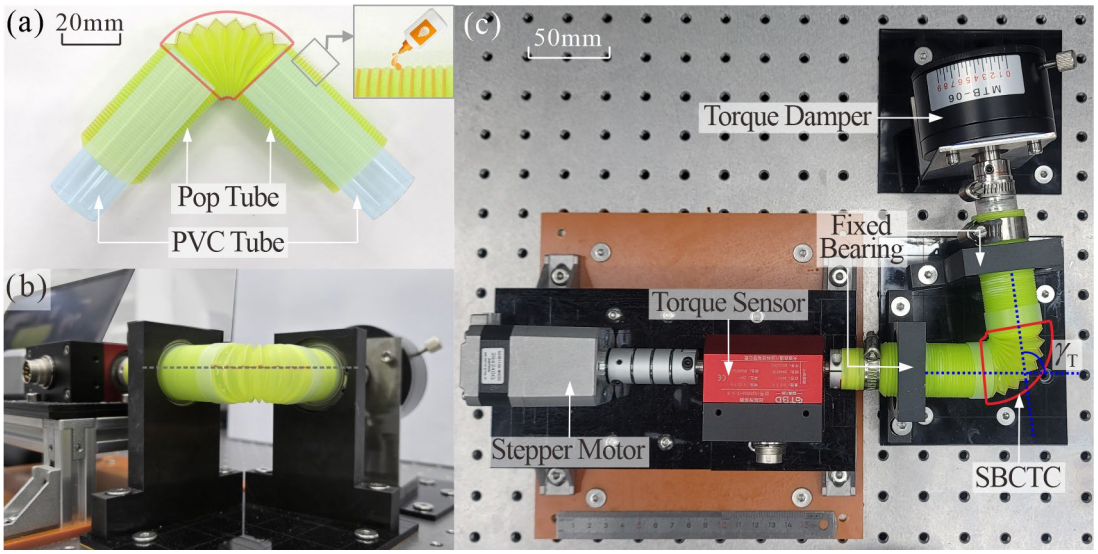

Fig. 3-18 Experimental setup for torque transmission efficiency testing of the SBCTC. (a) Selected *N* units for the experiments, and the non-test units served as fixed ends. (b) The side view of the assembled SBCTC. Radial reference lines marked in blue and red for deformation calibration. (c) The top view of the testing system, including the input end driven by a geared speed-adjustable stepper motor, the dynamic torque sensor for real-time input torque monitoring, and the adjustable torque damper at the output end.

It should be noted that to enhance interlocking stability, the experimental bending angle θ_{bd} was set to 14.0° per unit, slightly exceeding the 13.80° predicted by numerical analysis, which provides $\gamma_T = 14N^\circ$ for a system comprising *N* bent units. In addition, Figs. 3-19(a) and (b) illustrate the two typical scenarios of the same coupling. Under the lower loads, the red marker line remains horizontal from the side view, and each unit can still maintain a stable bending state during torsion. However, under excessive loads, the coupling experiences torsional deformation along with visible tilting and bending of the marker line, causing unsteady torque transmission.

3.5.2 Parametric Analysis of Torque Transmission

With the designed experimental platform, we can systemically investigate the effects of the torque transmission angle γ_T (i.e., the number of bent units *N*), output

torque τ_{OUT}, rotational speed of the stepper, and fatigue life on torque transmission, and determine whether the torque transmission is steady based on varied scenarios in Fig. 3-19. Furthermore, the difference $\Delta\tau$ and efficiency η between the input and output torques τ_{IN}, τ_{OUT} are introduced as parameters for the quantitative analysis of torque transmission, which can be expressed as follows.

$$\Delta\tau = \tau_{IN} - \tau_{OUT},\ \eta = \frac{\tau_{OUT}}{\tau_{IN}} = \frac{1}{[1+(\Delta\tau/\tau_{OUT})]}. \tag{3-19}$$

First, the torque transmission angle γ_T is varied from 0° to 98° corresponding to $N = 0$ to 7, with the torque damper ranging from 100 N·mm to 500 N·mm with 9 discrete levels, while fixing the stepper motor rotational speed at 3.0 r/min. When γ_T is 0°(N= 0), the system demonstrates constant $\Delta\tau_0$ of 2.079 N·mm regardless of applied load, primarily attributed to inherent friction of bearings.

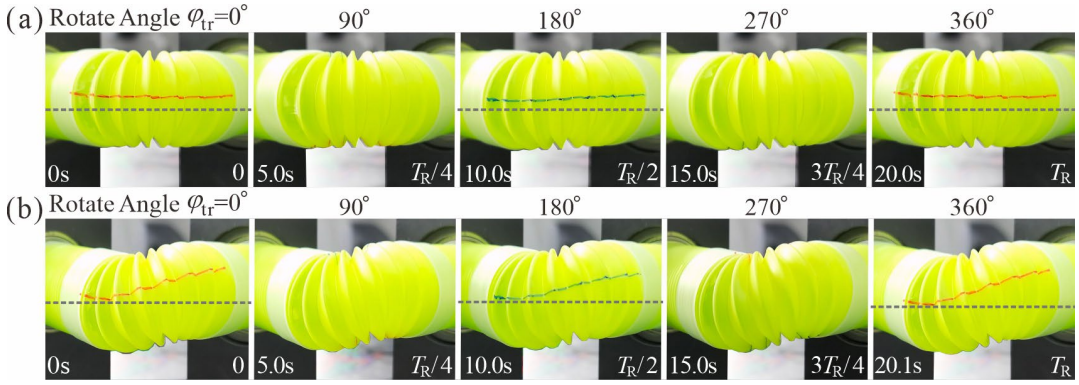

Fig. 3-19 Typical scenarios under different loads. (a) steady and (b) unsteady torque transmission.

As shown in Fig. 3-20(a), $\Delta\tau$ generally increases with both transmission γ_T and load τ_{OUT}. For the prototype with N = 1, the torque difference $\Delta\tau$ remains nearly constant regardless of the applied load τ_{OUT}, resulting in an increase in efficiency η. In contrast, for models with $N > 1$, $\Delta\tau$ rises significantly with load τ_{OUT}, leading to an overall decrease in transmission efficiency, as detailed in Figs. 3-20(c) and (d). We also observe that when the torque difference $\Delta\tau$ exceeds the threshold marked in blue, the torque transmission of the coupled system can no longer maintain steady. Furthermore, fitting analysis of the experimental data reveals that the critical load torque τ_{CR} of the coupling is in inverse proportion to the given number of units N, with the specific relationship given by $\tau_{CR} = 1314/N$ N·mm, as indicated by the magenta

marker in Fig. 3-20(a). For the efficiency η, the results can be derived from the derived $\Delta\tau$ and load τ_{OUT} according to Eq. (3-19), see Fig. 3-20(b).

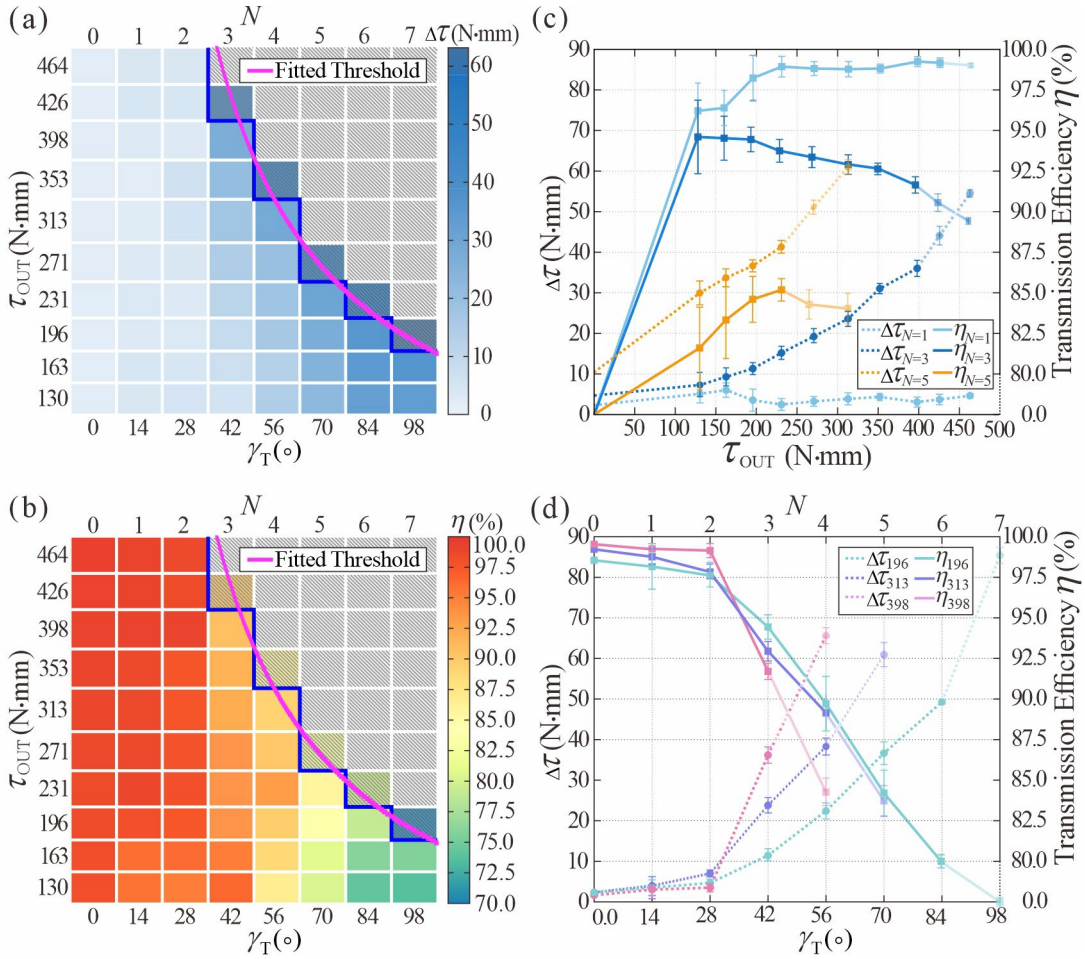

Fig. 3-20 Parametric analysis of the torque transmission. (a) The contour map represents torque difference ($\Delta\tau$) varied with torque transmission angle γ_T (i.e., the number of bent units N) and applied load τ_{OUT}. The local motion becomes unsteady higher than the magenta threshold lines. (b) The contour map represents the efficiency (η) varied with γ_T and τ_{OUT}. (c) The $\Delta\tau$ and η with varied torque transmission angle v at τ_{OUT} of 196, 313, 398N·mm and fixed rotational speed of 3r/min. (d) The $\Delta\tau$ and η with different applied load τ_{OUT} at N = 1, 3, 5 and rotational speed of 3r/min.

The output rotational speeds n_{OUT} of the torque transmission system were synchronously measured using video recording in 30 fps at a fixed input speed n_{IN} of 3 r/min, and listed in Tab. 3-2. During steady transmission, the speed deviation is confined to less than 0.02 r/min, indicating a near-perfect synchronization with a relative error well below 0.67%. whereas under unsteady conditions shaded in gray,

such as load fluctuations, start-stop transitions, or external disturbances, the deviation can increase to over 0.15 r/min with relative error over 5%.

Tab. 3-2 Torque Transmission for the SBCTCs with different unit number N and τ_{OUT}.

N	τ_{OUT} (N·mm)	τ_{IN} (N·mm)	$\Delta\tau$ (N·mm)	n_{IN} (r/min)	n_{OUT} (r/min)	η (%)
0	130.3	133.00	2.70	3	2.995	97.97
0	163.0	166.14	3.14	3	3.004	98.11
0	196.2	198.91	2.71	3	3.012	98.64
0	231.3	233.03	1.73	3	3.006	99.26
0	271.1	272.87	1.77	3	2.985	99.35
0	313.0	315.46	2.46	3	2.991	99.22
0	352.8	355.20	2.40	3	2.983	99.32
0	398.4	400.15	1.75	3	2.991	99.56
0	426.3	429.00	2.70	3	2.986	99.37
0	464.1	466.49	2.39	3	2.997	99.49
1	130.3	135.45	5.15	3	2.989	96.20
1	163.0	169.09	6.09	3	2.994	96.40
1	196.2	199.78	3.58	3	2.982	98.21
1	231.3	233.83	2.53	3	2.998	98.92
1	271.1	274.39	3.29	3	2.985	98.80
1	313.0	316.94	3.94	3	2.992	98.76
1	352.8	357.12	4.32	3	2.991	98.79
1	398.4	401.51	3.11	3	2.993	99.22
1	426.3	430.05	3.75	3	2.975	99.13
1	464.1	468.77	4.67	3	2.986	99.00
2	130.3	136.41	6.11	3	2.974	95.52
2	163.0	168.72	5.72	3	2.992	96.61
2	196.2	200.86	4.66	3	2.971	97.68
2	231.3	235.25	3.95	3	2.984	98.32
2	271.1	276.28	5.18	3	2.977	98.13
2	313.0	320.06	7.06	3	2.989	97.80
2	352.8	360.63	7.83	3	2.986	97.83
2	398.4	401.96	3.56	3	2.981	99.12
2	426.3	432.09	5.79	3	2.972	98.66
2	464.1	469.60	5.50	3	2.997	98.83
3	130.3	137.69	7.39	3	2.985	94.63
3	163.0	172.41	9.41	3	2.97	94.54
3	196.2	207.63	11.43	3	2.994	94.49

3	231.3	246.64	15.33	3	2.973	93.78

N	τ_{OUT} (N·mm)	τ_{IN} (N·mm)	$\Delta\tau$ (N·mm)	n_{IN} (r/min)	n_{OUT} (r/min)	η (%)
3	271.1	290.34	19.24	3	2.998	93.37
3	313.0	336.72	23.72	3	2.976	92.95
3	352.8	380.66	27.86	3	2.983	92.68
3	398.4	434.55	36.15	3	2.997	91.68
3	426.3	471.11	44.22	3	2.965	90.49
3	464.1	518.72	54.62	3	2.814	89.47
4	130.3	148.51	18.21	3	2.984	87.74
4	163.0	180.03	17.03	3	2.979	90.54
4	196.2	218.60	22.39	3	2.984	89.75
4	231.3	246.68	15.38	3	2.977	93.77
4	271.1	297.74	26.63	3	2.998	91.05
4	313.0	351.23	38.22	3	2.971	89.12
4	352.8	405.72	54.69	3	2.925	86.96
4	398.4	473.03	74.63	3	2.869	84.22
5	130.3	160.00	30.07	3	2.984	81.25
5	163.0	196.83	33.84	3	2.974	82.81
5	196.2	231.26	36.70	3	2.992	84.84
5	231.3	272.08	41.42	3	2.987	85.01
5	271.1	324.34	51.88	3	2.876	83.59
5	313.0	374.04	61.04	3	2.753	83.68
6	130.3	174.62	30.07	3	2.989	74.62
6	163.0	211.89	33.84	3	2.974	76.93
6	196.2	245.58	36.70	3	2.992	79.89
6	231.3	294.79	63.49	3	2.847	78.46
6	271.1	363.96	92.86	3	2.756	74.65
7	130.3	176.16	45.86	3	2.91	73.97
7	163.0	212.43	49.44	3	2.99	76.73
7	196.2	280.28	58.86	3	2.804	70.00

∗ Data corresponding to unsteady transmission are shaded in gray.

In addition to the load and the angle of torque transmission, we also investigated the rotational speed of the motor and the fatigue resistance of the SBCTC. During the experiments, the applied load was maintained at 398 N·mm and tests were performed on soft couplings with $N = 1$ or 2 SBCTC units, respectively. Experimental result in Fig. 3-21 illustrates that the input torques $\tau_{N=1}$ and $\tau_{N=2}$ remained within the ranges of

402.82 ± 1.33 N·mm and 406.29 ± 2.16 N·mm respectively, with corresponding transmission efficiencies $\tau_{N=1}$ and $\tau_{N=2}$ of 98.80 ± 0.33% and 97.95 ± 0.54%, which indicates high efficiency of our SBCTC regardless of rotational speed n_{IN}.

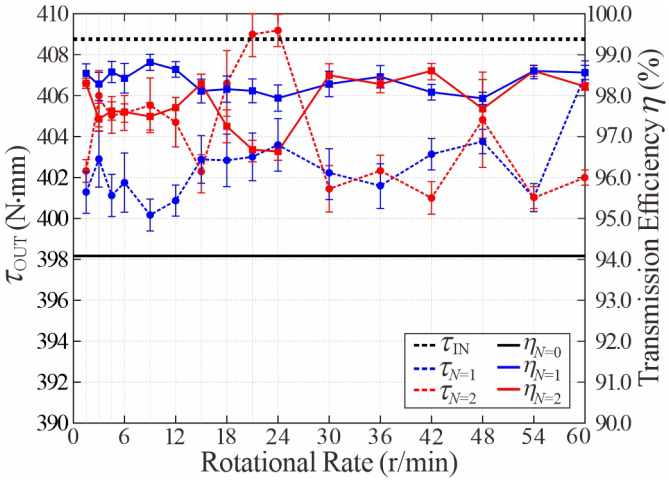

Fig. 3-21 Input torque τ_{IN} and transmission efficiency η vs. Rotational speed for the SBCTC with $N = 1$ and $N = 2$ unit at fixed torque $\tau_{\mathrm{OUT}} = 398$ N·mm.

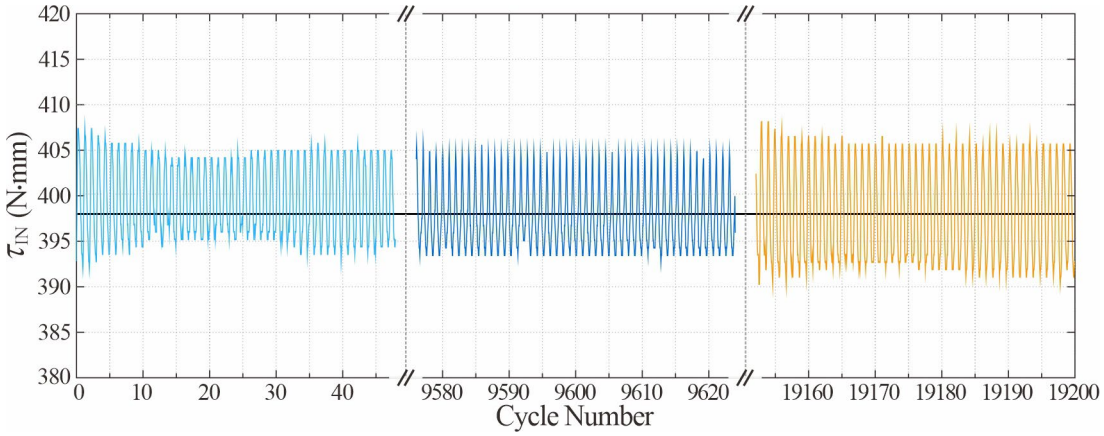

Fig. 3-22 Input torque τ_{IN} vs. Cycle Number for the SBCTC with $N = 1$ unit at fixed torque load $\tau_{\mathrm{OUT}} = 398$ N·mm.

Moreover, to demonstrate fatigue resistance of SBCTC[111], the $N = 1$ specimen successfully completed 19200 operational cycles. With increasing cycle numbers, the input torque $\tau_{N=1}$ fluctuated around 402.73 N·mm, maintaining η around 98.83% without observed failure as shown in Fig. 3-22. However, it can be noted that the fluctuation range of the torque expanded from 10.53 N·mm to 15.96 N·mm due to material fatigue.

Here, when γ_T (N = 0, 1, 2) is less than 30°, the efficiency reaches 97% and remains stable over a long period under different rotational speeds, demonstrating robust fatigue resistance. Efficiency η stays close to 90% with γ_T less than 60° (N = 3, 4). Even when γ_T exceeds 90° (N = 7), η remains above 75%. Compared to common soft couplings listed in Tab. 3-3, our cost-effective SBCTCs demonstrate outstanding transmission efficiency and a broad torque transmission angle here. Owing to their unique bistable configuration, our bent SBCTC resides in a deep energy potential well, enabling them to maintain its shape robustly when subjected to torsional disturbances. Consequently, the system can achieve high transmission efficiency without requiring additional energy input for elastic deformation even in the presence of manufacturing errors, provided the structure possesses its bending stable state.

3.6 Conclusions

In conclusion, prompted by the circumferential stability of a multistable straw in its bent state, we have successfully designed a novel compliant toque coupling. This coupling constructed from a series-connected frustum shells, harnesses this stability of the bent straw into static balance during torsion, allowing the ideal coupling to achieve perfect torque transmission without requiring external force or energy input.

Tab. 3-3 Comparison of our SBCTCs with common soft couplings.

Couplings	Transmission Angle Range	Transmission Efficiency	Ref.
Rigid coupling	0.0° ~ 0.1°	⩾ 99.6%	[176]
Elastic coupling	0.5° ~ 3.0°	85.0% ~ 98.0%	[176]
Steel bellow coupling	9.0° ~ 12.0°	93.3% ~ 99.8%	[178]
Rubber bellow coupling	⩾30.0°	70.0% ~ 90.0%	[178]
Truss TRUNC	⩾45.0°	85.0% ~ 90.0%	[178]
Flexible shaft	0.0° ~45.0° 45.0° ~90.0°	75.0% ~ 90.0% 50.0% ~ 75.0%	[179]
SBCTC	0.0° ~30.0° 30.0° ~60.0° 60.0° ~90.0°	98.0° ~99.8° 88.0° ~98.0° 75.0° ~88.0°	**This work**

Through numerical analysis of the bending process, we have investigated the mechanical behavior and geometric evolution, particularly the curvature distribution. Parametric studies identified key factors influencing bending stability, which enabled

the development of a simplified beam model to predict stable states and guide parameter selection for torque transmission. Subsequently, numerical analysis of the bent SBCTC under torsion has unveiled the fact that periodic circumferential deformation of material elements and mutual strain energy compensation ensures the preservation of total energy and overall geometry, validated by experimental reconstruction of frustum shells. Additionally, precise tests further verified the stable and efficient torque transmission capabilities of the SBCTC under different loads and operating conditions, significantly outperforming existing industrial flexible couplings.

However, our current SBCTC exhibits certain limitations. Notably, the research lacks a corresponding theoretical model, which will be a focus of our future work. Experimental results indicate that its torque transmission capacity is subjected to a distinct upper limit under large transmission angles, which is inferior to that of industrial alternatives. To extend its applicability, developing robust multi-scale models is also essential for SBCTC to ensure reliable performance across different scales. Nevertheless, in comparison with commercial couplings listed in Tab. 3-3, we anticipate that our lightweight and low-cost SBCTCs of varying scales will enable ultra-efficient torque transmission across dimensional scales, advancing applications from forefront robotics systems to precision micro-manufacturing beyond this prototype.

Chapter 4 Geometry of the Threefold Möbius Strip

4.1 Introduction

The SBCTC demonstrated in Chapter 3 can achieve neutral stability with invariant overall geometry under torsion, enabling high-efficiency rotation and torque transmission in confined spaces. To leverage shape-preserving property for emerging applications, researchers have developed ZEEM-based soft actuators in integration of well-designed geometry, intelligent materials and tailored actuation strategies[175].

According to Section 1.2.4, geometric design is particularly crucial for achieving both ZEEMs and neutral stability, as it determines their structural integrity and motion performance. Here, we selected the generalized Möbius strip as the basic structure for the actuator, due to its closed-loop continuity. The inherent developable geometry of the inextensible strip facilitates straightforward and simple manufacturing process from thin films through bending and bonding.

To further investigate influence of twisting number of the generalized Möbius strip[108,109], we fabricated samples with twist numbers N_{Tw} from 1 to 5 corresponding to the twisting angle α_{Tw} ranging from 180° to 900°. A rectangular strip of polyformimide film (3M™ 1205 Electrical Insulating Tape) with a length of l, a width of $w = 10$ mm, and a thickness of $t = 25$ μm is folded back and forth for N_{Tw} times with α_{Tw} of $180N_{\mathrm{Tw}}$°, and then joining two ends with the tape (20 μm, 3M™ 9495LE) in length of $l_{\mathrm{T}} = 0.5$ mm, whose detailed geometrical parameters are listed in Appendix Tab. A2. Then, the fabricated samples were adhered on the substrate to maintain their N_{Tw}-fold rotational symmetry ($N_{\mathrm{Tw}} = 1, 2, 3, 4, 5$) of the structure in Figs. 4-1(a) and (b).

However, as shown in Fig. 4-1(c), when detached from the adhesive substrate below, samples with N_{Tw} of 1, 2, 4, 5 became flipped or curled on the substrate, which exhibits morphological instability. In particular, samples with N_{Tw} of 1 and 2 were prone to completely flipping on the substrate, which causes uneven exposure to the stimuli. Meanwhile, those with $N_{\mathrm{Tw}} = 4$ and 5 collapsed to the curling configurations with the minimum strain energy due to inadequate prestress[109]. Even with a reduced aspect ratio l/w, the responsive material could not generate sufficient actuation needed for the required shape deformation. Meanwhile, without support, only the threefold Möbius sample ($N_{\mathrm{Tw}} = 3$) can maintain stability with moderate prestress, demonstrating potential for shape preservation to achieve neutral stability in actuator applications. The principle

that “three points define a plane” further ensures consistent and reliable contact with the substrate. Consequently, threefold symmetric design ($N_{Tw} = 3$, $\alpha_{Tw} = 540°$) is selected for the Möbius actuator in this study. Prior to experimental tests and motion analysis of the threefold Möbius actuator detailed in Chapter 5, morphological characterization and geometric reconstruction of the standstill model was first conducted to provide a geometrical foundation for developing theoretical model and performing mechanical-guided parametric optimization.

The outline of this chapter is structured as follows. Section 4.2 elaborates on the experimental setup and the data processing for scanning the standstill Möbius actuator, from which fundamental hypotheses of the overall model are further formulated. The boundary conditions are predetermined in accordance with the threefold symmetric geometry in Section 4.3. Accordingly, Section 4.4 establishes a mathematical model of developable surfaces for inextensible strips, allowing for the complete derivation of the geometric configuration. The parametric analysis of the geometric configurations is further discussed in Section 4.5. Finally, the conclusions are given in Section 4.6, which summarizes the main findings in this chapter.

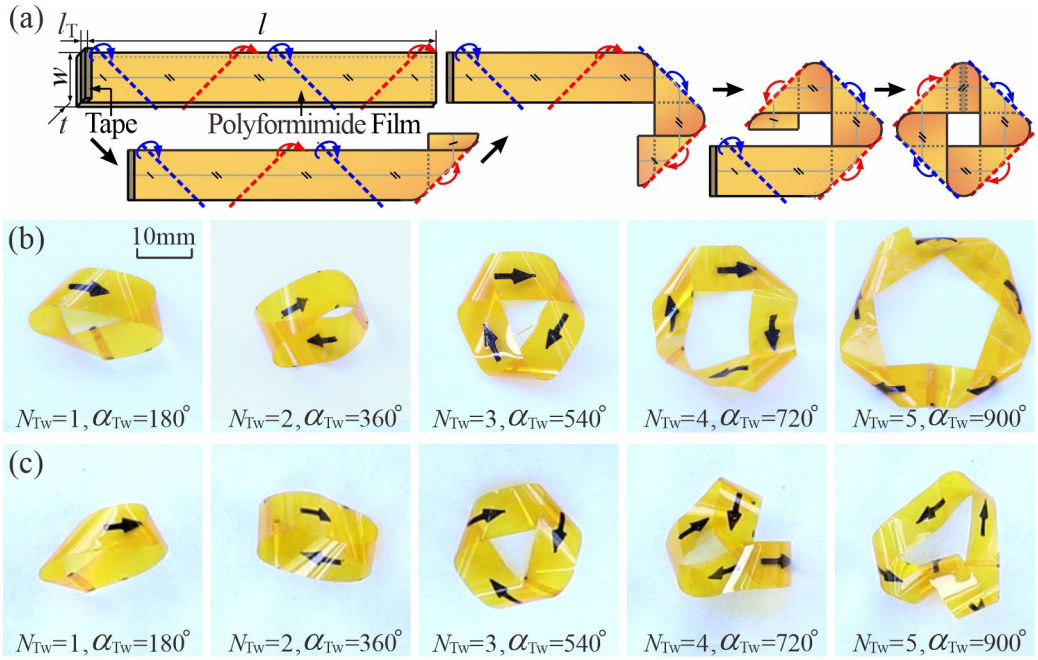

Fig. 4-1 Fabrication and morphological stability of N_{Tw}-fold Möbius strips. (a) Fourfold Möbius samples with N_{Tw}=4 and α_{Tw} = 720°, where the blue and red arrows represent the twist directions.

Comparison of N_{Tw}-fold Möbius samples (N_{Tw} = 1, 2, 3, 4, 5): (b) constrained and (c) standstill states on the substrate.

4.2 Geometrical Reconstruction of the Möbius Strip

We first conducted morphological characterization of the Möbius actuator by geometrically reconstructing the standstill as-fabricated physical model from white polyformimide film in thickness t of 25 μm dyed in white (Sano Aerosol Paint #191) in Fig. 4-2(a). For subsequent motion track of our Möbius actuator in Chapter 5, the white AG film dyed with titanium dioxide powder, as detailed in Appendix A, was applied here for optical scanning.

Digital image correlation (DIC) system (CSI Vic-3D9M) in a frame time of 500ms was applied here to capture the curved surface morphology from a top view with speckles in density of 12.12 mm^{-2} and a maximum error of 0.05 mm, as shown in Fig. 4-2(b). As a supplementary measurement, three flipped corners of the Möbius strip uncaptured by DIC systems were scanned by a 3D scanner (Artec Space Spider, Artec 3D, Luxembourg) with a scatter density of 14.32 mm^{-2} and a maximum error of 0.10mm to ensure accurate and complete geometrical reconstruction, see Fig. 4-2(c).

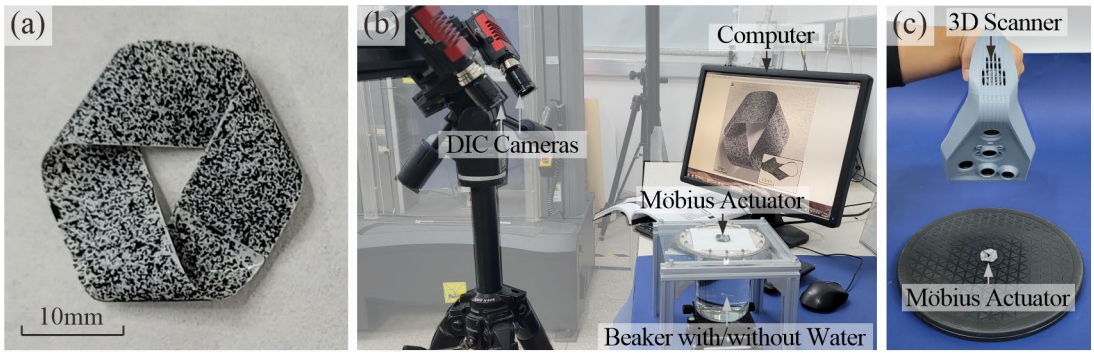

Fig. 4-2 Experimental setup of the DIC and 3D scanning tests. (a) The white Möbius sample painted with black scatters (l = 56 mm, w = 8 mm, t = 25 μm); (b) experimental setup of the DIC system with the standstill sample on the dry horizontal substrate, and the actuator in motion on a humid substrate of RH_{sub} = 90%; (c) the experimental setup of 3D scanning with the standstill sample on the dry substrate.

After acquiring the scattered points on the sample surface, we performed a simplification of the geometric morphology. Given that the thickness t was maintained significantly smaller than its dimensions l and w in our research, our Möbius sample

can be modeled as an inextensible and developable surface[108,109], which provides essential constraints for geometrical reconstruction.

First, the maximum principal curvature κ_1 of the surface can be determined through bivariate polynomial fitting in MATLAB 2023a, which yields the curvature distribution in Fig. 4-3(b). Combining the side view in the embedded figure of Fig. 4-3(a) and the κ_1 contour map in Fig. 4-3(b) reveals that the Möbius surface is composed of three identical cylindrical regions with uniform curvature along its parallel generator (red frames) and three nearly flat trapezoidal regions, where κ_1 ranges from 0 to 0.10 mm^{-1} (blue frames). Then, considering the developability of Möbius geometry, the cylindrical regions and the nearly flat trapezoidal regions can only be cylindrical and conical surfaces, respectively.

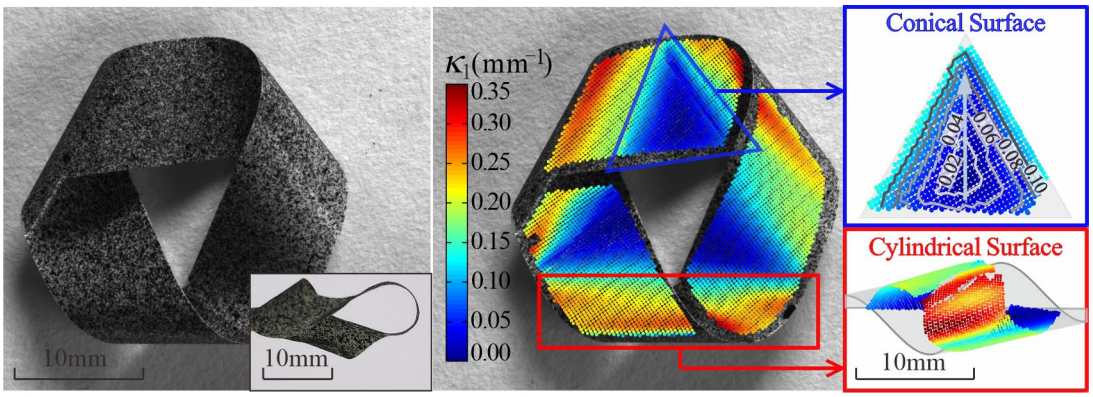

Fig. 4-3 Experimental scanning of the Möbius sample. (a) Original DIC photos taken from the top view and side view (the inset picture) of a white Möbius sample (l = 56 mm, w = 8 mm, t = 25 μm); (b) the contour map of the maximum principal curvature κ_1 of the actuator and the inset enlarged triangle conical region calculated from the DIC results. The flipped regions are obtained from 3D scanning.

Based on the results above, a simplified geometrical model of the Möbius strip is presented as shown in Fig. 4-4(a). The reconstructed geometrical model consists of three identical silver cylindrical surfaces (N_1N_1', N_2N_2', N_3N_3') with a teardrop-shaped cross section in the red shadow winding along three silver cylinders with a constant helical angle β_0, which are interconnected by three identical nearly-trapezoid conical surfaces ($N_1'N_3$, $N_3'N_2$, $N_2'N_1$) in blue shadow.

Given the threefold rotational symmetry of our Möbius strip, we only needed to analyze one-third of the geometry called P_1P_2. To determine the geometry of P_1P_2, we

defined P_1P_2 in the *oxyz* coordinate system, aligning the principal directions at point Q_3 with the *x*-axis and *y*-axis, while the generatrix of the cylindrical surface is parallel to the *z*-axis as shown in Fig. 4-4(b), and then projected its center line on the *oxy* plane, as the gray scatters in Fig. 4-4(c). Based on observation of the 3D scanned data, we utilized a modified Cassinian oval curve to fit the central curve N_3N_3' in red for the cylindrical surface and a clothoid curve in blue to fit the central curves N_3P_1 and $N_3'P_2$ for the conical surfaces, thus obtaining the exact one-third central curve of P_1P_2 in Fig. 4-4(b). By extruding the center line P_1P_2, the complete geometry of the Möbius strip can be obtained.

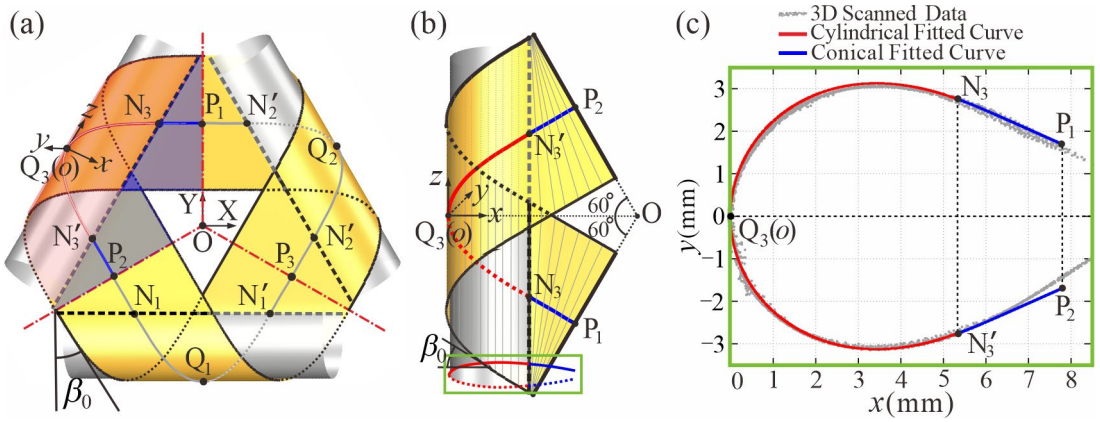

Fig. 4-4 Geometrical modelling of the Möbius sample. (a) The proposed geometrical model with the helical angle β_0; (b) the detailed one-third geometrical model; (c) the projected center lines of the cylindrical surface N_3N_3' (red) and the conical surface N_3P_1, $N_3'P_2$ (blue) of the geometrical model, and the corresponding center lines from 3D scanning (gray).

Following our geometric simplification, we first processed and analyzed the scattered point coordinates collected from 3D scanning to derive the cross-sectional projection of one-third Möbius surface detailed as follows.

First, the scanned points of a Möbius sample ($l = 70$ mm, $w = 10$ mm, $t = 25$ μm) painted in gray are illustrated in Fig. 4-5(a) with the serrated and fuzzy edge due to measurement error. Here, we traced its edge with the gray solid line to magnify its right-handed topology. The top profile of the Möbius sample is close to a hexagon with a triangle dug out in its center. In Fig. 4-5(b), each vertex O_i of the inner triangle connected to the neighboring two vertices F_i, G_i ($i = 1, 2, 3$) of the outer hexagon, which neatly cut the entire Möbius sample into three bilayer twisted triangle pieces marked in

blue and three monolayer quadrilateral pieces marked in red. To reduce the error introduced by the blurred boundary, the scatters around the center line are extracted in the width of 1.60 mm to characterize the surface feature of the Möbius sample as shown in Fig. 4-5(c).

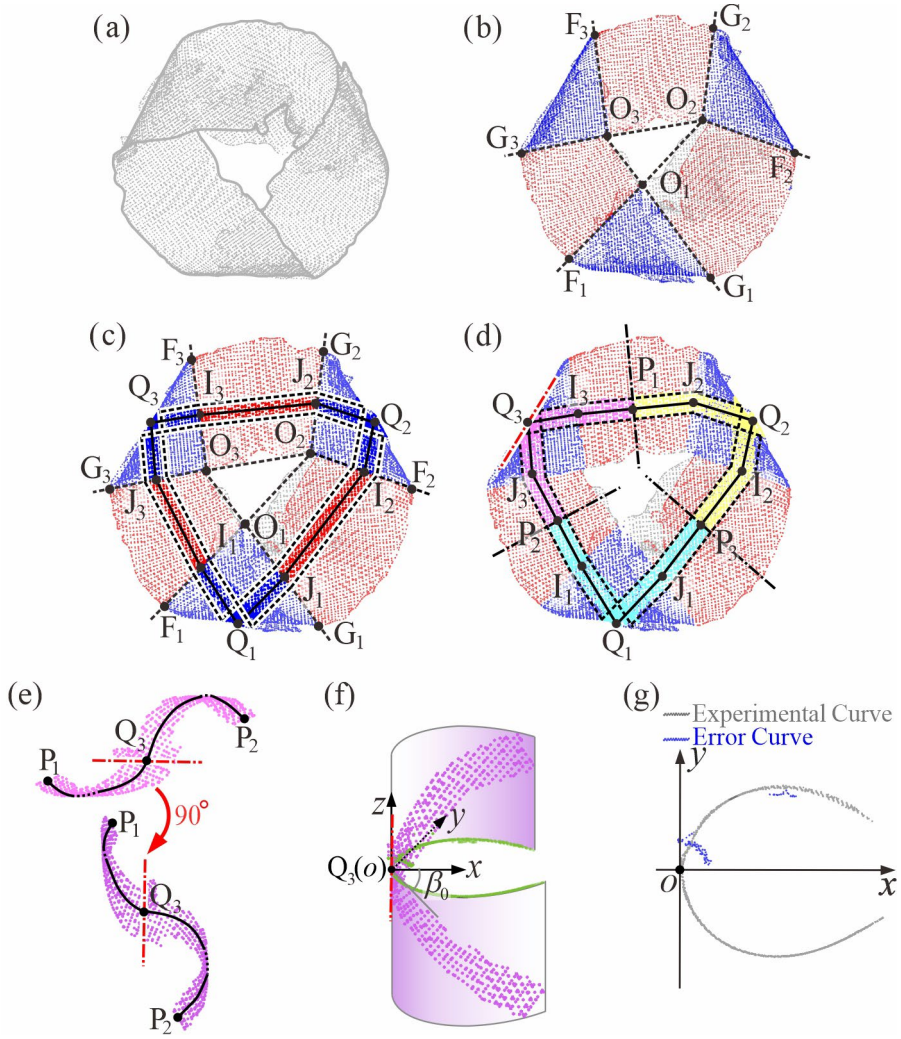

Fig. 4-5 Data processing of 3D-scanned coordination of the Möbius sample. (a) The original 3D scanned result of the Möbius sample from the vertical view (l = 70 mm, w = 10 mm, t = 25 μm); (b) the divided pieces of the Möbius sample with three bilayer twisted triangle pieces marked in blue and three monolayer quadrilateral pieces marked in red; (c) the selected scatters around the middle line of each piece; (d) the trisection of the selected scatters with three sections painted in cyan, pink, and yellow respectively; (e) the side view of the pink section with the symmetric center Q_3 and the vertical red dash-dotted line through Q_3 with consistent curvature (upper); the rotated view of the pink section painted in purple with the horizontal red dash-dotted line through Q_3 after rotating 90° anticlockwise (downer); (f) the imaginary cylinder in light purple based on the cylindrical surface

in the oxyz coordinate system; (g) the projection of purple scatters on the xoy plane marked in gray, while the scatters painted in blue were filtered out.

For bilayer triangle twisted regions marked in blue, the middle line I_iQ_i connects the middle point I_i of the segment O_iF_i and middle point Q_i of the segment F_iG_i, while Q_iJ_i connects the point Q_i and J_i of the segment O_iG_i ($i = 1, 2, 3$) following their twisting path. For monolayer quadrilateral pieces marked in red, the line segments I_1J_3, I_2J_1, I_3J_2 connected with the segments I_iQ_i and Q_iJ_i ($i = 1, 2, 3$) forming a closed line $Q_1Q_2Q_3Q_1$ marked in black solid line. Then, scatters marked in blue or red circular dots are bounded between parallel black dashed lines.

Subsequently, we cut the selected scatters from the perpendicular bisectors in the black dash-dotted line through middle points P_1, P_2, P_3 of the line segments I_2J_3, I_1J_2, I_3J_1 into three symmetric sections painted in cyan, pink and yellow in Fig. 4-5(d). The side view of the pink section is rotated as shown in the upper picture of Fig. 4-5(e), which is almost rationally symmetric through point Q_3. Based on the rotational symmetry of cylindrical surface mentioned in Fig. 4-4(b), the symmetric generator of the cylinder is marked in a red dash-dotted line. Then, the selected scatters painted in light purple are rotated 90° clockwise with the red dash-dotted line as the *z*-axis. Here, point Q_3 is in coincidence with the origin point *o*, while the red dash-dotted line is in coincidence with the *z*-axis, as shown in Fig. 4-5(f). The *y*-axis is tangent to the rotated scatters. The imaginary cylindrical surface in light purple is drawn in the *oxyz* coordinate system with point Q_3 coincident with the origin point *o*. The selected scatters painted in gray are projected on the *xoy* plane as the cross-section of the cylinder. A few distributed scatters painted in blue are filtered out to achieve a better geometrical model painted in gray in Fig. 4-5(g), which corresponds to the gray points projected on the *oxy* plane in Fig. 4-4(c). The data processing was all realized in MATLAB R2023a.

4.3 Threefold Rotational Symmetry of the Möbius Strip

Prior to deducing the specific geometry of the Möbius strip, the corresponding boundary conditions based on rotational symmetry requires prioritized analysis and determination. For instance, the selected configuration with $N_{Tw} = 3$ has threefold rotational symmetry. It can be regarded as a closed continuous strip composed of six congruent pieces painted in green and yellow, divided by three inflection points P_1, P_2, P_3 and cylindrical points Q_1, Q_2, Q_3 at its center line in black solid line in Fig. 4-6(a).

Under the Frenet-Serret framework defined by {$\boldsymbol{t}$, $\boldsymbol{n}$, $\boldsymbol{b}$} consisting of the tangent vector $\boldsymbol{t}$, normal vector $\boldsymbol{n}$ and binormal vector $\boldsymbol{b}$, any two neighboring pieces colored in green and yellow around three inflection points $P_1(s = 0)$, $P_2(s = l/3)$, $P_3(s = 2l/3)$ can be obtained from each other by rotating 180° around unit binormals $\boldsymbol{b}_{P_1}, \boldsymbol{b}_{P_2}, \boldsymbol{b}_{P_3}$ respectively. Besides, any two neighboring pieces around three cylindrical points Q_1 ($s = l/6$), Q_2 ($s = l/2$), and $Q_3(s = 5l/6)$ can also be obtained from each other by rotating 180° around unit normals $\boldsymbol{n}_{Q_1}, \boldsymbol{n}_{Q_2}, \boldsymbol{n}_{Q_3}$ respectively. Therefore, a Cartesian coordinate system OXYZ is established here with its origin O coinciding with the center point of three inflection points P_1, P_2, P_3. These points also define the XOY plane, with point P_1 located on the Y-axis.

According to its rotational threefold symmetry, the coordination and binormal vector $\boldsymbol{b}_{P_i}$ of the inflection points P_i ($i = 1, 2, 3$) respectively in the OXYZ coordinate system can be denoted as follows with a unknown value Z_P.

$$r_P = \left\|\overrightarrow{OP_1}\right\| = \left\|\overrightarrow{OP_2}\right\| = \left\|\overrightarrow{OP_3}\right\|, \tag{4-1a}$$

$$\mathbf{P_1}(s = 0) = \left[0,\ \ r_P,\ \ 0\right]^T,\ \boldsymbol{b}_{P_1} = \frac{1}{\sqrt{1 + {Z_P}^2}}\left[0,\ \ 1,\ \ Z_P\right]^T; \tag{4-1b}$$

$$\mathbf{P_2}\left(s = \frac{l}{3}\right) = \left[-\frac{\sqrt{3}r_P}{2},\ \ -\frac{r_P}{2},\ \ 0\right]^T,\ \boldsymbol{b}_{P_2} = \frac{1}{\sqrt{1 + {Z_P}^2}}\left[-\frac{\sqrt{3}}{2},\ \ -\frac{1}{2},\ \ Z_P\right]^T; \tag{4-1c}$$

$$\mathbf{P_3}\left(s = \frac{2l}{3}\right) = \left[\frac{\sqrt{3}}{2}r_P,\ \ -\frac{r_P}{2},\ \ 0\right]^T,\ \boldsymbol{b}_{P_3} = \frac{1}{\sqrt{1 + {Z_P}^2}}\left[\frac{\sqrt{3}}{2},\ \ -\frac{1}{2},\ \ Z_P\right]^T. \tag{4-1d}$$

The binormal vector $\boldsymbol{b}_{P_1}$ rotating 180° around the axis $\boldsymbol{b}_{P_2}$ should be derived as $\boldsymbol{b}_{P_3}$. Substitute rotational angle $\varphi_u = 180°$ and rotational axis $\boldsymbol{u} = \boldsymbol{b}_{P_2}$ into the rotational matrix $\boldsymbol{R_u}(\varphi_u)$ as follows.

$$\boldsymbol{R}_{\boldsymbol{b}_{P_2}}(180^\circ) = \frac{1}{\sqrt{1 + {Z_P}^2}}\begin{bmatrix} 0.5 & 0.5\sqrt{3} & -\sqrt{3}Z_P \\ 0.5\sqrt{3} & -0.5 & -Z_P \\ -\sqrt{3}{Z_P}^2 & -Z_P & 2{Z_P}^2 - 1 \end{bmatrix}. \tag{4-2}$$

The rotated vector $\boldsymbol{b}_{P_1}^R$ of the binormal vector $\boldsymbol{b}_{P_1}$ can be derived as

$$\boldsymbol{b}_{P_1}^R = R_{\boldsymbol{b}_{P_2}}(180^\circ)\boldsymbol{b}_{P_1} = \frac{1}{\sqrt{1 + {Z_P}^2}}\begin{bmatrix} 0.5\sqrt{3} - {Z_P}^2\sqrt{3} \\ -0.5 - {Z_P}^2 \\ 2{Z_P}^3 - 2Z_P \end{bmatrix} = \boldsymbol{b}_{P_3}. \tag{4-3}$$

The rest rotated vectors $\boldsymbol{b}_{P_2}$ and $\boldsymbol{b}_{P_3}$ can be achieved by substituting into Eq. (4-3), leading to $Z_P = 0$. With the included angle θ_P between the tangent vector $\boldsymbol{t}_{P_1}$ and XOY plane, the tangent vector $\boldsymbol{t}_{P_1}$ of point P_1 is $[-\cos\theta_P,\ 0,\ \sin\theta_P]^T$, see Fig. 4-6(c). Then the principle normal $\boldsymbol{n}_{P_1}$ of the point P_1 can be derived as

$$\boldsymbol{n}_{P_1} = \boldsymbol{b}_{P_1} \times \boldsymbol{t}_{P_1} = \left[\sin\theta_P,\ \ 0,\ \ \cos\theta_P\right]^T. \tag{4-4}$$

Then we can deduce two other unit normals $\boldsymbol{n}_{P_2}$, $\boldsymbol{n}_{P_3}$ and binormals $\boldsymbol{b}_{P_2}$, $\boldsymbol{b}_{P_3}$ at points P_2, P_3. The coordination and Frenet-Serret framework of the inflection points P_1, P_2, P_3 can be expressed as

$$\begin{cases} \mathbf{P_1}(s=0) = \left[0,\ \ r_P,\ \ 0\right]^T \\ \boldsymbol{t}_{P_1} = \left[-\cos\theta_P,\ \ 0,\ \ \sin\theta_P\right]^T \\ \boldsymbol{n}_{P_1} = \left[\sin\theta_P,\ \ 0,\ \ \cos\theta_P\right]^T \\ \boldsymbol{b}_{P_1} = \left[0,\ \ 1,\ \ 0\right]^T \end{cases}; \tag{4-5a}$$

$$\begin{cases} \mathbf{P_2}(s=l/3) = \left[-0.5\sqrt{3}r_P,\ \ -0.5r_P,\ \ 0\right]^T \\ \boldsymbol{t}_{P_2} = \left[0.5\cos\theta_P,\ \ -0.5\sqrt{3}\cos\theta_P,\ \ \sin\theta_P\right]^T \\ \boldsymbol{n}_{P_2} = \left[-0.5\sin\theta_P,\ \ 0.5\sqrt{3}\sin\theta_P,\ \ \cos\theta_P\right]^T \\ \boldsymbol{b}_{P_2} = \left[-0.5\sqrt{3},\ \ -0.5,\ \ 0\right]^T \end{cases}; \tag{4-5b}$$

$$\begin{cases} \mathbf{P_3}(s=2l/3) = \left[0.5\sqrt{3}r_P,\ \ -0.5r_P,\ \ 0\right]^T \\ \boldsymbol{t}_{P_3} = \left[0.5\sqrt{3}\cos\theta_P,\ \ 0.5\cos\theta_P,\ \ \sin\theta_P\right]^T \\ \boldsymbol{n}_{P_3} = \left[-0.5\sin\theta_P,\ \ -0.5\sqrt{3}\sin\theta_P,\ \ \cos\theta_P\right]^T \\ \boldsymbol{b}_{P_3} = \left[0.5\sqrt{3},\ \ -0.5,\ \ 0\right]^T \end{cases}. \tag{4-5c}$$

The unit binormal $\boldsymbol{b}_{P_3}$ of point P_3 can be derived as the unit binormal $\boldsymbol{b}_{P_2}$ of point P_2 rotating 180° around the unit normal $\boldsymbol{n}_{Q_1} = \left[n_{Q_1X},\ n_{Q_1Y},\ n_{Q_1Z}\right]^T$ of point Q_1. Substituting $\theta_R = 180°$ and the unit normal $\boldsymbol{n}_{Q_1}$ into the rotational matrix $\boldsymbol{R}_{\boldsymbol{n}_{Q_1}}(180^\circ)$ as Eq. (4-6).

$$\boldsymbol{R}_{\boldsymbol{n}_{Q_1}}(180^\circ) = \begin{bmatrix} 2n_{Q_1X}{}^2 - 1 & 2n_{Q_1X}n_{Q_1Y} & 2n_{Q_1X}n_{Q_1Z} \\ 2n_{Q_1X}n_{Q_1Y} & 2n_{Q_1Y}{}^2 - 1 & 2n_{Q_1Y}n_{Q_1Z} \\ 2n_{Q_1X}n_{Q_1Z} & 2n_{Q_1Z}n_{Q_1Y} & 2n_{Q_1Z}{}^2 - 1 \end{bmatrix}. \tag{4-6a}$$

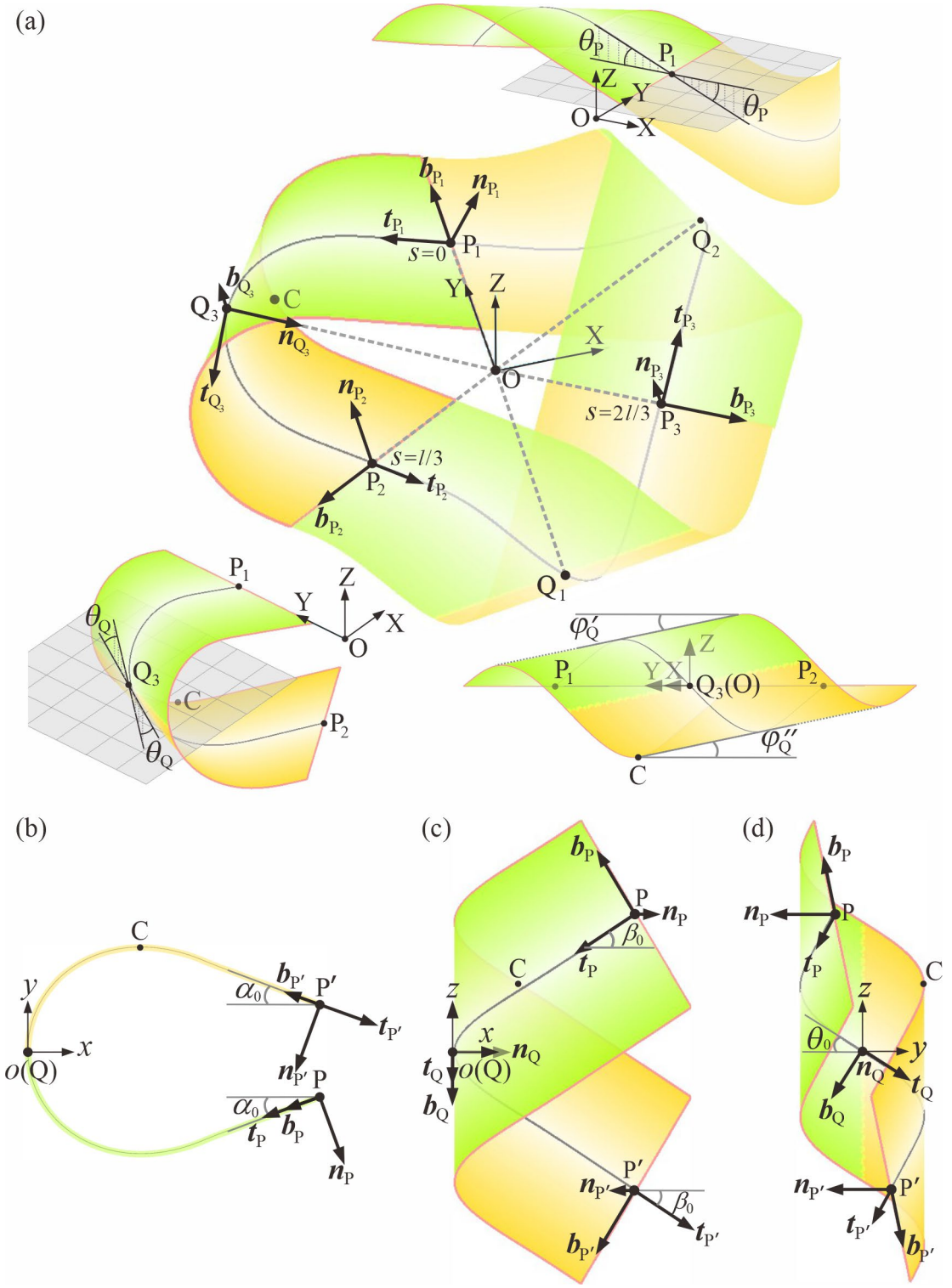

Fig. 4-6 The threefold rotational symmetry of the Möbius strip. (a) The Möbius strip made of six congruent pieces (green and yellow) established in the OXYZ Cartesian coordinate system. The one-third Möbius strip established in the oxyz coordinate system via coordination transformation: (b) the one-third Möbius strip PQP′ projected on the *xoy* plane; (c) the projection on the *xoz* plane; (d) the projection on the *yoz* plane.

Then the unit normal $\boldsymbol{n}_{\mathrm{Q}_1}=\left[0,\ 1,\ 0\right]^{\mathrm{T}}$ can be derived from

$$\boldsymbol{b}_{\mathrm{P}_2}^{\mathrm{R}}=\boldsymbol{R}_{\boldsymbol{n}_{\mathrm{Q}_1}}(180°)\boldsymbol{b}_{\mathrm{P}_2}=\boldsymbol{b}_{\mathrm{P}_3}. \tag{4-7}$$

Here, we define the included angle θ_{Q} between the tangent vector $\boldsymbol{t}_{\mathrm{Q}_1}$ and the XOY plane. Therefore, the unit tangent $\boldsymbol{t}_{\mathrm{Q}_1}$ of Point Q_1 is $[\cos\theta_{\mathrm{Q}},\ 0,\ \sin\theta_{\mathrm{Q}}]^{\mathrm{T}}$, and the unit binormal $\boldsymbol{b}_{\mathrm{Q}_1}$ can be deduced as $[-\sin\theta_{\mathrm{Q}},\ 0,\ \cos\theta_{\mathrm{Q}}]^{\mathrm{T}}$ by applying Eq. (4-7).

According to the threefold rotational symmetry, the Frenet-Serret framework and coordination of the cylindrical points Q_2, and Q_3 can be achieved by rotating 120° and 240° respectively around the Z-axis as follows.

$$r_{\mathrm{Q}}=\left\|\overrightarrow{\mathrm{OQ}_1}\right\|=\left\|\overrightarrow{\mathrm{OQ}_2}\right\|=\left\|\overrightarrow{\mathrm{OQ}_3}\right\|, \tag{4-8a}$$

$$\begin{cases}\mathbf{Q_1}(s=0)=\left[0,\ -r_{\mathrm{Q}},\ 0\right]^{\mathrm{T}}\\ \boldsymbol{t}_{\mathrm{Q}_1}=\left[\cos\theta_{\mathrm{Q}},\ 0,\ \sin\theta_{\mathrm{Q}}\right]^{\mathrm{T}}\\ \boldsymbol{n}_{\mathrm{Q}_1}=\left[0,\ 1,\ 0\right]^{\mathrm{T}}\\ \boldsymbol{b}_{\mathrm{Q}_1}=\left[-\sin\theta_{\mathrm{Q}},\ 1,\ \cos\theta_{\mathrm{Q}}\right]^{\mathrm{T}}\end{cases}, \tag{4-8b}$$

$$\begin{cases}\mathbf{Q_2}(s=5l/6)=\left[0.5\sqrt{3}r_{\mathrm{Q}},\ 0.5r_{\mathrm{Q}},\ 0\right]^{\mathrm{T}}\\ \boldsymbol{t}_{\mathrm{Q}_2}=\left[-0.5\cos\theta_{\mathrm{Q}},\ -0.5\sqrt{3}\cos\theta_{\mathrm{Q}},\ \sin\theta_{\mathrm{Q}}\right]^{\mathrm{T}}\\ \boldsymbol{n}_{\mathrm{Q}_2}=\left[-0.5\sqrt{3},\ -0.5,\ 0\right]^{\mathrm{T}}\\ \boldsymbol{b}_{\mathrm{Q}_2}=\left[0.5\sin\theta_{\mathrm{Q}},\ -0.5\sqrt{3}\sin\theta_{\mathrm{Q}},\ \cos\theta_{\mathrm{Q}}\right]^{\mathrm{T}}\end{cases}, \tag{4-8c}$$

$$\begin{cases}\mathbf{Q_3}(s=l/6)=\left[0.5\sqrt{3}r_{\mathrm{Q}},\ -0.5r_{\mathrm{Q}},\ 0\right]^{\mathrm{T}}\\ \boldsymbol{t}_{\mathrm{Q}_3}=\left[-0.5\sqrt{3}\cos\theta_{\mathrm{Q}},\ \sin\theta_{\mathrm{Q}},\ 0\right]^{\mathrm{T}}\\ \boldsymbol{n}_{\mathrm{Q}_3}=\left[0.5\sqrt{3},\ -0.5,\ 0\right]^{\mathrm{T}}\\ \boldsymbol{b}_{\mathrm{Q}_3}=\left[-0.5\sin\theta_{\mathrm{Q}},\ -0.5\sqrt{3}\sin\theta_{\mathrm{Q}},\ \cos\theta_{\mathrm{Q}}\right]^{\mathrm{T}}\end{cases}. \tag{4-8d}$$

Here, based on the derived Frenet-Serret framework of the inflection points and cylindrical points from Eqs. (4-5) to (4-8), we can conclude that all three inflection points P_i and three cylindrical points Q_i (i = 1, 2, 3) are in the same XOY plane, while the binormal $\boldsymbol{b}_{\mathrm{P}_i}$ of point P_i and normal $\boldsymbol{n}_{\mathrm{Q}_i}$ of point Q_i are also parallel to the XOY plane.

To simplify its geometrical relation, the one-third Möbius strip can be cut through vectors $\overrightarrow{OP_1}$, $\overrightarrow{OP_2}$ bounded in a red solid line as shown in Fig. 4-6(a). Then we place the selected section in the Cartesian coordinate system *oxyz* with point Q_3 as the origin point *o*. The unit normal $\boldsymbol{n}_{Q_3}$ through point Q_3 is defined as the horizontal *x*-axis. The generator through the cylindrical point Q_3 is rotated as the vertical *z*-axis, dividing the selected section into the yellow and green halves, see Figs. 4-6(b) to (d). Points P_1, P_2, and Q_3 in the original OXYZ coordinate system correspond to points P, P′ and Q in the *oxyz* coordinate system. The corresponding coordinations under Frenet-Serret frameworks are listed as follows. We first define the included angle α_0 between the projection of the binormal vector $\boldsymbol{b}_{P'}$ on the *xoy* plane and the *x*-axis, the included angle β_0 of the tangent $\boldsymbol{t}_{P'}$ on the *xoz* plane and the *x*-axis, and the included angle θ_Q between the projection of the tangent $\boldsymbol{t}_{Q'}$ on the *yoz* plane and the *y*-axis.

$$\begin{cases} \mathbf{Q} = \left[0,\ \ 0,\ \ 0\right]^{\mathrm{T}} \\ \boldsymbol{t}_{\mathrm{Q}} = \left[0,\ \ \cos\theta_{\mathrm{Q}},\ \ -\sin\theta_{\mathrm{Q}}\right]^{\mathrm{T}} \\ \boldsymbol{n}_{\mathrm{Q}} = \left[1,\ \ 0,\ \ 0\right]^{\mathrm{T}} \\ \boldsymbol{b}_{\mathrm{Q}} = \left[0,\ \ -\sin\theta_{\mathrm{Q}},\ \ -\cos\theta_{\mathrm{Q}}\right]^{\mathrm{T}} \end{cases}; \tag{4-9a}$$

$$\begin{cases} \mathbf{P} = \left[x_{\mathrm{P}},\ \ y_{\mathrm{P}},\ \ z_{\mathrm{P}}\right]^{\mathrm{T}} \\ \boldsymbol{t}_{\mathrm{P}} = \left[-\cos\alpha_0\cos\beta_0,\ \ -\sin\alpha_0\cos\beta_0,\ \ -\sin\beta_0\right]^{\mathrm{T}} \\ \boldsymbol{n}_{\mathrm{P}} = \left[\sin\alpha_0,\ \ -\cos\alpha_0,\ \ 0\right]^{\mathrm{T}} \\ \boldsymbol{b}_{\mathrm{P}} = \left[-\cos\alpha_0\sin\beta_0,\ \ -\sin\alpha_0\sin\beta_0,\ \ \cos\beta_0\right]^{\mathrm{T}} \end{cases}; \tag{4-9b}$$

$$\begin{cases} \mathbf{P}' = \left[x_{\mathrm{P}}, -y_{\mathrm{P}}, -z_{\mathrm{P}}\right]^{\mathrm{T}} \\ \boldsymbol{t}_{\mathrm{P}'} = \left[\cos\alpha_0\cos\beta_0, -\sin\alpha_0\cos\beta_0, -\sin\beta_0\right]^{\mathrm{T}} \\ \boldsymbol{n}_{\mathrm{P}'} = \left[-\sin\alpha_0, -\cos\alpha_0, 0\right]^{\mathrm{T}} \\ \boldsymbol{b}_{\mathrm{P}'} = \left[-\cos\alpha_0\sin\beta_0, \sin\alpha_0\sin\beta_0, -\cos\beta_0\right]^{\mathrm{T}} \end{cases}. \tag{4-9c}$$

Now we can deduce the rotation matrix $\boldsymbol{R}_{\mathbf{xz}}$ and the translation vector $\boldsymbol{T}_{\mathbf{M}}$ by substituting the coordination and Frenet-Serret framework of points P_1, P_2, and Q_3 in the OXYZ coordinate system to points P, P′, Q in the *oxyz* coordinate system. Here, the selected one-third section $P_1Q_3P_2$ in the original OXYZ coordinate system is first rotated by φ_X around the X-axis and then rotated by φ_Z around the Z-axis as the section PQP′ in the *oxyz* coordinate system.

$$\boldsymbol{T}_{\mathbf{M}} = \left[0.5\sqrt{3}r_{\mathrm{Q}},\ -0.5r_{\mathrm{Q}}\ \ 0\right]^{\mathrm{T}}, \tag{4-10}$$

$$\boldsymbol{R}_{\mathbf{XZ}} = \boldsymbol{R}_{\mathbf{X}}(\varphi_{\mathrm{X}})\boldsymbol{R}_{\mathbf{Z}}(\varphi_{\mathrm{Z}}) = \begin{bmatrix} 1 & 0 & 0 \\ 0 & \cos\varphi_{\mathrm{X}} & -\sin\varphi_{\mathrm{X}} \\ 0 & \sin\varphi_{\mathrm{X}} & \cos\varphi_{\mathrm{X}} \end{bmatrix} \begin{bmatrix} \cos\varphi_{\mathrm{Z}} & -\sin\varphi_{\mathrm{Z}} & 0 \\ \sin\varphi_{\mathrm{Z}} & \cos\varphi_{\mathrm{Z}} & 0 \\ 0 & 0 & 1 \end{bmatrix}. \tag{4-11}$$

Substituting $\boldsymbol{n}_{\mathrm{Q}_3}$ into the transformation formula in Eq. (4-12) yields $\varphi_{\mathrm{Z}} = \pi/6$.

$$\boldsymbol{n}_{\mathrm{Q}} = \boldsymbol{R}_{\mathbf{XZ}}\boldsymbol{n}_{\mathrm{Q}_3} = \begin{bmatrix} 0.5\sqrt{3}\cos\varphi_{\mathrm{Z}} + 0.5\sin\varphi_{\mathrm{Z}} \\ 0.5\sqrt{3}\sin\varphi_{\mathrm{Z}} - 0.5\cos\varphi_{\mathrm{Z}} \\ 0 \end{bmatrix} = \begin{bmatrix} 1 \\ 0 \\ 0 \end{bmatrix}. \tag{4-12}$$

When substituting $\boldsymbol{b}_{\mathrm{P}_1}$ into the rotation transformation formula in Eq. (4-13a), the relationship of α_0, β_0, φ_{X} can be derived as follows.

$$\boldsymbol{b}_{\mathrm{P}} = \boldsymbol{R}_{\mathbf{XZ}}\boldsymbol{b}_{\mathrm{P}_1} = \begin{bmatrix} -0.5 \\ 0.5\sqrt{3}\cos\varphi_{\mathrm{X}} \\ 0.5\sqrt{3}\sin\varphi_{\mathrm{X}} \end{bmatrix} = \begin{bmatrix} -\cos\alpha_0\sin\beta_0 \\ -\sin\alpha_0\sin\beta_0 \\ \cos\beta_0 \end{bmatrix}, \tag{4-13a}$$

$$\cos\alpha_0\sin\beta_0 = 0.5,\ \ \cot\varphi_{\mathrm{X}} = -\sin\alpha_0\tan\beta_0. \tag{4-13b}$$

The vectors and coordination above should also satisfy the rotational symmetry of the entire Möbius strip deduced from Eqs. (4-9) to (4-11). Therefore, the coordination of the rotated inflection points P and P′ should follow the rules that

$$\begin{aligned} &\mathbf{P} = \boldsymbol{R}_{\mathbf{XZ}}(\mathbf{P_1} - \boldsymbol{T}_{\mathrm{M}}) + \mathbf{Q}, \\ &\mathbf{P} = \left[-0.5r_{\mathrm{P}} - r_{\mathrm{Q}},\ \ 0.5\sqrt{3}\sin\varphi_{\mathrm{X}}r_{\mathrm{P}},\ \ 0.5\sqrt{3}\cos\varphi_{\mathrm{X}}r_{\mathrm{P}}\right]^{\mathrm{T}}; \end{aligned} \tag{4-14a}$$

$$\begin{aligned} &\mathbf{P'} = \boldsymbol{R}_{\mathbf{XZ}}(\mathbf{P_2} - \boldsymbol{T}_{\mathrm{M}}) + \mathbf{Q}, \\ &\mathbf{P'} = \left[-0.5r_{\mathrm{P}} - r_{\mathrm{Q}},\ \ -0.5\sqrt{3}\sin\varphi_{\mathrm{X}}r_{\mathrm{P}},\ \ -0.5\sqrt{3}\cos\varphi_{\mathrm{X}}r_{\mathrm{P}}\right]^{\mathrm{T}}. \end{aligned} \tag{4-14b}$$

Here, the slant angle φ_{Q} of the generator through the cylindrical point Q is equal to $\varphi_{\mathrm{X}} - \pi/2$ here, which can be obtained by measuring and averaging the slant angles φ'_{Q}, φ''_{Q} from the side view in Fig. 4-6(a). Based on Eqs. (4-11) and (4-12), the necessary boundary conditions to ensure the threefold rotational symmetry of the geometrical model can be concluded as

$$y_{\mathrm{P}}/z_{\mathrm{P}} = y_{\mathrm{P'}}/z_{\mathrm{P'}} = -\tan\varphi_{\mathrm{Q}}, \tag{4-15a}$$

$$\alpha_0 = \tan^{-1}(\sqrt{3}\sin\varphi_{\mathrm{Q}}), \tag{4-15b}$$

$$\beta_0 = \cos^{-1}(0.5\sqrt{3}\sin\varphi_{\mathrm{Q}}). \tag{4-15c}$$

4.4 Mathematical Derivation of the Geometrical Modelling

4.4.1 Mathematical Derivation of the Center Line

According to the definitions of the geodesic curve and developable surface, the center line of a one-third Möbius strip can be regarded as a helical curve winding around the *z*-axis with a constant helical angle β_0 in the *oxyz* coordinate system as shown in Fig. 4-4(b) in Section 4.2. Then, the slant angle $\alpha_0 = \text{atan}(\text{d}y_\text{P}/\text{d}x_\text{P})$ at the inflection points P and P′ can be derived from Eq. (4-14) satisfying the boundary conditions derived from the threefold rotational symmetry in Section 4.3.

To build the geometrical model of the one-third actuator configuration, its center line PQP′ projected on the *xoy* plane should be determined. Here, we first projected one-third of the physical specimen in Fig. 4-4(c) in Section 4.2 onto the *xoy* plane corresponding to the cross section through the cylindrical point Q, and then choose a modified Cassinian oval profile is adopted to fit their teardrop-shaped projection, as shown in Fig. 4-7.

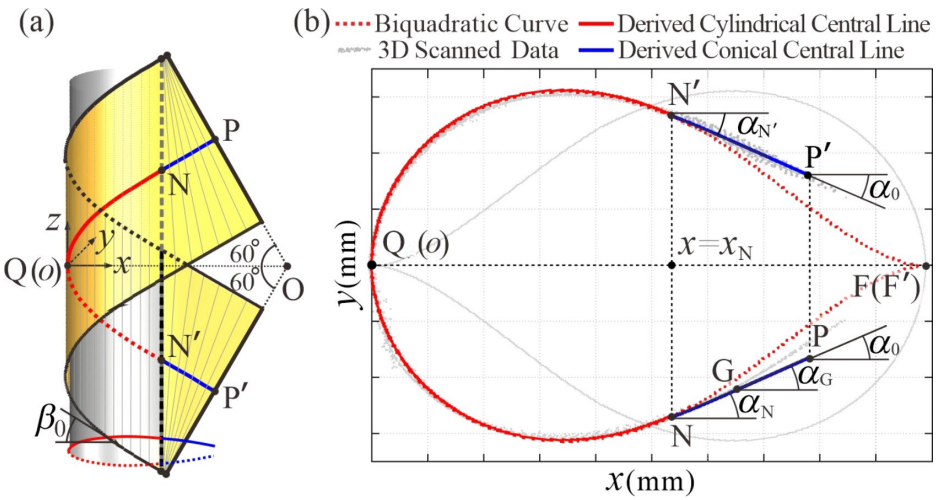

Fig. 4-7 Simplified geometrical model of one-third Möbius strip. (a) The detailed one-third geometrical model; (b) the flipped biquadratic curve FQF′ (red dotted line) symmetric to the *x*-axis. The center lines of the cylindrical surface NN′ (red solid line) and the conical surface NP, N′P′ (blue solid lines) of the geometrical model, and the corresponding center lines from 3D scanning (gray scattered data).

Consistent with experimental observations and the threefold rotational symmetry of the actuator, the teardrop-shaped curve FQF′ should be axially symmetric to the *x*-

axis with its sharp end normal to the line $x = 2a_{\mathrm{M}}$ and its blunt end tangent to the *y*-axis. Then the mathematical representation of this biquadratic oval curve can be determined with two unknowns a_{M}, b_{M} as

$$\left[(2a_{\mathrm{M}}-x)^2+y^2\right]^2 = 2a_{\mathrm{M}}(2a_{\mathrm{M}}-x)\left[(2a_{\mathrm{M}}-x)^2+y^2\right]-b_{\mathrm{M}}(a_{\mathrm{M}}y)^2,\ x\in[0,2a_{\mathrm{M}}]. \tag{4-16}$$

By fitting the teardrop-shaped curve with the experimental result, a_{M} and b_{M} can be respectively determined as 4.35 and 1.96, and the corresponding curve is drawn as a red dotted line in Fig. 4-7. By closely comparing the entire biquadratic curve FQ_3F' in red with the experimental gray scattered data, the deviation is mostly located at its sharp ends with nearly zero curvature. To solve this problem, the center line can be divided into three segments, NQN′ corresponding to the cylindrical region, NP and N′P′ corresponding to the conical ones.

Then, the center line NQN′ of the cylindrical surface is a helical spatial curve as expressed as follows, which projects onto the *xoy* plane as the biquadratic oval curve given in Eq. (4-16).

$$\begin{cases}\left[(2a_{\mathrm{M}}-x)^2+y^2\right]^2 = 2a_{\mathrm{M}}(2a_{\mathrm{M}}-x)\left[(2a_{\mathrm{M}}-x)^2+y^2\right]-b_{\mathrm{M}}(a_{\mathrm{M}}y)^2, \\ z = -\mathrm{sign}(y)\int_0^x \tan\beta_0\sqrt{1+\left(\mathrm{d}y/\mathrm{d}x\right)^2}\,\mathrm{d}x, \quad x\in[0,x_{\mathrm{N}}].\end{cases} \tag{4-17}$$

To this end, segments NP and N′P′ attached to curve NQN′ at points N and N′, respectively are modeled as clothoids characterized by a linearly varying curvature. To satisfy the curve continuity condition at points N and N′, the principal curvature κ_{N}, $\kappa_{\mathrm{N}'}$ and slant angle α_{N}, $\alpha_{\mathrm{N}'}$ should be consistent with Eq. (4-17), and the curvatures κ_{P}, $\kappa_{\mathrm{P}'}$ at the inflection point P and P′ are both zero. Then the principal curvature κ_{G} and slant angle α_{G} at any point G on segment NP can be expressed as

$$\kappa_{\mathrm{G}} = \kappa_{\mathrm{N}}\left(s_{\mathrm{GP}}/s_{\mathrm{NP}}\right), \tag{4-18a}$$

$$\alpha_{\mathrm{G}} = \alpha_{\mathrm{N}} + \frac{\kappa_{\mathrm{N}}{s_{\mathrm{GP}}}^2}{2\cos\beta_0 s_{\mathrm{NP}}}. \tag{4-18b}$$

The mathematical expression of curve NP can be derived as follows

$$\mathbf{G} = \begin{bmatrix}x_{\mathrm{G}}\\ y_{\mathrm{G}}\\ z_{\mathrm{G}}\end{bmatrix} = \begin{bmatrix}x_{\mathrm{N}} + \int_0^{s_{\mathrm{NG}}}\cos\alpha_{\mathrm{G}}\cos\beta_0\,\mathrm{d}s\\ y_{\mathrm{N}} + \int_0^{s_{\mathrm{NG}}}\sin\alpha_{\mathrm{G}}\cos\beta_0\,\mathrm{d}s\\ z_{\mathrm{N}} + s_{\mathrm{NG}}\sin\beta_0\end{bmatrix},\ s_{\mathrm{NG}}\in[0,s_{\mathrm{NP}}]. \tag{4-19}$$

Since that curve NP is rotationally symmetric to curve N′P′ about the *x*-axis, the coordination of any point G′ on N′P′ would be $\mathbf{G}'=\left[x_{\mathrm{G}},\ -y_{\mathrm{G}},\ -z_{\mathrm{G}}\right]^{\mathrm{T}}$. By combining Eqs. (4-17) to (4-19), the mathematical expression nave been derived for the center line. And, three undetermined parameters a_{M}, b_{M} and $x_{\mathrm{N}}(x_{\mathrm{N}'})$ are required to completely define the center line of the one-third actuator. Therefore, two additional geometrical parameters, the slant angle φ_{Q} and the maximum principal curvature κ_{Q} of the cylindrical point Q through the cylindrical point Q are measured experimentally and introduced here. The geometrical parameters α_0 and β_0 are determined by substituting φ_{Q} into Eq. (4-15). And the slant angle α_{N} at point N is given by Eq. (4-18).

$$\alpha_{\mathrm{N}} = \alpha_0 - \frac{\kappa_{\mathrm{N}} s_{\mathrm{NP}}}{2\cos\beta_0}. \tag{4-20}$$

With the obtained α_0 and β_0, the *y* coordinate of the inflection point P (P′) can be also worked out as follows.

$$z_{\mathrm{P}} = -z_{\mathrm{P}'} = \frac{l\sin\beta_0}{6},\ y_{\mathrm{P}} = -y_{\mathrm{P}'} = -\frac{l\sin\beta_0\tan\varphi_{\mathrm{Q}}}{6}. \tag{4-21}$$

When substituting $x_{\mathrm{Q}} = 0$ into Eq. (4-17), the maximum principal curvature κ_{Q} of the cylindrical point Q can be obtained as

$$\kappa_{\mathrm{Q}} = (4 + b_{\mathrm{M}})/4a_{\mathrm{M}}. \tag{4-22}$$

Once the three coefficients a_{M}, b_{M} and $x_{\mathrm{N}}(x_{\mathrm{N}'})$ are uniquely obtained by solving Eqs. (4-20) to (4-22), the center line PQP′ of the one-third Möbius strip is completely defined. Note that the arc length l_{NP} and $l_{\mathrm{N'P'}}$ should be slightly longer than $w\tan\beta_0/2$ to ensure that the conical surfaces have a trapezoid shape[107].

4.4.2 Extrusion of the Center Line

Based on the defined center line, we now extend it into the one-third strip surface based on the parametrization equations for a developable strip with a center line $\boldsymbol{r} = \left[x,\ y,\ z\right]^{\mathrm{T}}$ and width *w* in Fig. 4-8(a).

$$\begin{gathered}\boldsymbol{p}(s,d) = \boldsymbol{r}(s) + d\boldsymbol{g}(s) = \boldsymbol{r}(s) + d\left[\boldsymbol{b}(s) + \boldsymbol{t}(s)\tan\beta\right], \\ s \in \left[0,\ l/3\right],\ d \in \left[-w/2,\ w/2\right].\end{gathered} \tag{4-23}$$

in which *s* is the arc length along the curve from point P to point P′, and *d* is the geodesic distance to the center line. For a given ***r***, the unit tangent vector ***t*** and the unit normal ***n*** can be worked out. Hence, the only unknown parameter in Eq. (4-23) is the included

angle β between the generator ***g*** and the unit binormal ***b***.

For the cylindrical surface corresponding to NQN′, the generators are all parallel to the z axis and form a constant helical angle β_0. Thus this region can be directly extended from the center line by a width w, as highlighted in yellow, see Fig. 4-8(b).

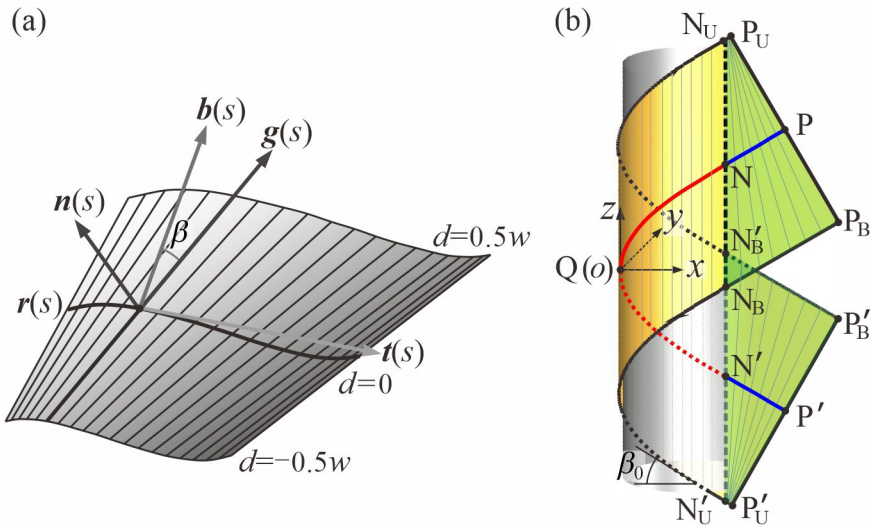

Fig. 4-8 The developable strip for the Möbius strip. (a) The developable strip composed of straight generators in the rectifying plane of unit tangent ***t***, normal ***n***, binormal ***b*** and generator ***g*** to the center line ***r***. The generators form an angle β with the tangent ***b***. (b) The one-third reconstructed cylindrical surface in yellow and conical surfaces in light green winding around the silver cylinder, extended from the fitted curve with a constant helical angle β_0.

However, for the trapezoidal conical surfaces in light green corresponding to NP and N′P′, the included angle β varies with s due to a series of non-parallel generators. Therefore, it is necessary to calculate its value subsequently.

Here, the distance from the conical apex K_G of an arbitrary point G on the curve NP to the tangent vector $\boldsymbol{t}_G$ passing through point G, referred to as D_G, is introduced to evaluate the conical degree of the generator at this point, see Fig. 4-9(a). Assuming G′ is a point with a small distance ds from G, the following equation can be obtained.

$$s_{G'G} = -D_G \tan\beta_{G'} + D_G \tan\beta_G, \tag{4-24a}$$

$$\frac{1}{D_G} = \lim_{s_{G'G}\to 0} \frac{\tan\beta_G - \tan\beta_{G'}}{s_{G'G}} = \frac{\mathrm{d}\tan\beta(s_G)}{\mathrm{d}s_G} = \sec^2\beta_G \frac{\mathrm{d}\beta(s_G)}{\mathrm{d}s_G}. \tag{4-24b}$$

The boundary conditions require continuity from the cylindrical surface to the

conical one at the segment point N. While at the inflection point P, the unit generator must lie along the width direction and its D_P should be longer than $0.5w$ for zero curvature on the generator.

$$D_N \to +\infty,\ \beta_N = \beta_0;\ \ D_P < w/2,\ \beta_P = 0. \tag{4-25}$$

According to Ref. [108], there exists a partition point M between points N and P, whose generator $\boldsymbol{g}_M$ must pass through the apex point P_U on the upper edge, and divides the conical surface NP into the nearly zero-curvature triangular area enclosed by M_BP_B, P_BP_U, and P_UM_B, and the conical trapezoidal surface enclosed by N_BP_B, P_BP_U, P_UN_U and N_UN_B. Here, D_M is $0.5w$, and the boundary condition of point M is

$$D_M = \frac{w}{2},\ \beta_M = \operatorname{atan}\left(\frac{2s_{MP}}{w}\right). \tag{4-26}$$

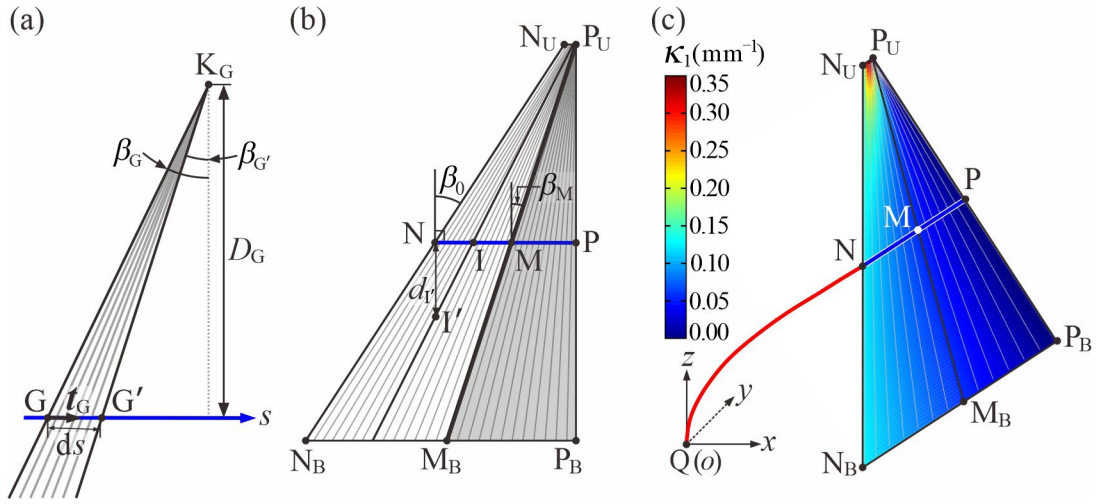

Fig. 4-9 The deduction of conical surface. (a) The schematic of geometrical parameter DG; (b) the developed conical surface $N_B'P_BP_UN_U'$ with straight generators; (c) the κ_1 contour map of the surface $N_B'P_BP_UN_U'$.

For any point I on the center line NM, the following relationship for D_I can be developed by combining geometrical analysis of the actuators with various geometrical configurations according to empirical fitting. Also, the tangent of angle β between the generator $\boldsymbol{g}$ and the unit binormal $\boldsymbol{b}$ can be integrated from Eq. (4-24) and satisfies Eqs. (4-25) and (4-26).

$$\frac{1}{D_I(s)} = \frac{2(1+\mu_D)}{w}\left(1 - \frac{1}{\sqrt[3]{K_D s + 1}}\right),\ s \in [0, s_{NM}]. \tag{4-27a}$$

$$\tan\beta_1(s)=\int\frac{1}{D(s)}\mathrm{d}s=-\frac{2(1+\mu_D)}{w}\left\{s-\frac{3}{2K_D}[(K_Ds+1)^{\frac{2}{3}}-1]\right\}+\tan\beta_0. \quad (4\text{-}27b)$$

where s is the arc length along the curve from point N, and K_D, μ_D are fitted proportional constant for the apex distance.

Here, μ_D can be obtained by experimental data. Then, substituting Eq. (4-27) into Eq. (4-26) at partition point M, the parameter K_D, s_{NM} can be determined.

$$K_D=\frac{(1+\mu_D)^3/{\mu_D}^2-\mu_D-3}{2s_{\mathrm{NP}}-w\tan\beta_0},\ s_{\mathrm{NM}}=\frac{1}{K_D}[(\frac{\mu_D+1}{\mu_D})^3-1]. \quad (4\text{-}28)$$

The maximum principal curvature $\kappa_{\mathrm{I}'}$ of any point I′ in the entire quadrilateral $\mathrm{N'_BP_BP_UN_U}$ can be derived as

$$\kappa_{\mathrm{I}'}=\kappa_{\mathrm{I}}/(1-\frac{d_{\mathrm{I}'}}{D_{\mathrm{I}}}). \quad (4\text{-}29)$$

Combining Eqs. (4-24) to (4-29), the conical region can be completely generated, and the corresponding contour map of the maximum principal curvature is shown in Fig. 4-9(c). Therefore, the sole unknown β of in Eq. (4-23) within the domain PQ and QP′ are expressed as the following piecewise functions.

$$\mathrm{PQ}:\ \beta(s)=\begin{cases}\operatorname{atan}(2s/w),\ [0,s_{\mathrm{MP}}]\\ \operatorname{atan}\left(\int_0^{s_{\mathrm{PN}}-s}\frac{1}{D(s)}\mathrm{d}s\right),\ [s_{\mathrm{MP}},s_{\mathrm{MN}}];\\ \beta_0,\ [s_{\mathrm{MN}},l/6]\end{cases} \quad (4\text{-}30a)$$

$$\mathrm{QP}':\ \beta(s)=\begin{cases}\beta_0,\ [l/6,l/3-s_{\mathrm{PN}}]\\ \operatorname{atan}\left(\int_0^{s-l/3+s_{\mathrm{PN}}}\frac{1}{D(s)}\mathrm{d}s\right),\ [l/3-s_{\mathrm{PN}},l/3-s_{\mathrm{PM}}].\\ \operatorname{atan}(2s/w),\ [l/3-s_{\mathrm{PM}},l/3]\end{cases} \quad (4\text{-}30b)$$

Therefore, substituting Eq. (4-30) into Eq. (4-23), the one-third surface PQP′ can be extruded from curve PP′ here. According to the threefold rotational symmetry, the entire threefold Möbius strip can be obtained now.

4.4.3 Validation of the Reconstructed Model

After obtaining the reconstructed geometry (Fig. 4-10(a)) via the aforementioned mathematical deduction in Sections 4.4.3, the reconstructed model was verified in

comparison with the scanned result of Möbius sample. It can be found that the distribution of the maximum principal curvature (κ_1) of the reconstructed model is highly consistent with the scanning results. Moreover, to quantitatively verify the accuracy of the geometrical model, distance deviation measured by the shortest distance between the geometrical and experimentally reconstructed surfaces was found to be within 0.20 mm for 91.7% of the area, see Fig. 4-10(b).

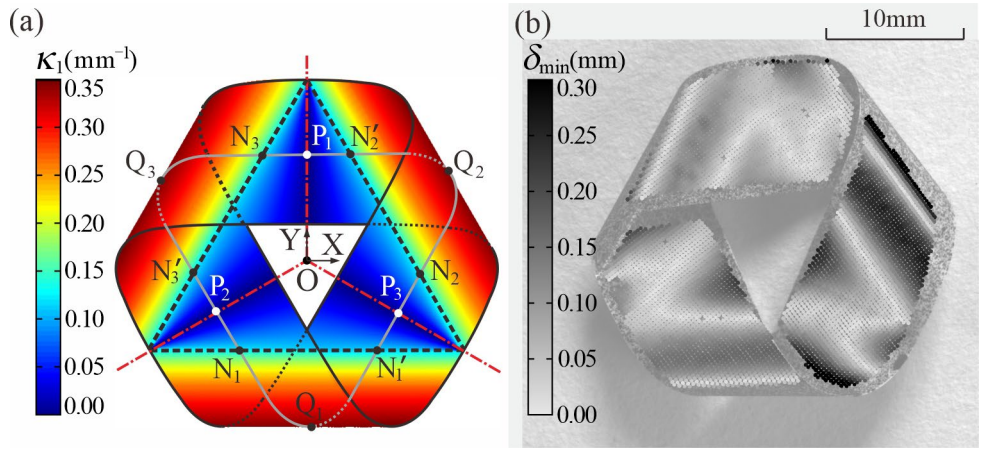

Fig. 4-10 Reconstructed model and verification of the Möbius sample (l = 56mm, w = 8mm, t = 25μm). (a) The κ_1 contour map of the geometrical model; (b) comparison of the geometrical model and the experimentally reconstructed Möbius strip.

4.5 Parametric Analysis of Structural Parameters

4.5.1 Effects on Geometrical Configurations

The derived theoretical model enables the prediction of geometric configurations of the Möbius strips across varying geometries. The key parameters for the strip considered include an aspect ratio l/w ranging from 5.5 to 8.0 and a width w varying from 6 to 10 mm. The dimensionless aspect ratio defines the curvature distribution of the Möbius strips, while w serves as a scale factor for actuators with identical aspect ratios. Given that the actuator thickness t is negligible compared to its length l and width w, the strip remains effectively inextensible, satisfying our theoretical model.

Here, the geometrical configurations of actuators with identical l/w are similar to each other with equal angles and proportional dimensions. Then, the introduced two parameters φ_Q, κ_Q should be parameterized and represented by w and l/w in advance.

For φ_Q, we build the relationship between the aspect ratio *l/w* and the introduced angle φ_Q by linearly fitting the average $\overline{\varphi}_Q$ of specimens with varying *w* and identical *l/w* as follows. The specific φ_Q of varying geometry, average $\overline{\varphi}_Q$ and fitted $\hat{\varphi}_Q$ are listed in Tab. 4-1.

$$\hat{\varphi}_Q = \left[11.7 + 0.6 \times \left(\frac{l}{w}\right)\right]\left(\frac{\pi}{180}\right), \quad \frac{l}{w} \in [5.5, 8.0]. \tag{4-31}$$

Substituting Eq. (4-31) into Eq. (4-15), the helical angle β_0 can also be completely represented by *l/w*.

$$\beta_0 = \cos^{-1}\left(\frac{\sqrt{3}}{2}\cos\hat{\varphi}_Q\right) = \cos^{-1}\left\{\frac{\sqrt{3}}{2}\cos\left[\frac{13\pi}{200} + \frac{\pi}{300}\left(\frac{l}{w}\right)\right]\right\}. \tag{4-32}$$

For the principal curvature κ_Q, we assume the inverse relationship between κ_Q and the projected arc length s_{QM}^{xy} of the curved center line QM on the *xoy* plane. By fitting the arc length of curve NP with the geometrical models of the actuators with varying $5.5 < l/w < 8.0$ and w = 6, 8, 10mm, μ is found to be 1/3. According to Section 4.4.2, the surfaces extruded from various curved center lines QM are similar to each other after removing the triangle area $\Delta P_U M P_B$ extended from curve MP. Accordingly, s_{QM}^{xy} can be calculated from Eqs. (4-26) to (4-28) as

$$s_{QM}^{xy} = (s_{NP} - s_{MP})\cos\beta_0 = \frac{l\cos\beta_0}{6} - \frac{7w\sin\beta_0}{2} + 6s_{NP}\cos\beta_0. \tag{4-33}$$

Referring to Ref. [108], the conical region of the actuator is a trapezoid approximate to a triangle with extremely short upper edge $N_U P_U$. By investigating the geometrical models of various Möbius samples, $w\tan\beta_0/20$ is taken as the average length of the upper edge $s_{P_U N_U}$, and substitute it into Eq. (4-34). Then the fitted curvature $\hat{\kappa}_Q$ can be also obtained from (4-35).

$$s_{QM}^{xy} = w\left[\left(\frac{l}{6w}\right)\cdot\cos\beta_0 - \frac{\sin\beta_0}{5}\right] = \frac{w}{12}\left[2\left(\frac{l}{w}\right)\cos\beta_0 - \frac{12}{5}\sin\beta_0\right], \tag{4-34}$$

$$\hat{\kappa}_Q = K_Q / s_{QM}^{xy}. \tag{4-35}$$

where the fitting constant K_Q=2.762 was determined by fitting the measured curvatures κ_Q of various reconstructed Möbius strips in Tab. 4-1. The fit yields an average R-square of 0.9817, confirming a close correlation of the fitted result.

Now, the two geometrical parameters φ_Q, κ_Q in Section 4.4.1 have been simply represented by *l/w* and *w.* Combining Eqs. (4-16) to (4-22), the center line of the one-third actuator can both be completely worked out without measurement. Thus, the entire geometry of Möbius strips can be extruded from the known center line by following mathematical deductions in Section 4.3.

As presented in Fig. 4-11, the curvature distributions of Möbius strips with varying dimensions *w* and *l/w*. The contours in the top row corresponds to threefold Möbius strips with a constant aspect ratio *l/w* of 7.0 and varying widths *w* of 6, 8, and 10 mm. Conversely, the other contours represent Möbius strips with a fixed width *w* of 8 mm and aspect ratios *l/w* of 5.5, 6.0, 6.5, 7.0, 7.5, 8.0.

Tab. 4-1 Measured and theoretical slant angle φ_Q, $\overline{\varphi}_Q$, $\hat{\varphi}_Q$ principal curvature κ_Q, $\hat{\kappa}_Q$ and tensile stress σ_T vs. *w* and *l/w*.

w (mm)	*l/w*	φ_Q (°)	$\overline{\varphi}_Q$ (°)	φ_Q^{THE} (°)	κ_Q (mm^{-1})	κ_Q^{THE} (mm^{-1})	σ_T (kPa)
6	5.5	14.86	15.04	15.00	0.6975	0.7004	4.398
6	6.0	15.25	15.27	15.30	0.6275	0.6346	3.712
6	6.5	15.66	15.62	15.60	0.5604	0.5803	3.184
6	7.0	16.02	15.87	15.90	0.5270	0.5346	2.769
6	7.5	16.21	16.21	16.20	0.5069	0.4958	2.436
6	8.0	16.33	16.46	16.50	0.4718	0.4623	2.164
8	5.5	15.19	15.04	15.00	0.4935	0.5253	2.474
8	6.0	15.38	15.27	15.30	0.4646	0.4759	2.088
8	6.5	15.47	15.62	15.60	0.4357	0.4352	1.791
8	7.0	15.85	15.87	15.90	0.3921	0.4010	1.558
8	7.5	16.34	16.21	16.20	0.3865	0.3718	1.370
8	8.0	16.71	16.46	16.50	0.3494	0.3467	1.217
10	5.5	15.08	15.04	15.00	0.3908	0.4202	1.583
10	6.0	15.18	15.27	15.30	0.3678	0.3808	1.336
10	6.5	15.75	15.62	15.60	0.3508	0.3482	1.146
10	7.0	15.74	15.87	15.90	0.3401	0.3218	1.018
10	7.5	16.08	16.21	16.20	0.3182	0.2975	0.877
10	8.0	16.34	16.46	16.50	0.2739	0.2773	0.779

∗ Data corresponding to unsteady motion are shaded in gray.

With the increase in both the aspect ratio l/w and width w, the maximum curvature κ_Q of any cylindrical point Q gradually decreases, while the quasi-planar region ($\kappa_1 <$ 0.10) expands from a narrow triangle into a pronounced trapezoidal area, which dramatically reduces the curvature gradient between points Q and P.

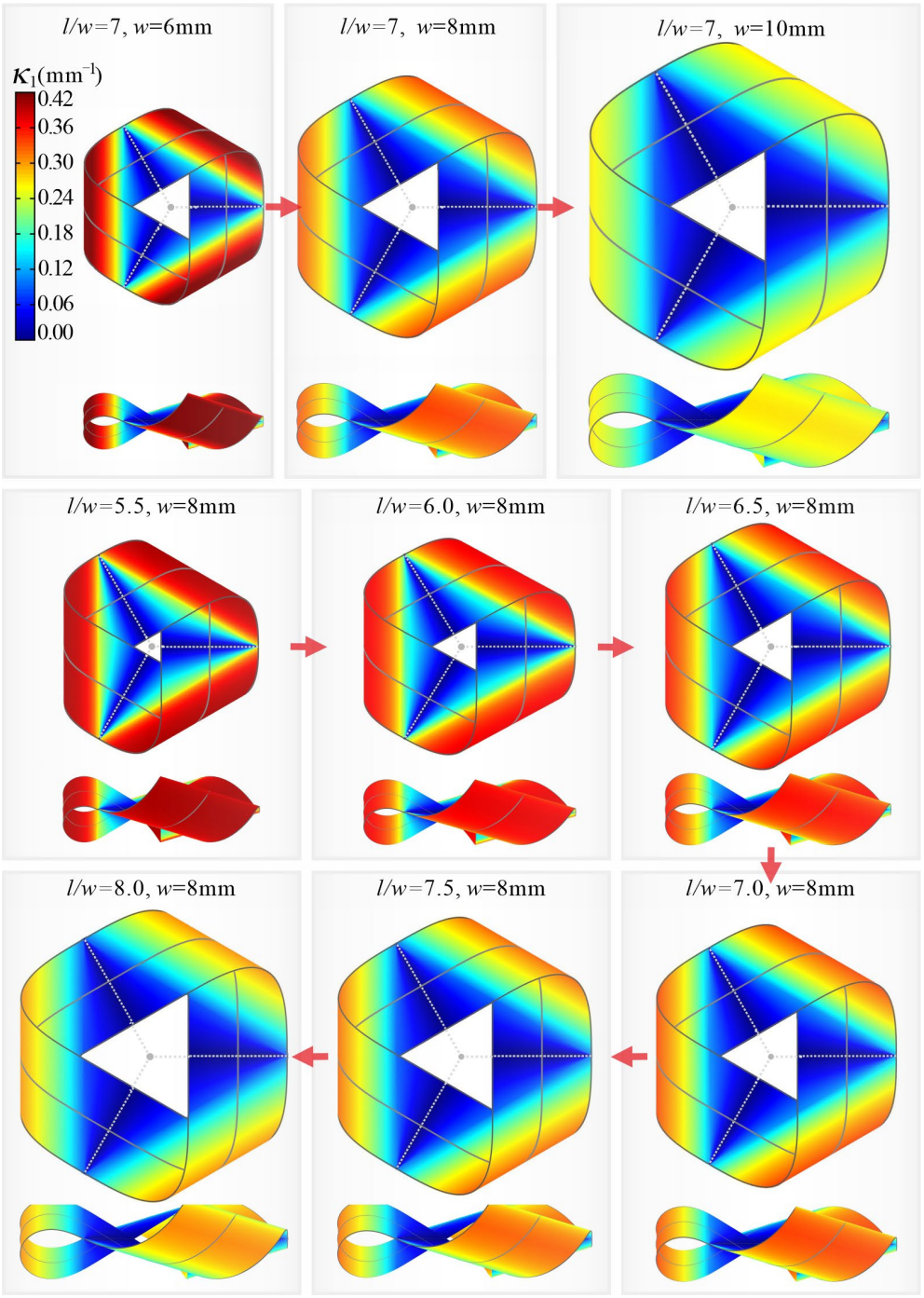

Fig. 4-11 The κ_1 contour of the Möbius strips of varying l/w = 5.5, 6.0, 6.5, 7.0, 7.5, 8.0 and w = 6, 8, 10mm in the OXYZ coordinate system.

4.5.2 Effects on Structural Looseness

Having obtained the geometrical configurations, the structural overall looseness arises primarily from the reduced tensile stress in the flattened conical regions and can be quantified by the tensile stress σ_{T} parameter at the inflection point P. According to the equilibrium of forces and moments, forces and moments on the cross section of the strip can be integrated as a resultant force system on the middle point of the section in Fig. 4-12.

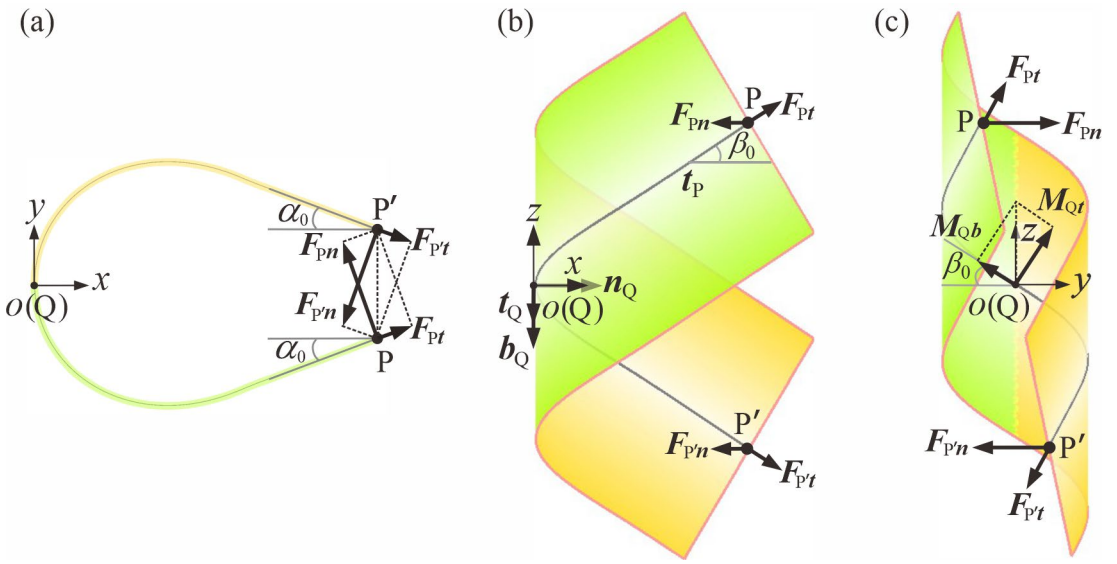

Fig. 4-12 Force and moment schematic of the one-third Möbius strip in the *oxyz* coordinate system. (a)The one-third actuator projected on the *xoy* plane; (b) the one-third actuator projected on the *xoz* plane; (c) the one-third actuator projected on the *yoz* plane.

According to the threefold rotational symmetry of the Möbius strip, the spatial force systems at the specific points Q, P and P′ should satisfy the following boundary conditions[108] in Eq. (4-36) respectively expressed under the Frenet-Serret framework in the *oxyz* coordinate system.

$$\mathrm{Q}: \boldsymbol{F}_{\mathrm{Q}\boldsymbol{n}} = \boldsymbol{0},\ \boldsymbol{M}_{\mathrm{Q}\boldsymbol{n}} = \boldsymbol{0},\ \eta_{\mathrm{Q}} = 0; \tag{4-36a}$$

$$\mathrm{P}: \boldsymbol{F}_{\mathrm{P}\boldsymbol{b}} = \boldsymbol{0},\ \boldsymbol{M}_{\mathrm{P}\boldsymbol{b}} = \boldsymbol{0},\ \kappa_{\mathrm{P}} = 0; \tag{4-36b}$$

$$\mathrm{P}': \boldsymbol{F}_{\mathrm{P}'\boldsymbol{b}} = \boldsymbol{0},\ \boldsymbol{M}_{\mathrm{P}'\boldsymbol{b}} = \boldsymbol{0},\ \kappa_{\mathrm{P}'} = 0. \tag{4-36c}$$

Substituting Eqs. (4-8) and (4-9) into Eq. (4-36), the moment $\boldsymbol{M}_{\mathrm{Q}}$ of point Q can be deduced with its direction parallel to the z-axis. The resultant forces $\boldsymbol{F}_{\mathrm{P}}$, $\boldsymbol{F}_{\mathrm{P}'}$ at the specific points P and P′ according to its rotational symmetry can be derived as

$$\boldsymbol{F}_{\mathrm{P}}+\boldsymbol{F}_{\mathrm{P}'}=\boldsymbol{0},\ F_{\mathrm{P}}=\left|\boldsymbol{F}_{\mathrm{P}}\right|=\left|\boldsymbol{F}_{\mathrm{P}'}\right|, \tag{4-37a}$$

$$\boldsymbol{F}_{\mathrm{P}}=\frac{2F_{\mathrm{P}}}{\sqrt{3}}\left[0,\ \cos\beta_0,\ \sin\alpha_0\sin\beta_0\right]^{\mathrm{T}}, \tag{4-37b}$$

$$\boldsymbol{F}_{\mathrm{P}'}=-\frac{2F_{\mathrm{P}}}{\sqrt{3}}\left[0,\ \cos\beta_0,\ \sin\alpha_0\sin\beta_0\right]^{\mathrm{T}}. \tag{4-37c}$$

where F_{P} denotes the value of the resultant force at the inflection points P and P′. According to boundary conditions in Eq. (4-36), the moments M_{P}, $M_{\mathrm{P}'}$ are orthogonal to the binormal vector with zero binormal vectors at P and P′. The moments $\boldsymbol{M}_{\mathrm{Q}}$, $\boldsymbol{M}_{\mathrm{P}}$ and $\boldsymbol{M}_{\mathrm{P}'}$ at the specific points Q, P and P′ can be derived in Eq. (4-38).

$$\boldsymbol{M}_{\mathrm{P}'}+\boldsymbol{M}_{\mathrm{P}}+\mathbf{PP}'\times\boldsymbol{F}_{\mathrm{P}'}=\boldsymbol{0},\ \boldsymbol{M}_{\mathrm{Q}}=\boldsymbol{M}_{\mathrm{P}}+\mathbf{QP}\times\boldsymbol{F}_{\mathrm{P}}. \tag{4-38}$$

Thus, the components of $\boldsymbol{M}_{\mathrm{P}}$ and $\boldsymbol{M}_{\mathrm{P}'}$ along the x, y, and z axes are given by

$$\begin{cases} M_{\mathrm{P}x}=M_{\mathrm{P}'x}=F_{\mathrm{P}}(-y_{\mathrm{P}}\tan\alpha_0\tan\beta_0+z_{\mathrm{P}}/\cos\alpha_0) \\ M_{\mathrm{P}y}=-M_{\mathrm{P}'y}=\dfrac{2F_{\mathrm{P}}x_{\mathrm{P}}\sin\alpha_0\sin\beta_0}{\sqrt{3}} \\ M_{\mathrm{P}z}=-M_{\mathrm{P}'z}=\tan\beta_0(\cos\alpha_0M_x^{\mathrm{P}}+\sin\alpha_0M_y^{\mathrm{P}}) \end{cases}. \tag{4-39}$$

Substituting Eq. (4-8) into Eq. (4-38), the resultant moment M_{Q} of Point Q can be deduced with its direction parallel to the z-axis. According to its geometrical features on its cylindrical point Q, the moment can be also expressed as

$$M_{\mathrm{Q}}=M_{\mathrm{Q}z}=M_{\mathrm{P}z}+\frac{2F_{\mathrm{P}}x_{\mathrm{P}}\cos\beta_0}{\sqrt{3}}=\frac{Ewt^3\kappa_{\mathrm{Q}}^{\mathrm{THE}}}{12}. \tag{4-40}$$

Combing Eqs. (4-25, 4-38, 4-39), F_{P} can be derived from the known M_{Q}.

$$F_{\mathrm{P}}=\frac{\sqrt{3}Et^3\hat{\kappa}_{\mathrm{Q}}}{2[K_{\mathrm{F}}(l/w)-1.2\tan\beta_0]\cos\beta_0}, \tag{4-41a}$$

where the constant K_{F} is

$$K_{\mathrm{F}}=\cos^2\alpha_0+\tan^2\beta_0+\frac{x_{\mathrm{P}}(\tan\alpha_0\sin\alpha_0+2\cos\beta_0)}{s_{\mathrm{QM}}^{xy}}. \tag{4-41b}$$

Therefore, the tensile stress σ_{T} of the inflection point P can be deduced from its tension components $F_{\mathrm{P}t}$ by dividing its sectional area from Eq. (4-37).

$$\sigma_{\mathrm{T}} = \frac{2F_{\mathrm{P}}\sin\alpha_0}{\sqrt{3}wt} = \frac{Et^2\hat{\kappa}_{\mathrm{Q}}\sin\alpha_0}{w[K_{\mathrm{F}}(l/w) - 1.2\tan\beta_0]\cos\beta_0}. \tag{4-42}$$

Our deduced equation (4-42) provides the theoretical tensile stress σ_{T} for the actuators listed in Tab. 4-1, with varying width *w* and aspect ratio *l/w*, given a fixed thickness *t* of 25μm and Young's modulus *E* = 2.902GPa, which indicates that the tensile stress σ_{T} decreases with increasing *w* and *l/w*.

4.6 Conclusions

In conclusion, precise geometric reconstruction of the threefold Möbius strip has been achieved by integrating experimental observations and theoretical derivation, which should satisfy boundary conditions based on threefold rotational symmetry. A complete parametric design framework has been established, laying a solid geometric foundation for subsequent investigation of humidity-driven motion in the next chapter. Moreover, the established framework provides a transferable modeling methodology for designing soft structures with complex topological features, enabling systematic coordination of geometry, mechanics, and stimuli-response. This integrative approach, combining differential geometry with material science, offers novel insights into the fundamental relationship between topological constraints and actuator functionality.

Chapter 5 Threefold Möbius Actuator

5.1 Introduction

Our investigation into the SBCTC system in Chapter 2 has revealed that shape preservation is an effective strategy for realizing a single-component SBCM. However, conventional driving strategies struggle with complex actuation challenges posed by the structural complexity of the threefold Möbius strip proposed in Chapter 4. Over the past decades, soft-matter actuators fabricated from stimuli-responsive materials can realize diverse controllable and programmable shape transformations in response to external stimuli, which holds great potential for intelligent autonomous systems and offers a novel approach to addressing actuation challenges. Particularly, certain soft actuators with uniquely designed geometries can exhibit periodic deformations and self-sustainable motions in response to unchanging stimuli to execute diverse tasks autonomously without any artificial control. When intelligent materials are combined with the SBCMs, the systems can sustain continuous motion while maintaining unchanged shape with constant total strain energy, thereby achieving the specific "zero-elastic-energy modes" (ZEEMs).

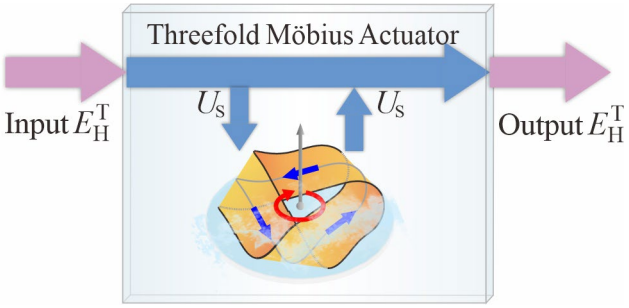

Fig. 5-1 Energy flow of the humidity-responsive Möbius actuator.

This chapter explores the humidity-responsive films with the threefold Möbius strip to develop actuators with self-sustainable locomotion under constant graded humidity. This system serves as a case study to tackle the complex actuation problem arising from the inherent structural complexity of a single-component statically balanced system. Moreover, an in-depth physical model is established to provide guidance for matching geometric design with the actuation strategy (Fig. 5-1), thereby allowing for the quantitative prediction of motion behaviors and the systematic optimization of its capabilities.

The outline of this chapter is structured as follows. In Section 5.2, the material properties and experimental setup of the Möbius actuator are elaborated. Section 5.3 presents the basic locomotion modes of the actuators, as well as its motion behaviors under varied environmental conditions in this section. Both standstill and dynamic states of the actuators are also compared here to verify their shape preservation. Then, in Section 5.4, a theoretical model based on moisture diffusion and developable surfaces is formulated to unveil the curvature-driven motion mechanism of these actuators. The parametric analysis of the geometric configurations and environmental conditions on local and global motions are both discussed in Section 5.5. Leveraging their self-sustainable motion, demonstrations including long-term motion, mechanical work output, and ambient humidity meter are further presented in Section 5.6. Finally, the conclusions and discussion are given in Section 5.7, and this section summarizes main findings in this chapter.

5.2 Material Properties of Agarose Film

As introduced in Section 1.2.5, agarose (AG) was selected and integrated with our Möbius strips to realize an optimal combination of ultra-fast humidity response speed, considerable actuation force and practical operational convenience[111]. When placed in a humid environment, the abundant humidity-sensitive hydroxyl groups in the agarose films combine with water molecules through hydrogen bonds with the oxygen atoms of the water molecules and release the chemical energy of the hydrogen bonds. The chemical energy subsequently triggers localized hygroscopic expansion in the film and makes it bend. When moisture evaporates, the film flattens back due to desiccation shrinkage by absorbing the chemical energy to break the hydrogen bond, see Fig. 5-2. The four-step preparation procedure for fabricating AG films of different colors and thicknesses is also summarized in Appendix A.

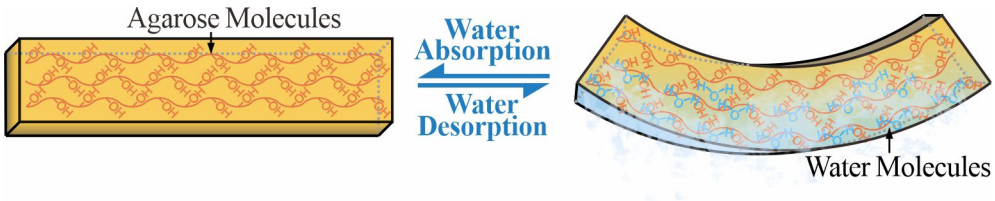

Fig. 5-2 Bending and unbending of the AG film by absorption and desorption of water molecules

According to Fick's first and second law of diffusion for steady diffusion[145], the diffusion flux is proportional to the magnitude of the concentration gradient of the steady-state diffusion. By analogy, the humidity absorption rate ξ of the AG film is also directly proportional to relative humidity gradient $\nabla RH = \mathrm{d}RH/\mathrm{d}Z$ at a constant room temperature of 25℃ and 1.0 standard atmosphere (atm), where the Z-axis is defined as pointing vertically upward from the humid substrate. Within the motion space Z_M of 15 mm above the substrate, RH_{sub} and RH_{up} are relative humidity of the substrate and upper surface of the motion space under a constant room temperature of 25℃ and 1.0 atm, respectively. The average humidity gradient $\overline{\nabla} RH$,as derived from Eq. (5-1) can be approximated as roughly equal to ∇RH.

$$\overline{\nabla} RH = \frac{RH_{sub} - RH_{up}}{Z_M} = \frac{\Delta RH}{Z_M}. \tag{5-1}$$

Here, ΔRH is relative humidity difference between RH_{sub} and RH_{up}, which is also theoretically proportional to the humidity absorption rate ξ.

To verify our theoretical derivation above, tests of the film bending performance were conducted in a humidity chamber (RiuKai, RK-TH-800L), maintaining ambient relative humidity RH_{am} around 35% under room temperature of 25℃ and 1.0 atm. Regardless of RH_{sub}, RH_{up} was consistently maintained at approximately 40%, which was 5% higher than RH_{am}. During operation, the device in Fig. 5-3(a) was utilized to periodically expose the flat strip (l_{AG} = 15 mm, w_{AG} = 5 mm, t_{AG} = 25 μm) to moisture for T_{AG} of 60 ms at a cycle of 8 s. The device was composed of a motor-driven disc featuring a 32 mm diameter hole covered with filter paper and rotated at a cycle of 8.0 s, a vessel below containing water at different temperature to modulate substrate humidity RH_{sub} from 40% to 95% and a horizontal arm to hold the AG film. The side view of the deformed strip after 60 ms exposure was captured by a high-speed HD camera (Zeiss Batis 135/3.5) in Fig. 5-3(b) and processed through circular fitting in MATLAB R2023a to obtain the average curvature $\overline{\kappa}_{AG}$ marked in blue in Fig. 5-3(c). The humidity absorption rate ξ per unit area normal to the humid source per unit time could be generally derived as

$$\xi = \frac{U_{S,bd}}{(l_{AG} w_{AG}) T_{AG}} = \frac{(\overline{\kappa}_{AG})^2 (t_{AG})^3}{12 T_{AG}}. \tag{5-2}$$

The red line in Fig. 5-3(c) indicates that the absorption rate ξ exhibits a roughly linear increase with ΔRH ranging from 5% to 55%, consistent with our deduction. Besides, a series of AG films with varying thicknesses t were tested and substituted into the exponential correlation with ξ in Eq. (5-3).

$$\xi = t^{0.5} K_{\xi} \Delta RH \ . \tag{5-3}$$

where K_{ξ} is a material constant characterizing the humidity absorption/desorption capability and in the value of 2.2326×10^{-4} N/mm^2, and is adopted in the following theoretical analysis.

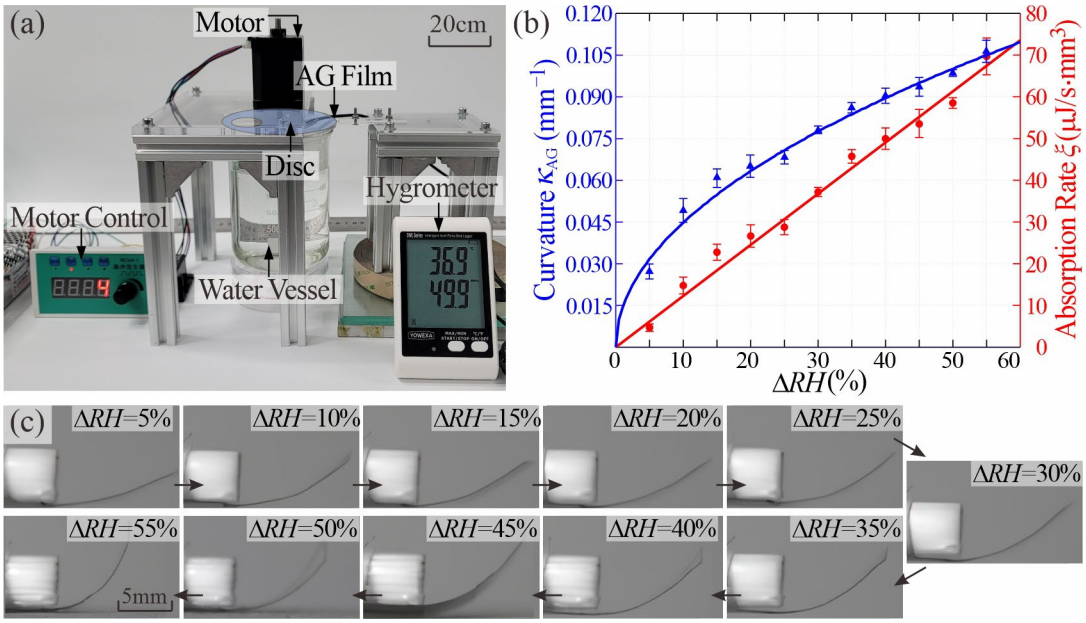

Fig. 5-3 Experimental setup of the bending response of the agarose film under different humidity. (a) The device composed of a motor-driven disc featuring a 32mm diameter hole covered by filter paper, a vessel filled with water, and a horizontal arm to hold the AG film; (b) the side view of the strip (l = 15 mm, w = 5 mm, t = 25 μm) at 60ms under humidity difference ΔRH from 5% to 55%; (c) humidity difference ΔRH vs. curvature and energy absorption rate.

Tensile tests of the 25μm AG film were performed on an Instron universal testing machine (Model 5943) at a rate of 5mm/min in RH_{am}=35% to obtain its mechanical properties. According to the resulting stress vs. strain curve, the AG film yields a Young's modulus E of 2.902 GPa, Poison's ratio v of 0.35, a fracture stress σ_F of 62.945 MPa, and a fracture strain ε_F of 0.309. Given that E of the AG film is close to

3.02 GPa of the polyformimide film, the elastic geometric configuration established in Chapter 4 can be directly applied.

5.3 Design and Motion of the Möbius Actuators

5.3.1 Fabrication and Experimental Setup

Similar to the fabrication process in Section 4.1, a Möbius actuator is fabricated by first cutting an humidity-responsive AG film into a rectangular strip with a length of $l + l_T$ and a width of w and a thickness of t by a laser cutter (Trotec Speedy 300), then attaching a double-sided adhesive tape (20 μm, 3M™ 9495LE) with tape length of l_T = 0.50 mm and width of w to one end of the film and subsequently twisting one end of the strip 180° anticlockwise or clockwise at each trisection point before adhering to the other end, thereby forming the left-handed (LH) and right-handed (RH) Möbius actuators with threefold rotational symmetry with the twisting angle α_{Tw} of 540°, see Figs. 5-4(a) and (b).

For a typical Möbius actuator (l = 56 mm, w = 8 mm, t = 25 μm), the weight of the film was 19.4 ± 0.8 mg, and the weight of the tape was 0.2 ± 0.1 mg leading to the total weight m_M of 19.6 ± 0.9 mg. Therefore, the dynamic influence of the adhesive tape to the Möbius actuator can be neglected. Additionally, low Young's modulus E (0.69 GPa) and minimal area of the tape also implies limited impact on the overall structural stiffness.

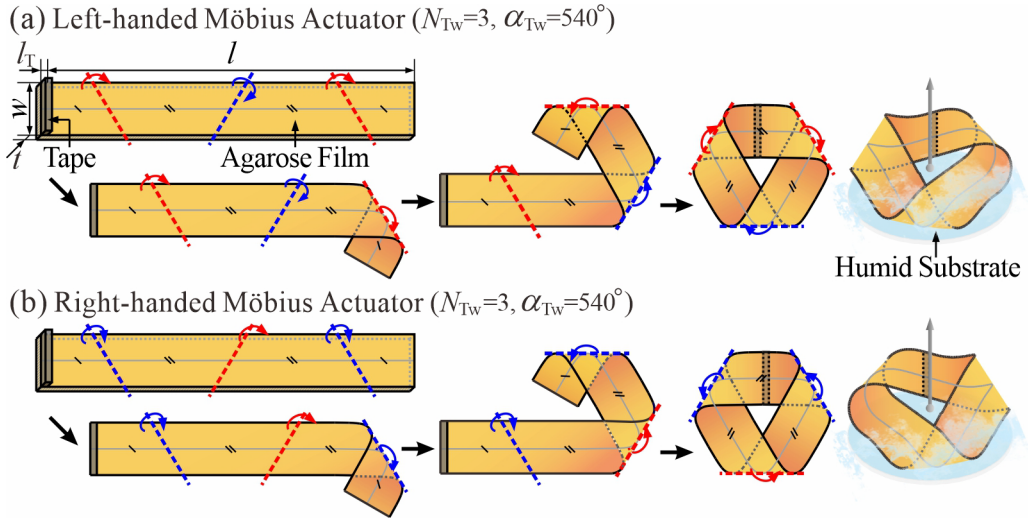

Fig. 5-4 The Möbius actuators fabricated from humidity-sensitive AG films. (a) and (b) threefold left-handed (LH) and right-handed (RH) Möbius actuators with twisting angles α_{Tw} of 540° respectively, where blue and red arrows represent the twisting directions.

The motion experiments of the Möbius actuators were conducted in the humidity chamber (RiuKai, RK-TH-800L) with latex operating gloves. Actuators with varying geometries were positioned on the circular filter paper (φ15, GB/T1914-2007) 30mm above the water level in the beaker. A metal filter mesh (φ15, 200 mesh numbers) was placed between the beaker and the filter paper to ensure the uniform humidification.

During operation, ambient RH_{am} in the humidity chamber was maintained around 35% at room temperature of 25℃ under 1.0 atm. Water in the beaker at temperatures ranging from 25℃ to 75℃ was utilized to tune RH_{sub} from 45% to 95% measured by a humidity sensor (±2%, Anymetre TH21E), which in turn established a relative humidity difference ΔRH of 5% to 55% for our experiments (Fig. 5-5(b)) and ensured adequate driving stimuli while preventing material dissolution due to excessive moisture.

Since RH_{sub} and RH_{am} remained constant during experiments, a steady-state diffusion was realized from the filter paper to the environment, thereby providing a constant humidity gradient. The motion of Möbius actuators was recorded by cameras (Canon EOS 70D), and the rotational rates were calculated through movies.

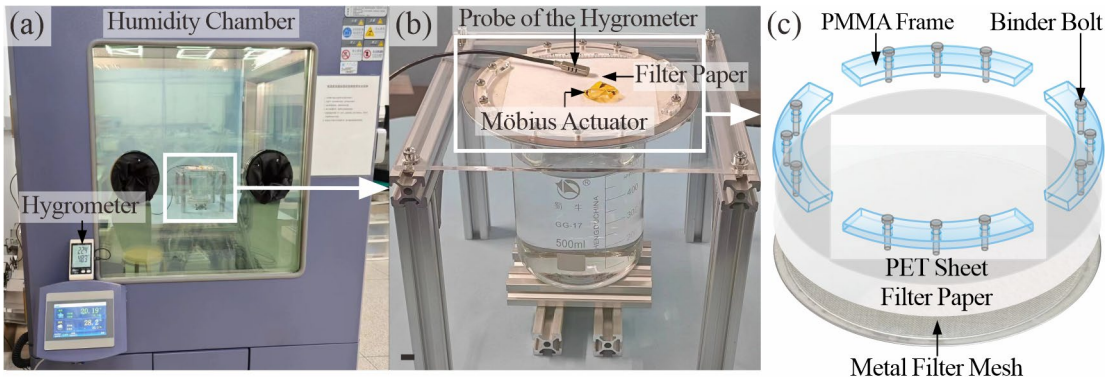

Fig. 5-5 Experimental setup for the humidity-driven Möbius actuators. (a) The humidity chamber to provide a constant humid environment with a hygrometer outside; (b) the Möbius actuator placed on a wet circular filter paper 30 mm above the water level in the beaker, and RH_{sub} constantly measured by the protruded probe of the hygrometer; (c) the humid substrate composed of a filter paper flatted by the polyethylene terephthalate (PET) sheet in the perimeter and a metal filter mesh, both of which are fixed to a circular plate by polymethyl methacrylate (PMMA) frames and PET sheets.

5.3.2 Motion of the Möbius Actuator

To elaborate the motion of threefold Möbius actuators, a right-handed specimen

with l=56 mm, w=8 mm, and t=25 μm was fabricated and placed on a humid substrate with RH_{sub} =90% and ΔRH=50%. Three numbers (1, 2 and 3) were drawn uniformly along the length of the Möbius strip to facilitate motion visualization. If tracking the movement of marked numbers and ignoring the relative movement between the actuator and the substrate, see Fig. 5-6(a), the material flows along the length of the strip through bending and unbending to adapt to the varying curvature of the Möbius actuator at different positions, which is similar to the motion of a conveyor belt. Hence, we call it "***local motion***". When each number passes through the three curved regions and returns to the nearly flat region, one cycle of local motion (T_L) is completed. Meanwhile, if taking the Möbius actuator as a whole in a hexagonal profile, it rotates clockwise about its central axis perpendicular to the substrate, which is thus referred to as "***global motion***" in Fig. 5-6(b). Once all six outer contour lines of the actuator are parallel to the reference black dashed line in turn, one cycle of global motion (T_G) is then completed. It is noted that due to the uneven humid substrate surface, some random translational motion of the actuator on the substrate is also observed.

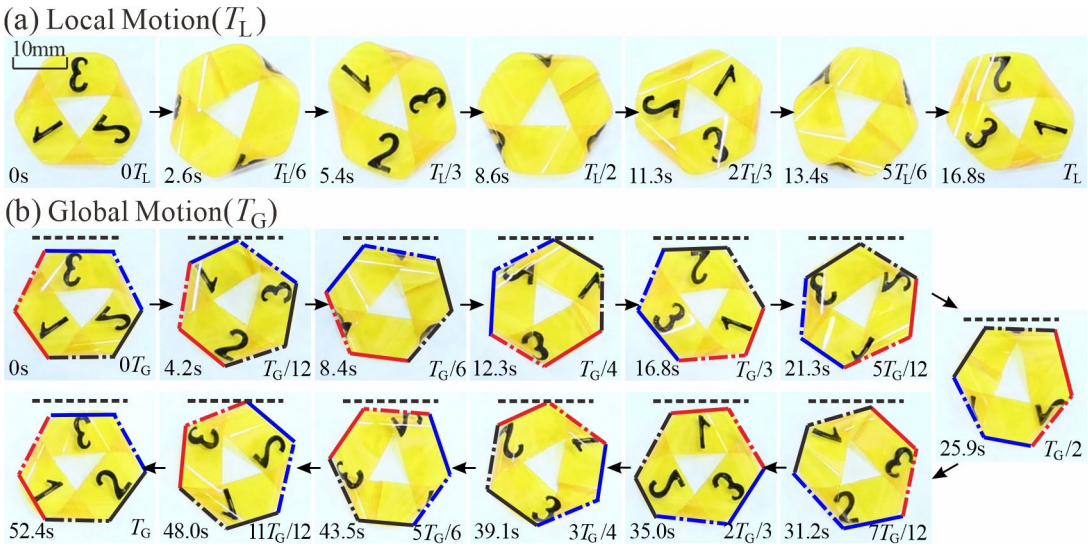

Fig. 5-6 Motion of the threefold Möbius actuator. (a) Local motion and (b) global motion of the Möbius actuator made from AG film (l = 56 mm, w = 8 mm, t = 25 μm) at RH_{sub} = 90% and ΔRH = 50%. The outline of the actuator is contoured by three pairs of solid and dotted dash lines, each in red, blue and black. A black dashed line is also introduced as a reference.

It is noteworthy that both the chirality of the Möbius actuators and the direction of humidity source influence its locomotion direction. Specifically, when placed on the

consistent humid substrate, a LH Möbius actuator exhibits clockwise global rotation, while the RH actuator rotates anticlockwise. Furthermore, when moisture originates from the top, the local and global motion directions of the Möbius actuator are both reversed, as indicated in Fig. 5-7.

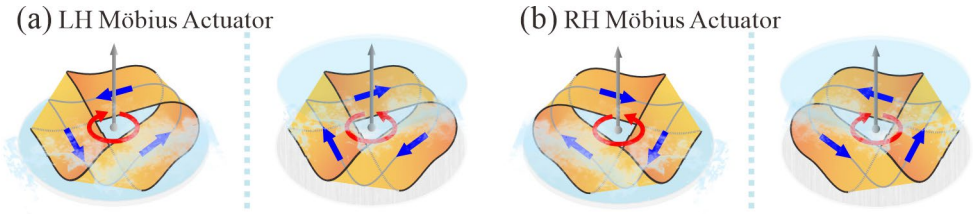

Fig. 5-7 Motion directions of the Möbius actuators. (a) The LH actuators and (b) the RH Möbius actuators driven by humidity from the substrate and the top, respectively. The cyan surfaces represent the source of humidity. The blue and red arrows represent the directions of local and global motions, respectively.

5.3.3 Comparison of the Static and Dynamic Configurations

As depicted in Fig. 5-6, the Möbius actuator maintained almost unchanged shape during motion through direct observation. For detailed verification, the DIC method mentioned in Section 4.2 was applied to track the geometrical configuration of the identical white actuator (l = 56 mm, w = 8 mm, t = 25 μm) in motion when placed on a humid substrate with RH_{sub} = 90%.

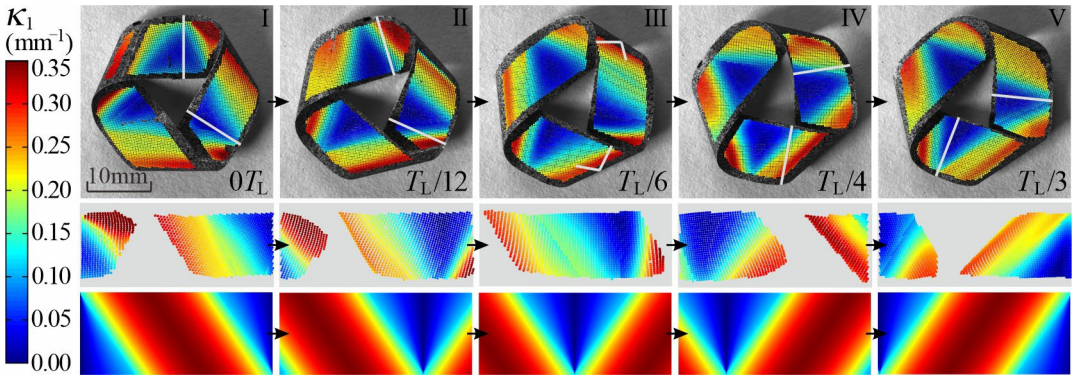

Fig. 5-8 The κ_1 contour map of the Möbius actuator (l = 56mm, w = 8mm, t = 25μm) during a one-third cycle of local motion in comparison with that of the corresponding geometrical model.

The configurations of the actuator contoured by κ_1 at 0, T_L/12, T_L/6, T_L/4, and T_L/3 are presented in Fig. 5-8, revealing that both the curvature distribution and overall

geometry nearly remain unchanged during motion. It clearly demonstrates their shape-preserving capability. Moreover, by further comparing dynamic and standstill curvature distributions in Fig. 4-10(a), the Möbius actuator can retain its shape in both static and dynamic states.

This conclusion is also echoed by comparing curvature distribution of one-third actuator bounded by the two gray lines in the developed strip and the corresponding reconstructed one derived from the proposed geometrical model in Section 4.2, from which a quantitative match is also observed.

5.4 Theoretical Model of Local and Global Motions

Having precisely reconstructed the geometry of the Möbius actuator in Chapter 2, we established a theoretical model to elucidate the underlying mechanism for the steady local and global motion of the Möbius actuator with shape preservation.

5.4.1 Theoretical Model of Local Motion

During local motion, all material elements must move along the length direction of the strip at a constant speed, v_{L}, otherwise the strip would be stretched or wrinkled. Subsequently, the energy method is adopted here to trace the energy transformation between chemical potential energy and mechanical energy during motion. Since the sum of gravitational potential and kinematic energies accounts for 0.38% of the strain energy U_{S}, the humidity energy E_{H} acts exclusively on the elastic deformation of the Möbius actuator. Moreover, to simplify our analysis, we assume that the AG films bend or unbend only by absorbing or desorbing moisture at the same rate ξ derived from Eq. (5-3) when facing towards or away the humidity source.

Next, consider transformation of an infinitesimal quadrilateral stripe in width of Δl (highlighted in blue) at point A in the cylindrical region N_3Q_3 (light blue area), see Fig. 5-9(a). At an arbitrary moment T, the stripe is located at any point A on the center line with a maximum principal curvature of κ_1^{T}. Considering negligible tensile strain, the strain energy $U_{\mathrm{S}}^{\mathrm{T}}$ of the selected stripe can be expressed as

$$U_{\mathrm{S}}^{\mathrm{T}} = \frac{EI\Delta l}{2}(\kappa_1^{\mathrm{T}})^2 = \frac{Ewt^3\Delta l}{24}, \tag{5-4}$$

where E is the Young's modulus of the AG film determined from the tensile experiment in Section 5.2, and $I = wt^3/12$ is moment of inertia of the stripe. At the moment T+ΔT,

it moves to the neighboring point A′ with a larger principal curvature $\kappa_1^{T+\Delta T}$. The increase in U_S^T is entirely attributed to environmental moisture it absorbs during a brief time interval ΔT. Then, the increase in strain energy of the stripe from T to T+ΔT is

$$\Delta U_S^T = U_S^{T+\Delta T} - U_S^T = \frac{EI\Delta l}{2}\left[(\kappa_1^{T+\Delta T})^2 - (\kappa_1^T)^2\right]. \tag{5-5}$$

Meanwhile, the stripe facing towards the humidity source absorbs the humidity energy ΔE_H^T during the time interval ΔT, as

$$\Delta E_H^T = \xi(w\Delta l\cos\theta^T)\Delta T, \tag{5-6}$$

in which, ξ is the moisture absorption/desorption rate per unit area normal to the humid substrate and proportional to the relative humidity difference ΔRH as derived in Section 5.2. θ^T is the included angle between the quadrilateral stripe around point A and the substrate plane in the detailed Fig. 5-9(b).

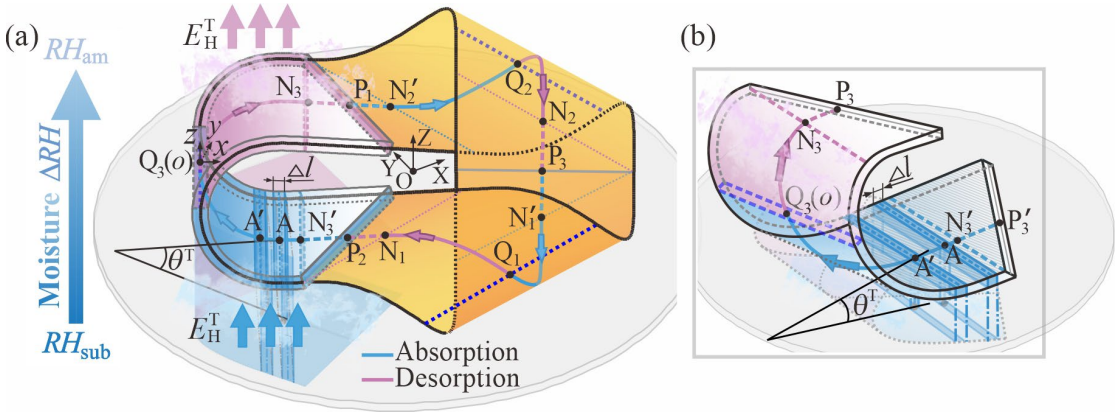

Fig. 5-9 Theoretical modeling of local motion. (a) Schematic overview of the humidity absorption (light blue area) and desorption (plum area) process of the Möbius actuator; (b) detailed view of the one-third Möbius actuator.

By combining Eqs. (5-5) and (5-6) and taking the derivative of the time T, we can obtain the following equation.

$$\frac{dE_H^T}{dT} = \frac{dU_S^T}{dT} = \xi(w\cos\theta^T) = \frac{Ewt^3}{12}(\kappa_1^T\frac{d\kappa_1^T}{dT}). \tag{5-7}$$

According to our geometrical model, the center line is a helical curve with the helical angle β_0, while the selected quadrilateral stripe at point A moves at a uniform

local speed v_L to point A′. Substituting $dT=ds/v_L$ and $\kappa_1^T=d\theta^T/(\cos\beta_0 ds)$ into Eq. (5-7) yields the following differential equation Eq. (5-8a).

$$\frac{d\theta^T}{ds}\left(\frac{d^2\theta^T}{ds^2}\right)=\frac{12\xi\cos\theta^T}{Ewt^3v_L}\cos^3\beta_0. \tag{5-8a}$$

By multiplying both sides by $d\theta^T/ds$ and integrating indefinitely, we can obtain

$$\int\left(\frac{d\theta^T}{ds}\right)^2\left(\frac{d^2\theta^T}{ds^2}\right)ds=\int\frac{12\xi\cos\theta^T}{EI^3v_L}\cos^3\beta_0 d\theta, \tag{5-8b}$$

$$\frac{1}{3}\left(\frac{d\theta^T}{ds}\right)^3=\frac{1}{3}(\kappa_I^T\cos\beta_0)^3=\frac{12\xi\cos^3\beta_0}{Ewt^3v_L}(\sin\theta^T+C). \tag{5-8c}$$

Here, C is the integration constant. The two undetermined parameters C and v_L can be solved by applying the principal curvatures κ_Q, κ_N and included angle θ_Q, θ_N at points Q_3, N_3 as boundary conditions.

$$Q_3:\ \kappa_1=\kappa_Q,\ \theta^T=\pi/2;\ N_3:\ \kappa_1=\kappa_N,\ \theta^T=\pi+\theta_N. \tag{5-9}$$

Then the local speed v_L and the absorption /desorption trajectory curve of the strip can both be derived in Eq. (5-8).

$$v_L=\frac{36\xi(1+\sin\theta_N)}{Et^3(\kappa_Q^3-\kappa_N^3)}; \tag{5-10}$$

$$\kappa_1=\frac{d\theta}{d(\cos\beta_0 s)}=\sqrt[3]{\frac{(\kappa_Q^3-\kappa_N^3)(-1+\sin\theta)}{1+\sin\theta_N}+\kappa_Q^3}. \tag{5-11}$$

When the stripe enters the cylindrical region Q_3N_3' (plum area) away from the humidity source, it also experiences gradual unbending process as it desorbs moiture at the same rate ξ. The principal curvature κ_N and included angle θ_N at the endpoints N_3' are equal to those at point N_3, which can also be described by Eq. (5-8).

And the local rotational rate n_L per minute can also be calculated as follows.

$$n_L=\frac{60}{l/v_L}=\frac{2160\xi(1+\sin\theta_N)}{Et^3(\kappa_Q^3-\kappa_N^3)l}. \tag{5-12}$$

With the known v_L derived from Eq. (5-10) calculates the local rotational rate n_L per minute by substituting the track length *l* of local motion. Herein, local motion of the actuator powered by the absorption and desorption of the environmental moisture has

been theoretically modeled. This model elucidates the intrinsic curvature-driven mechanism with shape preservation. Notably, the conical areas are deemed not to play a crucial role in the local motion due to the small curvature variation (κ_1 <0.10) in Fig. 4-10(b), and thus omitted in this theoretical analysis for simplicity.

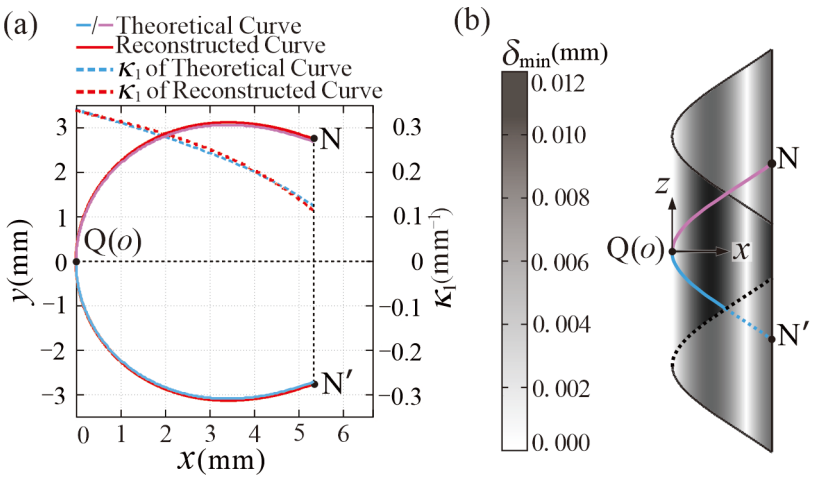

Fig. 5-10 Comparison of the theoretical and reconstructed geometry. (a) The derived theoretical curve NQN′ and the principal curvature κ_1 of cylindrical surface NQN′ during local motion; (b) the distance deviation δ_{min} between the reconstructed model and the theoretical model.

Utilizing the derived principal curvature κ_1, we not only reproduced the curved axis NQN′ and the extruded cylindrical surface NQN′ in Fig. 5-10, but also compared with the reconstructed result from Chapter 4, and the distance deviation δ_{min} between them is below 0.012 mm. This agreement further verifies the consistence of standstill and shape-preserving configurations in motion.

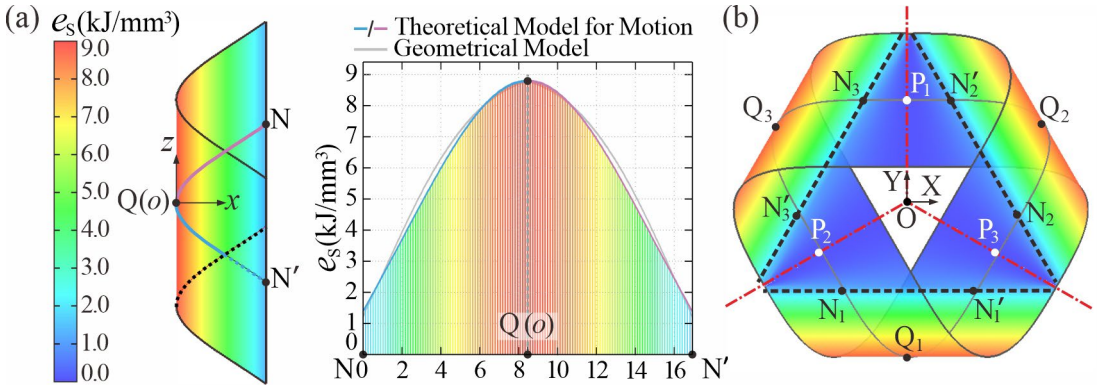

Fig. 5-11 The distribution of bending strain energy density e_S. (a) The e_S contour of cylindrical surface during local motion; (b) the e_S contour derived from the reconstructed geometry.

Additionally, we calculated the bending strain energy density $e_S = U_S^T / \Delta V$ of the strip at different positions of the cylindrical surface (Fig. 5-11(a)), where ΔV is the volume of the selected stripe. Comparing its e_S contour derived from the geometrical model in Fig. 5-11(b), a good match was obtained, further confirming that the actuator could maintain its shape during motion.

5.4.2 Theoretical Model of Global Motion

The global motion is driven by the rolling friction generated between the substrate and the actuator in convey-belt motion. When local motion initially occurs, kinetic friction forces are generated at the three contact points C, D and E as depicted in Fig. 5-12(a), and the direction of which are opposite to local velocity directions at the corresponding points. Owing to the threefold rotational symmetry of the actuator, three friction forces yields a zero resultant force, thus implying zero translational movement.

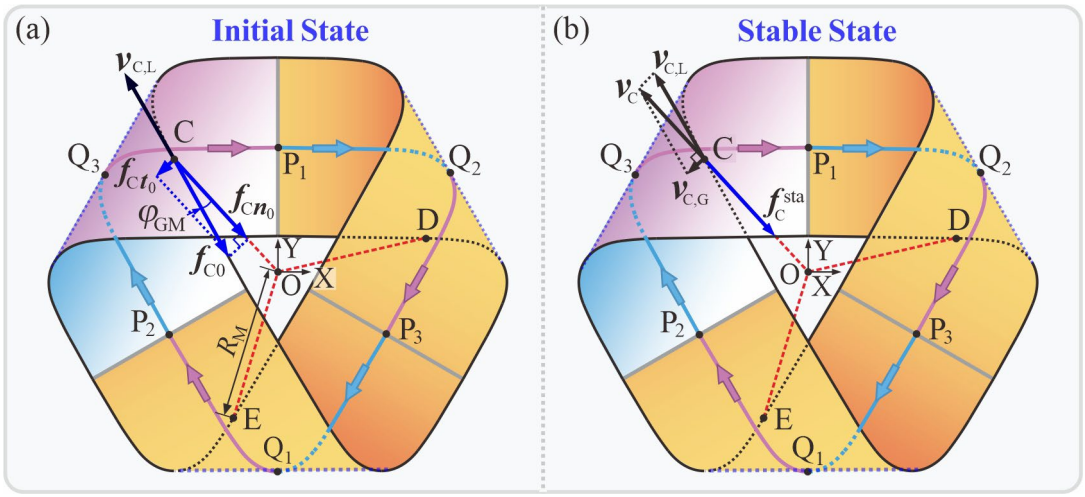

Fig. 5-12 Theoretical modeling of global motion. The force analysis of (a) the initial state, and (b) the steady motion state of the actuator from the top view.

Considering the contact point C as an instance, the tangential component f_{Ct_0} of the friction force f_C induces a global rotation, generating a global velocity. Initially, while f_C also changes simultaneously to maintain opposite to that of the resultant velocity $v_C = v_{C,L} + v_{C,G}$ at the contact point C. The global motion velocity $v_{C,G}$ continuously increases and becomes steady until the tangential component of the friction force f_{Ct_0} is zero, when the friction force f_C^{sta} points directly to the central point O as symmetrical centripetal forces. At this moment, the ratio of local motion

speed v_{L} and global motion speed v_{G} should be $1:\sin\varphi_{\mathrm{GM}}$, where φ_{GM} is the included angle between the line OC and the direction of $v_{\mathrm{C,L}}$ in Fig. 5-12(b).

The track of global motion is a circle around Point O with a radius of R_{C}, which is the distance from the center O to the contact points C, D, and E on the XOY plane. With the known v_{L} derived from Eq. (5-12), the global motion speed v_{G} and the global rotational rate per minute n_{G} can be readily derived, and the ratio of local to global rotational rate can be calculated by substituting $v_{\mathrm{G}} = v_{\mathrm{L}}\sin\varphi_{\mathrm{GM}}$.

$$\frac{n_{\mathrm{L}}}{n_{\mathrm{G}}} = \left(\frac{60}{l / v_{\mathrm{L}}}\right) / \left(\frac{60}{2\pi R_{\mathrm{M}} / v_{\mathrm{G}}}\right) = \frac{2\pi R_{\mathrm{M}}}{l\sin\varphi_{\mathrm{GM}}}. \tag{5-12}$$

It is noteworthy from Eq. (5-12) that $n_{\mathrm{L}}/n_{\mathrm{G}}$ is fully determined by the geometrical parameters of the actuator, irrespective of the environmental humidity. Moreover, the local motion of the actuator driven by absorption and desorption of the environmental humidity has been theoretically formulated.

5.4.3 Theoretical Ratio of Local and Global Motion

To obtain the relationship between the ratio $n_{\mathrm{L}}/n_{\mathrm{G}}$ of local and global rational rate and geometrical parameters *l* and *w*, the coordination of the contact point C can be first expressed in the *oxyz* coordinate system in Fig. 4-6.

$$\mathbf{C}' = \begin{bmatrix} x_{\mathrm{C}'} \\ y_{\mathrm{C}'} \\ z_{\mathrm{C}'} \end{bmatrix} = \begin{bmatrix} \dfrac{(2a_{\mathrm{M}}+3)-\sqrt{(b_{\mathrm{M}})^2+b_{\mathrm{M}}+1}}{2(b_{\mathrm{M}}+1)}a_{\mathrm{M}} \\ (2a_{\mathrm{M}}-x_{\mathrm{C}'})\sqrt{\dfrac{2x_{\mathrm{C}'}-a_{\mathrm{M}}}{3a_{\mathrm{M}}-2x_{\mathrm{C}'}}} \\ -\int_0^{x_{\mathrm{C}'}} \tan\beta_0\sqrt{1+\left(\dfrac{\mathrm{d}y}{\mathrm{d}x}\right)^2}\,\mathrm{d}x + \dfrac{w}{2\cos\beta_0} \end{bmatrix}, \tag{5-14a}$$

$$\boldsymbol{v}_{\mathrm{C,L}} = \left[v_{\mathrm{L}}\cos\beta_0,\ \ 0,\ \ v_{\mathrm{L}}\sin\beta_0\right]^{\mathrm{T}}. \tag{5-14b}$$

Following Eqs. (4-10) to (4-13) in Section 4.4.3, the coordination of point C′ can be transferred back to point C in the global OXYZ coordination. r_{Q} is defined as the distance from the origin O to any cylindrical point Q_i ($i = 1, 2, 3$).

$$\mathbf{C} = \boldsymbol{R}_{\mathbf{Z}}(-\varphi_{\mathrm{Z}})\boldsymbol{R}_{\mathbf{X}}(-\varphi_{\mathrm{X}})\left(\mathbf{C}' + \boldsymbol{T}_{\mathbf{M}}\right), \tag{5-15a}$$

$$\mathbf{C}=\begin{bmatrix}\mathrm{X_C}\\ \mathrm{Y_C}\\ \mathrm{Z_C}\end{bmatrix}=\begin{bmatrix}\dfrac{\sqrt{3}}{2}(-r_{\mathrm{Q}}+x_{\mathrm{C'}})+\dfrac{-y_{\mathrm{C'}}\sin\varphi_{\mathrm{Q}}+z_{\mathrm{C'}}\cos\varphi_{\mathrm{Q}}}{2}\\ \dfrac{-x_{\mathrm{C'}}+r_{\mathrm{Q}}}{2}+\dfrac{\sqrt{3}}{2}(-y_{\mathrm{C'}}\sin\varphi_{\mathrm{Q}}+z_{\mathrm{C'}}\cos\varphi_{\mathrm{Q}})\\ -y_{\mathrm{C'}}\cos\varphi_{\mathrm{Q}}-z_{\mathrm{C'}}\sin\varphi_{\mathrm{Q}}\end{bmatrix}, \tag{5-15b}$$

$$\boldsymbol{v}_{\mathrm{C,L}}=\boldsymbol{R}_{\mathbf{Z}}\left(-\varphi_{\mathrm{Z}}\right)\boldsymbol{R}_{\mathbf{X}}\left(-\varphi_{\mathrm{X}}\right)\boldsymbol{v}_{\mathrm{L}}^{\mathrm{C'}}=v_{\mathrm{L}}\begin{bmatrix}-\dfrac{\sqrt{3}\cos\beta_0}{2}+\dfrac{\sin\beta_0\cos\varphi_{\mathrm{Q}}}{2}\\ \dfrac{\sqrt{3}\sin\beta_0\cos\varphi_{\mathrm{Q}}}{2}+\dfrac{\cos\beta_0}{2}\\ \sin\beta_0\sin\varphi_{\mathrm{Q}}\end{bmatrix}. \tag{5-15c}$$

Therefore, the projected distance R_{M} from the origin point O to the contact point C on the XOY plane, and the included angle φ_{GM} between the vector $\overline{\mathrm{OC}}$ and the local velocity $\boldsymbol{v}_{\mathrm{L}}^{\mathrm{C}}$ can be represented in Eq. (5-16).

$$R_{\mathrm{M}}=\sqrt{\mathrm{X_C^2}+\mathrm{Y_C^2}},\ \varphi_{\mathrm{GM}}=\left|\mathrm{atan}(\frac{\mathrm{Y_C}}{\mathrm{X_C}})-\mathrm{atan}(\frac{\cos\beta_0+\sqrt{3}\sin\beta_0\cos\varphi_{\mathrm{Q}}}{-\sqrt{3}\cos\beta_0+\sin\beta_0\cos\varphi_{\mathrm{Q}}})\right|. \tag{5-16}$$

For actuators of identical ratio *l/w*, their geometrical configurations are similar to each other with equal angles and proportional dimensions. Therefore, R_{M} is also proportional to the strip width *w*, and φ_{GM} is constant. Substituting R_{M}, φ_{GM} and *l* into Eq. (5-13), it is concluded that the ratio of local to global rotational rate $n_{\mathrm{L}}/n_{\mathrm{G}}$ is uniquely determined by the aspect ratio *l/w*.

Substituting the geometrical parameters a_{M}, b_{M}, R_{M} and φ_{GM} obtained in Section 4.4.2 into Eqs. (5-14) to (5-16), the theoretical ratio $n_{\mathrm{L}}^{\mathrm{THE}}/n_{\mathrm{G}}^{\mathrm{THE}}$ for actuators in width *w* of 10mm are listed in Tab. 5-1.

Tab. 5-1 Theoretical ratio of local to global rate $n_{\mathrm{L}}^{\mathrm{THE}}/n_{\mathrm{G}}^{\mathrm{THE}}$ vs. *l/w*.

l/w	*w* (mm)	b_{M}	a_{M}	R_{M} (mm)	φ_{GM} (°)	$n_{\mathrm{L}}^{\mathrm{THE}}/n_{\mathrm{G}}^{\mathrm{THE}}$
5.5	10	3.671	2.170	8.87	11.69	5.004
6.0	10	4.007	2.103	9.16	14.61	3.801
6.5	10	4.336	2.039	10.33	16.26	3.466
7.0	10	4.559	1.978	10.59	17.79	3.118
7.5	10	4.975	1.920	10.72	19.55	2.684
8.0	10	5.287	1.864	10.87	28.01	1.795

5.5 Parametric Analysis of Local and Global Motions

With the derived theoretical model, effects of different structural, environmental and material parameters can be readily investigated on the local and global motion behaviors of the Möbius actuators.

First, consider the aspect ratio *l/w* ranging from 5.5 to 8.0 and width *w* ranging from 6 to 10 mm, while fixing the film thickness *t* of 25 μm. The substrate humidity RH_{sub} of 95% and ambient humidity RH_{am} of 35% were both maintained at room temperature of 25℃ and 1.0 atm, which controlled the relative humidity difference ΔRH of 55% as described in Section 5.2.1. Then, the film thickness *t* varied from 25 to 50 μm and the relative humidity difference ΔRH varied from 5% to 55% are also investigated here, the width *w* and aspect ratio *l/w* of the Möbius actuator are fixed at 8 mm and 7.0, respectively.

5.5.1 Classification of Steady and Unsteady Motion

Before parametric investigating of the motion characteristics, it is necessary to first determine whether its motion is regular, which is generally governed by aspect ratio *l/w* and width *w* according to our observation. As compared in Fig. 5-13, noticeable back-and-forth twisting of the actuators with irregular motion in a distorted hexagon contour replaced the regular convey-belt motion. This was accompanied by uneven time intervals between movements, collectively leading to the decreased local rotational rate n_{L}. Meanwhile, such irregular deformation was accompanied by uneven time intervals within each one-sixth of the local motion cycle T_{L}, collectively which also caused T_{L} fluctuated.

Here, to quantify motion stability, we introduce the parameter μ_{L} in Eq. (5-17), which is defined by recording any five consecutive local motion cycles $T_{\mathrm{L}j}$ (j = 1, 2, 3, 4, 5) of a specific specimen with a thickness *t* of 25 μm under a ΔRH of 55%.

$$\mu_{\mathrm{L}} = \frac{\max(T_{\mathrm{L1}}, T_{\mathrm{L2}}, T_{\mathrm{L3}}, T_{\mathrm{L4}}, T_{\mathrm{L5}})}{\min(T_{\mathrm{L1}}, T_{\mathrm{L2}}, T_{\mathrm{L3}}, T_{\mathrm{L4}}, T_{\mathrm{L5}})}. \tag{5-17}$$

For actuators with regular motion, the lower bound of μ_{L} is usually lower than 1.10 within the error of T_{L} less than 10%. However, for Möbius actuators exhibiting irregular motion, it can be observed that when μ_{L} exceeded 1.30, the actuator will illustrate its pronounced fluctuation. Its $T_{\mathrm{L1}}, T_{\mathrm{L2}}, T_{\mathrm{L3}}, T_{\mathrm{L4}}, T_{\mathrm{L5}}$ and corresponding μ_{L} of the Möbius actuators with irregular motion are listed in Tab. 5-2.

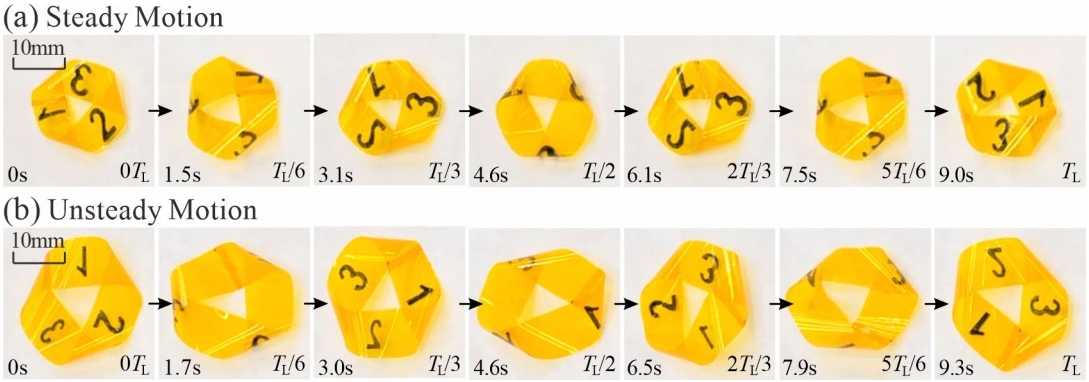

Fig. 5-13 Comparison of the Möbius actuator with steady and unsteady motion during one local motion cycle T_L. (a) Steady and shape-preserving motion with l = 56 mm, w = 8 mm and t = 25 μm. (b) Unsteady motion with significant shape distortion with l = 70 mm, w = 10 mm and t = 25 μm at RH_{sub} = 60% and ΔRH = 20%.

At w=6 mm, all actuators of varying aspect ratios exhibit regular local and global motion. For a width w of 8 mm and the aspect ratio l/w below 7.5, their motion is also consistent with the locomotion pattern depicted in our theoretical model. When l/w exceeds 7.0, the entire structure can hardly twist asymmetrically and keep conformal, breaking the continuous motion mechanism by humidity absorption and desorption. As w increases to 10 mm, the upper limit of the aspect ratio l/w decreases to 5.5 for steady motion.

Tab. 5-2 $T_{L1}, T_{L2}, T_{L3}, T_{L4}, T_{L5}$ and μ_L of the actuators with irregular motion vs. l/w and w.

w (mm)	l/w	T_L^1 (s)	T_L^2 (s)	T_L^3 (s)	T_L^4 (s)	T_L^5 (s)	μ_L
8	7.5	3.53	2.57	2.93	2.67	2.40	1.47
8	8.0	3.10	2.70	2.73	2.47	3.43	1.39
10	6.0	2.47	1.50	2.20	2.47	2.53	1.69
10	6.5	2.23	1.87	2.53	1.83	2.37	1.35
10	7.0	2.30	2.53	1.93	2.30	1.97	1.31
10	7.5	3.20	3.13	2.43	2.77	2.37	1.35
10	8.0	1.90	2.50	2.07	3.37	2.37	1.77

We reckon this unsteady motion is attributed to the insufficient internal stress in the structure to preserve the initial symmetric geometry of the Möbius actuator. To qualitatively quantify structural looseness, we employ the tensile stress σ_T of the cross section through the inflection points P_i (i = 1, 2, 3) with detailed calculation provided in Section 4.5.2. The tensile stress σ_T values for different structural parameters (listed in Tab. 4-1) reveal a critical lower threshold of 1.60 kPa for stable motion. For actuators

with σ_T below 1.60 kPa, the prestress in the Möbius actuators can hardly preserve its geometry to maintain the regular convey-belt motion, which causes the entire structure to twist with largely reduced n_L . For Möbius actuators with varied geometrical parameters, dimensionless aspect ratio *l*/*w* defines the curvature distribution, while strip width *w* can be regarded as a scale factor for the actuators with identical aspect ratios. As illustrated in the blue contour σ_T with the critical threshold $\sigma_T = 1.60$ kPa highlighted in Fig. 5-14(a), σ_T reduces with either increasing *l*/*w* or *w*, which defines upper design limits of width $w \leq 10$ mm and aspect ratio $l/w \leq 8.0$. Conversely, when *w* and *l*/*w* are too small, humidity response cannot overcome the excessive prestress to initiate regular motion, which also defines lower design limits of width $w \geq 6$mm and aspect ratio $l/w \geq 5.0$.

5.5.2 Effects of Structural Parameters

The theoretical local motion rate n_L^{THE} of the Möbius actuators can be obtained by substituting all the given variables except humidity energy absorption rate ξ into Eq. (5-10). By substituting RH_{sub} of 95% and ΔRH of 55% into Eq. (5-3), ξ takes the value of 54.6 J/(s·mm^2) for the AG film in thickness *t* of 25 μm. As shown in Fig. 5-14(a), the theoretical local motion rate n_L^{THE} (red contour) increases with both *l*/*w* and *w*. For actuators with identical *w*, increasing *l*/*w* results in a reduction in the maximum curvature κ_Q in the twisted region of the Möbius actuator. Hence, under identical humidity energy absorption efficiency ξ, it takes less time to accumulate the required bending deformation to pass through the flipped cylindrical region, which leads a larger local motion rate. For those with fixed *l*/*w* and varied *w*, since the magnitude of the curvature is inversely proportional to the scale factor *w* according to the definition of similar shapes, causing n_L^{THE} to increase in proportion to w^2 according to Eq. (5-13).

The global motion rate n_G^{THE} can be determined by first calculating the ratio of local and global motion n_L^{THE} / n_G^{THE} derived from Eq. (5-13). As deduced in Section 5.4.3, the ratio n_L^{THE} / n_G^{THE} is uniquely determined by the aspect ratio *l*/*w*. As shown in the yellow contour in Fig. 5-14(b), n_G^{THE} is also positively correlated with both *l*/*w* and *w*. For actuators with fixed *w*, increasing *l*/*w* leads to a declination of n_L^{THE} / n_G^{THE}, and consequently n_G^{THE} increases with *l*/*w* at a higher rate than n_L^{THE}. When fixing *l*/*w* and varying *w*, the geometric similarity implies that the dimensionless n_L^{THE} / n_G^{THE} remains

constant regardless of *w*. Therefore, the global motion rate n_G^{THE} holds the same scaling relationship with *w* as n_L^{THE}.

Here, n_L^{THE} and n_G^{THE} exist the utterly contrary trend to tensile stress σ_T, which demonstrates an upper bound for the motion rate. To achieve this bound, the design strategy is to select the largest feasible width *w* and aspect ratio *l*/*w*. Guided by this strategy, our Möbius actuator achieved the theoretical peak performance: the maximum n_L^{THE} of 26.13 r/min at *l*/*w* = 7.0 and *w* = 8 mm, and a maximum n_G^{THE} of 10.89 r/min at *l*/*w* = 6.0 and *w* = 10 mm.

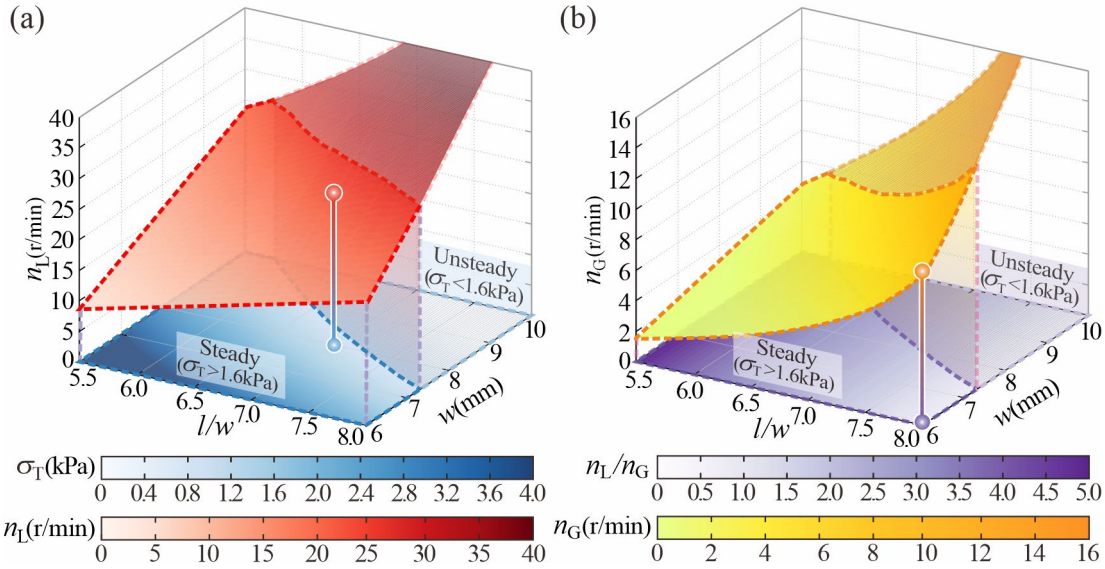

Fig. 5-14 The contour map of local and global motion. (a) The contour map depicted in red represents the theoretical local rotational rate (n_L^{THE}) varied with width w and length to width ratio *l*/*w*. The contour map depicted in blue represents the tensile stress σ_T. The local motion becomes unsteady when σ_T <1.60kPa. (b) The contour map depicted in yellow represents the theoretical global rotational rate (n_G^{THE}) varied with *w* and *l*/*w*. The contour map depicted in purple represents the ratio of theoretical local to global rotational rate (n_L^{THE}/n_G^{THE}). The maximum n_L^{THE} and n_G^{THE} are both marked in bars.

To validate our theoretical model, we further compared the experimental results from physical actuators against the theoretical predictions across a range of the above-mentioned parameters. In Fig. 5-15(a), the theoretical model predicts the experimental results with reasonable accuracy when *w* = 6 mm (relative error less than 15%). For *w* = 8 mm, a good prediction is yielded when *l*/*w* is less than 7.5. While at *w* of 10mm,

only the actuator with *l*/*w* = 5.5 matches the theoretical value. Notably, actuators that do not comply with the theoretical predictions were observed to lose threefold symmetric geometry and shape preservation during motion, but result in structural distortion and asymmetry. As a result, a noticeable back-and-forth twisting replaced the regulated convey-belt motion in Figs. 5-7(a) and (b), ultimately resulting in the reduced n_{L}. The experimental and theoretical local rotational rates of *w* and *l*/*w* are listed in Tab. 5-3. For actuators with steady motion marked in white shadow, the average R-square here is 0.8475, which reveals that the fitting is acceptable with the error range from 0.69% to 18.91% in comparison of n_{L} and $n_{\mathrm{L}}^{\mathrm{THE}}$. However, for actuators exhibiting irregular motion in gray shadow, the experimental local motion rate n_{L} falls below 70% of the theoretical value.

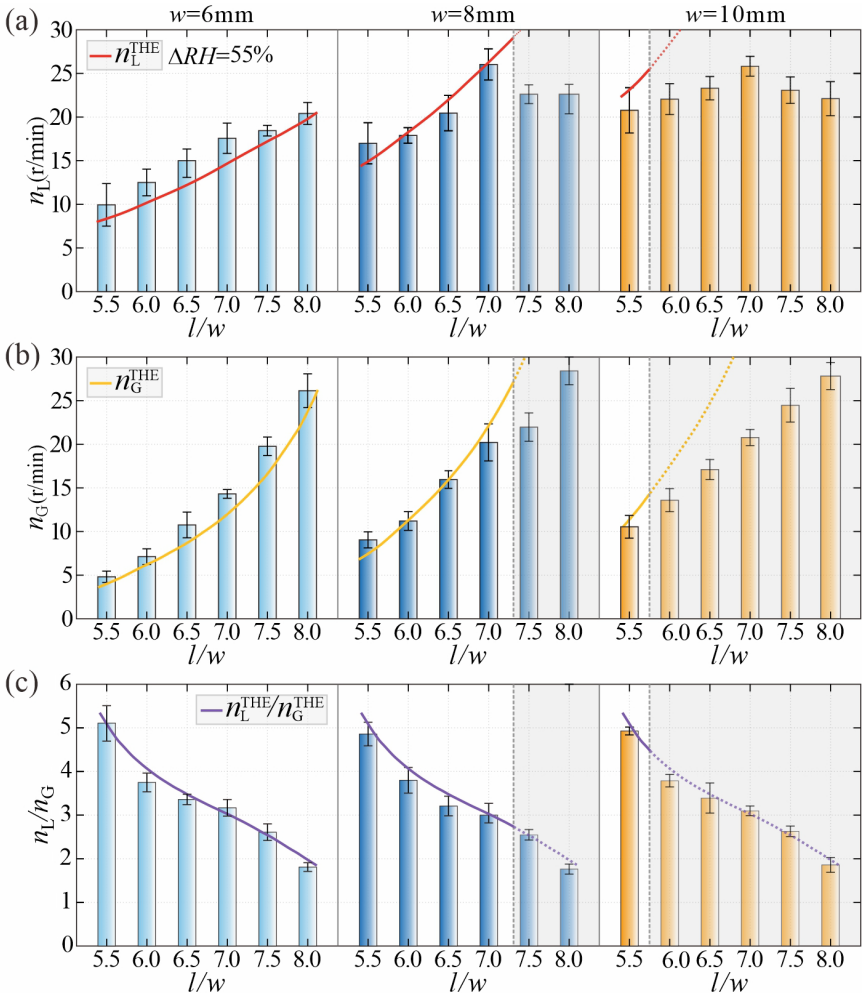

Fig. 5-15 Parametric analysis of the actuator motions with varied *l*/*w* and *w*. (a)-(c) The motion rates of the actuators with fixed film thickness *t* = 25 μm, and varied *w* and *l*/*w* at RH_{sub} = 95% and Δ*RH* = 55% in comparison with theoretical curves. (a) n_{L}; (b) n_{G}; (c) $n_{\mathrm{L}}/n_{\mathrm{G}}$.

In comparison of the experimental ratio n_L/n_G and theoretical ratio n_L^{THE}/n_G^{THE}, the maximum error is less than 10% in Tab. 5-3. Therefore, the theoretical global rotational rate n_G^{THE} can be derived from n_L^{THE} by dividing n_L^{THE}/n_G^{THE}, as listed in Tab. 5-3. Here, it can be noticed that for actuators with irregular motion in gray, the global rotational rate n_G is almost proportionally reduced to the decreased local rotational rate n_L. The average R-square of n_G^{THE} and n_G here is 0.9226 in white, which reveals that the fitting is acceptable with the error range from 1.19% to 20.91% in white. However, for those with irregular motion, the experimental global motion rate n_G only reaches at most 36.82% of the theoretical rate n_G^{THE}.

Tab. 5-3 Theoretical and experimental n_L, n_G and n_L/n_G vs. w and l/w when t = 25μm, ΔRH = 55%.

w (mm)	l/w	n_L^{THE} (r/min)	n_L (r/min)	n_G^{THE} (r/min)	n_G (r/min)	n_L^{THE}/n_G^{THE}	n_L/n_G
6	5.5	8.33	9.98 ± 2.44	1.68	1.93 ± 0.35	5.00	5.11 ± 0.40
6	6.0	10.27	13.82 ± 1.92	2.67	3.65 ± 0.63	3.80	3.75 ± 0.22
6	6.5	12.40	15.20 ± 1.63	3.73	4.96 ± 1.18	3.47	3.30 ± 0.06
6	7.0	14.72	17.48 ± 1.74	4.72	6.39 ± 0.40	3.12	3.17 ± 0.19
6	7.5	17.23	18.23 ± 0.30	6.55	8.29 ± 1.64	2.68	2.61 ± 0.19
6	8.0	19.92	19.03 ± 1.26	10.89	10.53 ± 1.55	1.80	1.81 ± 0.10
8	5.5	14.81	16.99 ± 2.36	2.98	3.45 ± 0.43	5.00	4.86 ± 0.27
8	6.0	18.26	17.91 ± 0.89	4.74	4.86 ± 0.86	3.80	3.80 ± 0.30
8	6.5	22.50	20.48 ± 2.03	6.03	6.39 ± 0.81	3.47	3.21 ± 0.23
8	7.0	26.13	25.95 ± 1.79	8.39	8.29 ± 1.70	3.12	3.05 ± 0.23
8	7.5	30.63	22.41 ± 1.08	11.64	8.83 ± 1.30	2.68	2.55 ± 0.12
8	8.0	33.83	20.82 ± 1.66	19.36	11.94 ± 1.27	1.80	1.76 ± 0.12
10	5.5	23.14	19.46 ± 2.60	3.97	4.67 ± 0.58	5.00	4.93 ± 0.09
10	6.0	28.53	22.07 ± 1.77	5.82	7.42 ± 1.06	3.80	3.79 ± 0.15
10	6.5	34.90	22.13 ± 1.34	6.85	9.42 ± 0.92	3.47	3.39 ± 0.35
10	7.0	40.89	25.66 ± 1.14	8.32	13.11 ± 0.37	3.12	3.10 ± 0.11
10	7.5	47.86	22.86 ± 1.52	8.86	18.19 ± 1.70	2.68	2.53 ± 0.12
10	8.0	52.86	20.78 ± 1.96	11.14	30.25 ± 1.24	1.80	1.86 ± 0.17

∗Data corresponding to unsteady motion are shaded in gray.

Thus, within the stable motion range of the current study, the optimal parameters l/w = 7.0 and w = 8 mm with the largest n_L can be selected. While, n_G is more significantly influenced by l/w, larger l/w of 8.0 and smaller w of 6mm are balanced here to achieve the maximum. Finally, as depicted in Fig. 5-15(c), the theoretical and

experimental ratios of n_L/n_G can keep in close agreement, regardless of whether the motion is shape-preserving or not.

5.5.3 Effects of Material and Environmental Parameters

In Figs. 5-16(a-c), the effects of film thickness t by selecting w = 8 mm and l/w = 7.0 in a humid substrate of RH_{sub} = 95% are investigated here. Here, the local motion rate n_L with its thickness t varied from 25 μm to 50 μm can be achieved by substituting Eq. (5-3) into Eq. (5-11). Due to its identical geometrical model, n_L^{THE}/n_G^{THE} remains constant 3.118. As expected, to overcome growing strain energy that scales with t^3, both motion rates n_L^{THE}, n_G^{THE} reduce with increasing t in accordance with the law of $t^{2.5}$ due to higher absorption/desorption rate ξ that scales with $t^{0.5}$. The R-square is 0.9692, indicating excellent agreement with experimental data. The maximum errors are 15.5% for n_L and 7.96% for n_G, see Fig. 5-16(c)

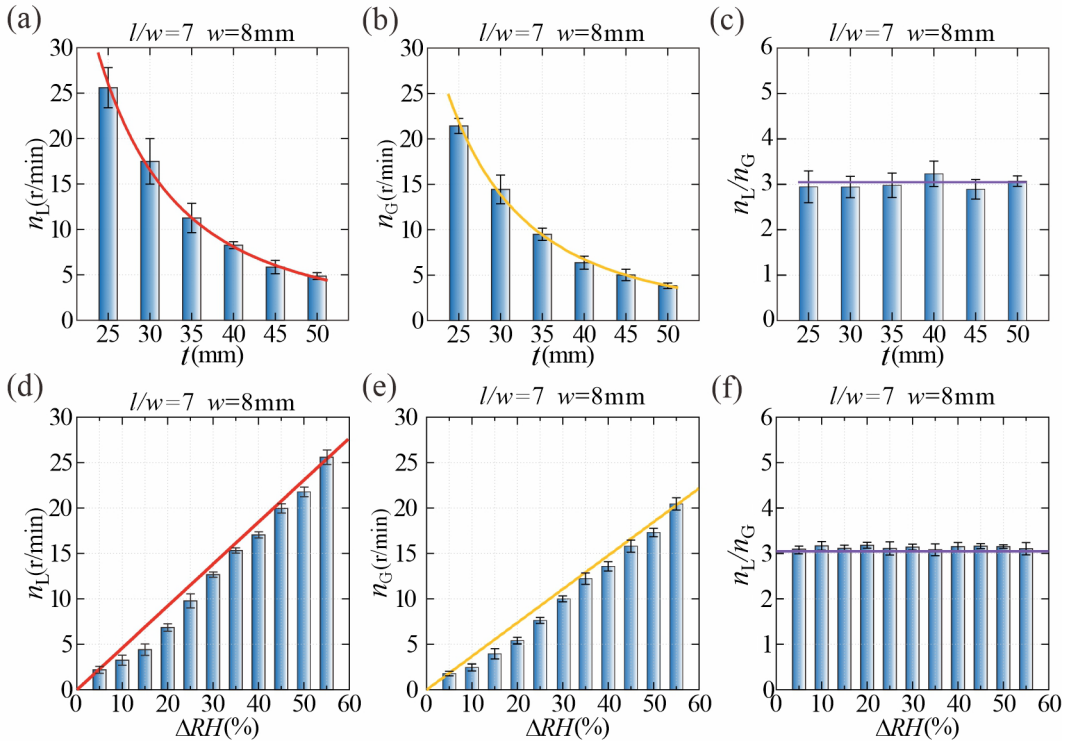

Fig. 5-16 Parametric analysis of the actuator motions with varied t and different ΔRH. (a)-(c) The motion rates of the Möbius actuator with fixed l = 56 mm and w = 8 mm, and varied t from 25 μm to 50 μm at RH_{sub} = 95% in comparison with theoretical curves: (a) n_L; (b) n_G; (c) n_L/n_G. (d)-(f) The motion rates of the Möbius actuator with fixed l = 56 mm, w = 8 mm, t = 25 μm, and varied ΔRH from 5% to 55% in comparison with theoretical curves. (d) n_L; (e) n_G; (f) n_L/n_G.

Tab. 5-4 Experimental and theoretical n_L, n_G and n_L/n_G vs. t when l/w = 7.0, w = 8 mm, ΔRH=55%.

t (μm)	n_L^{THE} (r/min)	n_L (r/min)	n_G^{THE} (r/min)	n_G (r/min)	n_L^{THE}/n_G^{THE}	n_L/n_G
25	26.13	25.40 ± 2.21	8.38	8.57 ± 0.34	3.12	2.96 ± 0.35
30	16.92	20.03 ± 2.51	5.42	6.82 ± 0.42	3.12	2.94 ± 0.24
35	11.71	11.21 ± 1.61	3.75	3.80 ± 0.27	3.12	2.96 ± 0.27
40	8.51	8.18 ± 0.39	2.73	2.55 ± 0.21	3.12	3.23 ± 0.28
45	6.43	5.82 ± 0.73	2.06	2.01 ± 0.25	3.12	2.89 ± 0.22
50	4.99	4.86 ± 0.36	1.56	1.59 ± 0.09	3.12	3.07 ± 0.12

Tab. 5-5 Experimental and theoretical n_L, n_G and n_L/n_G vs. ΔRH when l/w = 7.0, w = 8 mm, t = 25 μm.

ΔRH(%)	n_L^{THE} (r/min)	n_L (r/min)	n_G^{THE} (r/min)	n_G (r/min)	n_L^{THE}/n_G^{THE}	n_L/n_G
5	2.37	2.27 ± 0.39	0.76	0.71 ± 0.10	3.12	3.18 ± 0.09
10	4.75	3.24 ± 0.56	1.52	0.98 ± 0.16	3.12	3.27 ± 0.10
15	7.12	4.41 ± 0.63	2.28	1.58 ± 0.23	3.12	3.19 ± 0.07
20	9.50	6.85 ± 0.41	3.04	2.16 ± 0.15	3.12	3.18 ± 0.07
25	11.87	9.44 ± 0.78	3.81	3.05 ± 0.13	3.12	3.10 ± 0.15
30	14.25	12.68 ± 0.29	4.57	4.04 ± 0.13	3.12	3.14 ± 0.07
35	16.62	15.34 ± 0.29	5.33	4.89 ± 0.25	3.12	3.08 ± 0.13
40	19.00	17.06 ± 0.34	6.09	5.43 ± 0.21	3.12	3.15 ± 0.09
45	21.37	19.98 ± 0.51	6.85	6.32 ± 0.28	3.12	3.16 ± 0.06
50	23.75	21.80 ± 0.53	7.61	6.92 ± 0.19	3.12	3.15 ± 0.04
55	26.13	25.62 ± 0.99	8.37	8.18 ± 0.27	3.12	3.14 ± 0.14

Besides the geometrical parameters of the strip, the effect of relative humidity is also investigated using the identical Möbius actuator with w = 8 mm, l/w = 7.0, and t = 25 μm. The local and global rotational rates n_L, n_G increase proportionally with the humidity gradient within the range of ΔRH between 5% and 55%, see Figs. 5-16(d-f). Furthermore, a good agreement between theoretical and experimental motion rates n_L, n_G are achieved, while n_L/n_G remains unaffected with identical l/w. Notice that the Möbius actuator cannot be driven, when ΔRH is less than 5% and becomes rapidly over-hydrated when ΔRH exceeds 55%. The increased moisture absorption/desorption rate ξ in a more humid environment is consistent with Fick's laws of diffusion under a constant and infinite source[145], which further validates our deduction in Section 5.2.

As summarized in Tab. 5-5, the maximum deviations between experimental and theoretical results are 2.71 r/min for n_L, 0.82 r/min for n_G, and 0.18 for n_L/n_G. These deviations, obtained by applying ΔRH and ξ to Eq. (5-3) and Eq. (5-10), are acceptable, confirming the reliability of our theoretical model for actuators in varying humid environments.

5.6 Demonstrations of the Möbius Actuators

5.6.1 Demonstration of *Long-term Motion*

Sustaining continuous and reliable operation over a long period is crucial for actuators in ambient conditions. Here, the test of motion durability was conducted in the sealed chamber (RiuKai, RK-TH-800L) with latex operating gloves at room temperature of 25℃ with ambient RH_{am} of 30 ± 5% controlled by 200 g scattered silicone desiccants (Suzhou Shengda Desiccant Co., Ltd.) to maintain the humidity. Ambient water in the beaker below maintained RH_{sub} of the humid substrate at a steady level of 45 ± 5%, and this experimental setup is consistent with Fig. 5-5(b).

Given the limited humidity gradient, we chose the optimal geometric parameters for local motion, setting l/w=7.0 and w=8 mm, while further reducing the film thickness to t = 25 μm to facilitate the motion of the actuator. A monitor (Xiaomi, PTZ 2K) was applied here to record its motion simultaneously, and the flatness and humidity of the substrate were checked every 6 hours (Fig. 5-17(a)). Every 2 days, the discolored desiccant was replaced to maintain the RH_{am} in the chamber, and the water in the beaker was added to its initial level to compensate for its evaporation. The experiment of *long-term motion* started at 0 a.m. March 13, 2019, and finished at 12 p.m. March 23, 2019 in Tianjin, China. As shown in Fig. 5-17(b), the fabricated Möbius actuator stably rotated for 252 hours (over 10.5 days) and completed a total of over 47,500 local motion cycles, and the humidity-driven strip underwent more than 140,000 transitions between bending and unbending, dramatically outperforming existing soft self-sustainable actuators[171] in constant humid environments.

Notably, both n_L and n_G remain nearly constant during the prolonged process as shown in Fig. 5-17(c), while the local to global motion ratio n_L/n_G fluctuated slightly around the theoretical ratio of 3.112, further validating the superb shape preservation during long-term operation in Fig. 5-17(d). This result indicates that our actuator can

effectively harness plentiful atmospheric moisture for mechanical work, which validates the design strategy for self-sustainable actuators in practice and renders it an ideal solution to power untethered soft robots in nature. The detailed data of local and global motion rate n_L, n_G and the motion rate ratio n_L/n_G vs. time duration are listed in Tab. 5-6.

Tab. 5-6. n_L, n_G and n_L/n_G vs. Time Duration.

Time Duration (hours)	n_L (r/min)	n_G (r/min)	n_L / n_G	n_L^{THE} / n_G^{THE}
0	2.92 ± 0.05	0.96 ± 0.03	3.04 ± 0.07	3.12
6	3.16 ± 0.06	0.99 ± 0.03	3.21 ± 0.10	3.12
12	3.25 ± 0.03	0.99 ± 0.06	3.28 ± 0.09	3.12
18	3.20 ± 0.05	0.95 ± 0.07	3.35 ± 0.08	3.12
24	3.43± 0.05	1.11 ± 0.04	3.10 ± 0.04	3.12
30	3.11 ± 0.06	0.98 ± 0.10	3.20 ± 0.23	3.12
36	3.35 ± 0.07	1.05 ± 0.05	3.21 ± 0.12	3.12
42	3.42 ± 0.07	1.12 ± 0.03	3.05 ± 0.08	3.12
48	3.31 ± 0.06	1.07 ± 0.03	3.10 ± 0.08	3.12
54	3.17 ± 0.04	0.99 ± 0.05	3.20 ± 0.07	3.12
60	3.34 ± 0.08	1.09 ± 0.06	3.06 ± 0.14	3.12
66	3.33 ± 0.06	1.06 ± 0.06	3.14 ± 0.08	3.12
72	3.24 ± 0.02	1.05 ± 0.05	3.09 ± 0.14	3.12
84	3.17 ± 0.08	1.00 ± 0.05	3.17 ± 0.02	3.12
96	3.13 ± 0.06	0.99 ± 0.03	3.16 ± 0.16	3.12
108	3.27 ± 0.04	1.05 ± 0.02	3.11± 0.01	3.12
120	3.20 ± 0.08	1.02 ± 0.08	3.14 ± 0.09	3.12
132	3.14 ± 0.05	1.01 ± 0.03	3.13 ± 0.14	3.12
144	3.28 ± 0.03	1.04 ± 0.02	3.15 ± 0.04	3.12
156	3.17 ± 0.05	1.02 ± 0.05	3.11 ± 0.11	3.12
168	3.15 ± 0.07	1.03 ± 0.02	3.05 ± 0.13	3.12
180	3.03 ± 0.12	0.98 ± 0.07	3.11 ± 0.22	3.12
192	3.17 ± 0.10	1.05 ± 0.05	3.13 ± 0.14	3.12
204	3.16 ± 0.07	1.02 ± 0.04	3.08 ± 0.10	3.12
216	3.15 ± 0.04	1.04 ± 0.07	3.04 ± 0.13	3.12
228	3.23 ± 0.03	1.05 ± 0.04	3.07 ± 0.16	3.12
240	3.23 ± 0.03	1.03 ± 0.07	3.14 ± 0.18	3.12
252	3.22 ± 0.07	1.04 ± 0.02	3.08 ± 0.09	3.12

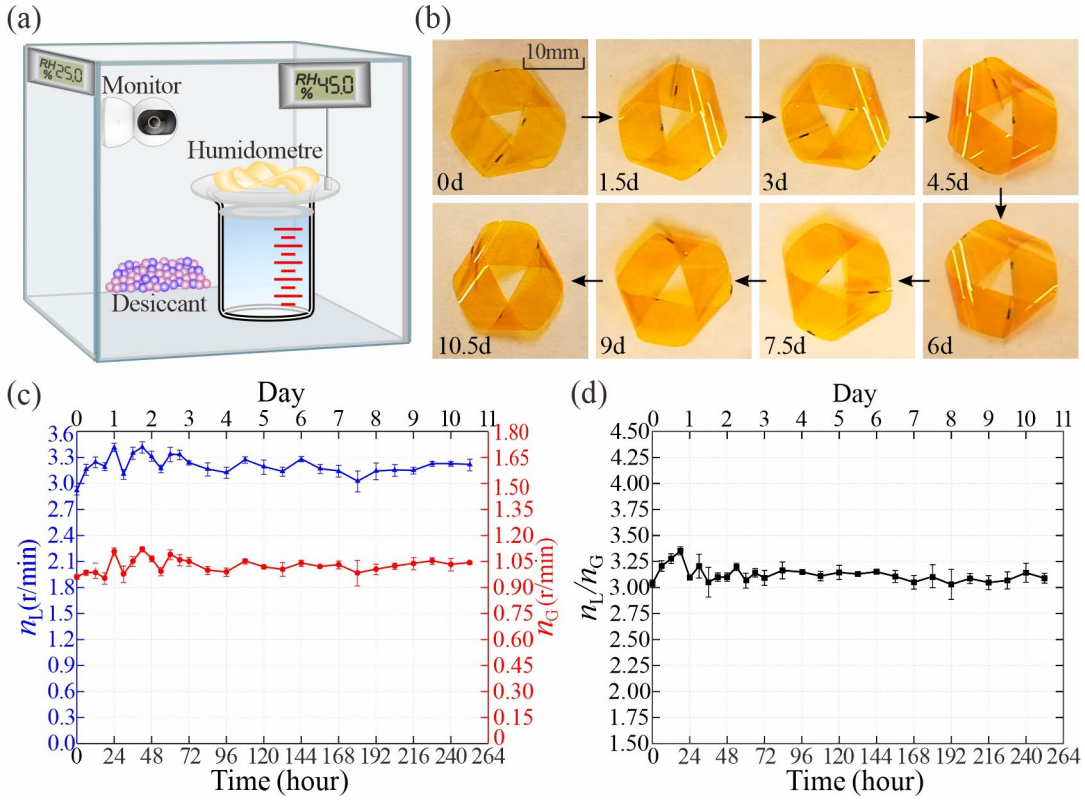

Fig. 5-17 Demonstration of *Long-term motion*. (a) Schematic of the experimental setup for a Möbius actuator (l = 56 mm, w = 8 mm, t = 20 μm) placed on a filter paper with RH_{sub} = 45% in a closed environment with ambient RH_{am} = 25% for 252 hours (10.5 days); (b) the motion process of the Möbius actuator during the entire time duration; (c) the local and global rotational rate n_L and n_G, and (d) their ratio n_L/n_G vs. time.

5.6.2 Demonstration of *Mechanical Work Output*

As a proof-of-concept application to output work, a series of paper disks with varying weights were designed and placed on top of Möbius actuators as shown in Fig. 5-18(a). Three symmetrical clips measuring 10 mm in length and 1 mm in width were integrated with a basic paper disk that possessed an outer radius R_D of 11.5 mm, an inner radius r_D of 1.5 mm, and a mass m_D of 20 mg. These clips engaged securely with the flipped corners of the actuator, thereby ensuring efficient transmission of global rotation of the actuator to the disk above. To adjust the total weight of the loaded paper disk, a series of disks fabricated from different materials were attached to the basic paper disk by pasting them together with small drops of white glue (M&G washable white glue ABJ97209) and fully dried in ventilated environment, as shown in Fig. 5-18(b). These disks were cut from lens paper (Kimtech, Delicate Task Wipers),

printing paper (Deli, Color Copy Paper No. 7391), and cardboard (Deli, Color DIY Cardboard No. 74804), with standard weights of 20, 40, and 80 mg respectively.

Then, the disks of weights (m_D) ranging from 40 to 200 mg at an interval of 20 mg were comprised of one paper disk with three symmetrical clips at the bottom and several weight disks on top. The weight error of the disk was limited to ±1 mg. Then the Möbius actuator and the disk were both through the plastic rob (2.40 mm in diameter, 120 mm in length, PLA Polymaker) with the clips of the disk stuck on the flipped corners of the actuator.

It was determined from experiment that the geometric parameters with the largest global motion rate led to an insecure engagement between the actuator and the disk due to the small width, and therefore the parameters of $l/w = 7.0$, $w = 8$ mm and $t = 25$ μm were selected instead for Möbius actuator ($m_M = 20$ mg). As the disk weight m_D increases from 40 mg to 200 mg, the rotational rate of the disk n_D identical to n_G monotonically decreases at $RH_{sub} = 90\%$ at a room temperature of 25°C and an ambient relative humidity RH_{am} of 35%, which controlled the relative humidity difference ΔRH of 50% (Fig. 5-18(c)). This is because under heavier disks, the maximum principal curvature κ_Q of the pressed actuator increases, which in turn causes reduction in global motion rate as described in Eq. (5-13). The experimental results demonstrate that the Möbius actuator can stably rotate while carrying a disk weighing up to 200 mg, 10 times of its own weight m_M, demonstrating the relatively strong actuation capability compared to other humidity-responsive actuators, as detailed in Tab. 5-7. The rotational rate (n_D) of the disk monotonically decreased with the weight of the disk (m_D), as illustrated in Fig. 5-18(d). The obtained kinetic energy E_D of the disk can be derived by Eq. (5-18), which is marked in a red solid line.

$$E_D = \int_{r_D}^{R_D} \frac{1}{2}\left[\frac{m_D}{\pi(R_D^2 - r_D^2)} 2\pi r \mathrm{d}r\right]\left(\frac{2\pi n_D r}{60}\right)^2 = \frac{m_D \pi^2 n_D^2}{3600}(R_D^2 + r_D^2). \quad (5\text{-}18)$$

Moreover, the kinetic energy of the disk E_D is found to first rise with the weight of the disk m_D, reaching its maximum 3.53×10^{-11} J at $m_D = 140$ mg, and then gradually drops to approximately 65% of its maximum. Here, excessive mass imposes a high dynamic load that suppresses rotational speed and hinders mechanical energy output. Furthermore, four disks of 40 mg, 80 mg, 120 mg, and 160 mg in weight were adopted in this demonstration to investigate the continuous mechanical work output of the

Möbius actuator. It has been discovered that the Möbius actuator can complete 156, 122, 43, 17 rotation cycles respectively under the four disks in Fig. 5-18(e). In the case of 40 mg and 80 mg, the Möbius actuators can roughly maintain the original shape after finishing their maximum rotation cycles.

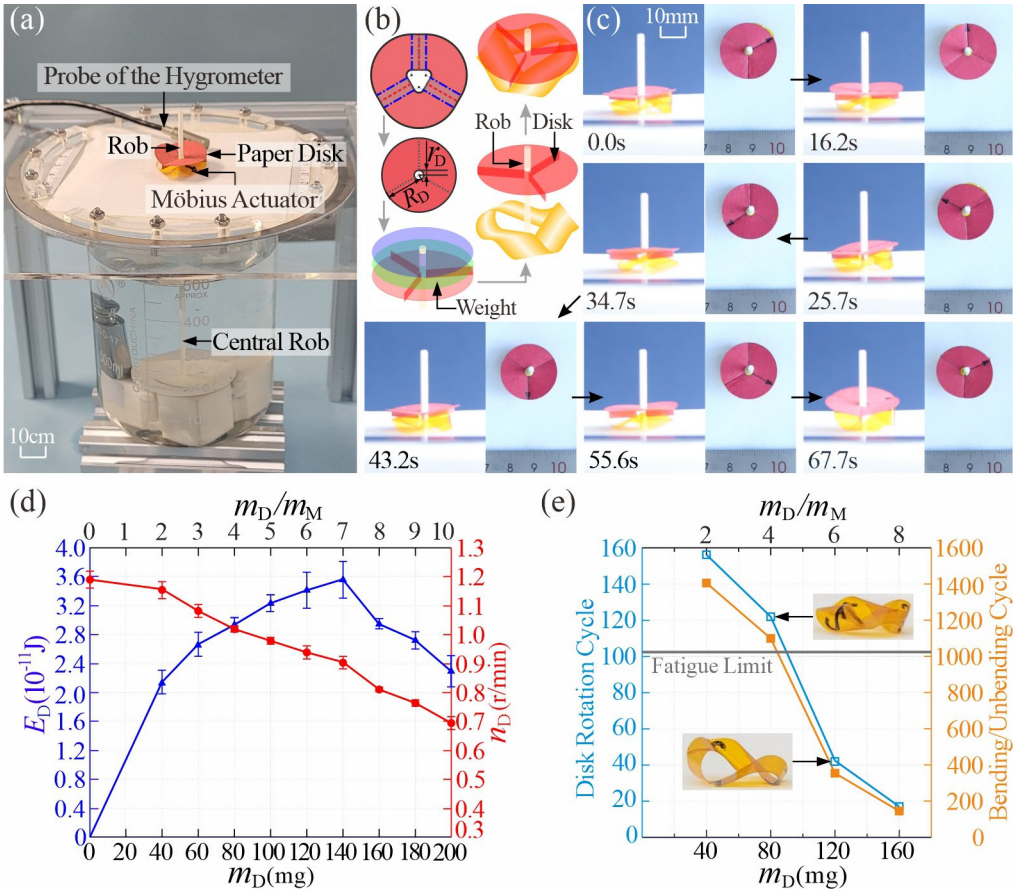

Fig. 5-18 Demonstration of *Mechanical Work Output*. (a) Experimental setup; (b) schematic assembly of the Möbius actuator and the paper disk above through the central PLA rob, and the developed slope of the paper disk; (c) motion of a paper disk with three clips (11.5mm in radius, m_D = 80 mg) placed on the top of a Möbius actuator (l = 56 mm, w = 8 mm, t = 25 μm) rotating around a rod in the center; (d) the kinetic energy E_D and rotation rate n_D of the disk varied with the mass of the disk m_D and the ratio to the actuator self-weight (m_D/m_M) at RH_{sub} = 90%; (e) the disk rotational cycle and film bending/unbending cycle varied with the mass of the disk m_D at RH_{sub} = 90%, with inside figures of the Möbius actuator after finishing the maximum rotation cycles of disks weighted 80 mg and after finishing the maximum rotation cycles of disks weighted 160 mg.

Having been proved in Section 5.2, the AG film can undergo more than 1000

transitions between bending and unbending, which approaches the reported fatigue life[174]. This result indicates that the ability of continuous work output is ultimately limited by the fatigue life of the AG film under specific humidity conditions. However, when the disk weights m_D increased to 120 mg and 160 mg, the actuator exhibited noticeable deformation and became closer to the filter paper, see the inner figure in Fig. 5-18(e), leading to film over-hydration before the intrinsic fatigue life, which caused the actuator to lose its original shape and reduce the disk weights m_D.

Tab. 5-7 n_D, E_D vs. w and m_D.

m_D (mg)	n_D (r/min)	E_D (10^{-11}J)
0	1.201 ± 0.0372	0 ± 0.0158
40	1.162 ± 0.0303	1.775 ± 0.0161
60	1.086 ± 0.0195	2.260 ± 0.0096
80	1.022 ± 0.0139	2.680 ± 0.0113
100	0.981 ± 0.0101	3.176 ± 0.0242
120	0.939 ± 0.0199	3.259 ± 0.0247
140	0.906 ± 0.0194	3.535 ± 0.0068
160	0.813 ± 0.0047	3.406 ± 0.0116
180	0.764 ± 0.0105	3.333 ± 0.0210
200	0.694 ± 0.0214	3.275 ± 0.0159

5.6.3 Demonstration of *Ambient Humidity Meter*

In addition to performing mechanical work, the Möbius actuator can accurately sense ambient humidity RH_{am} when maintaining RH_{sub} around 90% controlled by 60℃ hot water 30mm below the wet filter paper. To achieve rapid humidity detection, we also selected geometric parameters with the largest local motion rate, l/w = 7.0, w = 8 mm, t = 25 μm. Three black striped markers were evenly drawn with a 0.5 mm fine liner along the strip length as recognized features here for actuator vision.

All the sensory experiments of the Möbius actuators were conducted in the humidity chamber (RiuKai, RK-TH-800L) with varying humidity of 20%, 35%, 50%, 65%, and 80% at a constant temperature of 25℃ and pressure of 1.0 atm. It should be noted that during the experimental process, the ventilation system in the humidity chamber needs to turn off to avoid blowing the actuator away which inevitably causes the set humidity in a short time, especially when it exceeds 50%. Therefore, once the

actuator starts its stable operation, the entire image acquisition process should be controlled within 2 minutes to feedback with relatively accurate ambient humidity RH_{am}. When measuring the indoor humidity of the laboratory, the experimental duration can be extended to 4 minutes as long as the humidity RH_{sub} of the substrate maintains over 90%. In July 2024, the indoor humidity in our laboratory was maintained around 55 ± 1.5% at a constant temperature of 25℃ and pressure of 1.0 atmosphere controlled by the air conditioner. The indoor humidity RH_{am} and RH_{sub} of the substrate are both measured by a humidity sensor with a metal probe (±2%, Anymetre TH21E), see Fig. 5-19(a).

The hardware part of the machine vision system for ambient humidity feedback is composed of a laptop (ThinkPad neo14), a 4K HD camera (RER USB4KHDR01 V100, Shenzhen Rervison Company), and a matched camera holder with built-in light to brighten the image. The software part is developed on MATLAB R2023a to control cameras taking shots and a resolution of 1920×1080 pixels at a frequency of 3.33 Hz in a top-down view with the support of MATLAB Support Package for Webcams. The identification and tracking of the black marker in each frame are also analyzed synchronously through color-based recognition by MATLAB R2023a within 0.15 s, as shown in Fig. 5-19(b).

The three-step procedure to measure ambient humidity RH_{am} is summarized here as an instance. First, the image acquisition system should be started and captured in a resolution of 1920×1080 pixels at a frequency of 3.33 Hz after RH_{sub} achieving 90%. Then the Möbius actuator is placed on the substrate for 30 s until the local motion gradually becomes steady. At this moment, the analysis program is initiated and runs concurrently with the image acquisition system, shooting the steady local motion during a time duration of 75 s, see Fig. 5-19(c). Finally, the ambient humidity RH_{am} can be synchronously obtained on the laptop after the maximum delay of 15 s, as shown in Fig. 5-19(d).

In each one-third cycle, the total length L_M of three visible markers captured by the camera varied from the maximum to the minimum, and back to its maximum, which was recorded by a top-down camera to count the number of local motion during the observation time window. Through waveform analysis of the L_M-Time plot in Fig. 5-19(e), the duration of one-third local motion cycle can be obtained, and from which the corresponding local motion rate n_L is derived.

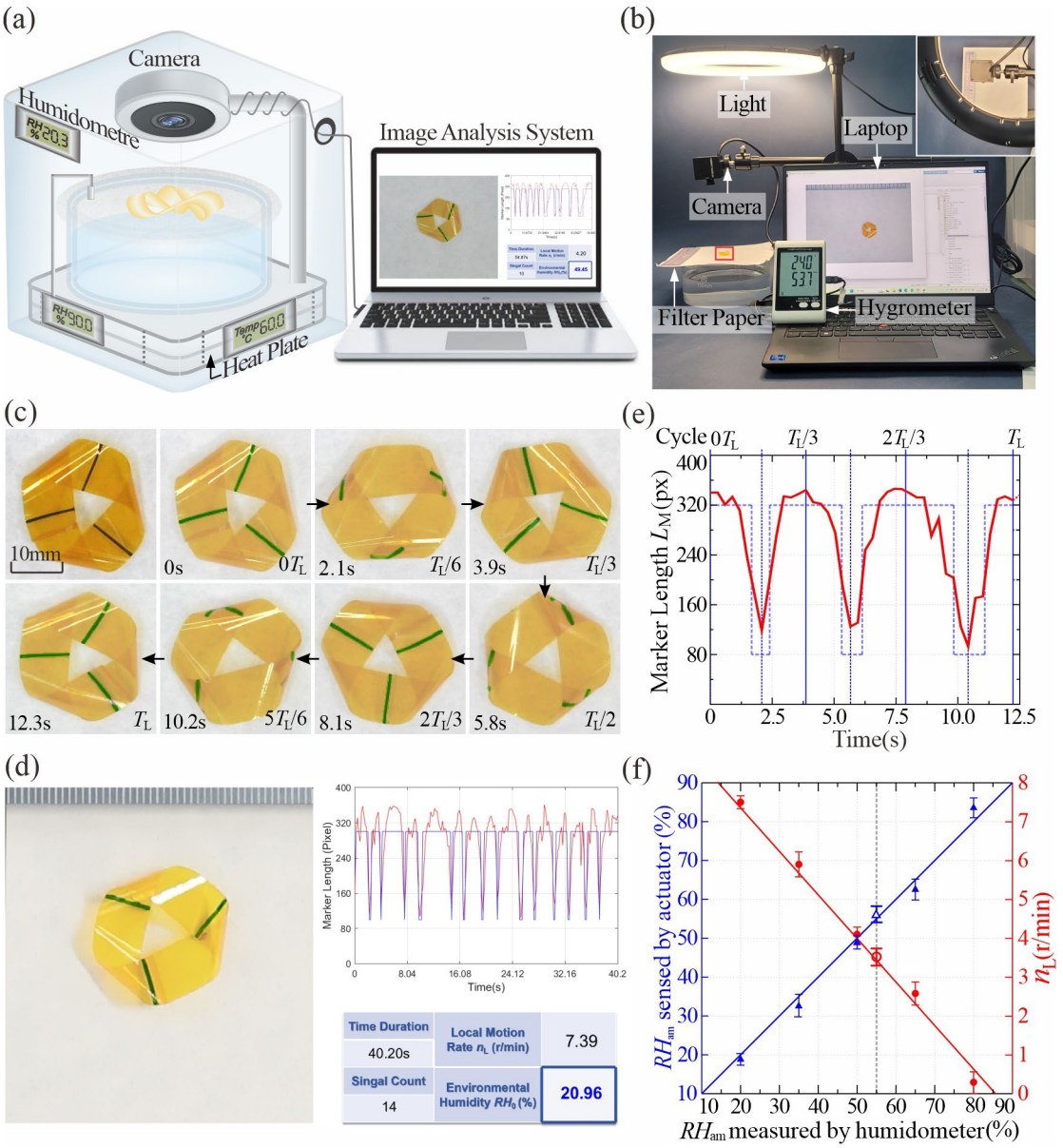

Fig. 5-19 Demonstration of *Ambient Humidity Meter*. (a) Schematic of the experimental setup for Möbius actuator (l = 56 mm, w = 8 mm, t = 25 μm). Three black lines are evenly drawn along the length placed on a filter paper with RH_{sub} = 90% and analyzed by machine vision overhead. (b) Experimental setup; (c) the snapped image of the Möbius actuator and identified black marks. (d) User Interface; (e) visible marker length L_M vs. Time; (f) local rotational rate n_L varied with RH_{am} measured by humidometer in comparison with RH_{am} sensed by the Möbius actuator. Tests were both conducted in a humidity chamber with the set RH_{am} of 20%, 35%, 50%, 65% and 80% (solid circle), and indoor environments of 53.7% (hollow circle).

According to the proportional relationship between the local motion rate n_L and the humidity difference ΔRH, as shown in Fig. 5-19(d). Therefore, $\Delta RH = RH_{sub} - RH_{up}$ can be deduced from our measured n_L, where RH_{sub} maintained around $90 \pm 1.5\%$. Through multiple experiments, we have verified that the ambient RH_{am} is around $5 \pm 0.80\%$ less than the humidity RH_{up} at the upper motion space of the actuator, which is 15 mm above the substrate. Therefore, RH_{am} can be obtained by subtracting 5% from the relative humidity RH_{up} at the upper surface of the actuator.

Tab. 5-8 Measured n_L and RH_{am} vs. Set RH_{am} and ΔRH.

Set RH_{am} (%)	Set ΔRH	n_L (r/min)	Measured RH_{am} (%)
20	65	7.51 ± 0.164	18.816 ± 1.464
35	50	5.87 ± 0.322	32.669 ± 1.464
50	35	4.10 ± 0.187	48.911 ± 1.670
53.8	31.2	2.58 ± 0.219	55.933 ± 1.955
65	20	0.98 ± 0.296	65.252 ± 2.643
80	5	0.28 ± 0.281	83.544 ± 2.509

By conducting tests in a humidity chamber with various RH_{am} ranging from 20% to 80%, our humidity meter can provide feedback on RH_{am} sensed by actuator, ensuring an error less than 5.37% within 2 minutes as listed in Tab. 5-8. When placed in an indoor environment, the sensed RH_{am} is 54.56%, which closely aligns with the RH_{am} of 53.7% measured by the humidometer, as depicted in Fig. 5-19(f).

5.7 Discussion and Conclusions

However, such motion phenomenon of the Möbius actuator is not uniquely observed from the bending deformation of isotropic humidity-sensitive AG film. To validate universality of the structural and driving mechanism, an alternative threefold Möbius actuator was fabricated from anisotropic thermal-sensitive liquid crystal elastomer (LCE) films (Appendix B). As mentioned in Section 1.2.5.1, LCEs transition from an anisotropic to an isotropic state, triggering concurrent contraction and elongation in perpendicular directions in Fig. 5-20(a).

Similar to the manufacture process of humidity-driven Möbius actuators, the rectangular strips of LCE films ($l + l_T = 72$ mm, $w = 10$ mm) were first cut along their nematic direction. Then a double-sided tape (20 μm, 3M^{TM}VHB^{TM} Tape 4910) with a

length of l_T = 2 mm and width of w was attached to one end of the film. Subsequently, one end of the strip was twisted 180° clockwise at each three-equidistant point and adhered to the other end to form the right-handed Möbius actuator with threefold rotational symmetry in the room temperature of 25℃ (± 1℃, Anymetre TH21E). The manufactured LCE actuator was put on the static hot plate preheated to 175 ± 2℃ (Heidolph, Hei-PLATE Mix Heat Core+).

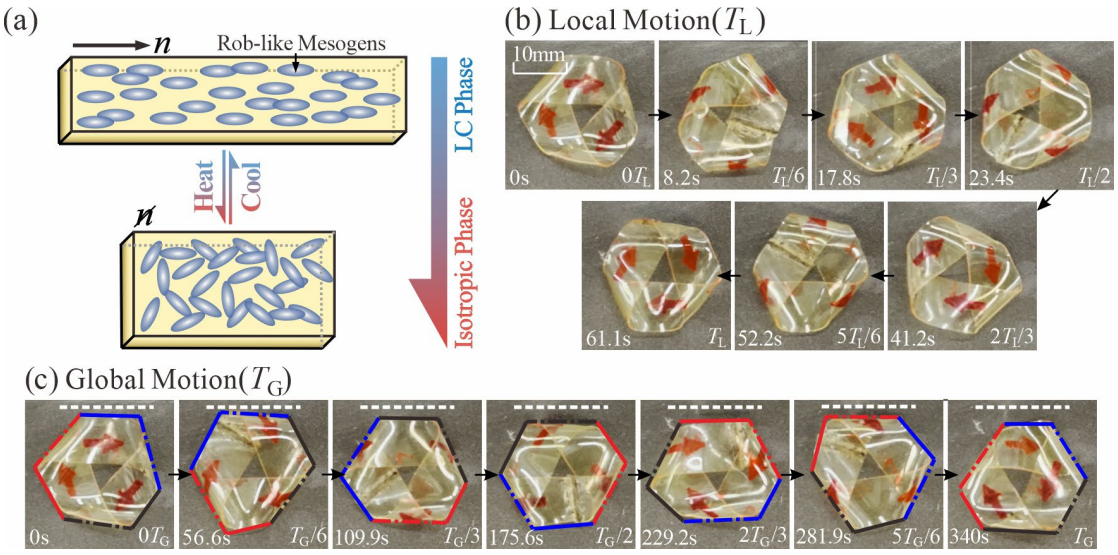

Fig. 5-20 Thermal-driven LCE-based Möbius actuator. (a) Contraction/Expansion of the LCE film through heating/cooling; (b) local motion and (c) global motion of the Möbius actuator made of LCE film (l = 70 mm, w = 10 mm, t = 180 μm) on a hot table heated to 175°C.

Remarkably, under uniform thermal stimulation, the LCE-based actuator exhibits similar local curvature propagation and global locomotion patterns as its counterpart fabricated from AG film, see Figs. 5-20(b) and (c). It confirms that no matter the humidity-driven AG film or the thermal-driven LCE film, it is clear that the Möbius structural design plays a crucial role in this type of environment-driven actuators to achieve a stable motion with unchanged overall geometry under constant stimuli, despite their distinct actuation mechanisms. This underlying principle can be attributed to the synergistic coupling between structural topology and the directional deformation of intelligent materials, further verifying the inherent potential of the single-component SBCM. The Möbius strip, with its non-orientable surface and curvature distribution, creates a deterministic mechanical pathway that converts localized deformations into coordinated conveyor-belt motion.

In conclusion, we present a threefold Möbius actuator fabricated from humidity - responsive materials, common AG films, which can achieve self-sustainable periodic motion with shape preservation, ultimately reaching ZEEMs. By relying solely on a constant humidity gradient, this design effectively simplifies driving strategy for the single-component SBCM featuring complex topological design.

Moreover, the underlying curvature-driven locomotion mechanism has been mathematically revealed by coupling moisture diffusion with developable surface geometry, thereby providing guidance for the integration of geometric design and external stimuli. The established correlation among the structural design, material deformation, and local/global motions of the actuator enables a parametric design based on specific requirements. Hence, we can demonstrate that the humidity-driven Möbius actuator can continuously conduct regular locomotion for over 252 hours, and output mechanical work. Furthermore, an ambient humidity meter was also developed utilizing machine vision and theoretical deduction to sense the ambient humidity, offering precise environmental monitoring to enhance the monitoring capabilities of environmental control systems.

Beyond this actuator, we anticipate that our theoretical model brings profound understanding to design novel soft actuators with distinctive topological structures to achieve enduring self-regulated locomotion driven by constant stimuli for forefront applications in advanced robotic systems. To further extend the engineering application of the Möbius actuators, simultaneous breakthroughs are required in three key aspects including materials, manufacturing, and application. This entails the development of novel composite materials with high fatigue resistance and stability, along with performance validation in fields such as sustainable energy and medical devices, in order to fully unlock their unique topological performance potential.

Chapter 6 Achievements and Future Works

This dissertation aims to establish a set of systematic design rules for SBCMs based on thin-walled structures. Through integration of geometric design, mechanical analysis, and actuation strategies, comprehensive theoretical models have been developed and validated through numerical and experimental methods. Beyond the core functionalities of SBCMs including precise control and high-efficiency transmission, our design methodologies also bring profound understanding to broaden forefront applications in advanced robotic systems. This chapter summarizes the main achievements of this dissertation and highlights opportunities for future work.

6.1 Main Achievements

- **Theoretical Model for the Bellow-shaped multi-component SBCM**

First, inspired by multistable drinking straws, the tubular outer balancer has been specially designed to dynamically mirror and neutralize the growing axial load under compression of the predefined inner bellow. The reverse-designed outer balancer has been coaxially assembled with the inner bellow to form a shell-based SBCM, which achieves a near-zero actuation force while maintaining a constant total strain energy through non-linear global deformation. A mechanical model based on discrete beam theory has been established to accurately predict the strain energy evolution of these tubular structures under axial loading, supplemented by parametric analysis of the balancer to elucidate the influence of key geometrical variables, thus guiding optimal design of the matched balancer. Subsequently, the effectiveness and reliability of the proposed design have been comprehensively verified through numerical simulation and a physical prototype. A case study has indicated that the compliant system could achieve a minimal actuation force with the largest value of 0.97 N, which only demands 3.62% of that of the stand-alone bellow.

The theoretical model, numerical analysis and experimental investigation of the novel bellow-shaped SBCM have been presented in Chapter 2. This technique has established an efficient design methodology for multi-component SBCMs by matching predefined shell structures with non-linear global deformation with well-designed balancers, thereby substantially reducing the required actuation force and enabling

precise control in applications, such as the oil bladder in the buoyancy system of undersea gliders.

- **Shape Preservation for Straw-inspired SBCTC Systems**

Second, motivated by the observation that a drinking straw can maintain stable bending at any circumferential direction, a statically balanced compliant torque coupling composed of series-connected frustum shells was proposed in Chapter 3. This novel single-component SBCM enables highly efficient torque transmission with conserved geometry through neutral stability across an infinite range of motion. To predict the bending stability and accurate bent configuration of the SBCTC, a simplified beam model based on the geometric features has been initially developed, which enables programmable design of the torque couplings. In addition, numerical simulation has uncovered the cyclic energy redistribution mechanism that preserves unchanged geometry with constant strain energy of a bent SBCTC unit under torsion, which has also been quantitatively verified by precise CT scanning. Furthermore, the torque transmission capabilities and limitations of the SBCTCs under different loads have been evaluated, which surpasses those of existing industrial flexible couplings.

The validated geometrical model of the bent SBCTC, numerical investigation, underlying mechanism of energy redistribution, scanning validation and experimental tests have been presented in Chapter 3. This novel design facilitates lightweight and low-cost SBCTCs capable of ultra-efficient torque transmission across dimensional scales, with potential applications from forefront robotics systems to precision micro-manufacturing beyond this prototype.

- **Geometry of the Möbius Strip**

Third, inspired by the shape-preserving characteristics of the single-component SBCM discussed in Chapter 2, the generalized Möbius strip was selected as the topological basis for designing a stimuli-responsive actuator. Initially, the precise geometry of the threefold Möbius strip has been achieved through integration of experimental measurements and theoretical derivation based on developable surfaces satisfying threefold rotational symmetry. This has led to a complete parametric design

framework, which provides the geometric basis for elucidating its self-sustainable motion with unchanged overall geometry. Furthermore, this framework provides a transferable methodology for designing structures with complex topology, enabling the systematic coordination of geometry, mechanics and actuation. Ultimately, this integrative approach bridges differential geometry and material properties, yielding novel insights into how topological constraints govern actuator functionality.

- **Actuation Strategy for the Möbius Actuator**

Finally, stimuli-responsive materials can address complex driving demands in single-component SBCMs featuring structural complexity, enabling self-sustainable motion under constant stimuli and realizing ZEEMs. Here, by overcoming challenges in geometric configuration, physical modeling, and mechanics-guided parametric optimization, a threefold Möbius actuator has been developed by integrating the threefold Möbius strips with humidity-responsive agarose films. A physical model is built here by coupling moisture diffusion with developable surfaces of the Möbius strip to unveil the curvature-driven locomotion mechanism with shape preservation, and to establish the quantitative correlations between the motion speed, the geometric and environmental parameters to optimize the design under given constraints. Hence, this has led to the development of diverse applications including long-term motion over 252 hours, mechanical work output and sensing environmental humidity.

The detailed geometrical reconstruction, the underlying motion mechanisms, experimental investigations and functional demonstrations have been presented in Chapter 4. This physical model established in this work not only provides theoretical guidance for the drive-structure matching in SBCMs, but also brings profound understanding to design novel soft actuators with distinctive topologies to achieve ZEEMs. Beyond these specific applications, an innovative design paradigm for cutting-edge applications in advanced robotics can be realized by combining static balance in SBCMs with stimuli-responsive materials.

6.2 Future Works

The research reported in this dissertation establishes design rules for statically balanced compliant shell mechanisms through topology optimization, mechanical

characterization based on three representative case studies, while also elucidating their strain energy evolution mechanisms. To enhance practical usage and universal adaptation of the theoretical framework, several potential topics can be further explored.

First, in our work on the bellow-shaped SBCM, the as-fabricated outer balancer with multiple units was rather difficult to deform synchronously under axial loads, leading to lower absolute values of forces in a limited effective reduction range than theoretical and numerical predictions, thus increasing the driving force of the SBCM. Considering the high sensitivity of the SBCM to manufacturing errors, it is necessary to employ more precise manufacturing processes or further optimize the geometric configuration to enhance system robustness, thereby reducing sensitivity to process variations and improving reliability of compliant systems.

Second, for our designed SBCTC units, a corresponding theoretical model based on mechanical constitutive relations has not yet been established, which constitutes a critical issue requiring resolution in subsequent research. Experimental results also indicate that its torque transmission capacity is subjected to a distinct upper limit under large transmission angles, which is inferior to that of industrial alternatives. To overcome this limitation, it is necessary to conduct an in-depth study of its failure mechanism to guide the iteration of high-performance designs. Furthermore, developing multi-scale models is also essential for SBCTC to perform reliably across different scales to extend its applicability.

Third, although numerical analysis has demonstrated strong applicability in previous research of the SBCMs made of traditional materials, the lack of constitutive relationships for stimuli-responsive materials significantly restricts the applicability of numerical analysis, which demands further exploration in material constitutive relationships. Besides, the soft and smart actuators are infinite-dimensional systems governed by highly nonlinear partial differential equations[181], which poses fundamental challenges to establishing generalized theoretical models for ZEEMs. Furthermore, systematic integration of various stimuli-responsive materials with diverse SBCMs requires further exploration to expand the functionality beyond sensing and multimodal locomotion. For instance, leveraging its long-term operational stability, these systems show promising potentials in emerging areas like autonomous environmental monitoring and adaptive energy harvesting.

Fourth, this study concentrates on theoredesign and verification of statically balanced compliant shell mechanisms under quasi-static and low-speed conditions. Future work will extend to the dynamics level, with an emphasis on investigating the natural frequency characteristics of compliant mechanisms and their influence on system stability, thereby refining the full-range performance model.

Finally, beyond the integrated design of geometry, materials, and actuation, statically-balanced compliant shell mechanisms still face precision fabrication hurdles to achieve high transmission efficiency and neutral stability. Although the introduction of the stimuli-responsive materials has offered one solution to address the actuation complexity in statically balanced systems, critical challenges still remain. Developing a generalized theoretical model to elucidate the shape preservation in SBCMs and investigating multi-physics coupled mechanisms for high-precision control present a crucial research frontier that demands further breakthroughs.

References

[1] Herder J L. Energy-free Systems. Theory, conception and design of statically balanced spring systems [D]. Delft, The Nederlands: Technische Universiteit Delft, 2001.

[2] Chheta Y R, Joshi R M, Gotewal K K, et al. A review on passive gravity compensation [C]. International Conference of Electronics, Communication and Aerospace Technology (ICECA). IEEE, 2017, 1: 184-189.

[3] Lubecki M, Stosiak M, Skačkauskas P, et al. Development of composite hydraulic actuators: A review [J]. Actuators, 2022, 11(12): 365.

[4] Karakuş R, Tanık E. Transmission angle in compliant four-bar mechanism [J]. International Journal of Mechanics and Materials in Design, 2023, 19(3): 713-727.

[5] Howell L L. Compliant mechanisms [M]. New York, The USA: John Wiley & Sons, 2008: 1-47.

[6] 陈贵敏, 于靖军, 马洪波等. 柔顺机构设计理论与实例 [M]. 北京: 高等教育出版社, 2015: 3-48.

[7] Megaro V, Zehnder J, Bächer M, et al. A computational design tool for compliant mechanisms [J]. ACM Transitions on Graphics, 2017, 36(4): 82:1-12.

[8] Ling M, Howell L L, Cao J, et al. Kinetostatic and dynamic modeling of flexure-based compliant mechanisms: a survey [J]. Applied Mechanics Reviews, 2020, 72(3): 030802.

[9] Ge J, Wang X, Drack M, et al. A bimodal soft electronic skin for tactile and touchless interaction in real time [J]. Nature Communications, 2019, 10(1): 4405.

[10] 张宪民. 柔顺机构拓扑优化设计 [J]. 机械工程学报, 2003, 39(11): 47-51.

[11] Hubbard N B, Wittwer J W, Kennedy J A, et al. A novel fully compliant planar linear-motion mechanism [C]. International Design Engineering Technical Conferences and Computers and Information in Engineering Conference. 2004, 46954: 1-5.

[12] Santiago-Prowald J, Baier H. Advances in deployable structures and surfaces for large apertures in space [J]. CEAS Space Journal, 2013, 5: 89-115.

[13] Seffen K A. Compliant shell mechanisms [J]. Philosophical Transactions of the Royal Society A: Mathematical, Physical and Engineering Sciences, 2012, 370(1965): 2010-2026.

[14] Kota S, Joo J, Li Z, et al. Design of compliant mechanisms: applications to MEMS [J]. Analog Integrated Circuits and Signal Processing, 2001, 29(1): 7-15.

[15] Norman A D, Seffen K A, Guest S D. Morphing of curved corrugated shells [J]. International Journal of Solids and Structures, 2009, 46(7-8): 1624-1633.

[16] Liu K, Tachi T, Paulino G H. Invariant and smooth limit of discrete geometry folded from bistable origami leading to multistable metasurfaces [J]. Nature Communications, 2019, 10(1): 4238.

[17] He G, Sparks C, Gravish N. Grasping and rolling in-plane manipulation using deployable tape spring appendages [J]. Science Advances, 2025, 11(15): eadt5905.

[18] Brown N C, Pruett H T, Bolanos D S, et al. Origami-inspired systems that improve adult diaper performance to enhance user dignity [J]. Wearable Technologies, 2022, 3: e6.

[19] Stacey J P, O'Donnell M P, Schenk M, et al. Visualizing compliance of composite shell mechanisms [C]. International Design Engineering Technical Conferences and Computers and Information in Engineering Conference. American Society of Mechanical Engineers, 2020, 83990: V010T10A007.

[20] 于靖军, 郝广波, 陈贵敏等. 柔性机构及其应用研究进展 [J]. 机械工程学报, 2015, 51(13): 53-68.

[21] Gallego Sánchez J A. Statically balanced compliant mechanisms: Theory and Synthesis [D]. Delft, The Nederlands: Technische Universiteit Delft, 2013.

[22] Gallego J A, Herder J L. Criteria for the static balancing of compliant mechanisms [C]. International Design Engineering Technical Conferences and Computers and Information in Engineering Conference. 2010, 44106: 465-473.

[23] Herder J L, van den Berg F P A. Statically balanced compliant mechanisms (SBCM's): an example and prospects [C]. International Design Engineering Technical Conferences and Computers and Information in Engineering Conference. American Society of Mechanical Engineers, 2000, 35203: 853-859.

[24] Plettenburg D H. The WILMER elbow orthosis [C]. 2007 IEEE 10th International Conference on Rehabilitation Robotics. IEEE, 2007: 1031-1035.

[25] Humans J M, Postema K, Geertzen J H B. Elbow orthoses: a review of literature [J]. Prosthetics and orthotics international, 2004, 28(3): 263-272.

[26] Kim H G, Kim D G, Do R H, et al. Development of deployable reflector antenna for the SAR-satellite: Part 1. Design and analysis of the main reflector using honeycomb sandwich composite structure [J]. Applied Sciences, 2024, 14(4): 1590.

[27] Tibert G. Deployable tensegrity structures for space applications [D]. Stockholm, Sweden: Kungliga Tekniska Högskolan, 2002.

[28] Yin S, Li X, Gao H, et al. Data-based techniques focused on modern industry: An overview [J]. IEEE Transactions on Industrial Electronics, 2014, 62(1): 657-667

[29] Yin S, Kaynak O. Big data for modern industry: challenges and trends [point of view] [J]. Proceedings of the IEEE, 2015, 103(2): 143-146.

[30] 张曙. 工业 4.0 和智能制造 [J]. 机械设计与制造工程, 2014, 43(8): 1-5.

[31] Ghobakhloo M. Industry 4.0, digitization, and opportunities for sustainability [J]. Journal of Cleaner Production, 2020, 252: 119869.

[32] Blind K, Kenney M, Leiponen A, et al. Standards and innovation: A review and introduction to the special issue [J]. Research Policy, 2023, 52(8): 104830.

[33] Nijssen J P A, Radaelli G, Kim C J, et al. Overview and kinetostatic characterization of compliant shell mechanism building blocks [J]. Journal of Mechanisms and Robotics, 2020, 12(6): 061009.

[34] Norman A D, Seffen K A, Guest S D. Multistable corrugated shells [J]. Proceedings of the Royal Society A: Mathematical, Physical and Engineering Sciences, 2008, 464(2095): 1653-1672.

[35] Hamouche W, Maurini C, Vincenti A, et al. Basic criteria to design and produce multistable shells [J]. Meccanica, 2016, 51(10): 2305-2320.

[36] Schenk, M. Textured shell structures [D]. Cambridge, The UK: University of Cambridge, 2012.

[37] Chi Y, Li Y, Zhao Y, et al. Bistable and multistable actuators for soft robots: Structures, materials, and functionalities [J]. Advanced Materials, 2022, 34(19): 2110384.

[38] Zhou C, Qing H, Sun H, et al. Multistable thin-shell metastructures for multiresponsive reconfigurable metabots [J]. Science Advances, 2025, 11(42): eadx4359.

[39] 邱海, 方虹斌, 徐鉴. 多稳态串联折纸结构的非线性动力学特性 [J]. 力学学报, 2019, 51(4): 1110-1121.

[40] Chen D H, Ozaki S. Numerical study of axially crushed cylindrical tubes with corrugated surface [J]. Thin-Walled Structures, 2009, 47(11): 1387-1396.

[41] Leemans J R, Kim C J, van de Sande W W P J, et al. Unified stiffness characterization of nonlinear compliant shell mechanisms [J]. Journal of Mechanisms and Robotics, 2019, 11(1): 011011.

[42] Meeussen A S, Van Hecke M. Multistable sheets with rewritable patterns for switchable shape-morphing [J]. Nature, 2023, 621(7979): 516-520.

[43] Dudek K K, Kadic M, Coulais C, et al. Shape-morphing metamaterials [J]. Nature Reviews Materials, 2025: 1-16.

[44] San H N, Lu G. Thin-walled corrugated structures: A review of crashworthiness designs and energy absorption characteristics [J]. Thin-Walled Structures, 2020, 157: 106995.

[45] Fang J, Yuan J, Wang M, et al. Novel accordion-inspired foldable pneumatic actuators for knee assistive devices [J]. Soft Robotics, 2020, 7(1): 95-108.

[46] Dizaji H S, Jafarmadar S, Asaadi S. Experimental energy analysis for shell and tube heat exchanger made of corrugated shell and corrugated tube [J]. Experimental Thermal and Fluid Science, 2017, 81: 475-481.

[47] Ino S, Sato M, Hosono M, et al. Development of a soft metal hydride actuator using a laminate bellows for rehabilitation systems [J]. Sensors and Actuators B: Chemical, 2009, 136(1): 86-91.

[48] Wharton P, You T L, Jenkinson G P, et al. Tetraflex: A multigait soft robot for object transportation in confined environments [J]. IEEE Robotics and Automation Letters, 2023, 8(8): 5007-5014.

[49] Aoki T, Ochiai A, Hirose S. Study on slime robot: development of the mobile robot prototype model using bridle bellows [C]. IEEE International Conference on Robotics and Automation, 2004. Proceedings. ICRA04. IEEE, 2004, 3: 2808-2813.

[50] Zang W, Chen M, Guo T, et al. Precise underwater gliders pitch control with the presence of the pycnocline [J]. Journal of Marine Science and Engineering, 2021, 9(9): 1013.

[51] Davis R E, Eriksen C C, Jones C P. Autonomous buoyancy-driven underwater gliders [J]. Technology and Applications of Autonomous Underwater Vehicles, 2002: 37-58.

[52] Eriksen C C, Osse T J, Light R D, et al. Seaglider: A long-range autonomous underwater vehicle for oceanographic research [J]. IEEE Journal of Oceanic Engineering, 2001, 26(4): 424-436.

[53] Yao Y, Chen Y, He L, et al. Design optimization for bellow soft pneumatic actuators in shape-matching [C]. 2023 IEEE International Conference on Soft Robotics (RoboSoft). IEEE, 2023: 1-7.

[54] Zhang B. Bistable and multi-stable thin-walled structures [D]. Oxford, The UK: University of Oxford, 2017.

[55] Bende N P, Yu T, Corbin N A, et al. Overcurvature induced multistability of linked conical frusta: how a “bendy straw” holds its shape [J]. Soft Matter, 2018, 14(42): 8636-8642.

[56] Wo Z, Filipov E T. Bending stability of corrugated tubes with anisotropic frustum shells [J]. Journal of Applied Mechanics, 2022, 89(4): 041005.

[57] Liu Y, Pan F, Ding B, et al. Multistable shape-reconfigurable metawire in 3D space [J]. Extreme Mechanics Letters, 2022, 50: 101535.

[58] Ben-Abu E, Zigelman A, Veksler Y, et al. Reprogrammable 3D Shapes from 1D Metamaterial [J]. Advanced Materials Technologies, 2025, 10(4): 2401113.

[59] Pan F, Li Y, Li Z, et al. 3D pixel mechanical metamaterials [J]. Advanced Materials, 2019, 31(25): 1900548.

[60] Ben-Abu E, Veksler Y, Elbaz S, et al. Growing structure based on viscous actuation of constrained multistable elements [J]. Advanced Materials Technologies, 2023, 8(14): 2202184.

[61] Ben-Abu E, Abramov Y, Fine A, et al. Directed instability as a mechanism for fabricating multistable twisting microstructure [J]. Advanced Engineering Materials, 2024, 26(12): 2400070.

[62] Peretz O, Ben Abu E, Zigelman A, et al. Multistable metafluid based energy harvesting and storage [J]. Advanced Materials, 2023, 35(35): 2301483.

[63] Flaum E, Prakash M. Curved crease origami and topological singularities enable hyperextensibility of *L. olor* [J]. Science, 2024, 384(6700): eadk5511.

[64] Russo A, Sinatra R, Xi F. Static balancing of parallel robots [J]. Mechanism and Machine Theory, 2005, 40(2): 191-202.

[65] Kobayashi K. Comparison between spring balancer and gravity balancer in inertia force and performance [J]. Journal of Mechanical Design, 2001, 123(4): 549-555.

[66] Kok S. Towards neutrally stable compliant shells [D]. Delft, The Netherlands: Technische Universiteit Delft, 2020.

[67] Schenk M, Guest S D. On zero stiffness [J]. Proceedings of the Institution of Mechanical Engineers, Part C: Journal of Mechanical Engineering Science, 2014, 228(10): 1701-1714.

[68] Schenk M, Herder J L, Guest S D. Design of a statically balanced tensegrity mechanism [C]. International Design Engineering Technical Conferences and Computers and Information in Engineering Conference. 2006, 42568: 501-511.

[69] Chaudhary G, Ganga Prasath S, Soucy E, et al. Totimorphic assemblies from neutrally stable units [J]. Proceedings of the National Academy of Sciences, 2021, 118(42): e2107003118.

[70] Merriam E G, Howell L L. Non-dimensional approach for static balancing of rotational flexures [J]. Mechanism and Machine Theory, 2015, 84: 90-98.

[71] Morsch F M, Herder J L. Design of a generic zero stiffness compliant joint [C]. International Design Engineering Technical Conferences and Computers and Information in Engineering Conference. 2010, 44106: 427-435.

[72] Juan S H, Tur J M M. Tensegrity frameworks: Static analysis review [J]. Mechanism and Machine Theory, 2008, 43(7): 859-881.

[73] Tolou N, Henneken V A, Herder J L. Statically balanced compliant micro mechanisms (SB-MEMS): Concepts and simulation [C]. International Design Engineering Technical Conferences and Computers and Information in Engineering Conference. 2010, 44106: 447-454.

[74] Hoetmer K, Woo G, Kim C, et al. Negative stiffness building blocks for statically balanced compliant mechanisms: design and testing [J]. Journal of Mechanisms and Robotics, 2010, 2(4): 041007.

[75] Tolou N, Estevez P, Herder J L. Collinear-type statically balanced compliant micro mechanism (SB-CMM): experimental comparison between pre-curved and straight beams [C]. International Design Engineering Technical Conferences and Computers and Information in Engineering Conference. 2011, 54839: 113-117.

[76] Stapel A, Herder J L. Feasibility study of a fully compliant statically balanced laparoscopic grasper [C]. International Design Engineering Technical Conferences and Computers and Information in Engineering Conference. 2004, 46954: 635-643.

[77] de Lange D J B A, Langelaar M, Herder J L. Towards the design of a statically balanced compliant laparoscopic grasper using topology optimization [C]. International Design Engineering Technical Conferences and Computers and Information in Engineering Conference. 2008, 43260: 293-305.

[78] Wilkes D F. Rolamite: a new mechanical design concept[R]. Sandia National Lab.(SNL-NM), Albuquerque, The USA, 1969.

[79] Ulozas R V. An investigation of slipping in rolamite-type mechanisms [J]. Journal of Mechanical Engineering, 2004, 50(6): 302-309.

[80] Pellegrino S, Kebadze E, Lefort T, et al. Low-cost hinge for deployable structures[R]. University of Cambridge, Cambridge, The UK, 2002.

[81] Vorobyov M, Prokopenko D. Hydraulic pump based on the rolamite mechanism [J]. Ukrainian Journal of Mechanical Engineering and Materials Science, 2018, 4(1): 105-115.

[82] Shaw L A, Chizari S, Dotson M, et al. Compliant rolling-contact architected materials for shape reconfigurability [J]. Nature Communications, 2018, 9(1): 4594.

[83] Radaelli G. Reverse-twisting of helicoidal shells to obtain neutrally stable linkage mechanisms [J]. International Journal of Mechanical Sciences, 2021, 202: 106532.

[84] Sadeghi F, Jalalahmadi B, Slack TS, Raje N, Arakere NK. A review of rolling contact fatigue [J]. Journal of Tribology, 2009, 131(4): 041403.

[85] Kebadze E, Guest S D, Pellegrino S. Bistable prestressed shell structures [J]. International Journal of Solids and Structures, 2004, 41(11-12): 2801-2820.

[86] Guest S D, Pellegrino S. Analytical models for bistable cylindrical shells [J]. Proceedings of the Royal Society A: Mathematical, Physical and Engineering Sciences, 2006, 462(2067): 839-854.

[87] Schultz M R, Hulse M J, Keller P N, et al. Neutrally stable behavior in fiber-reinforced composite tape springs [J]. Composites Part A: Applied Science and Manufacturing, 2008, 39(6): 1012-1017.

[88] Murphey T, Pellegrino S. A novel actuated composite tape-spring for deployable structures [C]. 45th AIAA/ASME/ASCE/AHS/ASC structures, Structural Dynamics & Materials Conference. 2004: 1528.

[89] Seffen K A, Guest S D. Prestressed morphing bistable and neutrally stable shells [J]. Journal of Applied Mechanics, 2011, 78(1): 011002.

[90] Guest S, Kebadze E, Pellegrino S. A zero-stiffness elastic shell structure [J]. Journal of Mechanics of Materials and Structures, 2011, 6(1): 203-212.

[91] Hamouche W, Maurini C, Vidoli S, et al. Multi-parameter actuation of a neutrally stable shell: a flexible gear-less motor [J]. Proceedings of the Royal Society A: Mathematical, Physical and Engineering Sciences, 2017, 473(2204): 20170364.

[92] van der Lans D, Amoozandeh Nobaveh A, Radaelli G. Reversible shape morphing of a neutrally stable shell by untethered local activation of embedded Ni-Ti wires [J]. Journal of Intelligent Material Systems and Structures, 2023, 34(14): 1664-1677.

[93] Kok S, Radaelli G, Nobaveh A A, et al. Neutrally stable transition of a curved-crease planar shell structure [J]. Extreme Mechanics Letters, 2021, 49: 101469.

[94] Kok S, Nobaveh A A, Radaelli G. Neutrally stable double-curved shells by inflection point propagation [J]. Journal of the Mechanics and Physics of Solids, 2023, 171: 105133.

[95] Thomson W T B, Tait P G. Treatise on natural philosophy [M]. Oxford, The UK: Clarendon Press, 1867: P.142-268.

[96] Kulić I M, Thaokar R, Schiessel H. Twirling DNA rings—Swimming nanomotors ready for a kickstart [J]. Europhysics Letters, 2005, 72(4): 527.

[97] Golestanian R, Ajdari A. Analytic results for the three-sphere swimmer at low Reynolds number [J]. Physical Review E—Statistical, Nonlinear, and Soft Matter Physics, 2008, 77(3): 036308.

[98] De Jong M G, Van De Sande W W P J, Herder J L. Properties of twofold tape loops: The influence of the subtended angle [J]. Journal of Mechanisms and Robotics, 2019, 11(2): 020912.

[99] Vehar C, Kota S, Dennis R. Closed-loop tape springs as fully compliant mechanisms: preliminary investigations [C]. International Design Engineering Technical Conferences and Computers and Information in Engineering Conference. 2004, 46954: 1023-1032.

[100] Yang Y, Qin Y, Tang Y, et al. Deployable closed-loop tape-spring manipulators with mobile drive components on localized folds [J]. Mechanism and Machine Theory, 2022, 167: 104553.

[101] Seffen K A, Pellegrino S. Deployment dynamics of tape springs [J]. Proceedings of the Royal Society of London. Series A: Mathematical, Physical and Engineering Sciences, 1999, 455(1983): 1003-1048.

[102] Filipov E T, Redoutey M. Mechanical characteristics of the bistable origami hypar [J]. Extreme Mechanics Letters, 2018, 25: 16-26.

[103] Katritch V, Bednar J, Michoud D, et al. Geometry and physics of knots [J]. Nature, 1996, 384(6605): 142-145.

[104] Lickorish W B R. An introduction to knot theory [M]. New York, The USA: Springer, 1997: 20-46.

[105] Adams C C. The knot book [M]. New York, The USA: American Mathematical Soc., 2004: 71-139.

[106] Beves J E. Metal template synthesis of molecular knots and links [J]. Chimia, 2012, 66(4): 170-170.

[107] Ayers P L, Boyd R J, Bultinck P, et al. Six questions on topology in theoretical chemistry [J]. Computational and Theoretical Chemistry, 2015, 1053: 2-16.

[108] Starostin E L, van der Heijden G H M. The shape of a Möbius strip [J]. Nature Materials, 2007, 6(8): 563-567.

[109] Starostin E L, van der Heijden G H M. Equilibrium shapes with stress localisation for inextensible elastic Möbius and other strips [J]. Journal of Elasticity, 2015, 119(1): 67-112.

[110] Yakubo K, Avishai Y, Cohen D. Persistent currents in Möbius strips [J]. Physical Review B, 2003, 67(12): 125319.

[111] Moore A, Healey T. Computation of elastic equilibrium of complete Möbius bands and their stability [J]. Mathematics and Mechanics of Solids, 2019, 24(4): 939-967.

[112] Chen Y, Fried E. Möbius bands, unstretchable material sheets and developable surfaces [J]. Proceedings of the Royal Society A: Mathematical, Physical and Engineering Sciences, 2016, 472(2192): 20160459.

[113] Rudolph L. Braided surfaces and Seifert ribbons for closed braids [J]. Commentarii Mathematici Helvetici, 1983, 58(1): 1-37.

[114] Cimasoni D, Florens V. Generalized Seifert surfaces and signatures of colored links [J]. Transactions of the American Mathematical Society, 2008, 360(3): 1223-1264.

[115] Van Wijk J J, Cohen A M. Visualization of Seifert surfaces [J]. IEEE Transactions on Visualization and Computer Graphics, 2006, 12(4): 485-496.

[116] Shen Z, Chen F, Zhu X, et al. Stimuli-responsive functional materials for soft robotics [J]. Journal of Materials Chemistry B, 2020, 8(39): 8972-8991.

[117] Magdanz V, Stoychev G, Ionov L, et al. Stimuli-responsive microjets with reconfigurable shape [J]. Angewandte Chemie, 2014, 126(10): 2711-2715.

[118] He S, Dai J, Wan D, et al. Biomimetic bimodal haptic perception using triboelectric effect [J]. Science Advances, 2024, 10(27): eado6793.

[119] Dong Y, Wang J, Guo X, et al. Multi-stimuli-responsive programmable biomimetic actuator [J]. Nature Communications, 2019, 10(1): 4087.

[120] Yang Z, Wang Y, Lan L, et al. Bioinspired H-bonding connected gradient nanostructure actuators based on cellulose nanofibrils and graphene [J]. Small, 2024, 20(36): 2401580.

[121] Huang Z, Wu Z, Li C, et al. Self-healing yet strong actuator materials with muscle-like diastole and contraction via multilevel relaxations [J]. Advanced Materials, 2025, 37(5): 2413194.

[122] Chen T, Pang Z, He S, et al. Machine intelligence-accelerated discovery of all-natural plastic substitutes [J]. Nature Nanotechnology, 2024, 19(6): 782-791.

[123] Fusi G, Del Giudice D, Skarsetz O, et al. Autonomous soft robots empowered by chemical reaction networks [J]. Advanced Materials, 2023, 35(7): 2209870.

[124] Zhang Q, Wang Y, Lv Y, et al. Bioinspired zero-energy thermal-management device based on visible and infrared thermochromism for all-season energy saving [J]. Proceedings of the National Academy of Sciences, 2022, 119(38): e2207353119.

[125] Feng H, Lv Y, Yang X, et al. Bimodal visual sensors based on mechanoluminescence and biosensing for artificial intelligence-assisted Orthodontics [J]. Advanced Functional Materials, 2025, 35(10): 2416437.

[126] Fang K, Wan Y, Wei J, et al. Hydrogel-based sensors for human-machine interaction [J]. Langmuir, 2023, 39(48): 16975-16985.

[127] Wang X Q, Ho G W. Design of untethered soft material micromachine for life-like locomotion [J]. Materials Today, 2022, 53: 197-216.

[128] Kotikian A, McMahan C, Davidson E C, et al. Untethered soft robotic matter with passive control of shape morphing and propulsion [J]. Science Robotics, 2019, 4(33): eaax7044.

[129] Zhao Y, Hong Y, Qi F, et al. Self-sustained snapping drives autonomous dancing and motion in free-standing wavy rings [J]. Advanced Materials, 2023, 35(7): 2207372.

[130] Wang H, Zhao Z, Liu P, et al. Stretchable sensors and electro-thermal actuators with self-sensing capability using the laser-induced graphene technology [J]. ACS Applied Materials & Interfaces, 2022, 14(36): 41283-41295.

[131] Ahn C, Li K, Cai S. Light or thermally powered autonomous rolling of an elastomer rod [J]. ACS Applied Materials & Interfaces, 2018, 10(30): 25689-25696.

[132] Hu Z, Li Y, Lv J. Phototunable self-oscillating system driven by a self-winding fiber actuator [J]. Nature Communications, 2021, 12(1): 3211.

[133] Yang H, Li J, Lim K Z, et al. Automatic strain sensor design via active learning and data augmentation for soft machines [J]. Nature Machine Intelligence, 2022, 4(1): 84-94.

[134] Gravert S D, Varini E, Kazemipour A, et al. Low-voltage electrohydraulic actuators for untethered robotics [J]. Science Advances, 2024, 10(1): eadi9319.

[135] Wu Y, Dong X, Kim J, et al. Wireless soft millirobots for climbing three-dimensional surfaces in confined spaces [J]. Science Advances, 2022, 8(21): eabn3431.

[136] Si Y, Hu J, Dong Z. Bioinspired magnetically driven liquid manipulation as microrobot [J]. Cell Reports Physical Science, 2021, 2(6).

[137] Zhou H, Mayorga-Martinez C C, Pané S, et al. Magnetically driven micro and nanorobots [J]. Chemical Reviews, 2021, 121(8): 4999-5041.

[138] Helps T, Romero C, Taghavi M, et al. Liquid-amplified zipping actuators for micro-air vehicles with transmission-free flapping [J]. Science Robotics, 2022, 7(63): eabi8189.

[139] Fusi G, Del Giudice D, Skarsetz O, et al. Autonomous soft robots empowered by chemical reaction networks [J]. Advanced Materials, 2023, 35(7): 2209870.

[140] 赵维强.亲水聚合物材料的抗污与湿敏性能研究及应用 [D]. 天津: 天津大学, 博士学位论文，2020.

[141] Zhao X, Tang G, Mei D, et al. Stimuli-responsive actuators in water environment: a review and future research agenda [J]. International Journal of Extreme Manufacturing, 2024.

[142] Zhang Y, Zhang C, Wang R, et al. Development and challenges of smart actuators based on water-responsive materials [J]. Soft Matter, 2022, 18(31): 5725-5741.

[143] El-Atab N, Mishra R B, Al-Modaf F, et al. Soft actuators for soft robotic applications: A review [J]. Advanced Intelligent Systems, 2020, 2(10): 2000128.

[144] Meng H, Hu J. A brief review of stimulus-active polymers responsive to thermal, light, magnetic, electric, and water/solvent stimuli [J]. Journal of Intelligent Material Systems and Structures, 2010, 21(9): 859-885.

[145] Fick A. V. On liquid diffusion [J]. The London, Edinburgh, and Dublin Philosophical Magazine and Journal of Science, 1855, 10(63): 30-39.

[146] Apsite I, Salehi S, Ionov L. Materials for smart soft actuator systems [J]. Chemical Reviews, 2021, 122(1): 1349-1415.

[147] Wang Y, Liu J, Yang S. Multi-functional liquid crystal elastomer composites [J]. Applied Physics Reviews, 2022, 9(1).

[148] Kularatne R S, Kim H, Boothby J M, et al. Liquid crystal elastomer actuators: Synthesis, alignment, and applications [J]. Journal of Polymer Science Part B: Polymer Physics, 2017, 55(5): 395-411.

[149] Pu W, Wei F, Yao L, et al. A review of humidity-driven actuator: toward high response speed and practical applications [J]. Journal of Materials Science, 2022, 57(26): 12202-12235.

[150] Xu Z, Ding C, Wei D W, et al. Electro and light-active actuators based on reversible shape-memory polymer composites with segregated conductive networks [J]. ACS Applied Materials & Interfaces, 2019, 11(33): 30332-30340.

[151] Hu W, Lum G Z, Mastrangeli M, et al. Small-scale soft-bodied robot with multimodal locomotion [J]. Nature, 2018, 554(7690): 81-85.

[152] Huang H W, Sakar M S, Petruska A J, et al. Soft micromachines with programmable motility and morphology [J]. Nature Communications, 2016, 7(1): 12263.

[153] Wang X, Tan C, Chan K, et al. In-built thermo-mechanical cooperative feedback mechanism for self-propelled multimodal locomotion and electricity generation [J]. Nature Communications, 2018, 9(1): 1-10.

[154] Wu S, Hong Y, Zhao Y, et al. Caterpillar-inspired soft crawling robot with distributed programmable thermal actuation [J]. Science Advances, 2023, 9, eadf8014.

[155] Shin B, Ha J, Lee M, et al. Hygrobot: A self-locomotive ratcheted actuator powered by environmental humidity [J]. Science Robotics, 2018, 3(14): eaar2629.

[156] Dong Y, Wang J, Guo X, et al. Multi-stimuli-responsive programmable biomimetic actuator [J]. Nature Communications, 2019, 10(1): 4087.

[157] Jiang Z, Xiao Y, Cheng R, et al. Dynamic liquid crystalline networks for twisted fiber and spring actuators capable of fast light-driven movement with enhanced environment adaptability [J]. Chemistry of Materials, 2021, 33(16): 6541-6552.

[158] Zhao Y, Hong Y, Qi F, et al. Self-sustained snapping drives autonomous dancing and motion in free-standing wavy rings [J]. Advanced Materials, 2023, 35(7): 2207372.

[159] Kim D S, Lee Y J, Kim Y B, et al. Autonomous, untethered gait-like synchronization of lobed loops made from liquid crystal elastomer fibers via spontaneous snap-through [J]. Science Advances, 2023, 9(20): eadh5107.

[160] Wang S, Gao Y, Wei A, et al. Asymmetric elastoplasticity of stacked graphene assembly actualizes programmable untethered soft robotics [J]. Nature Communications, 2020, 11(1): 4359.

[161] Jeon J, Choi J C, Lee H, et al. Continuous and programmable photomechanical jumping of polymer monoliths [J]. Materials Today, 2021, 49: 97-106.

[162] Zhao Y, Chi Y, Hong Y, et al. Twisting for soft intelligent autonomous robot in unstructured environments [J]. Proceedings of the National Academy of Sciences, 2022, 119(22): e2200265119.

[163] Fu L, Zhao W, Ma J, et al. A humidity-powered soft robot with fast rolling locomotion [J]. Research, 2022.

[164] Kim Y B, Yang S, Kim D S. Sidewinder-Inspired self-adjusting, lateral-rolling soft robots for autonomous terrain exploration [J]. Advanced Science, 2024, 11(14): 2308350.

[165] Baumann A, Sánchez-Ferrer A, Jacomine L, et al. Motorizing fibres with geometric zero-energy modes [J]. Nature Materials, 2018, 17(6): 523-527.

[166] Ziebert F, Kulić I M. The Hidden Wheel-Within [J]. arXiv preprint arXiv:2510.06830, 2025.

[167] Li K, Chen Z, Xu P. Light-propelled self-sustained swimming of a liquid crystal elastomer torus at low Reynolds number [J]. International Journal of Mechanical Sciences, 2022, 219: 107128.

[168] Deng Z, Li K, Priimagi A, et al. Light-steerable locomotion using zero-elastic-energy modes [J]. Nature Materials, 2024, 23(12): 1728-1735.

[169] Zhu Q, Liu W, Khoruzhenko O, et al. Animating hydrogel knotbots with topology-invoked self-regulation [J]. Nature Communications, 2024, 15(1): 300.

[170] Zhu Q, Liu W, Khoruzhenko O, et al. Closed twisted hydrogel ribbons with self-sustained motions under static light irradiation [J]. Advanced Materials, 2024, 36(28): 2314152.

[171] Nie Z, Zuo B, Wang M, et al. Light-driven continuous rotating Möbius strip actuators [J]. Nature Communications, 2021, 12(1): 2334.

[172] Nie Z Z, Wang M, Huang S, et al. Multimodal self-sustainable autonomous locomotions of light-driven Seifert ribbon actuators based on liquid crystal elastomers [J]. Angewandte Chemie, 2023, 135(25): e202304081.

[173] 聂振洲.液晶弹性体拓扑几何结构的协同驱动机制研究 [D]. 南京: 东南大学, 2023.

[174] Qi F, Li Y, Hong Y, et al. Defected twisted ring topology for autonomous periodic flip-spin-orbit soft robot [J]. Proceedings of the National Academy of Sciences, 2024, 121(3): e2312680121.

[175] Guo H, Li K, Priimagi A, et al. Emergent locomotion in self-sustained, mechanically connected soft matter rings [J]. Advanced Materials, 2025: 2503519.

[176] Zang T, Muhetaer R, Zhang C, et al. Self-sustained liquid crystal elastomer actuators with geometric zero-elastic-energy modes [J]. Macromolecular Rapid Communications, 2025: 2500134.

[177] Juvinall R C, Marshek K M. Fundamentals of machine component design [M]. New York, The USA: John Wiley & Sons, 2020: 701-711.

[178] Carton M, Kowalewski J F, Guo J, et al. Bridging hard and soft: Mechanical metamaterials enable rigid torque transmission in soft robots [J]. Science Robotics, 2025, 10(100): eads0548.

[179] Usman M, Khorasani A, Hubert T, et al. Modeling of flexible shaft for robotics applications [J]. Mechanism and Machine Theory, 2024, 197: 105647.

[180] McKeen L W. Fatigue and tribological properties of plastics and elastomers [M]. Oxford, The UK: William Andrew, 2016: 27-44.

[181] Armanini C, Boyer F, Mathew A T, et al. Soft robots modeling: A structured overview [J]. IEEE Transactions on Robotics, 2023, 39(3): 1728-1748.

[182] 王华, 康荣杰, 王兴坚等. 软体弯曲驱动器设计与建模 [J]. 北京航空航天大学学报, 2017, 43(5): 1053-1060.

Appendix

A. Preparation of Agarose Films

The four-step procedure to fabricate agarose films of 25μm is summarized as an instance. First, 6.0 g of AG powder was dissolved in 180ml of *N*, *N*-dimethylformamide (DMF, Tianjin Concord Technology Co., Ltd., AR grade) with vigorous stirring, and then the mixture was heated to 95°C until the AG powder was completely dissolved. After 4 hours of continuous stirring, 0.04 g of phenol red (PR, Beijing Solarbio Technology Co., Ltd., AR grade) was added to the solution as a dye to stain the films into orange for observation. The resultant solution was then cast onto two horizontally placed glass molds (180mm×180mm) and dried in a ventilated environment at 25 ± 5°C with the ambient relative humidity (RH_{am}) of 35 ± 10%. After 72 hours of drying, the AG films were gently taken off the glass and stored in dry-sealing bags. The film thickness *t* was adjusted by the amount of solution cast onto the glass mold, as shown in Fig. A2.

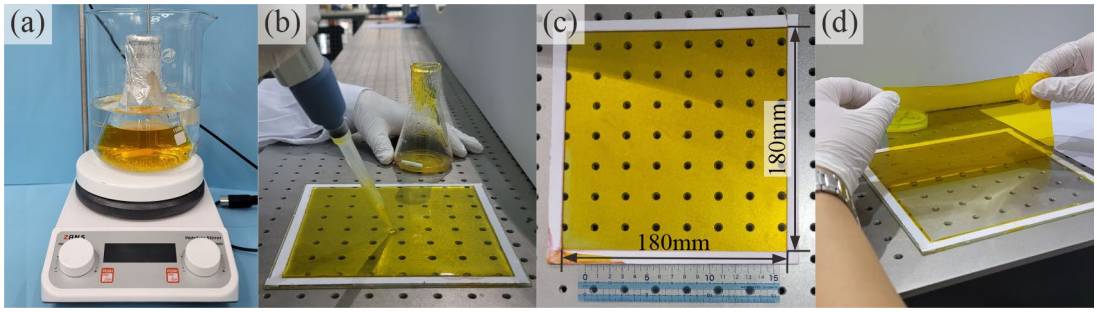

Fig. A1 Fabrication of AG films. (a) Dissolving AG powder into DMF and PR mixture on the hot plate stirrer; (b) casting the solution onto a horizontally placed glass mold; (c) drying the film in a ventilated environment; (d) taking the AG film off the plate.

Different from the second step of the fabrication process mentioned above, 0.20 g of titanium dioxide powder (TiO_2, Tianjin Heowns Technology Co., Ltd., analytical reagent) instead of phenol red was added to the solution as a dye to stain the films into white for DIC and 3D scanning tests. The film thickness *t* was adjusted by the amount of solution cast onto the glass mold, see Fig. A2. After full drying, the thickness of the films was volatilized to approximately one-quarter of the original thickness of the AG/DMF solution. Details of AG films of different colors and thicknesses, and AG

powders purchased from different manufacturers corresponding to different experiments are all provided in Tab. A1.

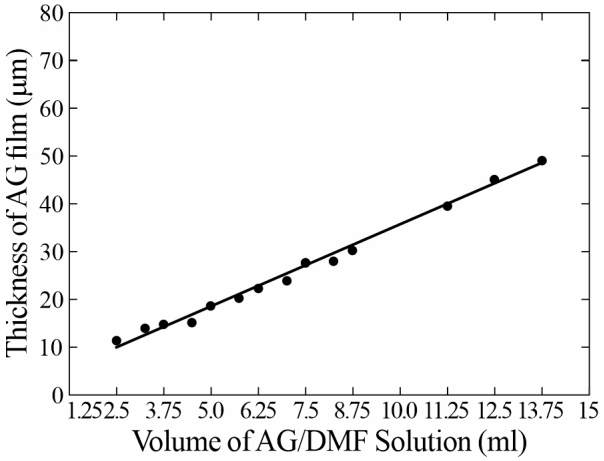

Fig. A2 Relationship of AG film thickness and the thickness of the AG/DMF solution.

Tab. A1 AG films fabricated from different AG power and staining agent.

Agarose Powder	Staining Agent	Experiments
$C_{24}H_{38}O_{19}$ Heowns, Biochemical Reagent	$C_{19}H_{14}O_5S$ Solarbio, Analytical Reagent	1. Local and global motions of Möbius actuators (Fig. 5-4) 2. Demo of *mechanical work output* (Fig. 5-18) 3. Demo of *Ambient Humidity Meter* (Fig. 5-19)
$C_{24}H_{38}O_{19}$ Yuanye, Biochemical Reagent	$C_{19}H_{14}O_5S$ Solarbio, Analytical Reagent	1. Tests of material properties (Fig. 5-3) 2. Möbius actuators in length l, width w, and thickness t in varied RH_{sub} (Figs.5-13 to 5-16) 3. Demo of *long-term motion* (Fig. 5-17)
$C_{24}H_{38}O_{19}$ Yuanye, Biochemical Reagent	TiO_2 Heowns, Analytical Reagent	The white Möbius actuators for DIC tests and 3D scanning (Fig. 5-8)

Tab. A2 Geometrical parameters of the N-fold Möbius actuators.

N	l (mm)	w (mm)	t (μm)
1	40	8	25
2	50	8	25
3	60	8	25
4	80	8	25
5	100	8	25

B. Fabrication of LCE Films and the Thermal-driven Möbius Actuator

To prepare thin, flat liquid crystal elastomer (LCE) films, we initially employed a mold with a sandwich-like structure, utilizing two glass plates and glass microspheres. The glass microspheres had a diameter of 400μm, and the glass plates in 10 × 10cm. Next, 1,4-bis-[4-(6-acryloyloxyhexyloxy)benzoyloxy]-2-methylbenzene (RM82) and pentaerythritol tetrakis (3-mercaptopropionate, PETMP) are prepared in a molar ratio of 2.75:1. A molar ratio of 2:1 of PETMP to 3,6-dioxa-1,8-octanedithiol (DODT), with the addition of 2wt% Irgacure 651 (I651) were also mixed in a chloroform solution. The thiol groups and acrylate groups were present in a 1:1.1 ratio. After ultrasonic dispersion for 10 minutes, a catalytic amount of dipropylamine (DPA) was introduced to the sonicated solution. Subsequently, this mixture was injected into the mold comprised of glass plates. After 4 hours of lower-crosslinking curing, the film precursors were formed and demolded. Finally, a strip of LCE precursors was stretched to 150% strain and irradiated with 365 nm light (0.22 W/cm^2) for 300 s to obtain thin and flat monodomain LCE films. Liquid crystal monomer RM82 were purchased from Shijiazhuang Yesheng Chemical Technology Co., Ltd. The chain extender (DODT), crosslinker PETMP, catalyst (DPA), and photoinitiator (I651) were obtained from Sigma-Aldrich.

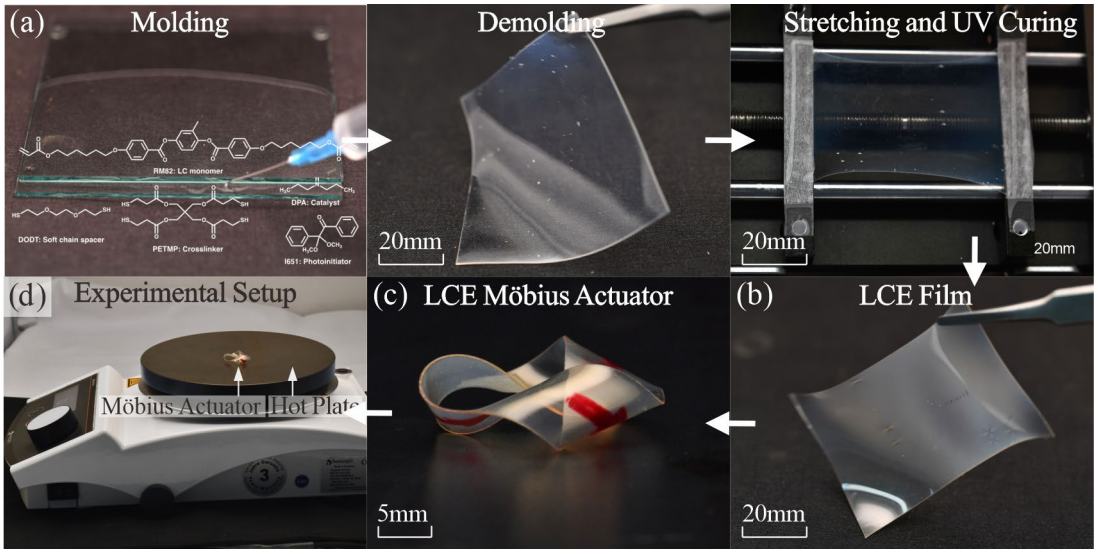

Fig. B1 Fabrication of LCE films and the thermal-driven Möbius actuator. (a) Experimental photographs of the processing procedures using the mold to prepare the monodomain LCE films. (b)-(c) Möbius actuators prepared by LCE films, in which the liquid crystal mesogens are aligned along the length axis of the strip; (d) experimental setup for the LCE Möbius actuators.

Similar to the manufacture process of humidity-driven Möbius actuators in Chapter 5, the rectangular strips of LCE films ($l + l_T = 72$ mm, $w = 10$ mm) were first cut along its nematic direction. Then a double-sided tape (20μm, 3M^{TM}VHB^{TM} Tape 4910) with a length of $l_T = 2$ mm and width of w was attached to one end of the film. Then, one end of the strip was twisted 180° clockwise at each three-equidistant point and adhered to the other end to form the right-handed Möbius actuator with threefold rotational symmetry in the room temperature of 25℃ (± 1℃, Anymetre TH21E). The manufactured LCE machine was put on the static hot plate preheated to 175 ± 2℃ (Heidolph, Hei-PLATE Mix 'n' Heat Core+).

中文大摘要

相较于传统的刚性机构，柔顺机构通过可变形的弹性元件来实现力、运动与能量的传递。其一体化成型的特点可有效消除装配误差，从而确保高运动精度，因而广泛适用于航空航天、医疗设备、精密仪器等尖端领域。其中，由曲面薄壁结构组成的柔顺壳体机构，兼具大范围可预测变形特性与可编程载荷调控能力，适用于空间受限且需大行程输出的应用场景。

常见的机械系统中普遍存在的摩擦、机械振动、材料迟滞及疲劳失效等问题，不仅因能量的过度耗散而降低系统效率，也会影响力学参数的精确传递与反馈。柔顺机构也不例外，其柔性构件以应变能形式储存的势能，亦会导致输入与输出端之间的能量损耗、进而降低整体运行效率。而将静平衡的概念引入柔顺机构，可为上述问题提供有效解决方案。静平衡柔顺机构通过其柔性组件内部的相互协调，在形变过程中始终保持系统的总应变能恒定，从而在理论上可实现无需外力与外部供能的自维持运行，并可在其运动范围内的任意位置保持静止，理论上使系统在运动全程的能量效率趋近 100%。

传统的静平衡柔顺机构通常采用多个杆件、弹簧等柔性组件协同作用，实现系统静平衡。其平衡机制依赖于组件间镜像对称的线性力学行为，使得各组件在变形过程中相互补偿与协同，从而保持系统整体的力与力矩恒等于零。然而，对于柔顺壳体构成的多组件系统，其显著的非线性力学特性使此类设计方法难以直接适用。因此，关键的挑战在于：如何将这一设计原理从梁模型拓展至壳体结构，以匹配由壳体大变形引起的非线性力-位移响应。除多组件协同机制外，静平衡可通过单组件系统内部应变能的动态重分布实现。例如，特定的壳体结构在变形过程中始终保持形状不变，以维持系统的总应变能的恒定。然而，该类系统的具体力学机理尚不明确，同时，这类结构的特殊几何构型也给驱动匹配带来挑战，如何选择合适的驱动策略仍需进一步探索。

综上所述，尽管静平衡柔顺壳体机构在工程轻量化与精密运动控制方面优势显著,与传统杆簧式静平衡系统相比，其固有的非线性大变形特性，也使其在结构设计、力学建模与驱动实现等方面仍然面临诸多挑战。为此，本研究融合构型设计与力学行为分析，系统设计了一系列基于壳体结构的静平衡柔顺机构，并结合刺激响应材料，实现了仅需恒定外部激励即可实现自持的周期性运动，从而为静平衡柔顺机构在新兴领域的工程应用提供了理论依据与技术支持。

本文首先设计了一种由波纹管与壳体平衡器构成的多组件静平衡柔顺壳体机构。通过建立波纹管轴向非线性大变形理论模型，实现了基于给定应变能曲线的逆向设计。进一步设计了与之匹配的壳体平衡器，并通过预应力装配使整个机构在往复变形中的总应变能近似恒定，在最优参数下驱动力较传统波纹管结构降低 96.38%。其次，提出一种基于多稳态吸管的单组件静平衡柔顺扭矩联轴器。

通过解析其弯曲稳态特性并确定相关的几何参数范围，建立了可精确预测稳态构型弯曲角度的简化梁模型。进一步结合数值仿真与扫描实验，揭示了联轴器单元在扭转过程中的形状保持与应变能重分配机制，从而实现了其在大弯曲角度下的高效扭矩传递。最后，通过融合莫比乌斯带几何与湿度响应材料，构建了三重对称莫比乌斯驱动器，使其在恒定的湿度梯度下可实现自持的周期性运动。结合可展曲面理论与三维扫描重建，完成了满足对称性边界条件的三重莫比乌斯几何重构，建立了驱动器自转与公转的理论模型，阐明了在恒定湿度梯度下的形状保持和持续运动机制，确立了运动速度与几何、环境参数之间的定量关系。参数优化后的驱动器可持续稳定运动超 252 小时，并兼具持续的机械功输出和环境湿度感知功能。本文的工作主要包括如下三个部分：

- **波纹管状静平衡柔顺机构的理论分析与设计**

在水下滑翔机的浮力调节系统中，波纹管状油囊通过改变内部液体体积实现浮力的精确控制。然而，该系统在运行中需持续克服波纹管变形时所产生的轴向刚度，从而导致能耗显著增加以及控制精度下降。针对这一问题，本研究旨在设计一种与波纹管形成镜像力学行为的柔顺壳体平衡器，从而构建多组件静平衡机构，实现近似零驱动力的高效运行。

首先，将波纹管结构沿周向离散化为一系列细长曲梁单元，并进一步将曲梁离散为多个直梁段。在欧拉-伯努利梁理论框架下，同时考虑弯曲应变能与环向应变能，建立了描述轴向压缩过程中结构变形与应变能演化的理论模型。采用数值方法求解了波纹管变形、作用力及应变能随位移变化的理论曲线，进而根据静平衡系统的驱动力始终为零，反推出为实现系统静平衡，外层套筒平衡器所需满足的力学曲线。受多稳态吸管压缩状态启发，设计了由圆弧、直线和三次多项式曲线组合构成截面的壳体平衡器。采用与波纹管相似的离散化方法与能量分析框架，建立了该平衡器在轴向拉伸下的理论模型，用以预测其应变能曲线。

接着，通过系统化的参数分析，明确了影响平衡器力学行为的关键几何参数：倾斜角与单元高度主导应变能的曲线形状，壳体厚度则决定应变能的大小。基于此，参数优化时先通过调节倾斜角与单元高度来调整形态，使平衡器的应变能曲线与波纹管相匹配、形成互补；再通过调节壳体厚度来标定量值，使机构总应变能维持在近似恒定的低水平。参数优化后的平衡器可精准匹配波纹管的应变能曲线，使二者的应变能互补并保持近似恒定，最终将机构的驱动力显著降低至单个波纹管驱动力最大值的 3.62%。

为验证理论模型的可靠性，我们分别建立了波纹管、平衡器及整体静平衡柔顺机构的有限元数值模型。计算结果表明，三者在加载过程中的变形演化、应变能积累以及力-位移响应曲线，均与理论分析结果高度一致，验证了数学模型与参数化分析方法的正确性。

在此基础之上，我们进一步通过实验对设计进行了验证。加工出的 3D 打印样机由于逐层堆积的制造工艺限制，存在一定的壁厚不均与轮廓几何误差，致使各平衡单元在实际变形中同步性略有降低。尽管如此，测试数据显示：在整个设计行程中超过 70%的范围内，机构输出的净作用力被稳定控制在单个波纹管最大驱动力的± 30%以内。这证明，即使存在工艺引入的偏差，该平衡机构仍能有效抵消波纹管的大部分非线性反力，显著降低了驱动需求。实验与仿真结果相互印证，充分验证了所述静平衡机构设计原理的正确性以及参数优化策略的有效性。

第二章的研究工作针对多组件静平衡柔顺壳体机构，基于其非线性力学特性，系统构建了相应的理论与技术体系，以实现近零驱动力下的稳定持续运动。

- **受多稳态吸管启发的静平衡柔顺扭矩联轴器**

虽已有诸多静平衡柔顺机构能实现无外部能量输入的精确力与位移传递，然而基于静平衡实现高效扭矩与旋转传递的结构设计仍待深入探索。与第 2 章所述波纹管式静平衡机构不同，静平衡亦可通过单一构件内部的协调实现，无需依赖构件间的相互补偿。

受多稳态吸管可在任意周向位置保持稳定弯曲这一独特力学特性的启发，本研究提出了一种由一系列串联的锥形壳单元构成的静平衡柔顺扭矩联轴器。该设计旨在将离散的中性稳定的状态转化为可在扭矩作用下实现连续、高效的扭矩与旋转运动传递。

首先，通过精细的数值模拟，我们系统分析了单个锥形壳单元在弯曲载荷下的稳态行为。模拟过程跟踪并记录了锥壳在变形过程中径向与周向曲率的动态演化。分析结果表明，变形并非均匀分布，而是高度集中于锥壳底部的局部反转区域。该区域作为柔性的“铰链”，是实现大角度弯曲的关键。与此同时，应变能也主要在此区域内集聚，并通过单元的串联结构沿轴向传递与重新分配，这一机制为联轴器实现整体扭矩平衡与低驱动能耗奠定了力学基础。

参数化研究表明，倾角和内径是决定双稳态能否实现及弯曲稳态角大小的关键，而壳体厚度仅影响力矩大小，与厚度立方近似成正比。基于数值结果揭示的几何特征，进一步建立了可准确预测弯曲稳态构型的简化梁模型，从而实现了联轴器单元的可编程化设计。

接着，对其单元扭转过程的数值分析表明，处于弯曲稳态的联轴器单元在扭转过程中始终保持总应变能恒定，且力矩为零，呈现出典型的静平衡特征。其机理在于材料沿锥壳周向的闭合路径发生周期性变形，且构件内部的应变能相互补偿与协调，实现扭转过程中的整体几何形态不变。进一步，对实物原型进行高精度 CT 扫描，重建了扭转过程中的三维几何形态，与数值模拟结果高度吻合，定量证实了形状保持性。

最后，为验证该联轴器在负载工况下的扭矩传递性能，本研究通过搭建专用实验平台开展的系统测试表明：当扭转传递角度小于 30°时，其传递效率超过 97%。即使当扭矩传递角度增大至 90°以上，效率仍可维持在 75%以上，显著优于传统柔性联轴器。

第三章的工作围绕单组件静平衡柔顺壳体机构展开，深入揭示了该静平衡柔性联轴器在扭转过程中的形状保持机制，并据此开发出一种新型柔性联轴器，实现了显著超越传统方案的扭矩传递效率。

- **莫比乌斯带的几何重建**

针对基于静平衡柔顺机构的驱动器，其周期性可持续运动的实现,关键依靠于特定的几何构型与刺激响应材料之间的协同设计。几何设计对实现零能量平衡机构与中性稳定至关重要，直接影响结构的完整性与运动性能。受静平衡柔顺扭矩联轴器揭示的“形状保持”特性，本研究中选择广义莫比乌斯带作为壳体驱动器的基本构型。该闭环构型本身的连续对称性，确保了其在运动过程中能够始终保持恒定的几何形状。此外，该莫比乌斯构型可通过简单的弯曲与粘接工艺，由薄膜材料直接制备，工艺简便且易于实现，为其与各类智能材料的集成及后续的功能化拓展提供了便利。

在确定基本构型后，需进一步优化其对称的扭转数以实现稳定驱动。经优化选择的三重对称莫比乌斯结构，既能克服一重、二重结构因接触不稳定而无法维持运动的问题，又可避免四重、五重结构因预应力匮乏而产生的局部褶皱。在分析莫比乌斯驱动器之前，首先采用三维扫描技术以及非接触全场应变测量系统（DIC），精确获取了湿度驱动莫比乌斯带驱动器在运动过程中的三维形貌。基于不可拉伸可展曲面理论框架，并结合其实际主曲率分布及三重对称边界条件，将复杂闭环结构合理简化为由三个近似平坦的梯形锥面与连接它们的柱面所组成的几何体系。通过进一步数值拟合，分别用二元四次椭圆方程拟合柱面区域，以及欧拉曲线拟合锥面区域，以得到了与实验数据高度吻合的驱动器几何模型。分析表明，驱动器在持续旋转运动中，整体形状与曲率分布保持高度稳定，并与静态的几何形状几乎一致。这一“形状保持”特性是实现驱动器稳态运动的重要几何基础。

第四章聚焦于结构设计，利用形状保持特性选择了三重莫比乌斯结构，并依据不可展曲面理论重构其几何形态，通过参数化分析与应力分布研究为后续设计提供理论依据。

- **三重对称的莫比乌斯驱动器**

利用琼脂糖薄膜中羟基的亲水特性，该薄膜在吸水时迅速弯曲、失水时迅速恢复平整。通过将其与三重对称莫比乌斯带相结合，构建出在恒定湿度梯度下可呈现两种耦合周期性运动的驱动器：其一，材料自身沿条带路径周期性地弯曲和伸直，适应各处的曲率变化，形成似传送带般的局部自转运动；其二，从整体来看，莫比乌斯驱动器的六边形轮廓绕其中心轴旋转，形成全局公转运动。

基于第四章中建立的精确几何模型，采用能量分析法系统揭示了驱动器运动过程中的能量转换机制。基于材料沿条带长度方向均匀运动的合理假设，研究提出在周期性旋转中，驱动器从环境中吸收的湿度能与释放的机械能之间保持动态平衡。通过融合湿度扩散动力学与可展曲面理论，从数学上推导出由局部曲率梯度驱动、并在整体形状约束下维持持续旋转的运动方程。进一步地，通过对接触区域滚动摩擦的建模分析，阐明了局部变形如何通过摩擦耦合转化为全局旋转。该理论模型不仅明确了条带宽度与长度、材料厚度、湿度差值等关键参数与运动性能之间的定量关系，从而为面向多样化场景的莫比乌斯驱动器结构设计、性能预测与系统优化提供了理论依据与设计指南。为系统验证所建立理论模型的精确性与可靠性，本研究在不同湿度环境下对多种几何参数的莫比乌斯驱动器进行了系列化实验测试。

结果表明，该莫比乌斯驱动器在最优条件下的自转速度可达 25.95r/min，显著超越现有受恒定刺激驱动的软体驱动器最大转速（约 1.92r/min），展现出优异的运动响应能力。进一步地，驱动器在恒定湿度环境下实现了长达 252 小时的连续稳定运行，其间累计完成超过 47500 次局部运动循环，充分证明了其在长期工作中的结构耐久性与运动可靠性。

除了长期稳定的运动特性外，该驱动器还表现出良好的机械功输出能力，例如通过公转运动驱动上方纸盘持续旋转，展现出作为软体致动器的潜在应用价值。此外，研究还将湿度响应特性与传感功能相结合，在单一静平衡系统中实现了驱动与传感的一体化集成：基于驱动器运动状态与环境湿度的耦合关系，结合机器视觉技术，系统可在 2 分钟内完成对环境湿度的快速、精准检测，从而拓展了其在环境交互与自主反馈系统中的功能潜力。

第五章将湿度响应琼脂糖薄膜与莫比乌斯几何相集成，构建出在恒定刺激下可实现自维持的周期性运动的驱动器。所建立的理论模型能为设计具有独特拓扑结构的新型软体驱动器提供了更为深入的理解，使其能够在恒定激励下实现持久的自调节运动，从而推动其在先进机器人系统等前沿领域的应用。

- **总结与展望**

本论文围绕静平衡柔顺壳体机构开展，通过结构设计与力学表征，实现该类机构在无外部能量或负载条件下的持续变形能力。进一步结合刺激响应材料，选择合适的驱动策略，为静平衡壳体柔顺机构的创新设计，以及新兴领域的工程应用奠定理论基础。

（1）受制造工艺制约，波纹管式多单元静平衡机构的外平衡器，以及内部波纹管在轴向载荷下难以协同变形，致使其实际驱动力的下降范围与幅值均低于理论预期，进而增加了整体机构的驱动力。由于该机构对几何误差极为敏感，亟需发展高精度成形工艺或推进鲁棒性几何优化，以减少由工艺波动产生的误差，提升机构在实际工况下的可靠性。

（2）针对所提出的静平衡柔性扭矩联轴器，目前尚未建立基于力学本构关系的理论解析模型，是后续研究需要解决的问题。实验结果表明，在大传动角工况下，其可稳定传递的最大扭矩存在明确上限，且目前仍低于工业同类产品。因此，需进一步揭示其失效机理在大角度传动下的失效机理与性能衰减规律，从而指导高性能设计与优化设计。此外，需建立跨尺度理论模型，以指导面向微小型传动系统与大型工业装备的定制化设计与可靠应用。同样地，该静平衡柔顺壳体机构在实现高传递效率与中性稳定方面仍面临精密制造瓶颈。

（3）尽管商业化数值模拟软件在分析传统材料构成的静平衡机构的力学分析方面已较为成熟，但对于刺激响应材料而言，由于缺乏准确描述其耦合力学-物理场关系的本构模型，现有软件难以直接用于该类材料驱动器的可靠分析与设计。此外，本研究目前建立的理论模型主要针对湿度响应驱动机制，尚缺乏系统性的拓展，未能涵盖热、光、电等其他典型物理场激励下的材料响应与驱动器行为模拟。因此，未来研究需进一步发展适用于多物理场耦合激励的本构理论，并构建相应的数值模拟框架，以支持更广泛类型的智能驱动器设计与优化。

（4）软体智能驱动器作为由非线性偏微分方程描述的无穷维系统，为建立基于零弹性能量模式的普适理论模型带来相应挑战。为拓展该类系统的应用边界，关键在于加强材料-结构-驱动的协同设计，以实现多功能集成，开拓其在传感，多模式运动之外的新兴领域应用。虽然刺激响应材料为系统驱动提供了新途径，但在形状保持机理的普适理论构建、多物理场耦合与高精度控制等方面，仍存在若干关键科学问题亟待突破，构成该领域未来重要研究方向。

（5）本研究聚焦于静平衡柔顺壳体机构在准静态、低速条件下的设计与实验验证。在此基础上，后续研究将拓展至动力学层面，重点考察柔顺机构的固有

频率特性及其对系统稳定性的影响机制，从而建立覆盖全工况的系统性能模型，为实际工程应用提供更完备的理论指导。

关键词：柔顺机构，多稳态，静平衡，吸管结构，莫比乌斯带

Publications and Research Projects

Journal Papers:

[1] Wang S, Yang X, Ma J*, Chen Y. A theoretical design of a bellow-shaped statically balanced compliant mechanism [J]. Mechanism and Machine Theory, 2021, 161: 104295. (学生一作，对应第二章)

[2] Yang X, Ma J*, Chen Y. A straw-inspired statically balanced compliant torque coupling [J]. Mechanical Sciences, 2025, 16, 831-849. (第一作者，对应第三章)

[3] Yang X#, Zhao W#, Ma J#, Fu L, Liu M, Xu C, Hu Z, Lv J, Chen Y*, Zhang L*. Threefold Möbius machine [J]. Advanced Functional Materials, 2025, 202420815. (共同第一作者，对应第四，五章)

Research Projects Participated in:

[1] 国家自然科学基金杰出青年项目：机构运动学与折展结构，项目编号 51825503, 参与。

[2] 国家自然科学基金重点项目：可编程超材料的构建理论与性能调控策略研究，项目编号 52035008, 参与。

[3] 国家自然科学基金重点国际（地区）合作研究项目：多模式折纸机器人的重构机构理论与机械智能设计研究，项目编号 52320105005, 参与。

Acknowledgments

First and foremost, I would like to express my deep gratitude to my two supervisors, Prof. Yan Chen and Prof. Jiayao Ma, for their sustained motivation, constant encouragement, patient guidance throughout my entire research career. Prof. Chen has been far more than an academic mentor to me. Not only does she generously share her deep expertise and richness of her life wisdom, but she also acts as a family who secured every opportunity for my growth and presentation. Meanwhile, Prof. Ma, with his exceptional clarity of logic and rigorous reasoning, consistently cleared away my confusion. The demeanor and character transcend the specific research , ultimately become my precious asset that nurture my future career.

In Chapter 2, I would like to extend my acknowledgment to Academician Shuxin Wang for his original conception of this research, and Mr. Jinrui Yu for his assistance with the experiments. Experiments in Chapter 3 benefited greatly from contributions of my colleague and friend, Mr. Xinrui Tao. I would be remiss not to mention the co-workers of Chapter 5, whose determinations are crucial in sustaining our efforts through seven rejections and the entire six-year research journey. For conceptual insights and detailed guidance on this research, I would deeply thank Prof. Lei Zhang and Prof. Jiu'an Lv. I also deeply acknowledge Dr. Xinmeng Liu, Mr. Lei Fu, Mr. Chuhan Xu, and Dr. Zhiming Hu for their experimental support. Particular gratitude goes to my collaborator, Dr. Weiqiang Zhao, who created the first prototype and completed the early-stage experiments with me. Moreover, I would thank all my colleagues in the Most Lab, in particular Miss Kaili Xi and Xin Zhang for their caring companion, Mr. Chuhan Xu, Mr. Zhe Jiang, Mr. Zhibo Wei, Mr. Zhenhao Jia, Mr. Mengyue Li for good humour and Dr. Weiqi Liu, Dr. Yuanqin Gu, Dr. Xiao Zhang, Dr. Tianshu Wang for generous help, which lightened endless challenges we faced.

Finally, my sincerest gratitude goes to my parents, Ms. Bo Zhang, Mr. Guohua Yang, and my parents-in-law, Mrs. Wen Cai, Mr. Zhaoxiong Wang, this work would not have been possible without your all-round support and unconditional love. I am eternally grateful and wish you lasting health and happiness. My deepest love goes to my husband, Mr. Zhirui Wang, who steadily illuminates my whole life much like his profession. With you, life can never be boring. This dissertation is a tribute to my late grandma Ms. Lijuan Zhang, who never doubted that I would complete this journey.